A METAL-INSULATOR-SEMICONDUCTOR STUDY OF THE BULK AND SURFACE PROPERTIES OF $Hg_{1-x}Cd_xTe$

by

Robert William Bechdolt

SUBMITTED IN PARTIAL FULFILLMENT
OF THE REQUIREMENTS FOR THE
DEGREE OF

BACHELOR OF SCIENCE
and
MASTER OF SCIENCE

at the

MASSACHUSETTS INSTITUTE OF TECHNOLOGY

May 1977

Signature of Author.....
Department of Electrical Engineering, May 18, 1977

Certified by.....
Thesis Supervisor (Academic)

Certified by.....
Cooperating Company)

Accepted by.....
Chairman, Departmental Committee on Graduate Students

A METAL-INSULATOR-SEMICONDUCTOR STUDY OF THE

BULK AND SURFACE PROPERTIES OF $Hg_{1-x}Cd_xTe$

by

Robert William Bechdolt

Submitted to the Department of Electrical Engineering on May 12, 1977 in partial fulfillment of the requirements for the Degrees of Bachelor of Science and Master of Science.

ABSTRACT

A theoretical and experimental study of metal-insulator-semiconductor (MIS) structures on (Hg,Cd)Te is presented. The development of an MIS structure which resulted in consistent, repeatable MIS properties is described. The MIS structure which was used most frequently consisted of an insulating film of vacuum evaporated ThF_4 and a gold-indium gate electrode. N-type $Hg_{0.6}Cd_{0.4}Te$ oriented in the (111) direction was the most extensively studied material, although p-type material and material with different x-values and orientations were also examined.

The fast surface state densities of the ThF_4/(Hg,Cd)Te interface were measured. The (111)A surface of $Hg_{0.6}Cd_{0.4}Te$ had fast surface state densities of about $10^{12}cm^{-2}eV^{-1}$ and the (111)B surface had densities of about $10^{11}cm^{-2}eV^{-1}$. Native oxide films on the (111)B surface exhibited interface state densities as low as $2 \times 10^{10}cm^{-2}eV^{-1}$. Other properties of the insulator-(Hg,Cd)Te interface, such as flat-band voltage and hysteresis, were also examined.

The MIS technique was successfully used to determine bulk properties, such as bulk doping, minority carrier lifetime, and bandgap. Bulk doping measurements were found to be in good agreement with Hall measurements. The MIS techniques for determining generation-recombination rates were analyzed and further developed. Minority carrier lifetimes ranging from 10^{-9} sec to

10^{-4} sec were measured with the large and small signal MIS techniques. Surface generation velocities ranging from 1 cm/sec to 100 cm/sec were also determined with the large signal method. Variable temperature measurements indicated that Shockley-Read generation-recombination was the dominant mechanism for the generation and recombination of minority carriers in the depletion regions of (Hg,Cd)Te MIS structures.

The diffusion of impurities and the self-diffusion of Hg into $Hg_{0.6}Cd_{0.4}Te$ were studied. A diffusion coefficient for the donor indium was determined at a few diffusion temperatures. A brief survey of the effects of various surface treatments on the MIS properties was conducted.

THESIS SUPERVISOR: C. G. Fonstad

TITLE: Associate Professor of Electrical Engineering

TABLE OF CONTENTS

Chapter	Title	Page
	Title Page	
	Abstract	
	Table of Contents	4
	List of Figures	5
	List of Symbols	11
	Acknowledgements	12
1	INTRODUCTION	13
2	BACKGROUND	17
2.1	Ideal Metal-Insulator-Semiconductor (MIS) Structure	17
2.1.1	Surface Space Charge Region	20
2.1.2	Ideal MIS C-V Curves	27
2.2	Non-Ideal Effects	35
2.2.1	Fixed Insulator Charge and Metal-Semiconductor Work Function Difference	35
2.2.2	Surface States	37
2.2.3	Determination of Surface Properties	40
2.2.3.1	Surface Potential	40
2.2.3.2	Surface State Density	46
2.3	Minority Carrier Generation-Recombination	56
2.3.1	Small Signal Techniques	56
2.3.2	Large Signal Techniques	76
3	EXPERIMENTAL METHODS	89
3.1	MIS Structures on (Hg, Cd) Te	89
3.1.1	(Hg,Cd)Te Description	89
3.1.2	MIS Geometry and Fabrication	90
3.2	Measurement Techniques	93
3.2.1	Test Dewars	93
3.2.2	Capacitance/Conductance Measurements	94
3.2.3	Spectral Response Measurements	97
4	EXPERIMENTAL RESULTS	101
4.1	Insulators	101
4.1.1	Zinc Sulfide (ZnS)	102
4.1.2	Thorium Fluoride (ThF_4)	105
4.1.3	Lanthanum Fluoride (LaF_3)	110
4.1.4	Silicon Monoxide (SiO_x)	112
4.1.5	Silicon Dioxide (SiO_2)	114
4.1.6	Cadmium Telluride (CdTe)	115
4.1.7	Anodization	116
4.2	Majority Carrier Doping	123
4.3	Surface State Densities	127
4.3.1	Comparison of (111)A and (111)B Surfaces	127
4.3.2	Unoriented Material and Other X-Values	143
4.3.3	Time Constant of Surface States	144
4.4	Minority Carrier Generation-Recombination	152
4.4.1	Small Signal Measurements	152

TABLE OF CONTENTS (continued)

Chapter	Title	Page
4.4.2	Large Signal Measurements	159
4.4.3	Comparison of Large and Small Signal Measurements	166
4.4.4	Temperature Dependence	182
4.4.4.1	Small Signal Measurements	183
4.4.4.2	Large Signal Measurements	191
4.5	Diffusion of Impurities	199
4.5.1	Gallium	199
4.5.2	Indium	202
4.5.3	Aluminum	208
4.5.4	Gold	213
4.6	Stoichiometric Mercury Anneal	216
4.7	Surface Preparation Experiments	222
4.7.1	Chemical Etches	222
4.7.1.1	Hydrochloric Acid (HCl)	222
4.7.1.2	Hydrogen Peroxide (H_2O_2)	223
4.7.1.3	Sulfuric Acid (H_2SO_4)	225
4.7.2	Mechanical Polish	227
4.7.3	Heat Treatments	229
5	DISCUSSION	231
5.1	Bulk Properties	231
5.1.1	Bandgap	231
5.1.2	Majority Carrier Concentration	233
5.1.3	Lifetime Measurements	2-35
5.2	Surface Properties	2-40
5.2.1	Surface Potential	2-40
5.2.2	Surface State Densities	235
5.3	Other Experiments	240
5.3.1	Insulators	240
5.3.2	Diffusion Experiments	242
5.3.3	Surface Preparation Experiments	246
6	SUMMARY AND CONCLUSIONS	246 247
APPENDIX A		249
A.1	IDENTIFICATION OF (111)A AND (111)B FACES	251
A.2	AUGER AND RADIATIVE GENERATION-RECOMBINATION IN DEPLETION REGIONS	255 255
A.2.1	Radiative Mechanism	256
A.2.2	Auguer Mechanism	256
A.3	SMALL SIGNAL CAPACITANCE TRANSIENT	261 265
REFERENCES		270

LIST OF ILLUSTRATIONS

Figure		Page
2.1	Metal-Insulator-Semiconductor Structure.....	21
2.2	Energy Band Diagram for an Ideal MIS Structure (n-type Semiconductor).....	22
2.3	Energy Band Diagram for an Ideal MIS Structure on an n-type Semiconductor.....	24
2.4	Energy Band Diagram of an Ideal MIS Structure on a p-type Semiconductor for $V_G > 0$.....	26
2.5	Variation of Space-Charge Density in the Semiconductor as a Function of the Surface Potential x_s for p-type Silicon with $N_A = 4 \times 10^{15}$ cm^{-3} at Room Temperature.....	29
2.6	Band Diagram and Charge Distribution for an Ideal MIS Structure Biased into Inversion (p-type Semiconductor)....	31
2.7	Ideal MIS Capacitance-Voltage Curves for a p-type Semiconductor.....	35
2.8	Extrapolation of Hg_{1-x} Cd_x Te Static Dielectric Constant Between Measured Values.....	37
2.9	High Frequency Minimum Capacitance "C_f" to Insulator Capacitance "C_i" Ratio Versus Doping Concentration for $Hg_{0.6}$ $Cd_{0.4}$ Te MIS Structures at 149K.....	38
2.10	MIS C-V Curves for a p-type Semiconductor, Illustrating the Effect of Surface States on the C-V Curve for High and Low Frequencies.....	41
2.11	Hysteresis Effects.....	44
2.12	Band Diagram Illustrating the $V_G = 0$ Surface Condition for the Case of a Uniform Distribution of Acceptor Like Surface States.....	47
2.13	Equivalent Circuits for (a) Depletion, (b) Weak Inversion.....	51
2.14	Circuits Equivalent to that of Figure 2.13.....	52
2.15	High Frequency MIS C-V Curves Showing the Skewing of the Experimental Curve Due to Surface States.....	57
2.16	Equivalent Circuit of an MIS Capacitor in Heavy Inversion.....	60
2.17	Integrating Circuit which Measures the Transient Response q(t) to an Incremental Change in Input Voltage.....	62
2.18	Relative Generation Rate Versus Distance from Surface for the Linear and Quadratic Potential Approximations for the Case $\tau_{no} = \tau_{po}$ and $E_t = E_i$.....	71
2.19	Transient Response of an MIS Structure After a Depleting Voltage Step According to the Theory of Heiman (Reference 20).....	80
2.20	"Zerbst" Plot Showing Difference Between Schroder's and Zerbst's Theory.....	83
3.1	MIS Structure Configuration.....	91
3.2	MIS Capacitance/Conductance - Voltage Test System.....	95
3.3	Spectral Response of an MIS Structure (Used to Obtain λ_c).....	99
3.4	MIS Spectral Measurement Setup.....	100

LIST OF ILLUSTRATIONS (continued)

Figure		Page
4.1	C-V Characteristic of an MIS Structure Using 4500 Å of ZnS as the insulator	105
4.2	C-V Characteristics for n and p-type (Hg,Cd)Te Using 5000 Å of ThF_4 as the Insulator	108
4.3	C-V Characteristic of p-type (Hg,Cd)Te Using 4000 Å LaF_3 as the Insulator	111
4.4	C-V Characteristics of p-type (Hg,Cd)Te Using 4000Å of Si O_x as the Insulator	114
4.5	C-V Characteristics of $Hg_{0.6}$ $Cd_{0.4}$ Te/CdTe Interface for Two Different Voltage Sweep Ranges	117
4.6	Capacitance-Voltage Characteristics of an Anodized MIS Structure	120
4.7	Comparison of Ideal and Measured C-V Curves for Anodized Surface	121
4.8	Surface State Density Versus Energy as Calculated by the Differentiation Technique for the Anodic Oxide/ThF_4 insulator system	123
4.9	Doping Measurements from MIS C-V Data on a $Hg_{0.6}$ $Cd_{0.4}$ Te Slab	126
4.10(a)	C-V Curves of the $ThF_4/Hg_{0.6}$ $Cd_{0.4}$ Te, (111)A Interface at Various Frequencies (n-type)	129
4.10(b)	C-V Curves of the $ThF_4/Hg_{0.6}$ $Cd_{0.4}$ Te, (111)B Interface at Various Frequencies (n-type)	130
4.11(a)	G_p/ω Versus ω on the (111)A $Hg_{0.6}$ $Cd_{0.4}$ Te Surface	131
4.11(b)	G_p/ω Versus ω on the (111)B $Hg_{0.6}$ $Cd_{0.4}$ Te Surface	132
4.12	Comparison of the Ideal and Experimental C-V Curves for the $ThF_4/Hg_{0.6}$ $Cd_{0.4}$ Te, (111)B Interface	135
4.13	Plot of Capacitance Versus Surface Potential for Example Shown in Figure 4.12	136
4.14	Surface Charge Versus Surface Potential for Example Shown in Figure 4.12	137
4.15	Surface State Density Versus Energy for Example Shown in Figure 4.12	138
4.16	Surface State Density Versus Energy for the $ThF_4/Hg_{0.6}$ $Cd_{0.4}$ Te, (111)A Interface (n-type)	139
4.17	Surface State Density Versus Energy for $ThF_4/Hg_{0.6}$ $Cd_{0.4}$ Te, (111)A Interface (p-type)	140
4.18	Surface State Density Versus Energy for the $ThF_4/Hg_{0.6}$ $Cd_{0.4}$ Te, (111)B Interface (n-type)	141
4.19	Surface State Density Versus Energy for the $ThF_4/Hg_{0.6}$ $Cd_{0.4}$ Te, (111)B Interface (p-type)	142
4.20	C-V plot of a $ThF_4/Hg_{0.63}$ $Cd_{0.37}$ Te MIS Structure (Unoriented Material)	145
4.21	Surface State Density Versus Energy for the Example Shown in Figure 4.20	146
4.22	C-V Plot of a ThF4/$Hg_{0.69}$ $Cd_{0.31}$ Te MIS Structure (Unoriented Material)	147

LIST OF ILLUSTRATIONS (continued)

Figure		Page
4.23	Surface State Density Versus Energy for the Example Shown in Figure 4.22	148
4.24	Time Constant of Surface States Versus $u_B - u_S$ for (111)A and (III)B Surfaces	150
4.25	C-V Curves at Various Frequencies for the $ThF_4/Hg_{0.6}$ $Cd_{0.4}$ Te, (111)B Interface (p-type)	154
4.26	G/ω Versus ω for the Example Shown in Figure 4.25	155
4.27	Small Signal Capacitance Transient for $Hg_{0.6}$ $Cd_{0.4}$ Te at 125K	157
4.28	Transient Response to Depleting Voltage Step	161
4.29	Zerbst Plot for Transient Shown in Figure 4.28	162
4.30	Transient Response for Anodized $Hg_{0.6}$ $Cd_{0.4}$ Te	164
4.31	Zerbst Plot for Transient Shown in Figure 4.30	165
4.32	Transient Responses for Increasing Voltage Step Sizes	167
4.33	Sketch of MIS Structure Biased Into Strong Inversion, Lateral Extension of Depletion Region	170
4.34	Circuit Model Valid in Strong Inversion Including Effects of Surface Recombination	175
4.35	τ_g/τ_{g-r} Versus $(E_t-E_i)/KT$ with $\tau po/\tau no$ as a parameter for p-type (Hg,Cd)Te	178
4.36	$\tau g/\tau g-r$ Versus $(E_t-E_i)/KT$ with $\tau po/\tau no$ as a parameter for n-type (Hg,Cd)Te	179
4.37	$\tau_g/\sqrt{\tau_{po}\ \tau_{no}}$ Versus $(E_t-E_i)/KT$ for n-type (Hg,Cd)Te	180
4.38	$\tau_{g-r}/\sqrt{\tau_{po}\ \tau_{no}}$ Versus $(E_t-E_i)/KT$ for n-type (Hg,Cd)Te	181
4.39	Measured R_o Versus 1/T for $Hg_{0.6}$ $Cd_{0.4}$ Te	185
4.40	$\tau g-r$ Versus 1/T for Samples 2 and 3	187
4.41	Calculated Temperature Dependence of $\tau_{g-r}/\sqrt{\tau_{po}\ \tau_{no}}$ for $(E_t-E_i)/K = 4.8 \times 10^2 K$	188
4.42	Storage Time Versus 1/T for 3 Samples	193
4.43	Calculated and Experimental T_S Versus 1/T for Sample 3	195
4.44	Calculated and Experimental T_S Versus 1/T for Sample 2	196
4.45	τg Versus 1/T for Samples 2 and 3	197
4.46	Illustration of the Procedure for Determining Doping Depth Profiles	200
4.47	MIS C-V Curve After One Hour, Room Temperature Indium Diffusion	204
4.48	Net Indium Donor Level Versus Depth at T = 95°C and t = 1 Hour	206
4.49	Net Indium Donor Level Versus Depth for T = 71°C and T = 95°C. (Calculated Distributions)	207
4.50	MIS C-V Characteristic Obtained After a 71°C, One Hour Aluminum Diffusion	211
4.51	Comparison of the C-V Plot of Figure 4.50 with Ideal Curve	211
4.52	Surface State Density Versus Energy as Calculated with the Differentiation Technique for the 71°C Aluminum Anneal	212
4.53	Dependence of Net Carrier Concentration Versus Anneal Temperature for the Hg Anneal	217

LIST OF ILLUSTRATIONS (continued)

Figure		Page
4.54	Net Impurity Concentration Versus Depth: Hg Anneal.....	221
4.55	MIS C-V Data on an H_2O_2 Treated Surface.....	224
4.56	MIS C-V Data on an H_2SO_4 Treated Surface.....	226
4.57	MIS C-V Data Comparing Polished and Etched Surfaces.....	228

LIST OF SYMBOLS

SYMBOL	MEANING	UNITS
A_G	Area of gate electrode	cm^2
C	Capacitance of MIS structure	pF/cm^2
C_D	Depletion region capacitance	pF/cm^2
C_i	Insulator capacitance	pF/cm^2
C_f	Minimum high frequency capacitance	pF/cm^2
C_{FB}	Flatband capacitance	pF/cm^2
C_s	Surface state capacitance	pF/cm^2
C_n	Capture probability for electrons	cm^3/sec
C_p	Capture probability for holes	cm^3/sec
c_o	Speed of light in vacuum	cm/sec
c	Speed of light in semiconductor	cm/sec
d	Thickness of insulator	Å
D	Diameter of gate electrode	cm
E_V	Valence band energy	eV
E_C	Conduction band energy	eV
E_i	Intrinsic Fermi energy	eV
E_F	Fermi energy	eV
E_g	Bandgap	eV

LIST OF SYMBOLS (Cont.)

SYMBOL	MEANING	UNITS
E_t	Energy of trap	eV
E_D	Demarcation energy	eV
ε_o	Permittivity of free space	F/cm
ε_s	Permittivity of semiconductor	F/cm
ε_i	Permittivity of insulator	F/cm
E	Electric field	V/cm
g	Generation rate	$sec^{-1}cm^{-3}$
G_r	Radiative generation rate	$sec^{-1}cm^{-3}$
G	Conductance of MIS structure	$mhos/cm^2$
h	Planck's constant	erg-sec
I	Current	Amperes
J	Current density	$Amperes/cm^2$
k	Boltzmann's constant	eV/°K
K_i	Semiconductor absorption coefficient	cm^{-1}
L_D	Extrinsic Debye length	cm
m	Mass of free electron	grams
m_e^*	Effective electron mass (normalized)	----
m_h^*	Effective hole mass (normalized)	----
n	Concentration of electrons in conduction band	cm^{-3}
n_o	Equilibrium concentration of electrons	cm^{-3}
n_i	Intrinsic carrier concentration	cm^{-3}

LIST OF SYMBOLS (Cont.)

SYMBOL	MEANING	UNITS
n_1	Concentration of electrons when $E_F=E_t$	cm^{-3}
N_A	Acceptor impurity concentration	cm^{-3}
N_D	Donor impurity concentration	cm^{-3}
N_B	Net impurity concentration	cm^{-3}
N_s	Concentration of minority carriers in inversion region	cm^{-2}
N_{ss}	Surface state density	$cm^{-2}\text{-}eV^{-1}$
N_{st}	Surface trap density	cm^{-2}
N_t	Bulk trap density	cm^{-3}
P	Concentration of holes in valence band	cm^{-3}
P_o	Equilibrium hole concentration	cm^{-3}
P_1	Hole concentration when $E_F=E_t$	cm^{-3}
q	Electronic charge	Coulomb
Q_M	Charge on metal gate electrode	C/cm^2
Q_s	Charge induced in semiconductor	C/cm^2
Q_{sc}	Charge in space charge region	C/cm^2
Q_n	Charge in inversion region	C/cm^2
Q_{ss}	Charge in surface states	C/cm^2
r	Recombination rate	$sec^{-1}\text{-}cm^{-3}$
R_{g-r}	Generation-recombination resistance of depletion region	$ohm\text{-}cm^2$
R_D	Diffusion resistance	$ohm\text{-}cm^2$

LIST OF SYMBOLS (Cont.)

SYMBOL	MEANING	UNITS
R_s	Surface state resistance	ohm-cm^2
R_{SP}	Resistance due to generation by surface states at perimeter of gate	ohm
R_{SG}	Resistance due to generation by surface states under gate	ohm
R_o	Total resistance of depletion region	ohm
S	Surface generation velocity	cm/sec
S_o	Surface generation velocity of depleted surface	cm/sec
T	Temperature	°K
T_s	Storage time	sec
τ_{no}	Lifetime for electrons in p-type semiconductor (S-R)	sec
τ_{po}	Lifetime for holes in n-type semiconductor (S-R)	sec
τ_{g-r}	Small signal depletion region lifetime	sec
τ_g	Large signal generation lifetime	sec
τ_B	Bulk lifetime	sec
τ_{ss}	Small signal time constant	sec
τ_s	Surface state time constant	sec
τ_A	Extrinsic Auger lifetime	sec
τ_{Ai}	Intrinsic Auger lifetime	sec
τ_R	Extrinsic radiative lifetime	sec
τ_{Ri}	Intrinsic radiative lifetime	sec

LIST OF SYMBOLS (Cont.)

SYMBOL	MEANING	UNITS
u_S	Normalized surface potential	----
u_B	Normalized bulk Fermi potential	----
U	Net recombination rate	sec^{-1}-cm^{-3}
U_s	Net surface recombination rate	$sec^{-1}cm^{-2}$
μ	Mobility	cm^2/V-sec
V_{th}	Average thermal velocity of carriers	cm/sec
V_G	Gate voltage	V
V_i	Voltage across insulator	V
W	Depletion region width	cm
W_m, W_f	Maximum equilibrium depletion region width	cm
Ψ	Electrostatic potential	V
Ψ_s	Surface potential	V
Ψ_s^o	Free surface potential	V
Ψ_B	Bulk Fermi potential	V
ϕ_m	Metal work function	V
ϕ_s	Semiconductor work function	V
ϕ_{ms}	Metal-semiconductor work function difference	V
ϕ_b	Potential barrier between metal and insulator	V
ϕ_n	Quasi-Fermi potential for electrons	V
ϕ_p	Quasi-Fermi potential for holes	V

LIST OF SYMBOLS (Cont.)

SYMBOL	MEANING	UNITS
ϕ_F	Fermi-potential	V
σ_n	Capture cross-section for electrons	cm^2
σ_p	Capture cross-section for holes	cm^2
λ	Wavelength	μm
ρ	Charge density	C/cm^3
χ	Semiconductor electron affinity	V
χ_i	Insulator	V
ν	Frequency of radiation	Hz
ω	Test frequency	Radians/sec

ACKNOWLEDGEMENTS

I would especially like to thank Jeff Beck, Prof. C. G. Fonstad, and Bob Broudy for their invaluable help in the formulation and supervision of this research. Jeff was especially helpful and was a constant source of assistance and encouragement throughout this work. Prof. Fonstad, Bob Broudy, and Nancy Aldrich provided excellent supervision and technical advice.

I would also like to thank all the engineers for their advice and technical assistance, especially Ross Murosako, Tim Tredwell, Jeff Gelpey, Ted Wong, and Bulusu Dutt. The work of Larry Gauthier, Bob Pierson, Bob Perras, Bob Baur, Don Smith, Chip Blair, and Lou Buldini in the fabrication of the MIS structures was invaluable. The testing work of Bob Woitunski, Dick Healey, and Jack Little is gratefully acknowledged. Many thanks as well to Dave Plummer and the rest of the publications crew who were so patient during the typing, illustration, and printing of this thesis. Finally, I would like to express my gratitude to all those people with whom I worked and associated at Honeywell for helping make this a rewarding, enjoyable experience.

This work was supported in part by AFML Contract No. F33615-76-C-5070 (Bob Hickmott, Supervisor).

SECTION 1

INTRODUCTION

The $Hg_{1-x}Cd_xTe$ ternary alloy system is a narrow bandgap II-VI semiconductor consisting of a mixture of HgTe and CdTe. The bandgap depends on the mole fraction x of the CdTe portion and can be continuously varied from 1.6 eV in CdTe to -0.3 eV in HgTe.

The Metal-Insulator-Semiconductor (MIS) structure has been used extensively in the determination of bulk and surface parameters of semiconductors.[36] The main purpose of this research was to develop the MIS structure and use it to determine bulk and surface parameters of $Hg_{1-x}Cd_xTe$.

MIS structures have previously been made on $Hg_{1-x}Cd_xTe$, primarily on x = 0.2 to x = 0.4 material (bandgaps from 0.1 to 0.4 eV).

The results of capacitance, conductance, and photoconductivity measurements versus applied gate voltage on MIS structures made of 0.09 eV $Hg_{0.8}Cd_{0.2}Te$ were reported by Tasch et al in 1970.[1] The MIS technique was also used to study the Landau levels in the inversion layer of p-type (Hg,Cd)Te.[2] More recently, MIS capacitance-voltage measurements were made

which studied the relationship between trapping effects and the surface in x = 0.3,[3,4] and x = 0.4[5] (Hg,Cd)Te. These investigations showed that the surface strongly influenced the trapping mechanism.

A MIS capacitance theory for nonparabolic band semiconductors has been formulated.[6] Based on this formulation, calculations of the capacitance and derivative of capacitance were carried out with x = 0.2 (Hg,Cd) Te as the example.

There have been several problems associated with (Hg,Cd)Te MIS structures. A high density of surface states causes a large amount of hysteresis in the capacitance-voltage characteristics.[4,5] The relaxation phenomena associated with charge trapping in these surface states makes accurate determination of bulk lifetime difficult. Surface inversion and tunneling effects have been reported, especially in x = 0.2 (0.1 eV bandgap) material.[3,4] These effects severely hinder the determination of minority carrier lifetime and majority carrier concentration.

However, in x = 0.3 and x = 0.4 material, tunneling and surface inversion effects are not limiting factors, primarily because of the larger bandgap. Because of this, it seemed feasible to utilize MIS data to determine surface and bulk parameters for this composition range.

All material used in this research was n or p-type $Hg_{1-x}Cd_xTe$ with composition range of x = 0.3 to x = 0.4, corresponding to bandgaps from 0.25 to 0.4 eV. In most cases, the material was single crystal oriented along major crystal axes.

The initial task of this research was to further develop and refine the MIS structure so that the various parameters could be determined more easily. A survey of the different available insulators, as well as the refinement of the method of surface preparation, was carried out. The insulator-semiconductor interface which resulted in minimal hysteresis and surface state density, and which exhibited consistently high yields, was then chosen for the bulk of the remaining work.

Next the theory of MIS structures was applied in the determination of the bulk properties, primarily majority carrier concentration and minority carrier lifetime, and the surface properties, primarily surface state densities, surface recombination velocity, hysteresis, and surface potential.

With the tools thus developed, it was possible to apply the methods to various engineering problems. Specifically, the effects of several chemical surface treatments on surface potential and surface state density were determined. In addition, the diffusion of impurities was studied and the effects of the stoichiometric anneal process on bulk properties were determined.

SECTION 2

BACKGROUND

2.1 IDEAL METAL-INSULATOR-SEMICONDUCTOR (MIS) STRUCTURE

The ideal MIS diode will be considered first in order to form a basis for the understanding of non-ideal MIS diode characteristics. The treatment here will closely follow the theory outlined in Sze.[7]

The MIS structure is shown in Figure 2.1 where d is the thickness of the insulator and V_G is the applied voltage on the metal field plate. An ideal MIS diode is defined as follows: (1) the metal-semiconductor work function difference is zero; (2) the only charge which can exist under any applied bias are those appearing in the semiconductor and the image charge on the metal plate; and (3) there is no charge transport through the insulator.

The energy band diagram for $V_G = 0$ is shown in Figure 2.2 for an n-type semiconductor. The metal-semiconductor work function difference ϕ_{ms} is defined as:

$$\phi_{ms} = \phi_m - \phi_s = \phi_m - (\chi + \frac{E_c - E_F}{q}) = \phi_m - (\chi + \frac{E_c - E_i}{q} - \psi_B) \qquad (2.1)$$

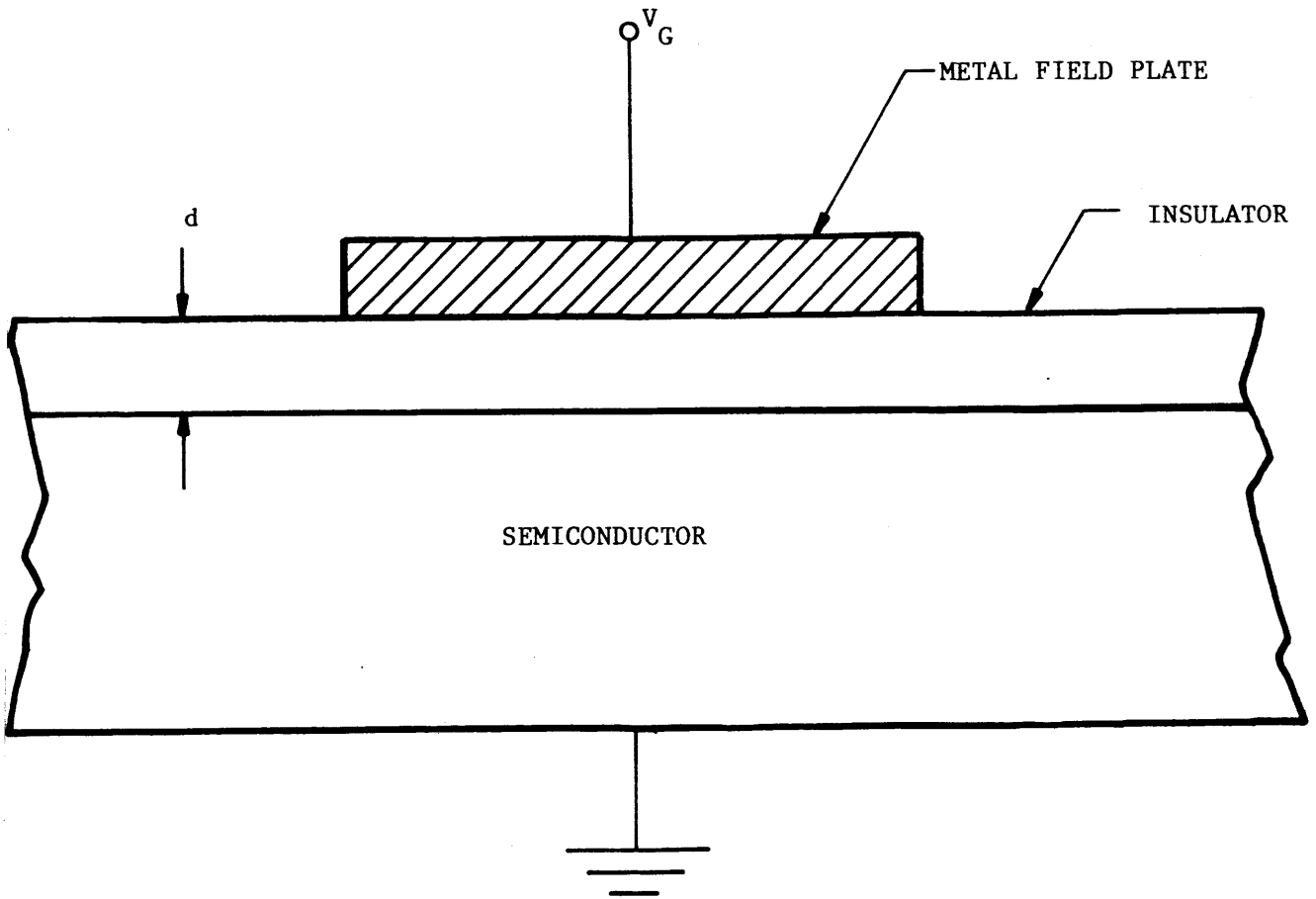

Figure 2.1. METAL-INSULATOR-SEMICONDUCTOR STRUCTURE

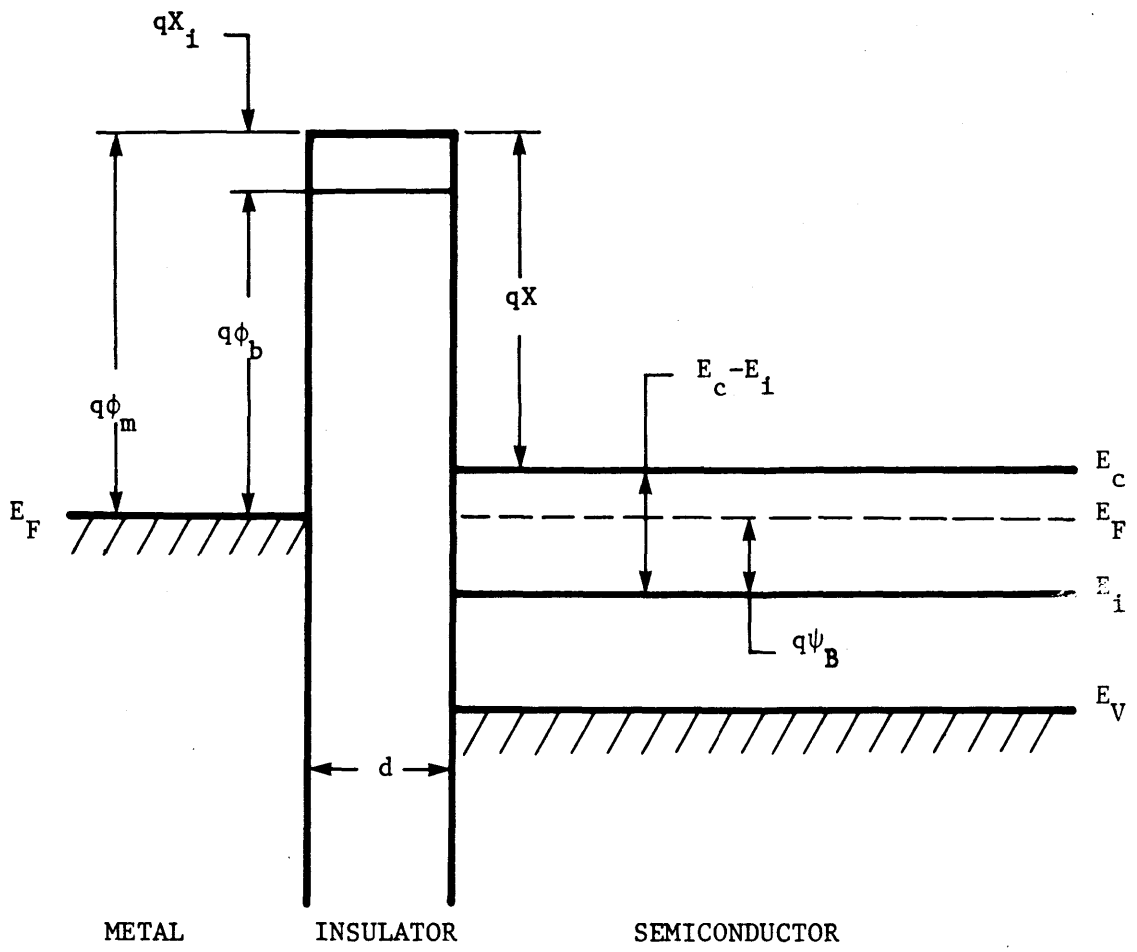

Figure 2.2. ENERGY BAND DIAGRAM FOR AN IDEAL MIS STRUCTURE (N-TYPE SEMICONDUCTOR)

for an n-type semiconductor, where ϕ_m is the metal work function, χ the semiconductor electron affinity, ψ_B the potential difference between the intrinsic Fermi level E_i and the Fermi level E_F, ϕ_B the potential barrier between the metal and insulator, and χ_i the insulator electron affinity. As shown in the figure, the work function difference is zero.

The energy band diagram of an ideal MIS structure for an n-type semiconductor for various values of gate voltage is shown in Figure 2.3. Notice that three possible cases exist. When $V_G > 0$, the bands are bent downward, so that majority carriers accumulate at the surface. This is the case of "accumulation." When a small negative voltage is applied ($V_G < 0$), the bands are bent upward so that majority carriers are depleted from the surface. This is the case of "depletion." At larger negative voltages, the bands are bent upward to such an extent as to cause the concentration of minority carrier holes near the surface to be equal or greater than the concentration of electrons in the bulk. This is the case of "inversion." Similar results are obtained for a p-type semiconductor, except that the polarity of the gate voltage is reversed.

2.1.1 Surface Space Charge Region

The relations between surface potential and surface charge will be derived in this subsection. The relations will then be used to derive the capacitance-voltage characteristics in the next subsection.

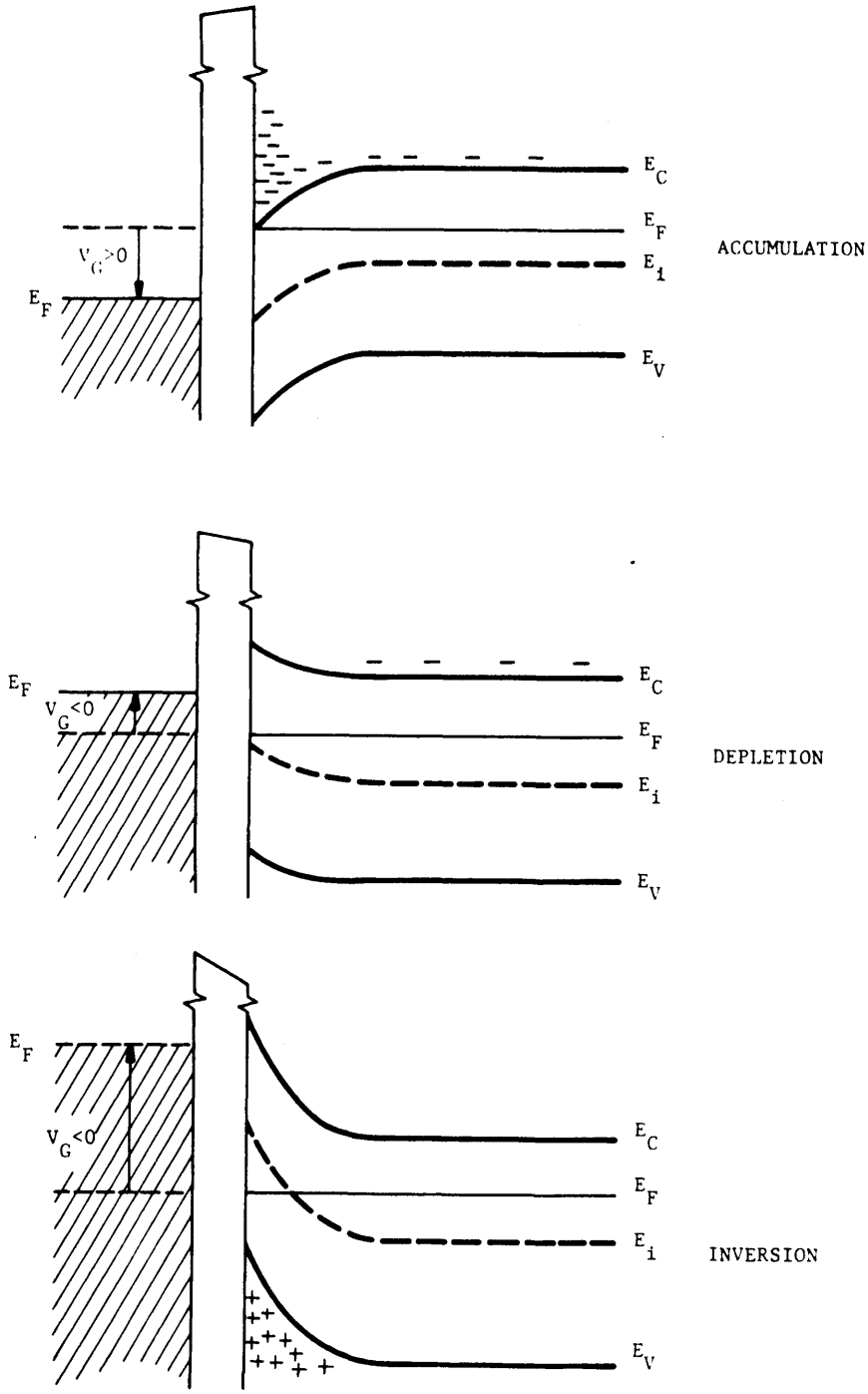

Figure 2.3. ENERGY BAND DIAGRAM FOR AN IDEAL MIS STRUCTURE ON AN N-TYPE SEMICONDUCTOR

The energy band diagram for a p-type semiconductor is shown in Figure 2.4 for a positive surface potential. The potential ψ is defined as zero in the bulk and is measured with respect to the intrinsic Fermi level E_i. At the semiconductor surface $\psi = \psi_s$, and ψ_s is called the surface potential. The electron and hole concentrations as a function of ψ are given by the following relations:

$$n_p = n_{po} \exp(\beta\psi);$$

$$p_p = p_{po} \exp(-\beta\psi) \tag{2.2}$$

where n_{po} and p_{po} are the equilibrium densities of electrons and holes, respectively in the bulk of the semiconductor, and $\beta = q/kt$. At the surface the densities are:

$$n_s = n_{po} \exp(\beta\psi_s)$$

$$p_s = p_{po} \exp(-\beta\psi_s) \tag{2.3}$$

The potential ψ as a function of distance is obtained by using the one-dimensional Poisson equation:

$$\frac{\partial^2 x}{\partial x^2} = -\frac{\rho(x)}{\varepsilon_s} \tag{2.4}$$

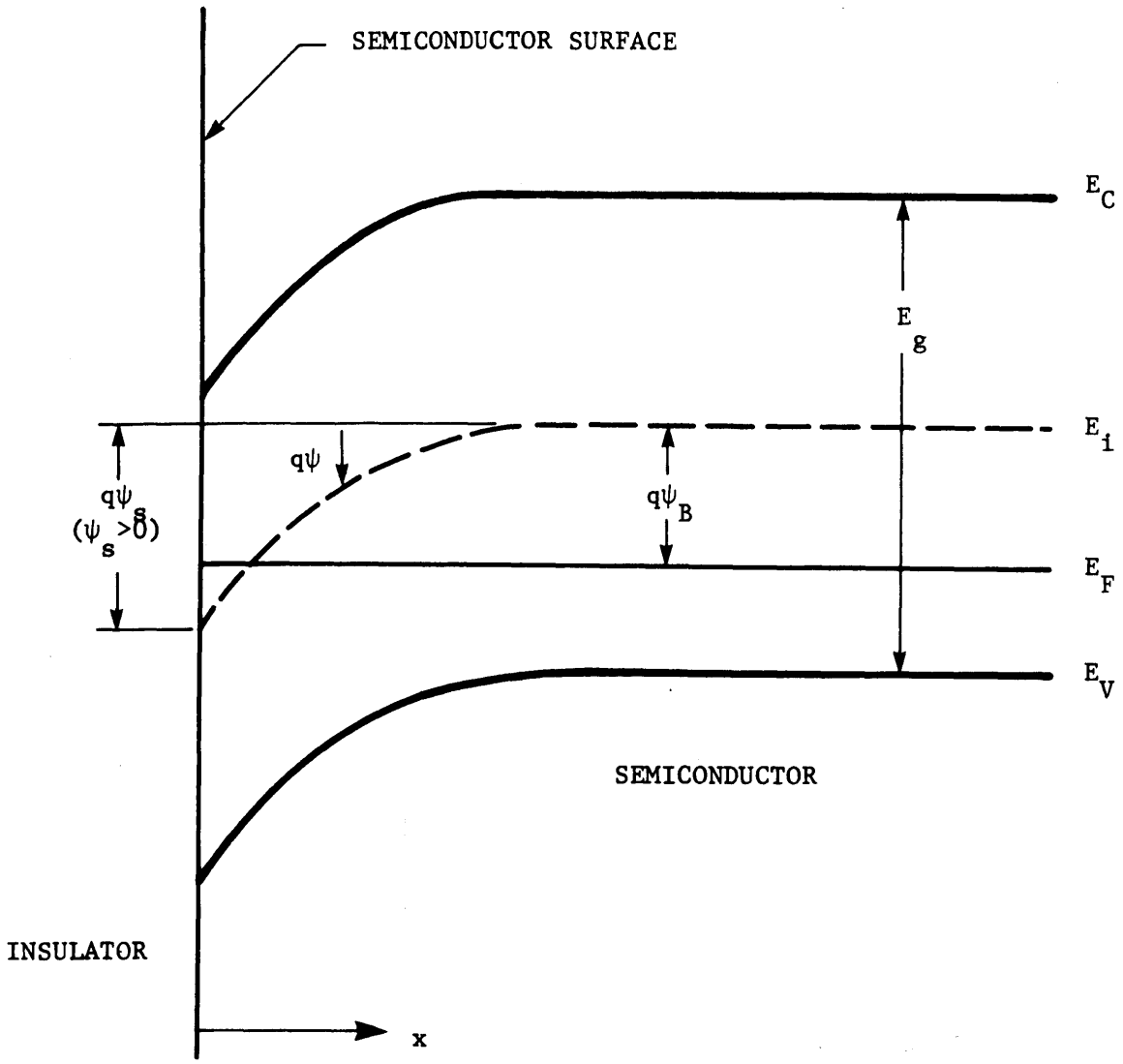

Figure 2.4. ENERGY BAND DIAGRAM OF AN IDEAL MIS STRUCTRUE ON A P-TYPE SEMICONDUCTOR FOR $V_G > 0$

where ε_s is the static dielectric constant of the semiconductor and $\rho(\chi)$ is the charge density given by:

$$\rho(\chi) = q(N_D^+ - N_A^- + p_p - n_p) = [p_p - p_{po} - (n_p - n_{po})] \tag{2.5}$$

where N_D^+ and N_A^- are the density of ionized donors and acceptors, respectively.

Equations 2.2 can be substituted into equation 2.5 to yield the following Poisson equation:

$$\frac{\partial^2 \psi}{\partial x^2} = - \frac{q}{\varepsilon_s} \left[p_{po}(e^{-\beta\psi}-1) - n_{po}(e^{\beta\psi}-1) \right] \tag{2.6}$$

This equation can be solved to yield the electric field:

$$E = - \frac{\partial \psi}{\partial x} = \pm \frac{2kT}{qL_D} F(\beta\psi, \frac{n_{po}}{p_{po}}) \tag{2.7}$$

where

$$L_D = \sqrt{\frac{2\varepsilon_s}{qp_{po}\beta}} \tag{2.8}$$

i.e., the extrinsic Debye length, and

$$F(\beta,\psi, \frac{n_{po}}{p_{po}}) = \left[(e^{-\beta\psi} + \beta\psi - 1) + \frac{n_{po}}{p_{po}} (e^{\beta\psi} - \beta\psi - 1) \right]^{1/2} \tag{2.9}$$

with the positive sign for $\psi > 0$ and the negative sign for $\psi < 0$. By Gauss' law the space charge per unit area required to produce this field is:

$$Q_s = \epsilon_s E_s = \pm \frac{2\epsilon_s kT}{qL_D} F(\beta\psi_s, \frac{n_{po}}{p_{po}}) \tag{2.10}$$

A typical variation of space charge density Q_s as a function of the surface potential ψ_s is shown in Figure 2.5 for p-type silicon with $N_A = 4 \times 10^{15}$ cm^{-3} at room temperature. Note the rapid increase of surface charge in strong inversion, when $\psi_s >> \psi_B$.

The onset of strong inversion occurs when the intrinsic Fermi level is below the Fermi level at the surface by as much as it is above the Fermi level in the bulk. Thus, the surface potential at the onset of strong inversion is given by:

$$\psi_s(\text{inv}) \cong 2\psi_B = \frac{2kT}{q} \ln (\frac{N_A}{n_i}) \tag{2.11}$$

The differential capacitance of the space-charge region (C_D) is given by:

$$C_D = \frac{\partial Q_s}{\partial \psi_s} = \frac{\epsilon_s}{L_D} \frac{\left[1 - e^{-\beta\psi_s} + \frac{n_{po}}{p_{po}} (e^{\beta\psi_s} - 1)\right]}{F(\beta\psi_s, \frac{n_{po}}{p_{po}})} \tag{2.12}$$

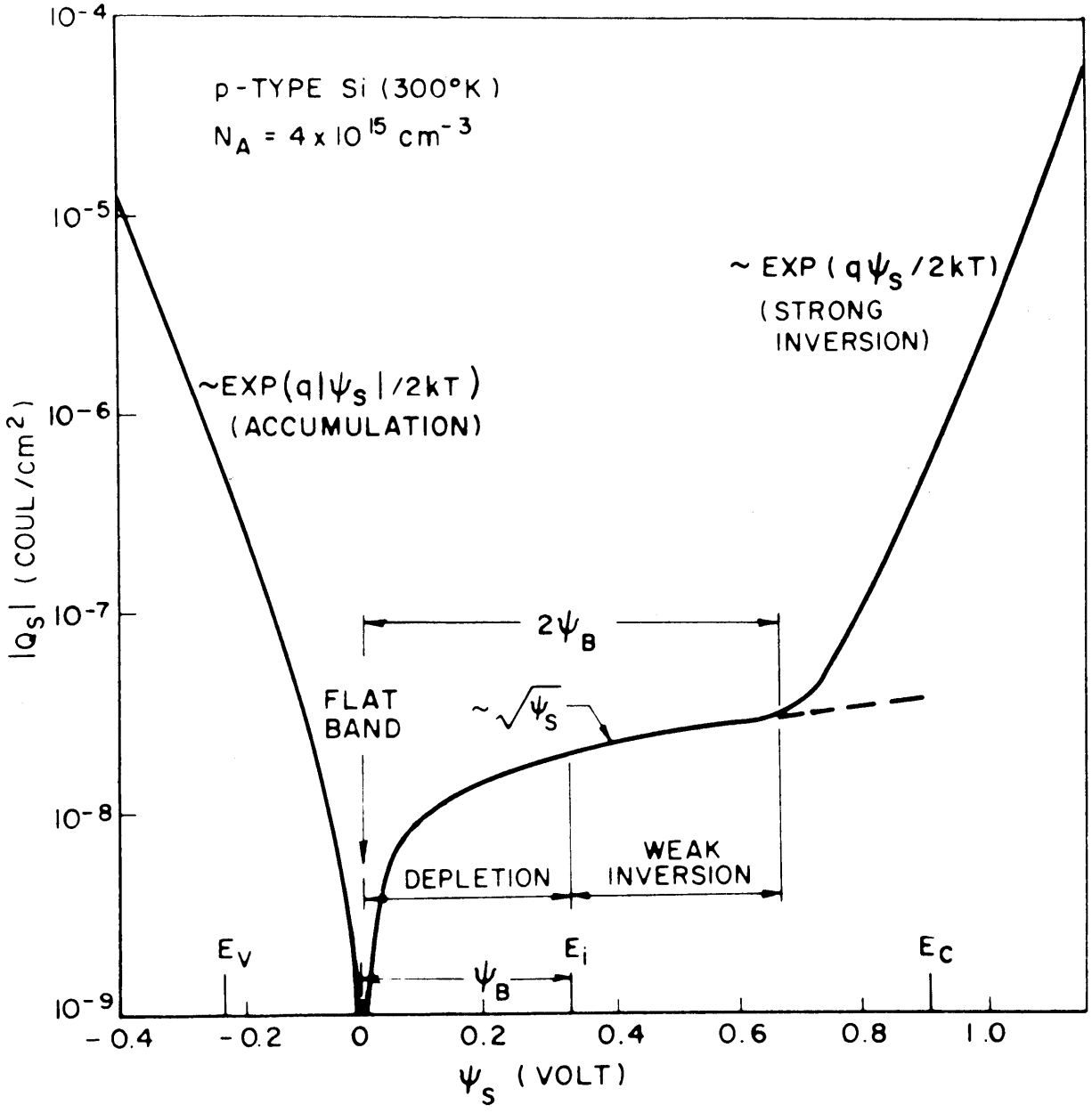

Figure 2.5. VARIATION OF SPACE-CHARGE DENSITY IN THE SEMICONDUCTOR AS A FUNCTION OF THE SURFACE POTENTIAL ψ_s FOR P-TYPE SILICON WITH $N_A = 4 \times 10^{15}\ cm^{-3}$ AT ROOM TEMPERATURE (After Sze, Reference 7)

2.1.2 Ideal MIS C-V Curves

Figure 2.6a shows the band diagram of an ideal MIS structure for the case of inversion. The charge distribution is shown in Figure 2.6b. Charge neutrality requires that:

$$Q_M = Q_n + qN_AW = Q_s \tag{2.13}$$

where Q_M is the charge per unit area on the metal, Q_n is the electron charge per unit area in the inversion region, and qN_AW is the ionized acceptor charge per unit area in the space charge region with space-charge width W.

The applied voltage will appear partly across the insulator and partly across the space-charge region, so that:

$$V_G = V_i + \psi_s \tag{2.14}$$

where V_i is the potential across the insulator and is given by:

$$V_i = \frac{Q_s d}{\varepsilon_i} = \frac{Q_s}{C_i} \tag{2.15}$$

where C_i is the insulator capacitance and ε_i is the dielectric constant of the insulator.

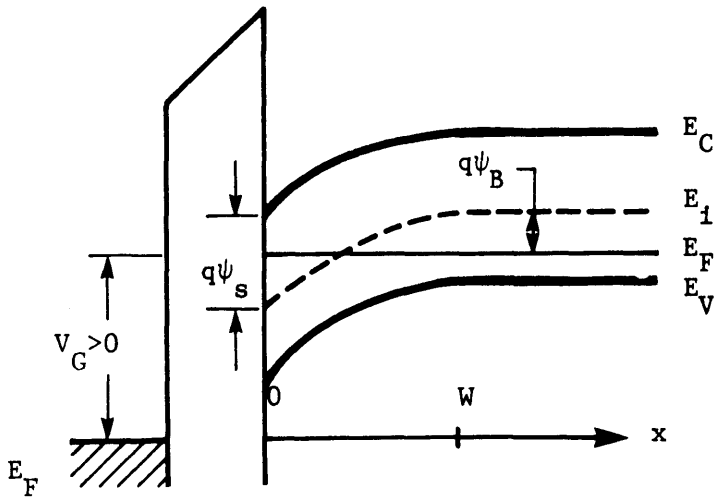

(a) BAND DIAGRAM

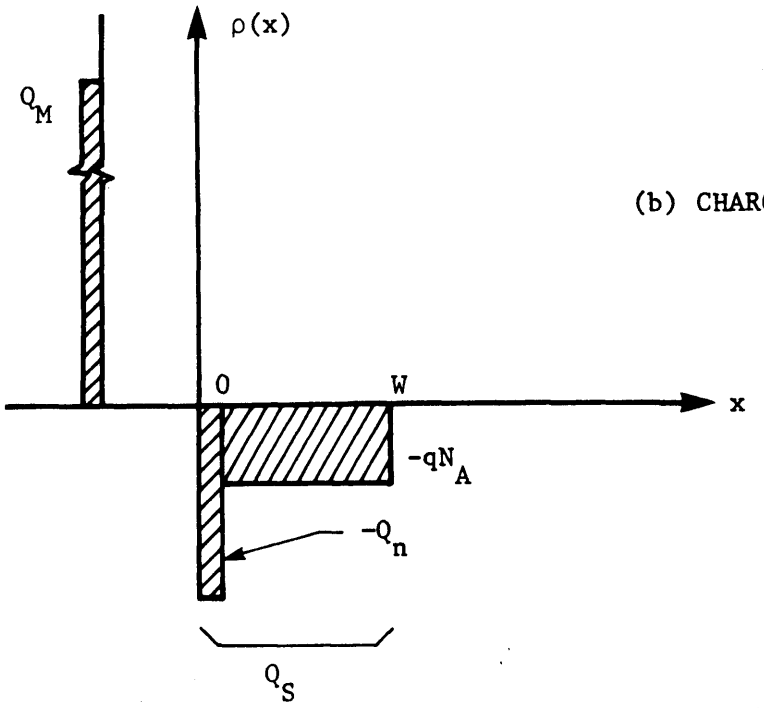

(b) CHARGE DISTRIBUTION

Figure 2.6. BAND DIAGRAM AND CHARGE DISTRIBUTION FOR AN IDEAL MIS STRUCTURE BIASED INTO INVERSION (P-TYPE SEMICONDUCTOR)

The total capacitance of the structure, C, is the series combination of insulator capacitance and space charge capacitance, so that:

$$C = \frac{C_i C_D}{C_i + C_D} \tag{2.16}$$

The value of C_i is constant, and the space-charge capacitance C_D depends on the surface potential through equation 2.12. Thus, the combination of equations 2.12, 2.14, 2.15 and 2.16 provides a complete description of the capacitance-voltage relationship of the structure. A sketch of this relationship is shown in Figure 2.7, curve (a).

The flat-band capacitance, C_{FB}, for $\psi_s = 0$ is given by:

$$C_{FB}(\psi_s = 0) = \frac{\varepsilon_i}{d + \frac{1}{\sqrt{2}} \frac{\varepsilon_i}{\varepsilon_s} L_D} \tag{2.17}$$

It should be emphasized that equation 2.12 is valid in strong inversion only at low frequencies, because it is assumed that the minority carrier concentration in the inversion layer can follow the applied ac signal. This can occur only at low frequenices when minority carrier generation-recombination can keep up with the small signal variation and lead to charge exchange with the inversion layer in step with the measurement signal.

The situation for high frequencies can easily be determined by considering the solution of Poisson's equation with the depletion approximation. With this approximation the potential distribution in the depletion region is found to be:

$$\psi = \psi_s \left(1 - \frac{x}{W}\right)^2 \tag{2.18}$$

where

$$\psi_s = \frac{qN_A W^2}{2\varepsilon_s} \tag{2.19}$$

As stated earlier, the onset of strong inversion occurs when $\psi_s = 2\psi_B$. Beyond this point, very small increases in ψ_s will cause large increases in the charge contained in the inversion region. Thus, the semiconductor is effectively shielded from further penetration of the electric field, and the depletion region width reaches a maximum. This maximum width, W_m, can be obtained from equations 2.11 and 2.19:

$$W_m = \sqrt{\frac{2\varepsilon_s \psi_s(\text{inv})}{qN_A}} = \sqrt{\frac{4\varepsilon_s kT \ln(N_A/n_i)}{q^2 N_A}} \tag{2.20}$$

At high frequencies the space-charge capacitance is given simply by:

$$C_D = \frac{\varepsilon_s}{W} \tag{2.21}$$

The total capacitance of structure at high frequencies will therefore reach a minimum value (C_f) in strong inversion given by:

$$C_f = \frac{\varepsilon_i}{d + \left(\frac{\varepsilon_i}{\varepsilon_s}\right) W_m} \tag{2.21}$$

The high frequency curve is shown in Figure 2.7, curve (b).

By combining equations 2.20 and 2.21, the doping concentration can be determined as a function of the insulator capacitance and the high frequency minimum capacitance, thus:

$$N_A = \frac{4kT \ln (N_A/n_i)}{\varepsilon_s q^2 \left(1/C_f - 1/C_i\right)^2} \tag{2.22}$$

The above arguments can be applied equally as well for an n-type semiconductor, except that the polarity of the gate voltage is reversed. The MIS structure will be accumulated for positive voltages and inverted for negative voltages, so that the capacitance-voltage relationship will simply be the mirror image of that for a p-type semiconductor. Thus the MIS C-V technique provides an unambiguous determination of majority carrier type.

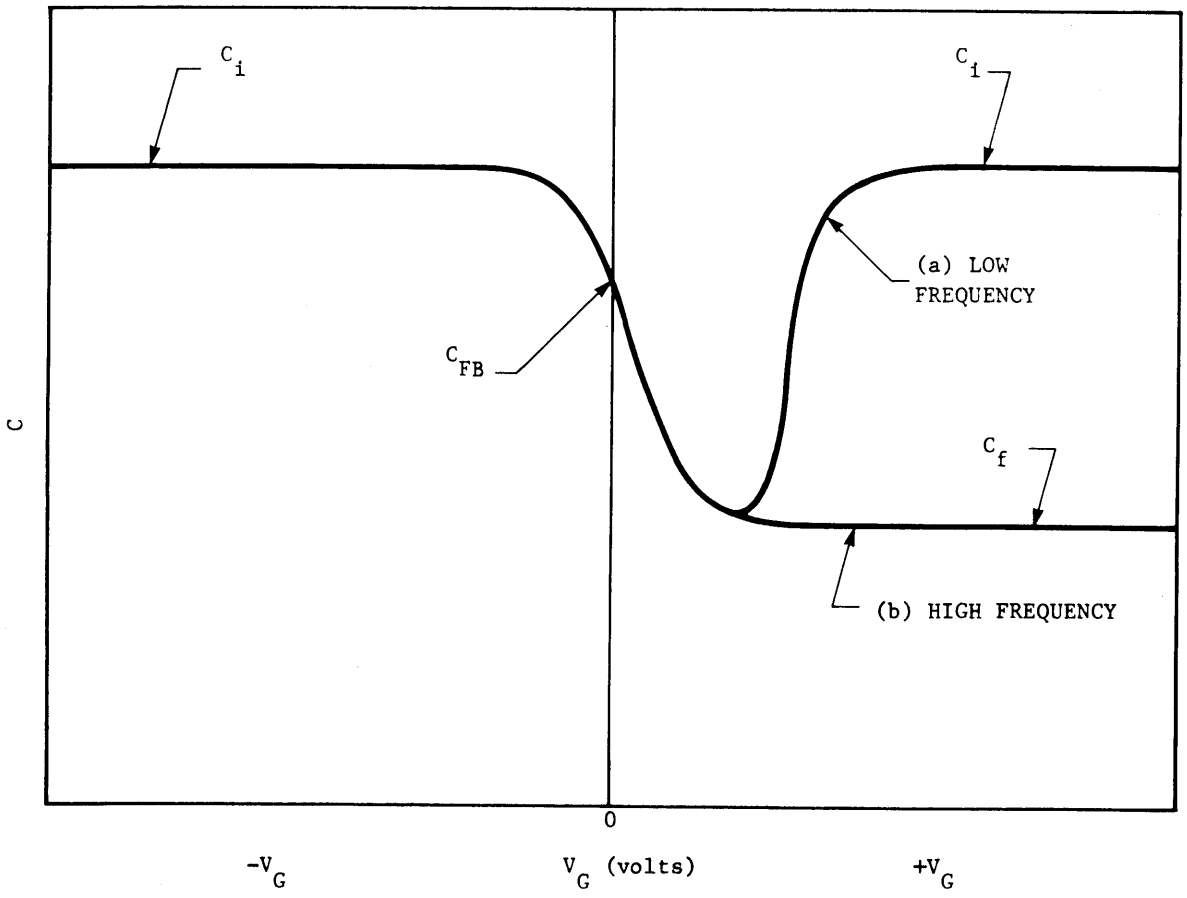

Figure 2.7. IDEAL MIS CAPACITANCE-VOLTAGE CURVES FOR A P-TYPE SEMICONDUCTOR

Equation 2.22 can be generalized to both n and p-type semiconductors, with N_A replaced by $N_B = |N_A - N_D|$. Thus:

$$N_B = \frac{4kT \ \ell n \ (N_B/n_i)}{\varepsilon_s q^2 \ (1/C_f - 1/C_i)^2} \tag{2.23}$$

By simply measuring the insulator capacitance, C_i, and the high frequency inversion layer capacitance, C_f, the net doping concentration can be determined.

It is necessary as well to know the dielectric constant and the intrinsic carrier concentration. For (Hg,Cd)Te, the dielectric constant is determined by extrapolating between the known value of x = 0.2 (Hg,Cd)Te and that of CdTe. This extrapolation is shown in Figure 2.8. The intrinsic carrier concentration is determined from an expression derived by Schmit:[8]

$$n_i = (8.445 - 2.875x - 0.00342 \ T)10^{14} \ E_g^{3/4} \ T^{3/2} \ \exp \ (-E_g/2kT) \tag{2.24}$$

where x is the mole fraction of Cd in (Hg,Cd)Te.

These parameters were used to construct a plot of N_B versus the minimum to insulator capacitance ratio, C_f/C_i, for x = 0.4 and T = 149 K. An insulator capacitance per unit area of 2×10^{-8} F/cm^2 was used because it corresponds closely to commonly occurring experimental values. This plot is shown in Figure 2.9.

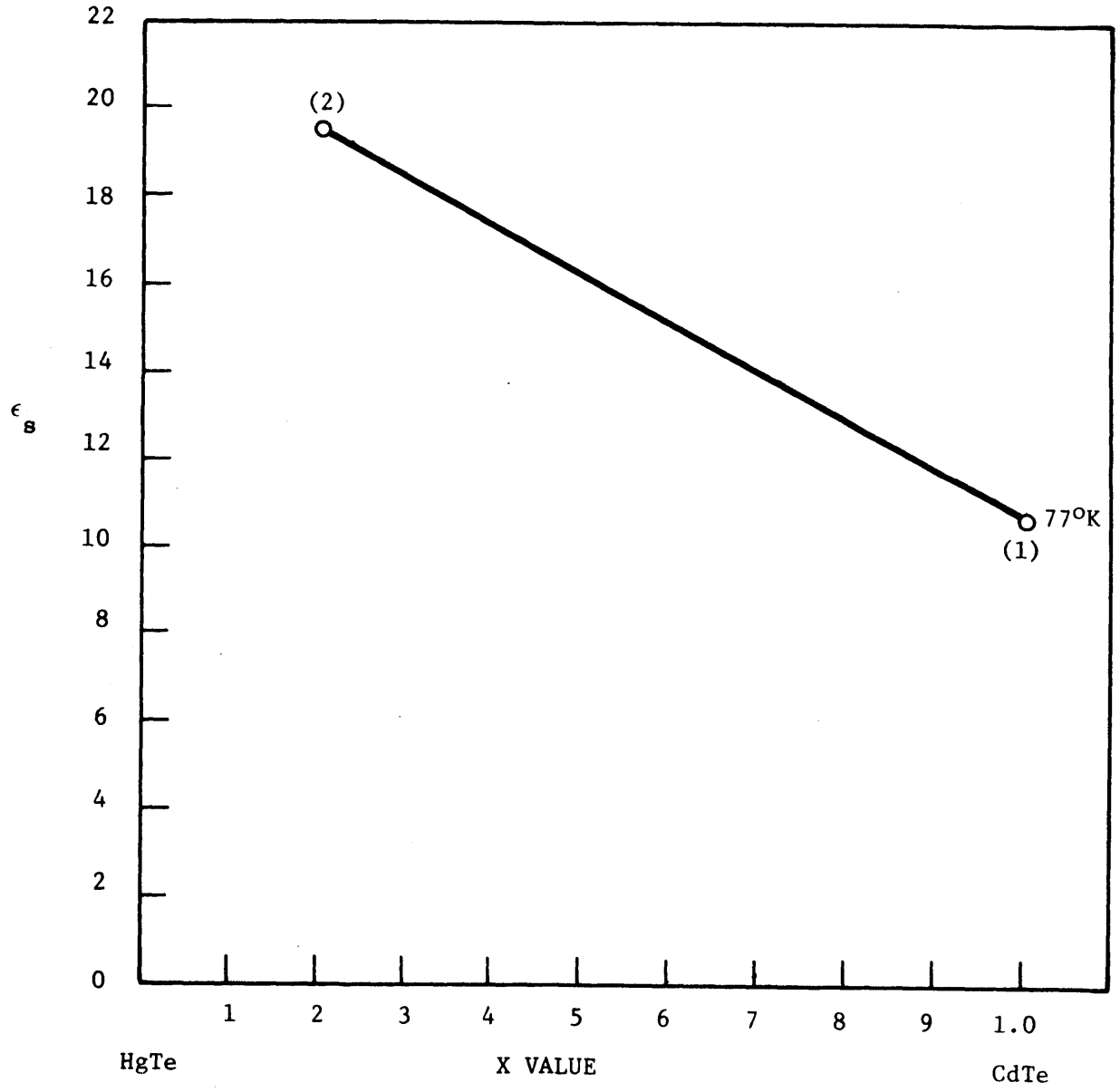

Figure 2.8. EXTRAPOLATION OF $Hg_{1-x}Cd_xTe$ STATIC DIELECTRIC CONSTANT BETWEEN MEASURED VALUES (1) J. BAARS AND F.SORGEN, S.S. COMM. 10, 875 (1972), (2) D.L. CARTER, M.A. KINCH AND D.D. BUSS, "PROC. CONT. ON PHYS. OF SEMIMETALS AND NARROW GAP SEMICONDUCTORS," P. 273 (1970)

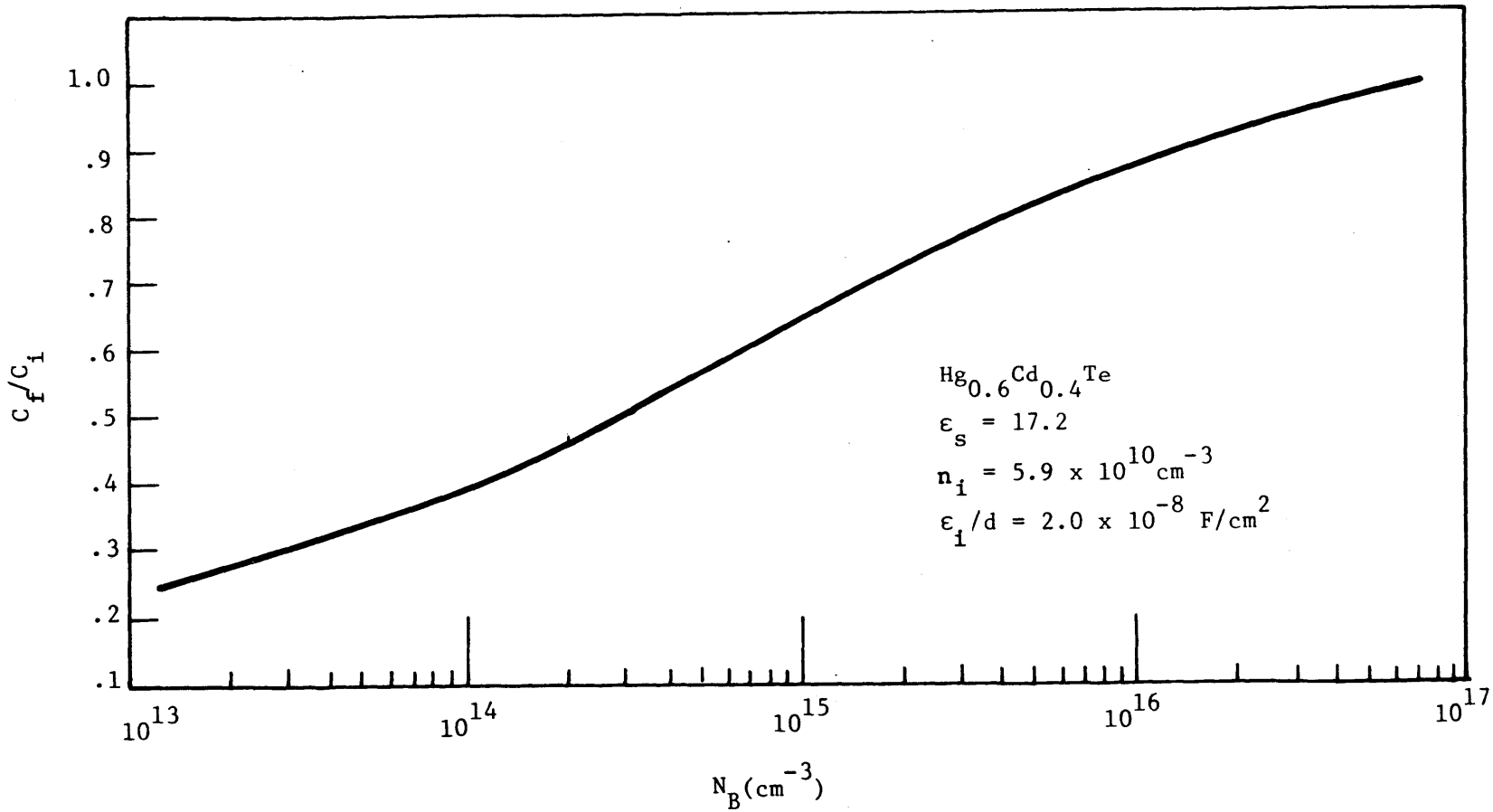

Figure 2.9. HIGH FREQUENCY MINIMUM CAPACITANCE "C_f" TO INSULATOR CAPACITANCE "C_i" RATIO VERSUS DOPING CONCENTRATION FOR $Hg_{0.6}Cd_{0.4}Te$ MIS STRUCTURES AT 149K. THE CURVE IS CALCULATED FOR $C_i/A_D = 2.0 \times 10^{-8}$ f/cm^2.

2.2 NON-IDEAL EFFECTS

Measured capacitance-voltage curves will generally be considerably distorted from the ideal curves. Common occurrences are hysteresis in the C-V curves, a shift of the curve along the voltage axis, and "smear-out" of curve, so that the transition between maximum and minimum capacitance occurs over a larger range of voltage than ideally. The causes of these effects will be examined in this section.

2.2.1 Fixed Insulator Charge and Metal-Semiconductor Work Function Difference

In many cases, an experimentally measured C-V curve will be shifted along the voltage axis away from the ideal case. The primary causes of this effect are fixed insulator charges and a non-zero metal-semiconductor work function difference, ϕ_{ms}.

In Section 2.1 it was assumed that ϕ_{ms} was zero. This, in general, is not true. ϕ_{ms} will depend on the particular metal being used, the doping concentration of the semiconductor, and the type of insulator. The effect of the work function difference is simply to shift the C-V curve along the voltage axis by an amount equal to ϕ_{ms}. The magnitude of ϕ_{ms} is typically not very large, usually on the order of a volt.

The presence of fixed insulator charge will also cause a shift of the C-V curve along the voltage axis. The fixed charges residing close to the insulator-semiconductor interface have the strongest effect. These

charges are generally not mobile except under high-temperature and large bias conditions. Their concentration depends on the type of insulator and the method of growth or deposition. In silicon[9], for example, thermally grown oxides tend to contain fixed positive charges which are thought to be due to excess silicon in the silicon dioxide. This can cause a p-type surface to be inverted with no applied bias.

2.2.2 Surface States

Surface, or interface states are the result of the termination of a periodic lattice. They are generally divided into two categories, fast and slow states. Fast states reside very close to the interface and exchange charge with the conduction or valence band rapidly. Slow states, on the other hand, reside in the insulator and require a longer time for charging.

In an MIS structure, fast surface states are assumed to be in equilibrium with the slowly varying ramp voltage applied to the gate. They may or may not be in equilibrium with the ac test signal used to measure the capacitance. When a voltage is applied, the surface state levels will move up or down with the valence and conduction bands while the Fermi level remains fixed. A change in charge will occur when they cross the Fermi level. This change in charge will contribute to the capacitance of the structure and alter the shape of the MIS capacitance-voltage curve. The presence of a more or less continuous distribution of surface states will cause a skewing of the C-V curve, as shown in Figure 2.10, since the surface

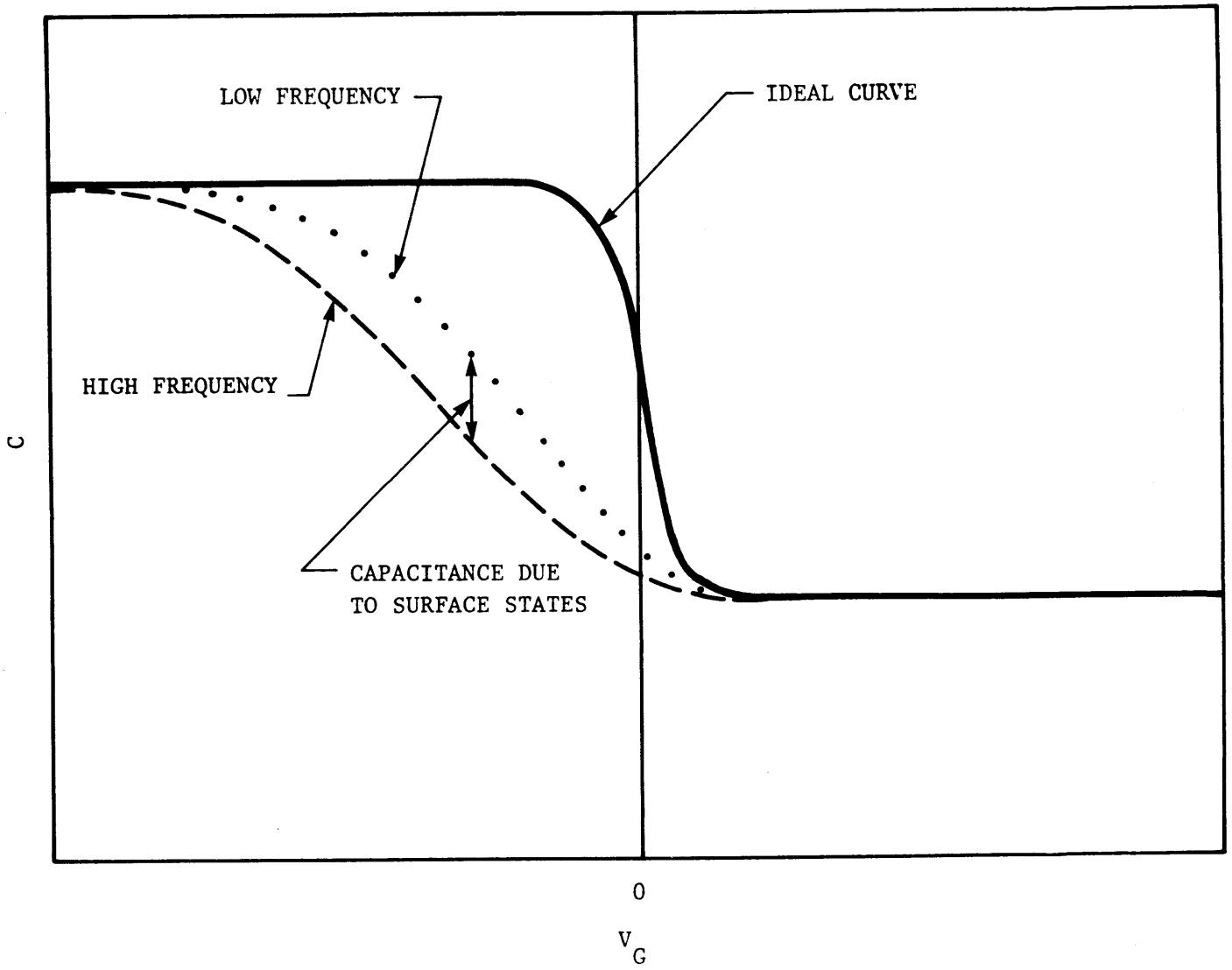

Figure 2.10. MIS C-V CURVES FOR A P-TYPE SEMICONDUCTOR, ILLUSTRATING THE EFFECT OF SURFACE STATES ON THE C-V CURVE FOR HIGH AND LOW FREQUENCIES.

potential is affected by the presence of charge in the surface states. If the measurement frequency is low enough, the charge exchange in the states will be able to follow the signal, and thus will cause an additional capacitance which appears in parallel with the space charge capacitance. The study of these dispersive effects yields valuable knowledge about the nature of the states, as will be discussed in a later section.

Slow states reside in the insulator. These states exchange charge with the semiconductor or metal gate by tunneling through the potential barrier presented by the insulator.[10] The effective capture cross-section of the states as viewed by a carrier at the semiconductor surface decreases exponentially with the distance of the states from the surface. The slow surface states often determines the surface potential of the semiconductor. Since the states exhibit long response times, the C-V relationship will depend on the initial bias, as well as the rate and voltage swing of the ramp voltage.

One problem commonly encountered is hysteresis in the capacitance-voltage characteristic. This is thought to be primarily due to unequal capture and emission rates of the slow surface states.[10] This inequality will result in a net accumulation of charge in the traps over one complete cycle of the voltage ramp, the sign of which depends on the type of charge injected. The following analysis was taken from Kendall.[11] The hysteresis can be described in terms of carrier injection into the insulator, either from the semiconductor or the metal or from both. As the bias sweeps between its limits in one direction, carriers are injected into the insulator and trapped. Upon sweeping in the opposite direction the bias is

added to or subtracted from the charge of the carriers still trapped, resulting in hysteresis. If the net potential of the semiconductor is positive with respect to the metal gate the semiconductor can inject holes and metal can inject electrons, and when the net potential is reversed the semiconductor can inject electrons and the metal can inject holes. When semiconductor injection dominates the sense of the hysteresis will be negative, which means the rising side of the hysteresis will be at a more negative voltage than the falling side. Domination of metal injection will result in positive hysteresis. The four possible types of hysteresis are illustrated in Figure 2.11.

2.2.3 Determination of Surface Properties

2.2.3.1 Surface Potential

It is desirable to know the surface potential which results from a particular insulator or surface treatment. The surface of the semiconductor can either be accumulated ($\psi_s > 0$ for an n-type semiconductor), depleted, or inverted ($\psi_s < 0$ for an n-type semiconductor). In most cases the surface potential can be at least qualitatively determined by measuring the capacitance-voltage characteristic.

The surface potential of an MIS structure is a function of the applied voltage V_G, fixed charges in the insulator Q_i, the metal-semiconductor work function difference ϕ_{ms}, and surface state charge Q_{ss}, which is also a function of V_G. When V_G is equal to zero, the surface potential

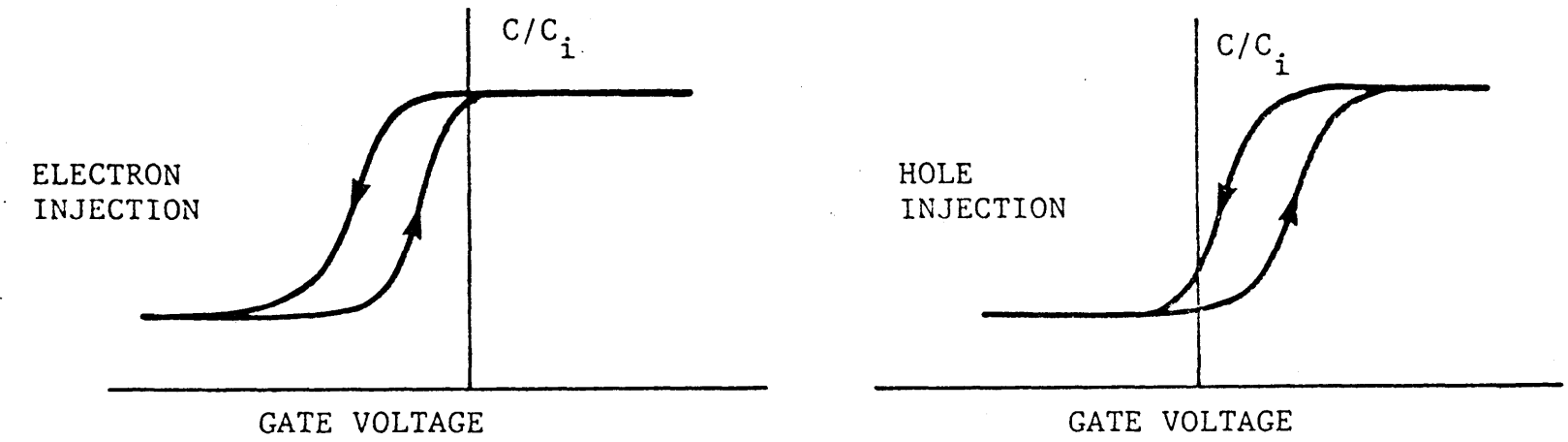

(a) METAL INJECTING CARRIERS INTO INSULATOR

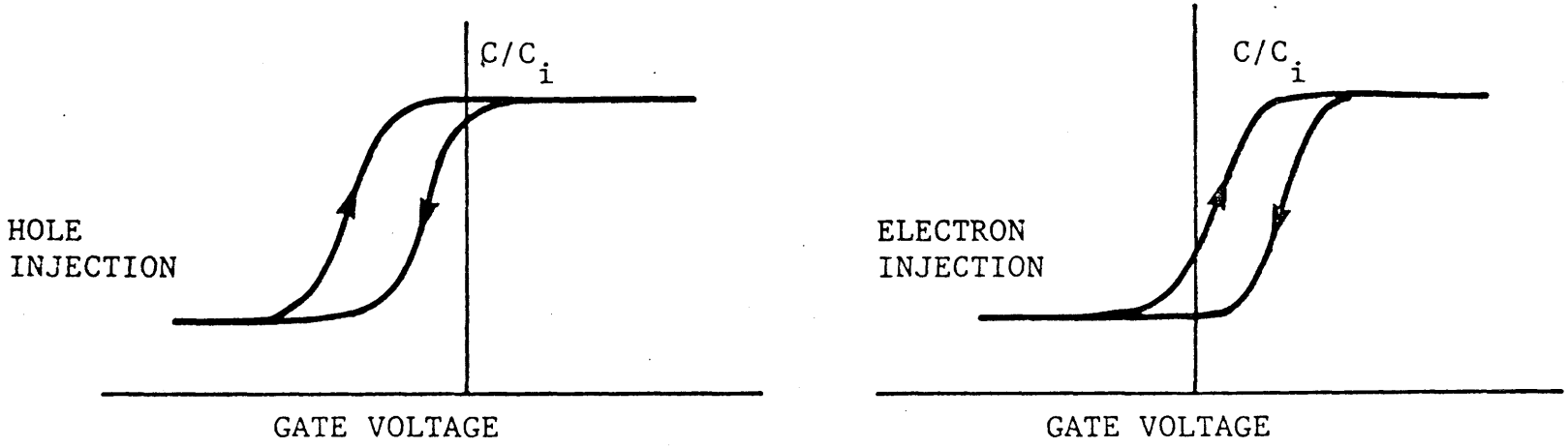

(b) SEMICONDUCTOR INJECTING CARRIERS INTO INSULATOR

Figure 2.11. HYSTERESIS EFFECTS

ψ_s^o is defined to represent the "free" surface condition at the insulator-semiconductor interface, except for the effect of ϕ_{ms} and image charge effects due to the presence of the metal gate. It is this unbiased surface condition, and hence, ψ_s^o which reflects the influence of the insulator coating and the surface treatment.

Although it is difficult to separate the insulator effects from those of the surface treatment, the effects of various treatments are compared using the same insulator which in our case was thorium tetrafluoride. Likewise, in the studies of the various insulators, the same surface treatment was used: the bromine-methanol etch procedure described in Section 3.1.

The metal-semiconductor work function difference will also influence the surface potential which is measured at $V_G = 0$. The same metal-insulator system was used in the surface treatment experiments and, therefore, relative influences on ψ_s^o could be studied in spite of the unknown, but fixed, value of ϕ_{ms} in the $Au/Thf_4/Hg_{0.6}Cd_{0.4}Te$ system.

The surface potential represents the amount of band bending which in turn determines the free carrier concentration at the surface and the occupancy demarcation level for the surface states. The demarcation level is the position of the extrinsic Fermi level with respect to the bandgap at the surface. Surface states below this level will be filled with electrons. The surface states above this level E_D will be empty of electrons. Within a few kT of E_D the states will be partially occupied. If, for example,

surface states are acceptor like, then they will be negatively charged when occupied by an electron and neutral when unoccupied. The surface potential will determine the position of the demarcation level and, hence, the net surface state charge Q_{ss}, but likewise, ψ_s^o will be affected by Q_{ss} which represents the net surface state charge in equilibrium when $V_G = 0$.

The unbiased surface condition is illustrated by the following example.* Consider a surface on n-type x = 0.4 $Hg_{0.6}Cd_{0.4}Te$ at 147K which has acceptor-like surface states distributed uniformly over the bandgap. The extrinsic Fermi level, being in the upper portion of the bandgap as shown in Figure 2.12, will result in most of the states being ionized, thus creating a negative sheet charge Q_{ss} which will bend the bands upward until the surface state charge is balanced by the semiconductor space charge Q_{sc} and the image charge on the metal gate. When this balance is achieved, the zero bias surface potential ψ_s^o is established.

In the example illustrated in Figure 2.12, the insulator charge Q_i and the metal-semiconductor work function difference are assumed to have a negligible influence on ψ_s^o.

The surface potential, ψ_s^o, can be determined quantitatively by measuring the capacitance at $V_G = 0$, and comparing it with the ideal capacitance versus surface potential relationships. For the case of depleted or

* The metal gate and the semiconductor substrate are at the same potential.

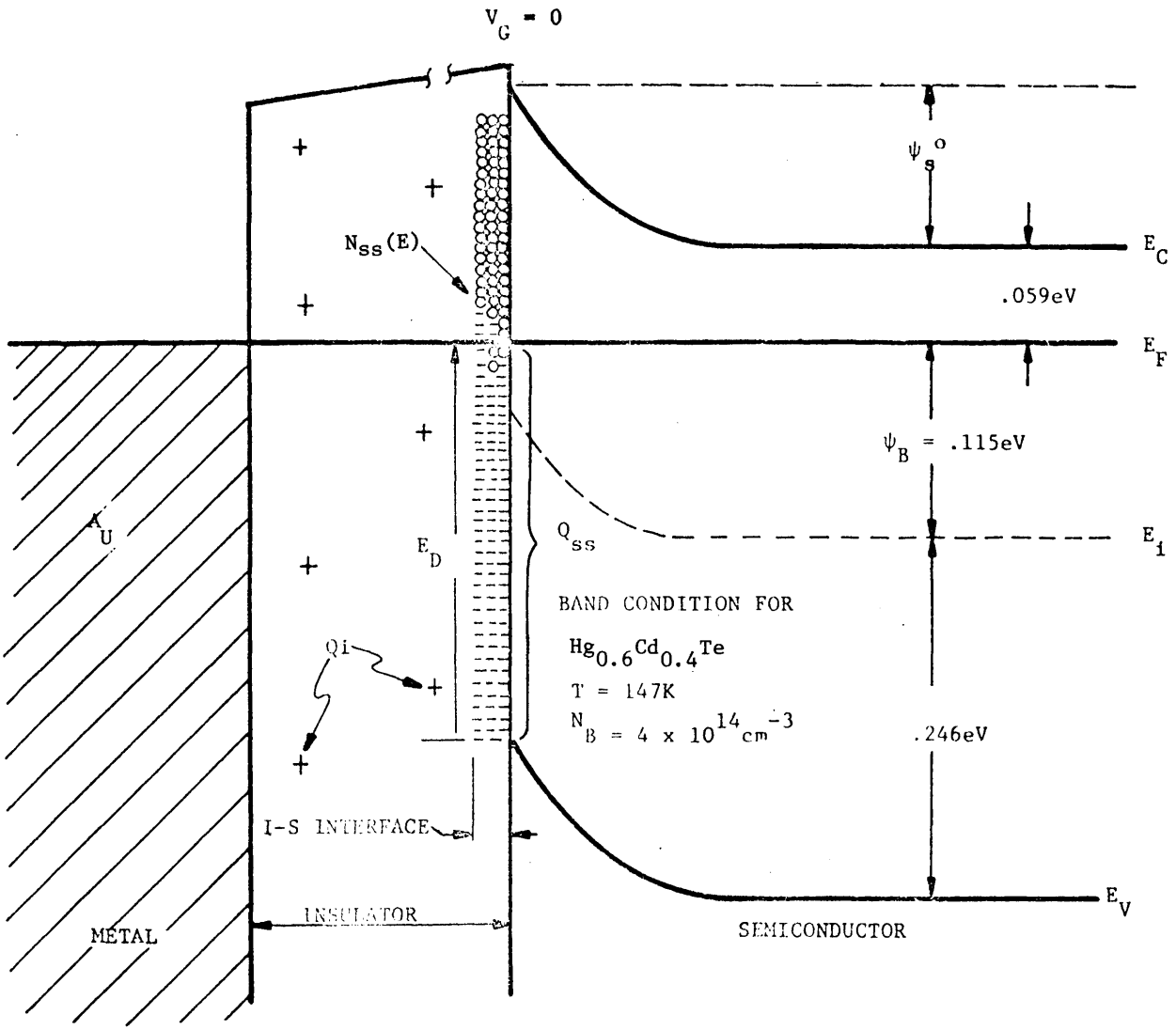

Figure 2.12. BAND DIAGRAM ILLUSTRATING THE $V_G = 0$ SURFACE CONDITION FOR THE CASE OF A UNIFORM CONTINUUM OF ACCEPTOR LIKE SURFACE STATES WHICH (BELOW E_D) ARE NEGATIVELY CHARGED AND CAUSE A DEPLETED SURFACE CONDITION IN THE N-TYPE $Hg_{0.6}Cd_{0.4}Te$.

weakly inverted surfaces, the ideal capacitance can be approximated with the depletion approximation, which was outlined in Section 2.1.2. In this case, the depletion capacitance (C_D) is related to the measured capacitance (C) by:

$$C_D = \frac{C\ C_i}{C_i - C} \tag{2.25}$$

and the surface potential is related to the depletion capacitance by:

$$|\psi_s| = \frac{q\ N_B\ \varepsilon_s}{2\ C_D^{\ 2}} \tag{2.26}$$

For surfaces which are accumulated or near flatband, the exact capacitance versus surface potential relationship must be used, such as that derived by Brews,[12] which must be solved numerically by computer.

An ambiguity in the determination of the surface potential arises when there is significant hysteresis in the capacitance-voltage data. The response times associated with the slow surface states can be quite long, so that in a given measurement a true equilibrium is not established. Generally, when the voltage ramp was stopped at $V_G = 0$, the capacitance would approach a value intermediate between the values for the rising and falling portions of the C-V relationship. Thus, it is still possible to estimate the equilibrium surface potential.

In some cases it was possible to infer the true surface condition by observing the time constant associated with the inversion layer under the metal gate. If anomalously short time constants were observed, this would sometimes imply that the free surface was inverted. This effect is due to the large supply of minority carriers surrounding the metal gate, and will be discussed further in Section 2.3.

In order to qualitatively evaluate the magnitude of ψ_s^o the following nomenclature will be used. This will apply for an n-type semiconductor. For a p-type semiconductor, the sign is changed and the direction of the inequalities reversed. For $\psi_s^o > 0$, the surface is accumulated. When $-\psi_B < \psi_s^o < 0$, the surface is depleted. If $-2\psi_B < \psi_s^o < \psi_B$, then the surface is weakly inverted, and if $\psi_s^o < -2\psi_B$, the surface is strongly inverted.

2.2.3.2 Surface State Density

Several methods have been established for measuring the effective surface state density of the MIS structure. Two methods will be described in this paper, the ac conductance technique suggested by Nicollian and Goetzburger,[13] and the differentiation technique discussed by Terman.[14]

Conductance Method

This method involves measuring the capacitance (imaginary component) and the conductance (real component) of the MIS structure as a function of

frequency and gate voltage. It is useful primarily for the cases of depletion ($0 < |\psi_s| < \psi_B$) and weak inversion ($\psi_B < |\psi_s| < 2\psi_B$).

In the case of depletion, one must consider a statistical model because of the statistical variation of the surface potential. In this case the effect of the surface states can be modeled by the circuit shown in Figure 2.13a.

In the case of weak inversion, the presence of minority carriers reduces the effect of the statistical variation of the surface potential, so that the simpler circuit model shown in Figure 2.13b can be used. This case is much simpler to treat analytically, so that most measurements were taken in weak inversion.

The parallel branch of the circuit in Figure 2.13b can be converted into a frequency-dependent capacitance C_p in parallel with a frequency-dependent conductance G_p as shown in Figure 2.14a, where:

$$C_p = C_D + \frac{C_s}{1 + \omega^2 \tau_s^2} \tag{2.27}$$

and

$$G_p/\omega = \frac{C_s \omega\tau_s}{1 + \omega^2\tau_s^2} \tag{2.28}$$

with

$$\tau_s \equiv R_s C_s \tag{2.29}$$

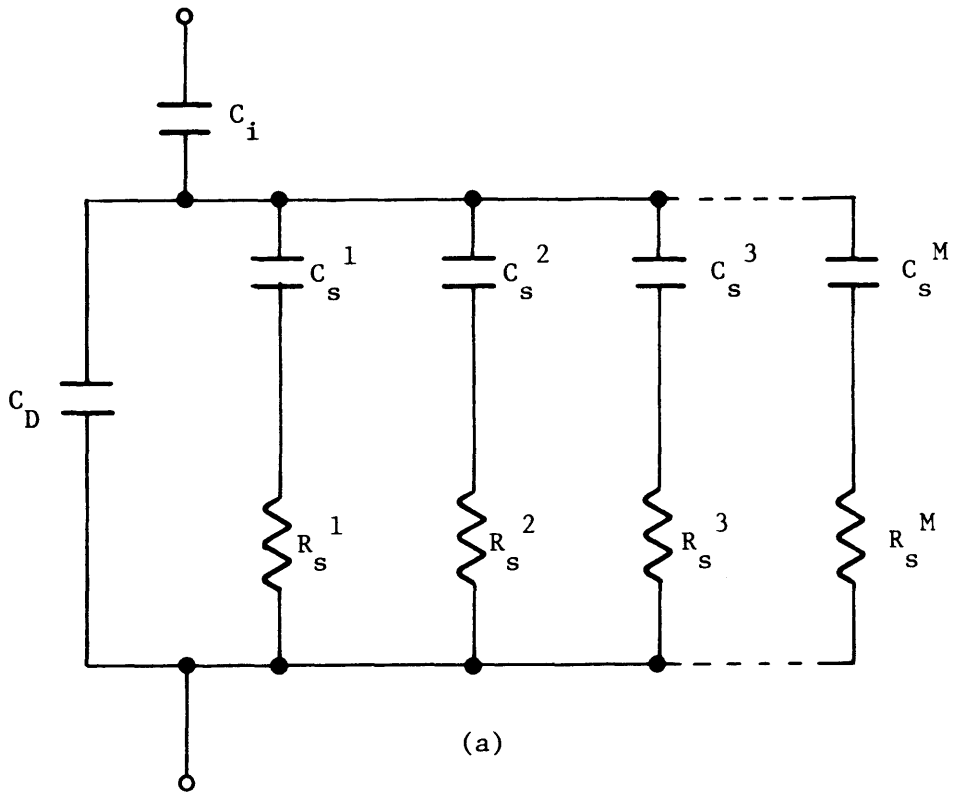

(a)

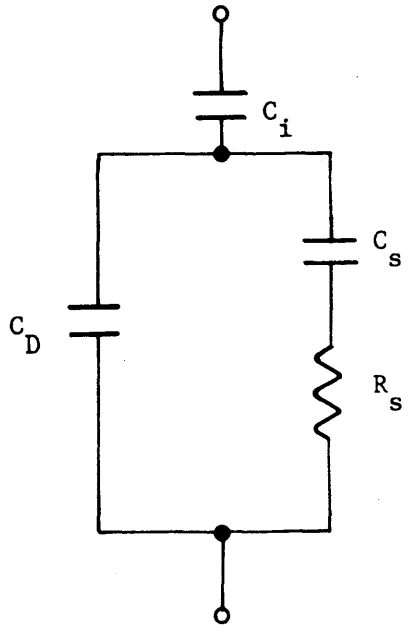

(b)

Figure 2.13. EQUIVALENT CIRCUITS FOR
(a) DEPLETION
(b) WEAK INVERSION

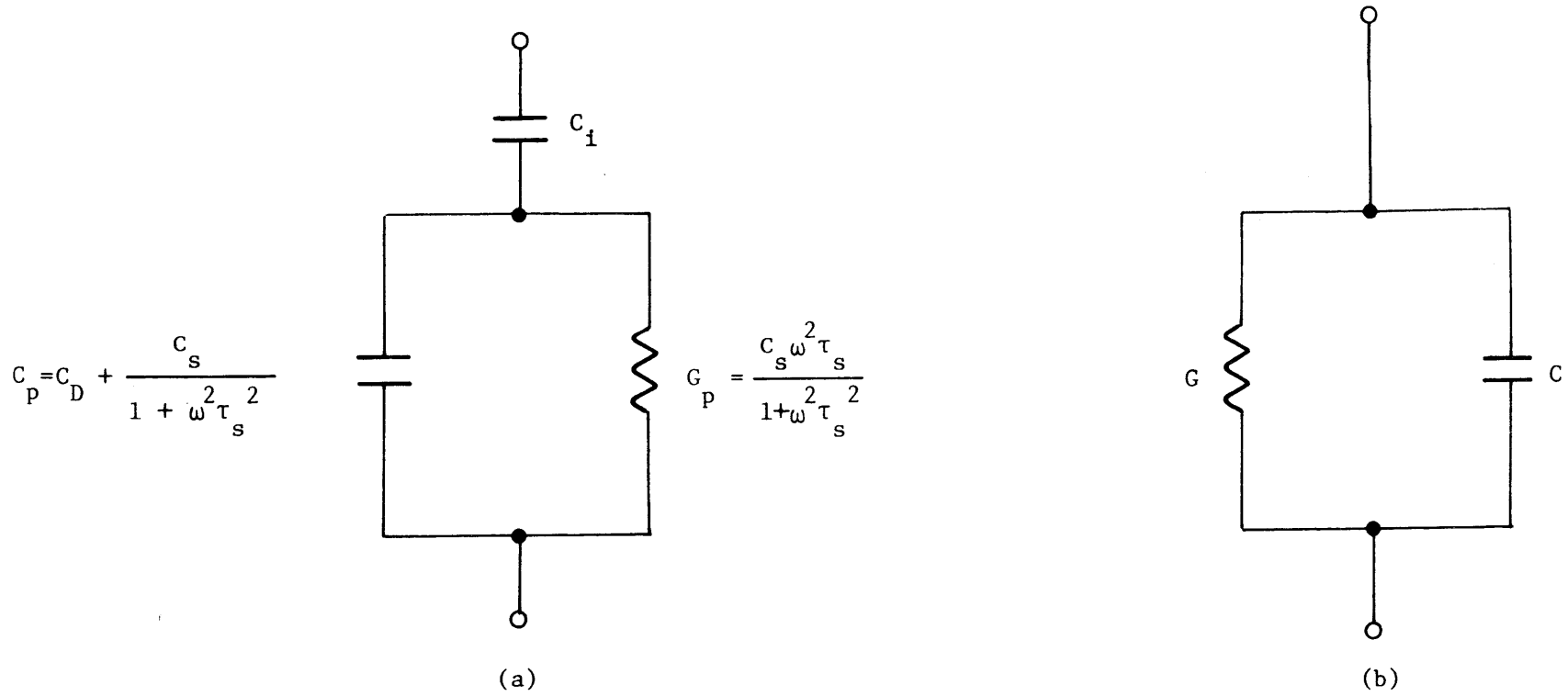

Figure 2.14. CIRCUITS EQUIVALENT TO THAT OF FIGURE 2.13

(a) PARALLEL BRANCH CONVERTED TO EQUIVALENT CAPACITANCE AND CONDUCTANCE

(b) ENTIRE CIRCUIT CONVERTED TO EQUIVALENT PARALLEL CAPACITANCE AND CONDUCTANCE, WHICH ARE THE EXPERIMENTALLY MEASURED VALUES.

The values for C_p and G_p/ω are calculated from the measured values of capacitance C and conductance G. The relationship of these quantities can be determined by converting the circuit of Figure 2.14a to that of Figure 2.14b. This results in the following relationships:

$$C_p = \frac{C_i\left[(G/\omega)^2+C^2\right]\left[C(C_i-C)-(G/\omega)^2\right]}{C_i^2(G/\omega)^2 + \left[C(C_i-C)-(G/\omega)^2\right]^2} \tag{2.30}$$

$$\frac{G_p}{\omega} = \frac{G}{\omega}\cdot\frac{C_i^2\left[(G/\omega)^2 + C^2\right]}{C_i^2(G/\omega)^2+\left[C(C_i-C)-(G/\omega)^2\right]^2} \tag{2.31}$$

Examination of equation 2.28 reveals that when $\omega\tau_s = 1$, G_p/ω will be maximum with a value of $C_s/2$. Thus, a plot of G_p/ω versus ω will determine C_s. The surface state density, N_{ss}, can be determined from C_s through the relationship:

$$N_{ss} = C_s/qA \tag{2.32}$$

where A is the area of the metal field plate.

The gate voltage at which the measurements are made can be related to the surface potential. Thus, a measurement of N_{ss} at various voltages will yield the distribution of surface states across a portion of the band-gap.

This method has the advantage that slow surface states do not effect the measurements, and is thus a direct measure of fast surface state density.

In addition to the density of surface states, the conductance technique also determines the time constant of the surface states. The time constant τ_s, defined as $R_s C_s$, is the reciprocal of the frequency at which Gp/ω is maximum (equation 2.28). The time constant is related to the capture probability and the surface potential in the following way:

$$\tau_s = \frac{1}{C_n n_i} \exp\left[-(u_s - u_B)\right] \text{ for n-type} \qquad (2.33)$$

and

$$\tau_s = \frac{1}{C_p n_i} \exp\ (u_s - u_B) \text{ for p-type}$$

where

C_n is the capture probability for electrons

C_p is the capture probability for holes

$u_s \equiv q\psi s/kT$

$u_B \equiv \ln(n_i/N_d)$ for n-type

and $u_B \equiv \ln(N_A/n_i)$ for p-type

If the capture probabilities are independent of surface potential, a plot of $\ln \tau_s$ versus $u_B - u_S$ will yield a straight line whose slope is 1 for n-type and -1 for p-type. When $u_B - u_S$ is equal to zero, equation 2.33 reduces to:

$$\tau_s = \frac{1}{C_n n_i} \quad \text{for n-type}$$

and

(2.34)

$$\tau_s = \frac{1}{C_p n_i} \quad \text{for p-type}$$

The surface recombination velocity S_o is related to the density of surface states and the capture probabilities of the states. For the special case of $C_n = C_p$ and constant density of states, the surface recombination velocity is given by[9]:

$$S_o = 1/2C\pi\ kT\ N_{ss} \tag{2.35}$$

where $C = C_n = C_p$ and N_{ss} is the density of surface states near the intrinsic Fermi energy. Although the above mentioned assumptions are not in general correct, it is expected that conductance measurements of τ_s and N_{ss} can provide a rough estimate of the surface recombination velocity.

Differentiation Method

In this method the capacitance is first measured at a high enough frequency such that the measurement is free of capacitance due to the surface states. This high frequency capacitance-voltage characteristic is then compared with the ideal relationship, such as that given by Brews.[12] The surface states will effect the surface potential in such a way as to cause a skewing of the C-V relationship from the ideal, as shown in Figure 2.15. One can construct a plot of ΔV_G versus V_G where ΔV_G is the voltage shift between the measured and ideal C-V curve at a given value of capacitance. The total charge in the surface states (Q_{ss}) at a given surface potential is then given by:

$$Q_{ss} = C_i \ (\Delta V) \ \text{coul/cm}^2 \tag{2.36}$$

The surface state density per unit energy (N_{ss}) is then obtained by graphical differentiation:

$$N_{ss} = \frac{1}{q}\left(\frac{\partial Q_{ss}}{\partial \psi_s}\right)_{\psi_s} \ \text{states/cm}^2\text{/eV} \tag{2.37}$$

This method is rather simple to apply; however, it does have problems associated with it. A major problem is that the effects of the metal-semiconductor work function difference and fixed charges in the insulator must be taken into account when constructing the plot of ΔV_G versus V_G. In

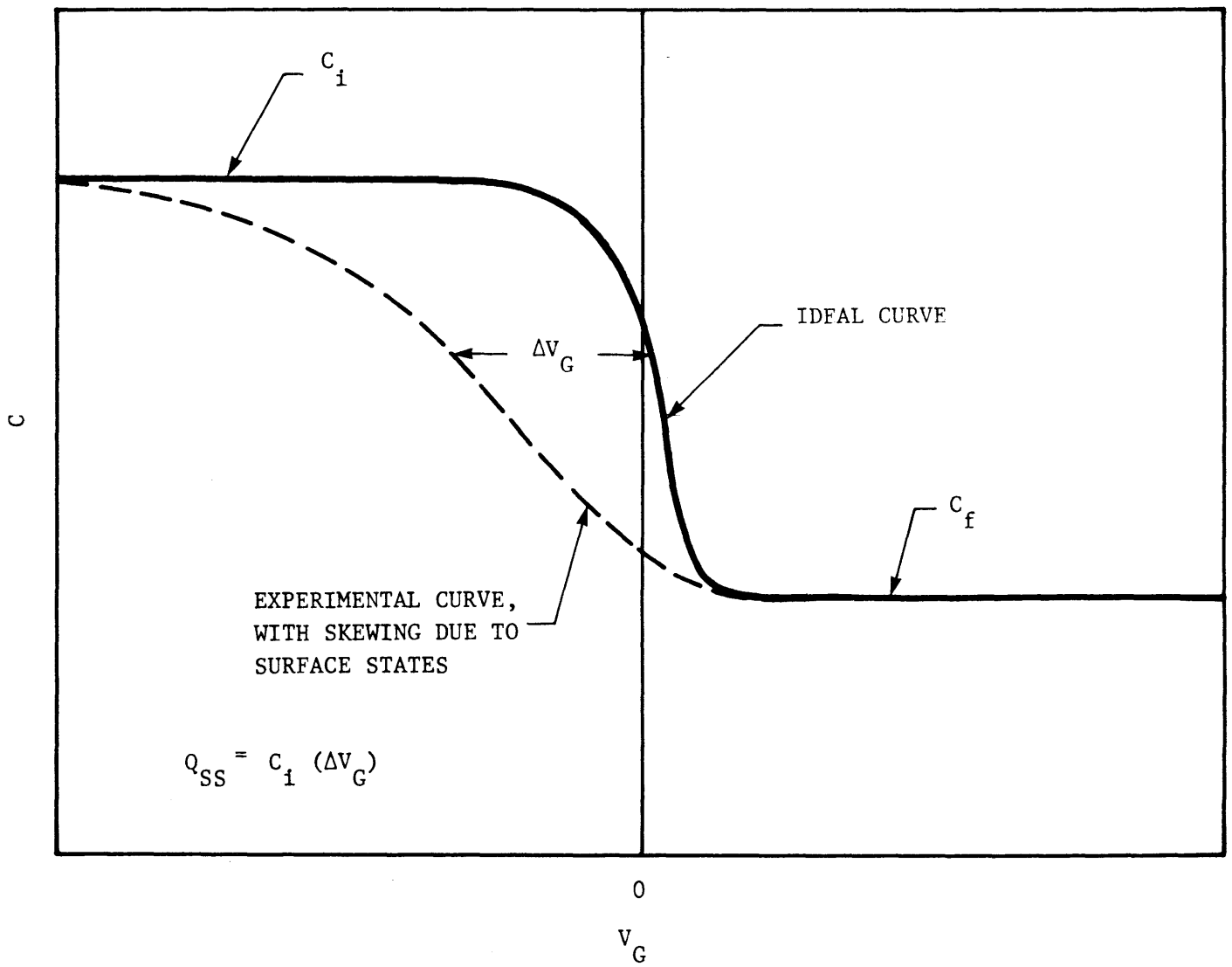

Figure 2.15. HIGH FREQUENCY MIS C-V CURVES SHOWING THE SKEWING OF THE EXPERIMENTAL CURVE DUE TO SURFACE STATES.

addition, the measurement will include the effects of slow surface states on the surface potential. The method is also subject to error due to the graphical differentiation. Even so, this method is useful for obtaining order of magnitude results, and for comparing different C-V characteristics.

2.3 MINORITY CARRIER GENERATION-RECOMBINATION

An important parameter which can be determined with the MIS structure is the thermal generation and recombination rates of minority carriers. The methods involve examining the response time of the inversion layer of minority carriers. The MIS techniques have the advantage over conventional techniques in that the measured quantities occur over a time period which is generally several orders of magnitude longer than the minority carrier lifetime of the semiconductor. The measurements are thus rather simple to make and do not require equipment with very fast response times.

There are several methods for determining the thermal generation and recombination rates. In this paper they will be divided into two categories: (1) the small signal techniques, which are essentially equilibrium measurements; and (2) the large signal techniques, which are non-equilibrium measurements that determine thermal generation rates.

2.3.1 Small Signal Techniques

Small signal techniques involve biasing the MIS structure into strong inversion and measuring a time constant associated with the inversion layer. At all times, the measuring signals are maintained at a low enough level so that a linear circuit model can be applied. The circuit model valid for strong inversion is shown in Figure 2.16. The effects due to minority carrier generation-recombination are included in the resistances R_{g-r} and R_D, which are due to generation-recombination in the

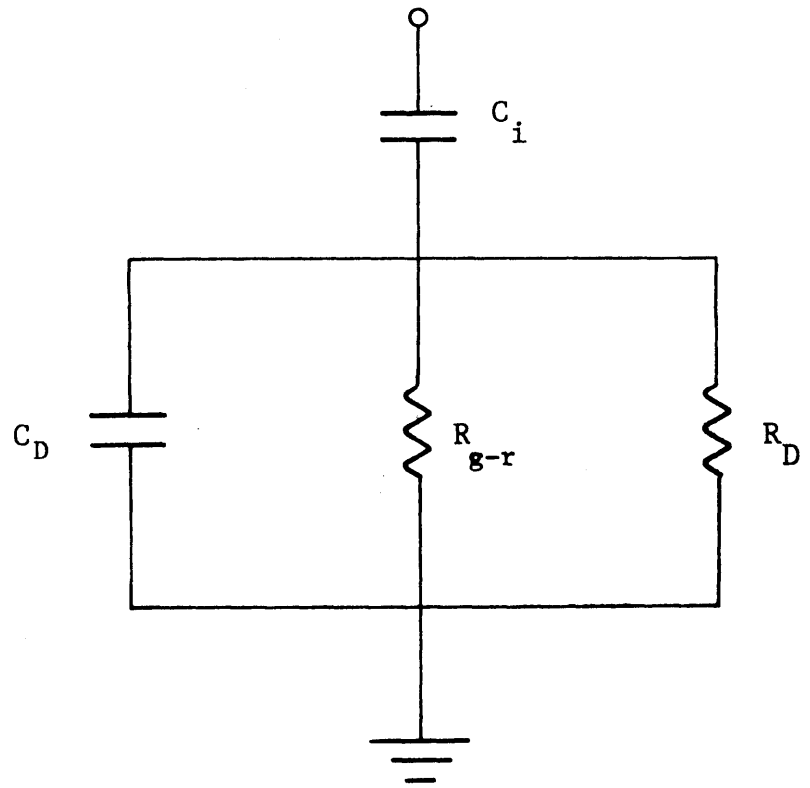

Figure 2.16. EQUIVALENT CIRCUIT OF AN MIS CAPACITOR IN HEAVY INVERSION

depletion region and diffusion from the bulk, respectively, which appear in parallel with the depletion capacitance C_D. It is assumed that generation-recombination by surface states can be neglected, due to the screening effect of the inversion layer. The characteristic time constant for this circuit is defined as

$$\tau_{ss} = (C_i + C_D)\ (R_{g-r} || R_D) \tag{2.38}$$

where C_i and C_D are the insulator and depletion capacitances, respectively, measured in Farads/cm^2, and $R_{g-r} || R_D$ is the resistance-area product of the depletion region. It is this time constant which is measured with the small signal techniques.

Hofstein[15] pointed out one method for determining this time constant. The structure is biased into inversion, and then a small amplitude square wave is superimposed. The charge which flows as a function of time is then measured, from which τ_{ss} can be determined. Analysis of the circuit shows that the charge as a function of time is given by

$$q(t) = C_i^2/(C_i + C_D)\ \ V_i\ e^{-t/\tau_{ss}} \tag{2.39}$$

where V_i is the amplitude of the square wave. A circuit which measures the transient response is shown in Figure 2.17.

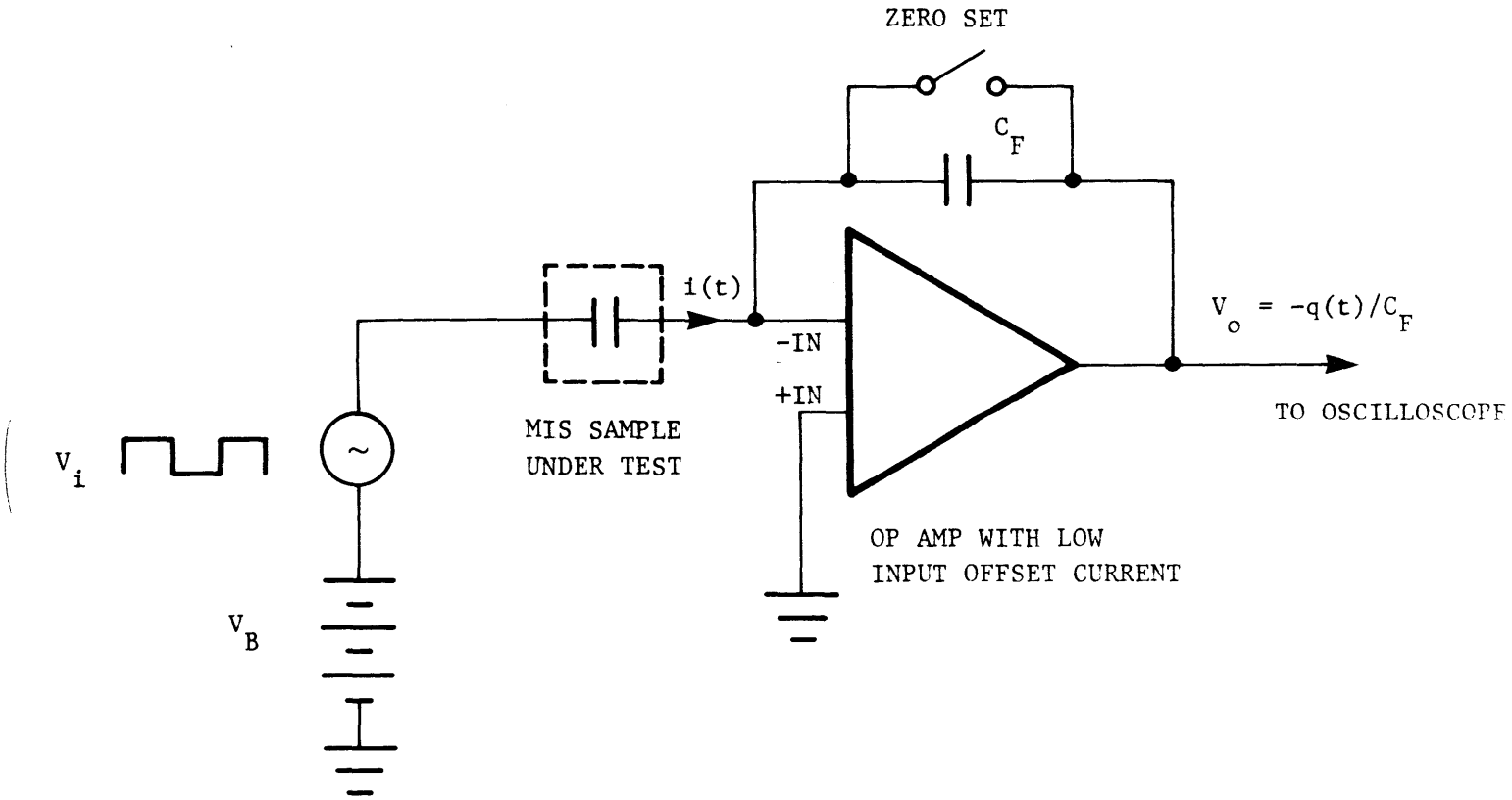

Figure 2.17. INTEGRATING CIRCUIT WHICH MEASURES THE TRANSIENT RESPONSE q(t) TO AN INCREMENTAL CHANGE IN INPUT VOLTAGE

An alternative but similar method is to measure the capacitance transient instead of the charge transient. To the best of the author's knowledge, this variation has not been previously reported in the literature. In this method, a high frequency measurement signal of small amplitude is superimposed onto the square wave and used to monitor the change in capacitance due to the square wave. It can be easily shown (see Appendix A.3) that the capacitance will decay to the equilibrium value C_f with the time constant τ_{ss}. This method has the advantage that the same circuitry can be used for the measurement as is used to make capacitance-voltage measurements. It is somewhat more noisy than the charge technique, but circumvents the problem of building a stable integrator.

A third method is to measure the capacitance and/or conductance of the MIS structure as a function of frequency. It is necessary to convert the circuit of Figure 2.16 into an equivalent parallel capacitance (C) and conductance (G), which are the measured quantities. Elementary circuit analysis shows that the conductance and capacitance as a function of frequency are given by

$$G = \frac{1}{\tau_{ss}} \left(\frac{C_i - C_f}{1 + 1/(\omega\tau_{ss})^2} \right) \tag{2.40}$$

and

$$C = \frac{C_f + C_i/(\omega\tau_{ss})^2}{1 + 1/(\omega\tau_{ss})^2} \tag{2.41}$$

where $C_f = \frac{C_i C_D}{C_i + C_D}$

These relationships can be solved for τ_{ss} to yield

$$\tau_{ss} = \frac{1}{G}\left[\frac{C_i - C_f}{2} \pm \sqrt{\left(\frac{C_i - C_f}{2}\right)^2 - (G/\omega)^2}\right] \tag{2.42}$$

and $$\tau_{ss} = \frac{1}{\omega}\frac{C_i - C}{C - C_f} \tag{2.43}$$

where the plus sign in equation 2.42 is for frequencies such that $\omega\tau_{ss} > 1$ and the minus sign is for frequencies such that $\omega\tau_{ss} < 1$.

When $\omega\tau_{ss} = 1$, equation 2.40 reduces to:

$$G/\omega = 1/2(C_i - C_f) \tag{2.44}$$

This is the peak in G/ω, which is the quantity measured with the test setup discussed in Section 3.2.

This method is particularly useful when the time constant τ_{ss} is too small to be measured easily by the transient methods (i.e., 20 ms or less).

After having determined the time constant τ_{ss}, it is now possible to determine the minority carrier lifetime. In order to do this, one must find a relationship between the resistances, R_{g-r} and R_D, and the minority carrier lifetime.

There are several mechanisms causing the generation and recombination of minority carriers which must be considered. Probably the most important is generation and recombination via trap levels located in the forbidden gap. This process can be important both in the space charge region and in the neutral bulk of the semiconductor. In addition, radiative and Auger mechanisms might also be important, especially when considering diffusion from the bulk.

Generation-recombination via traps was first considered in detail by Shockley and Read.[16] The concepts were later extended to generation and recombination in space charge regions by Sah, Noyce and Schockley.[17] Only the main results of these articles will be considered here.

For simplicity, only single energy level traps will be considered here. These traps can be characterized by four quantities: the density of traps, N_t, the energy of the traps, E_t, the capture cross section for holes, σ_p, and the capture cross section for electrons, σ_n. The net rate of recombination (U) under steady-state conditions is given by

$$U = (pn-n_i^2) \; / \; \left[(n + n_1)\tau_{po} + (p + p_1)\,\tau_{no}\right] \qquad (2.45)$$

where p = density of holes in valence band

n = density of electrons in conduction band

p_1 = density of holes in valence band when $E_F=E_t$

n_1 = density of electrons in conduction band when $E_F=E_t$

τ_{no} = lifetime of electrons injected into highly p-type specimen

τ_{po} = lifetime of holes injected into highly n-type specimen

The lifetimes, τ_{po} and τ_{no} are often defined in terms of the trap density and capture cross sections as [9]

$$\tau_{po} = \frac{1}{\sigma_p V_{th} N_t} \tag{2.46}$$

and $$\tau_{no} = \frac{1}{\sigma_n V_{th} N_t} \tag{2.47}$$

where $$V_{th} \equiv \sqrt{3kT/m} \tag{2.48}$$

In order to apply equation 2.45, one needs to determine the concentration of carriers in the valence and conduction bands as a function of the potential in the depletion region. Substitution of the following relations

$$
\begin{aligned}
p_1 &= n_i \exp\left[(E_i - E_t)/kT\right] \\
n_1 &= n_i \exp\left[(E_t - E_i)/kT\right] \\
p &= n_i \exp\left[(\phi_p - \psi)q/kT\right] \\
n &= n_i \exp\left[(\psi - \phi_n)q/kT\right] \\
E_i &= -q\psi
\end{aligned}
\tag{2.49}
$$

into equation 2.45 gives the following expression for the steady-state recombination rate:

$$
U = \frac{n_i}{\sqrt{\tau_{po}\,\tau_{no}}} \frac{\sinh \frac{q}{2kT}(\phi_p - \phi_n)}{\cosh\left[\frac{q}{kT}\left(\psi - \frac{\phi_p + \phi_n}{2}\right) + \ln\sqrt{\frac{\tau_{po}}{\tau_{no}}}\right] + \exp\left[\frac{-q}{2kT}(\phi_p - \phi_n)\right] \cosh\left(\frac{E_t - E_i}{kT} + \ln\sqrt{\frac{\tau_{po}}{\tau_{no}}}\right)} \tag{2.50}
$$

where ϕ_p and ϕ_n are the quasi-Fermi potentials for holes and electrons, respectively, ψ is the electrostatic potential, and E_i is the intrinsic Fermi energy.

If the applied voltage is small (i.e., $V_D = \phi_p - \phi_n \ll kT$) then the above expression can be simplified to

$$
U = \frac{n_i}{\sqrt{\tau_{po}\,\tau_{no}}} \frac{q/2kT\ V_D}{\cosh\left[\frac{q}{kT}(\psi - \phi_F) + \ln\sqrt{\frac{\tau_{po}}{\tau_{no}}}\right] + \cosh\left(\frac{E_t - E_i}{kT} + \ln\sqrt{\frac{\tau_{po}}{\tau_{no}}}\right)} \tag{2.51}
$$

where ϕ_F is the Fermi potential.

The resistance can now be calculated by using the relations

$$J = -q \int_o^{W_m} U \, dx$$

$$R_{g-r}^{-1} = \frac{\partial J}{\partial V_D} \approx \frac{q}{V_D} \int_o^{W_m} U \, dx \tag{2.52}$$

resulting in

$$R_{g-r}^{-1} = \frac{q^2 n_i}{2kT\sqrt{\tau_{po}\,\tau_{no}}} \int_o^{W_m} \frac{dx}{\cosh\left[\frac{q}{kT}(\psi-\phi_F) + \ln\sqrt{\frac{\tau_{po}}{\tau_{no}}}\right] + \cosh\left(\frac{E_t-E_i}{kT} + \ln\sqrt{\frac{\tau_{po}}{\tau_{no}}}\right)} \tag{2.53}$$

where W_m is the depletion region width.

In order to solve this integral, one needs to know how the potential varies with x. Sah, Noyce, and Shockley[17] make the assumption that ψ varies linearly with x, so that

$$\psi - \phi_F = \psi_B(1-2x/W_m) \tag{2.54}$$

where $\psi_B = \frac{kT}{q} \ln \frac{N_B}{n_i}$ for p-type and $\psi_B = \frac{kT}{q} \ln \frac{n_i}{N_B}$ for n-type.

With this substitution, equation 2.53 can be solved exactly to yield

$$R_{g-r}^{-1} = q\, n_i\, W_m\, f(b) / \left(\sqrt{\tau_{po}\, \tau_{no}}\, 2\psi_B \right) \tag{2.55}$$

where

$$b \equiv \cosh\left(\frac{E_t - E_i}{kT} + \ln \sqrt{\frac{\tau_{po}}{\tau_{no}}} \right) \tag{2.56}$$

and

$$f(b) = \frac{1}{2\sqrt{b^2-1}}\ \ln\left(\frac{b + \sqrt{b^2-1}}{b - \sqrt{b^2-1}} \right) \tag{2.57}$$

The actual potential variation is more closely quadratic in x, so that

$$\psi - \phi_F = \psi_B \left[2\left(1 - \frac{x}{W_m} \right)^2 - 1 \right] \tag{2.58}$$

In this case, the integral cannot be solved analytically, but can be solved by numerical methods. To get a feel for the error involved with using equation 2.55, the integral was solved with the assumptions that $E_t = E_i$ and $\tau_{po} = \tau_{no}$ and then compared with the results of the linear approximation. A plot of the relative generation rate across the depletion region for both potential distributions is shown in Figure 2-18.

The calculations were done for x = 0.4 $Hg_{1-x}Cd_xTe$ with $N_B = 1.0 \times 10^{15}$, T = 147k and $n_i = 4.7 \times 10^{10}$. Under these conditions, the resistance as calculated from equation 2.55 was about 70% of that calculated with the more exact equation. The error for a wide variation of doping and temperature was found to range from 25-30%.

The resistance can always be written in the form

$$R_{g-r}^{-1} = \frac{q\, n_i\, W_m}{2\psi_B\, \tau_{g-r}} \tag{2.59}$$

with

$$\tau_{g-r} \equiv \frac{\sqrt{\tau_{po}\, \tau_{no}}}{f(b)} \tag{2.60}$$

for the linear potential approximation, and

$$\tau_{g-r} = \frac{\sqrt{\tau_{po}\, \tau_{no}}}{g(b, \tau_{po}, \tau_{no})}$$

with (2.61)

$$g(b, \tau_{po}, \tau_{no}) \equiv \frac{\ln N_B/n_i}{W_m} \int_o^{W_m} \frac{dx}{\cosh\left[\frac{q}{kT}\,\psi_B\left[2\left(1-\frac{x}{W_m}\right)^2 - 1\right] + \ln\sqrt{\frac{\tau_{po}}{\tau_{no}}}\right] + b}$$

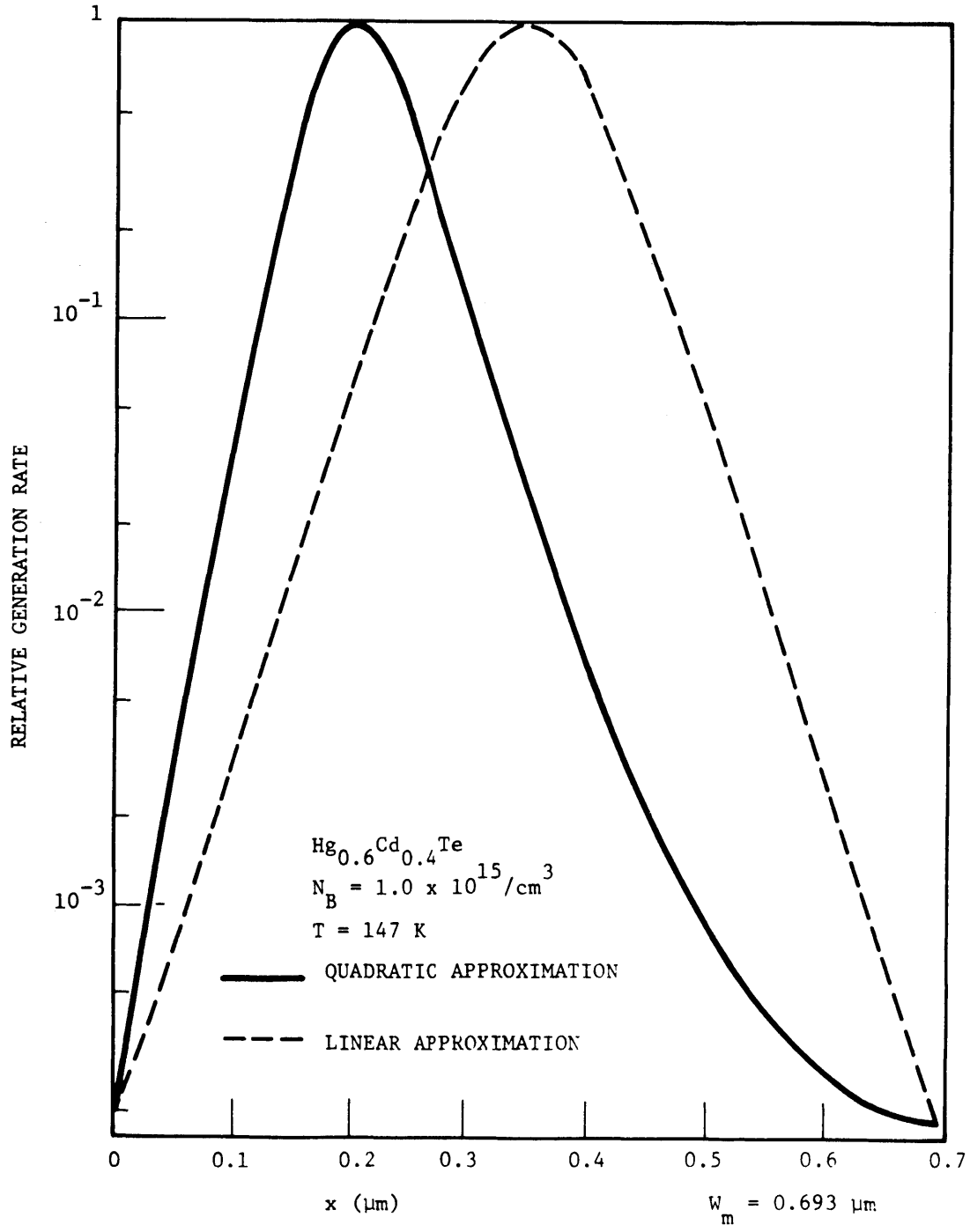

Figure 2.18. RELATIVE GENERATION RATE VERSUS DISTANCE FROM SURFACE FOR THE LINEAR AND QUADRATIC POTENTIAL APPROXIMATIONS FOR THE CASE $\tau_{no} = \tau_{po}$ AND $E_t = E_i$.

for the more exact quadratic approximation. This effective lifetime, τ_{g-r}, is what is commonly used to characterize the depletion region. It is not, in general, equal to the lifetime in the neutral bulk (τ_{po} for highly n-type material and τ_{no} for highly p-type material).

Equation 2.59 and equation 2.38 can be used to determine the relationship between τ_{g-r} and τ_{ss} for the case when $R_D \gg R_{g-r}$. The relation that results after a lot of algebra is

$$\tau_{g-r} = \tau_{ss} \frac{2\, n_i\, C_f}{N_B\, C_i} \tag{2.62}$$

Thus it can be seen that the measured time constant is on the order of N_B/n_i times the minority carrier lifetime of the depletion region.

In the above analysis it was assumed that radiative and Auger processes were not important in the depletion region. Application of the statistics of these processes to this problem shows that these processes are indeed much less important than generation-recombination by traps (see Appendix A.2).

For sufficiently high temperatures, diffusion from the bulk becomes an important process. A relationship between the diffusion resistance R_D and the bulk lifetime will be calculated next.

Since the depletion region of an MIS structure biased into inversion is analogous to that of a one-sided step junction, the well-known ideal diode equation can be used to calculate the resistance, so that

$$J = J_{sat} \left(e^{q\ V/kT}-1\right) \tag{2.63}$$

where

$$J_{sat} = q\ n_i^2/N_B \sqrt{\mu/\tau_B}\ \sqrt{kT/q} \tag{2.64}$$

τ_B is the bulk minority carrier lifetime, and μ is the mobility of minority carriers.

Thus

$$R_D = \left(\frac{\partial J}{\partial V}\right)^{-1}\Bigg|_{V=0} = \frac{kT}{q}\ \frac{1}{J_{sat}}$$

$$R_D = \frac{N_B}{q\ n_i^2} \sqrt{\frac{\tau_B}{\mu}}\ \sqrt{\frac{kT}{q}} \tag{2.65}$$

The three mechanisms which affect the bulk lifetime are Auger recombination, radiative recombination, and recombination via traps. The bulk lifetime due to traps has been determined by Shockley and Read[16]. Their

$$\tau_B(S\text{-}R) = \tau_{po}\left(\frac{n_o+n_1}{n_o+p_o}\right) + \tau_{no}\left(\frac{p_o+p_1}{n_o+p_o}\right) \tag{2.66}$$

result is where p_o and n_o are the equilibrium concentrations of holes and electrons, p_1 and n_1 are defined by equations 2.49, and τ_{po} and τ_{no} are defined by equations 2.46 and 2.47.

If the semiconductor is doped sufficiently p-type, such that $p_o \gg n_o$, n_1, p_1, then equation 2.66 reduces to

$$\tau_B = \tau_{no} \tag{2.67}$$

and likewise if it is doped sufficiently n-type such that $n_o \gg p_o$, n_1, p_1, then

$$\tau_B = \tau_{po} \tag{2.68}$$

It should be emphasized that the bulk lifetime defined by equation 2.66 is not the same as the depletion region lifetime defined by equation 2.61. Thus any measurement which determines the depletion lifetime $\tau_{g\text{-}r}$ does not necessarily directly determine the bulk lifetime as well.

Another important process is radiative recombination in which excess carriers recombine primarily by transistions between the valence and conduction bands with the release of a photon. The radiative lifetime can be

be calculated by considering the absorption coefficient of the material and the equilibrium density of photons. The number of photons generated thermally per unit time is given by[18]

$$G_r = 8\pi h^{-3} (n/c)^2 \int_0^\infty \frac{K_i (h\nu)^2 \, d(h\nu)}{[\exp(h\nu/kT)-1]} \tag{2.69}$$

where

h = Planck's constant

$h\nu$ = energy of photon with frequency ν

c/n = velocity of radiation in semiconductor

K_i = absorption coefficient of semiconductor

The lifetime is related to G_r and the densities of carriers by

$$\tau_R = \frac{n_i^2}{G_r(n_o+p_o)} \tag{2.70}$$

The radiative lifetime is thus roughly inversely proportional to carrier density and is maximum for intrinsic material, for which

$$\tau_{Ri} = \frac{n_i}{2G_r} \tag{2.71}$$

The quantity G_r is normally calculated using equation 2.69 and the experimentally measured value of K_i. These calculations have been carried out by Kinch[19] et al for (Hg,Cd)Te.

Auger generation-recombination occurs when fast carriers lose most of their kinetic energy in the act of creating an electron-hole pair, or carriers gain kinetic energy when a hole and electron recombine. The detailed theoretical treatment of the Auger mechanisms is difficult and will not be presented here (see, for example, Ref. 18). The main result, valid for n-type material for which electron-electron processes are dominant, is as follows:

$$\tau_A \cong \frac{2\, n_i^2}{n_o^2}\, \tau_{Ai} \tag{2.72}$$

where τ_{Ai} is approximately the lifetime for intrinsic material, and can be calculated theoretically. It can be seen that the lifetime is inversely proportional to the square of the electron density. Theoretical calculations of the Auger lifetime for (Hg,Cd)Te were carried out by Kinch[19] et al. For the compositions used in this work, the Auger lifetime was considerably longer than the radiative or Shockley-Read lifetime, and could thus be neglected.

With more than one of these processes present, the effective bulk lifetime can be approximately written as

$$1/\tau_B = 1/\tau_B(S\text{-}R) + 1/\tau_R + 1/\tau_A \qquad (2.73)$$

It can be concluded from the above discussion that the effective small signal time constant τ_{ss} defined by equation 2.38 is a function of two minority carrier lifetimes, the depletion lifetime τ_{g-r} and the bulk lifetime τ_B, which are, in general, not equal.

2.3.2 Large Signal Techniques

These methods rely on observing the rate at which the inversion layer forms under an MIS capacitor. A step voltage is applied to the gate of an MIS capacitor of proper polarity to deplete majority carriers from the semiconductor surface (negative for n-type, positive for p-type). Initially, a deep depletion region forms in the semiconductor. As minority carriers are generated in the depletion region or within a diffusion length of the depletion region, they are swept by the field to the insulator-semiconductor interface where they accumulate to form an inversion layer. The generated majority carriers flow to the edge of the depletion region where they partially neutralize the ionized impurity sites, which reduces the width of the depletion region. Thus, the MIS capacitance decays from the initial low value to the higher equilibrium value C_f.

There are three sources of minority carriers during the transient: (1) generation of carriers in the depletion region under the gate; (2) generation of carriers by surface states under the gate and around the

perimeter of the gate; and (3) diffusion of carriers from the bulk of the semiconductor. The diffusion current is negligible except at high temperatures, and will be neglected in most of the analysis.

Heiman presented an analysis of the transient for the case of no surface states and negligible diffusion current.[20] In this case the net generation rate of electron-hole pairs per unit area is given by

$$g = \frac{n_i}{2\tau_g} \quad (W-W_f) \tag{2.74}$$

where W_f is the equilibrium depletion width and τ_g is the "generation" lifetime whose definition will be discussed later in this section. The rate of change of inversion layer charge (N_s) is then given by

$$\frac{dN_s}{dt} = g = \frac{n_i}{2\tau_g} \quad (W-W_f) \tag{2.75}$$

The total voltage V_G is related to the depletion width and inversion charge by

$$V_G = (q/C_i) \quad (N_B W + N_s) + \frac{q \, N_B \, W^2}{2\epsilon_s} \tag{2.76}$$

Differentiation of 2.76 and use of 2.75 yields the following differential equation for the time dependence of W.

$$\frac{dW}{dt}\left(1 + \frac{C_i}{\varepsilon_s} W\right) + \frac{W-W_f}{T} = 0 \tag{2.77}$$

where $T \equiv 2\tau_g \frac{N_B}{n_i}$ (2.78)

The solution of equation 2.77 in terms of the initial capacitance C_o and the final capacitance C_f is

$$\ln\left(\frac{C_f/C-1}{C_f/C_o-1}\right) + (C_f/C - C_f/C_o) = -\frac{C_f t}{C_i T} \tag{2.79}$$

A sketch of C vs t/T is shown in Figure 2.19.

A useful relationship can be found by rewriting equation 2.77 in terms of C, C_f, and C_i:

$$\frac{dC}{dt} = \frac{C^2}{C_i T}(1- C/C_f) \tag{2.80}$$

The equation relates the slope of the C-t transient simply to the quantity T, which determines the generation lifetime through equation 2.78.

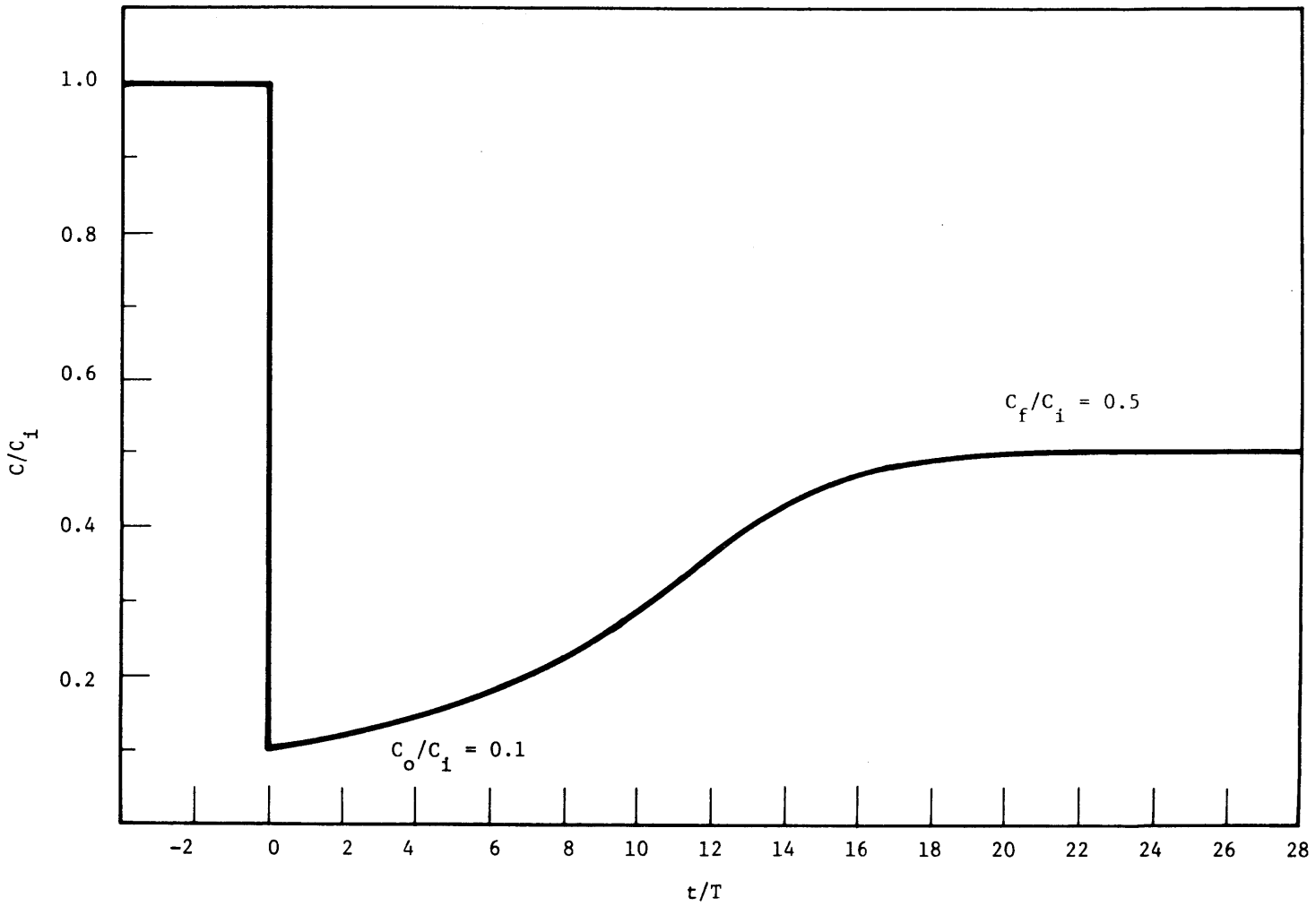

Figure 2.19. TRANSIENT RESPONSE OF AN MIS STRUCTURE AFTER A DEPLETING VOLTAGE STEP ACCORDING TO THE THEORY OF HEIMAN (REF. 20)

In general, generation by surface states cannot be neglected. Zerbst[21] was the first to include the effects of surface generation in the analysis. He assumed that surface generation was constant during the entire transient. In this case a term must be added to equation 2.75, so that

$$\frac{dN_s}{dt} = \frac{n_i}{2\tau_g} (W-W_f) + n_i S \tag{2.81}$$

where S is the surface generation velocity.

Writing the derivative of equation 2.76 in terms of derivatives of W^2 with respect to time, and substituting equation 2.81 results in

$$\frac{d(W^2)}{dt} \left(\frac{1}{2C_i W} + \frac{1}{2\epsilon_s} \right) = \frac{1}{C_i N_B} \left(\frac{n_i}{2\tau_g} (W-W_f) + n_i S \right) \tag{2.82}$$

which can be rewritten in terms of C, C_i and C_f as

$$- \frac{d}{dt} \left(\frac{C_i}{C} \right)^2 = \frac{n_i C_i}{N_B C_f} \left(\frac{C_f}{C} - 1 \right) \frac{1}{\tau_g} + \frac{2n_i C_i}{N_B \epsilon_s} S \tag{2.83}$$

It can be seen that a plot of - d/dt $(C_i/C)^2$ versus $(C_f/C-1)$ will yield a straight line whose slope is inversely proportional to τ_g and which has an intercept at $C_f/C-1 = 0$ proportional to S. This plot will be referred to as a "Zerbst" plot.

Experimental data soon indicated that equation 2.83 was not valid over a considerable portion of the transient. The portion of the curve corresponding to the initial part of the transient often had a large slope initially, which decreased with time until it became constant for the rest of the transient. This effect is illustrated in Figure 2-20.

Schroder and Nathanson[22] explained this effort by assuming that S is a strongly nonlinear function of time. This is to be expected, since S is a function of the carrier densitites at the surface, which change over the course of the transient. Specifically, S will be considerably larger for a depleted surface, as is the case at the beginning of the transient, than for an inverted surface which occurs towards the end of the transient.

In addition, they showed that the surface generation of the lateral portion of the space charge region was important, and that this generation was approximately proportional to $W-W_f$. Equation 2.81 then becomes

$$\frac{dN_s}{dt} = n_i \left[(W-W_f) \ (1/2\tau_g + S_o \ P/A) + S \frac{A_G}{A} \right] \tag{2.84}$$

where P is the perimeter of the gate, A_G is the area of the gate, A is the total area of the space charge region and S_o is the surface generation velocity of a depleted surface. This is similar in form to equation 2.78, with τ_g replaced by τ_g', where

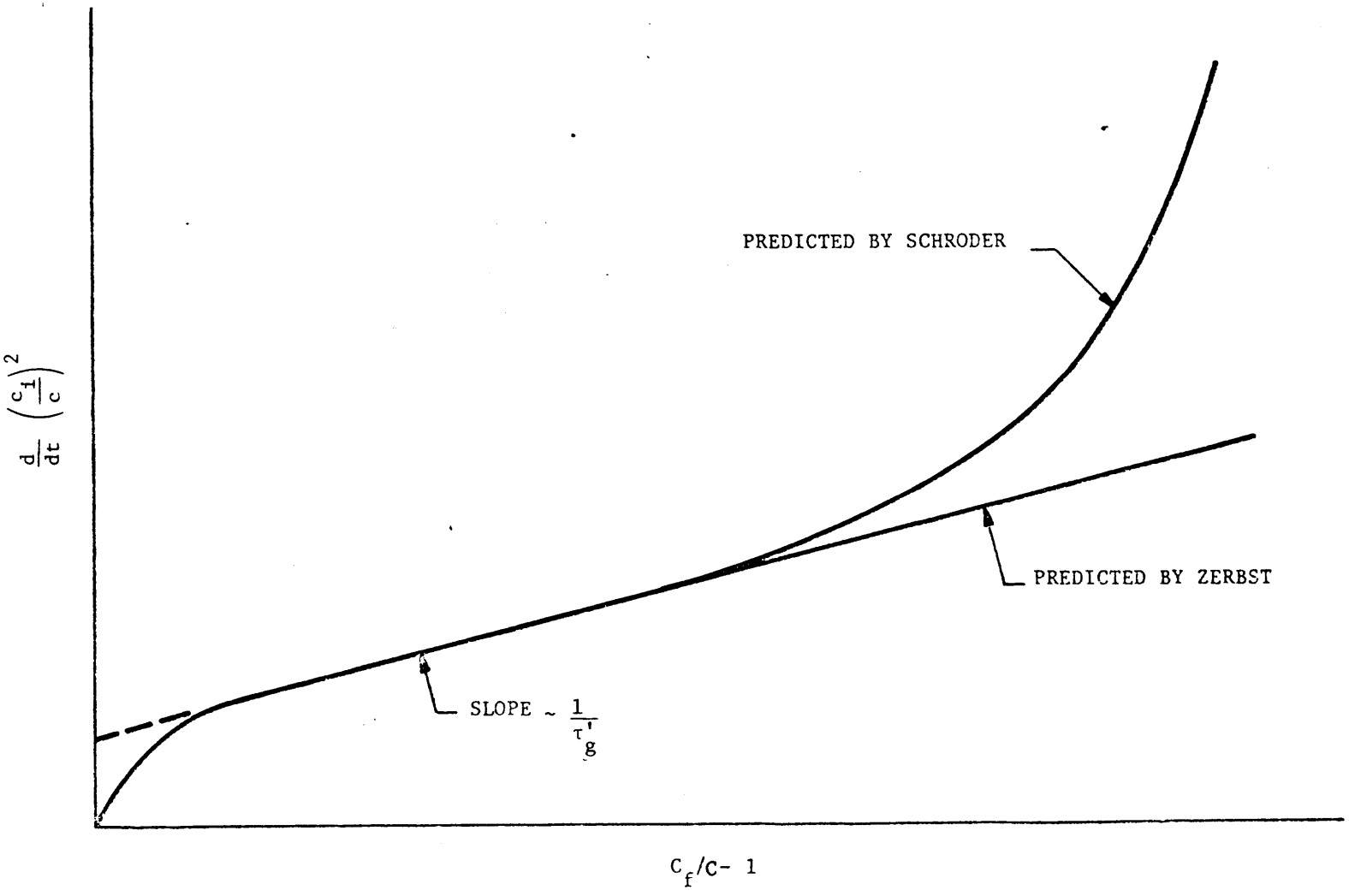

Figure 2.20. "ZERBST" PLOT SHOWING DIFFERENCE BETWEEN SCHRODER'S AND ZERBST'S THEORY

$$\frac{1}{2\tau_g'} = \frac{1}{2\tau_g} + S_o P/A$$

$$\cong \frac{1}{2\tau_g} + \frac{4S_o}{D} \qquad (2.85)$$

where D is the diameter of the gate. The slope of the linear portion of the Zerbst plot would thus determine τ_g', which could be converted to τ_g once S_o was known. They stated that S_o could be determined from the initial slope of the Zerbst plot, for t = 0. With Schroder's modification a Zerbst plot determines both the generation lifetime and the surface generation velocity for a depleted surface.

An important assumption made by Heiman, Zerbst and Schroder is that the generation of carriers can be described by a generation lifetime, τ_g, which is constant during the entire transient. Sah[23,24] has indicated that this is not necessarily correct. The large electric fields which occur during the first part of the transient can lead to interband impact generation of hole-electron pairs, which would cause the effective generation lifetime to be smaller at the beginning of the transient. Thus τ_g will be a function of time as well. Sah also showed that the initial portion of the transient is dominated by readjustment of charge in the surface states and depletion region traps. It is, therefore, unlikely that the surface generation velocity can be accurately determined from slope at the beginning of the transient, as implied by Schroder.

The presence of a linear portion in the Zerbst plot does, however, imply that τ_g is essentially constant over the latter part of the transient, when the electric field is lower. If generation in the depletion region is much larger than surface generation, then a Zerbst plot will still provide important information about the generation lifetime of the depletion region.

The definition of the generation lifetime, τ_g, will now be considered in terms of the statistics for a single level trap presented in Section 2.3.1. It will be assumed that impact ionization is negligible, so that the emission probabilities of the traps will be essentially the same as in equilibrium.

For the case of a strongly reverse biased depletion region it can be assumed that the carrier densities are much smaller than n_i over most of the depletion region. Under these conditions, equation 2.45 will become

$$U \cong - n_i^2/(n_1 \tau_{po} + p_1 \tau_{no}) \tag{2.86}$$

Substitution of the relations 2.49 then results in

$$\begin{aligned} -U &= n_i/[\tau_{po} \exp(E_t-E_i)/kT + \tau_{no} \exp(E_i-E_t)/kT] \\ &= n_i/2\tau_g \end{aligned} \tag{2.87}$$

where $\tau_g \equiv \sqrt{\tau_{po}\ \tau_{no}}\ \cosh\ (E_t - E_i/kT + 1/2\ \ln\ \tau_{po}/\tau_{no})$

$$= b\sqrt{\tau_{po}\ \tau_{no}} \tag{2.88}$$

and b is defined by equation 2.56. The number of carriers generated per unit time is then given by

$$g = -U(W-W_f) = \frac{n_i}{2\tau_g}(W-W_f) \tag{2.89}$$

This generation lifetime is not, in general, equal to the small signal lifetime, τ_{g-r}, defined approximately by equation 2.60 or more exactly by equation 2.61. Their ratio is given by

$$\tau_g/\tau_{g-r} = b\ f(b) \tag{2.90}$$

for the linear potential approximation, and

$$\tau_g/\tau_{g-r} = b\ g(b,\tau_{po},\tau_{no}) \tag{2.91}$$

for the quadratic potential approximation.

For higher temperatures, diffusion of carriers from the bulk can become an important process. Over most of the transient the current due to diffusion will be equal to the saturation current of a reverse biased

depletion region, as defined by equation 2.64. Equation 2.81 must now be modified to include the diffusion current, so that

$$\frac{dN_s}{dt} = \frac{n_i}{2\tau_g} (W-W_f) + n_i S + J_{sat}/q \qquad (2.92)$$

Since the diffusion term is constant, its effect on the Zerbst plot will be to shift the curve vertically along the axis of $-d/dt(C/C_i)^2$. If the surface generation term is small, the intercept on this axis should be proportional to the saturation current.

In some cases, it is interesting to know that total duration of the transient, which is often called the storage time, T_s. This can be accomplished by integrating equation 2.92, i.e.,

$$T_s = \int_0^{N_{SF}} \left[\frac{n_i}{2\tau_g} (W-W_f) + n_i S + J_{sat}/q \right]^{-1} dN_s \qquad (2.93)$$

where N_{sf} is the equilibrium concentration of carriers in the inversion layer. This integral will be difficult to solve since both τ_g and S cannot generally be considered constant. Steckl[25] solved this integral with the assumption that τ_g and S are constant. His result (with a minor change of notation) is

$$T_s = A\left(\frac{C_i}{C_o} - \frac{C_i}{C_f}\right) + A(1-AB)\ \ln\left(\frac{AB + C_i/C_o - 1}{AB + C_i/C_f - 1}\right) \qquad (2.94)$$

where

$$A = \frac{2\tau_g N_B}{n_i}\ ,\ B = \frac{n_i C_i}{N_B \varepsilon_s} S + \left(\frac{n_i}{N_B}\right)^2 \frac{C_i}{\varepsilon_s} \sqrt{\frac{kT\ \mu}{q\ \tau_B}}$$

and C_o and C_f are the initial and equilibrium values of capacitance, respectively. This equation will be useful in analyzing storage time versus temperature data.

It can be seen that the MIS structure is a useful tool for examining the various mechanisms for generation of minority carriers. It is important, however, to understand the assumptions made and the definitions of the lifetime used in the analysis of experimental data.

SECTION 3

EXPERIMENTAL METHODS

3.1 MIS STRUCTURES ON (Hg,Cd)Te

3.1.1 (Hg,Cd)Te Description

The material used in this research was $Hg_{1-x}Cd_xTe$ with x values ranging from x = 0.3 to x = 0.4. These compositions correspond to band-gaps at 80K of 0.25 eV and 0.41 eV, respectively. Most of the work was done on compositions with $x \cong 0.4$.

Several different types of material were used. The majority of experiments utilized single crystal n-type material oriented in the (111) direction. This material had an extrinsic carrier concentration of about 2×10^{14} cm^{-3} and a 77K Hall mobility in excess of 2×10^4 $cm^2/V\text{-}s$. The (111)A and (111)B faces of this crystal were distinguished by the procedure described in Appendix A.1. Measurements were also performed on p-type material oriented in the (100) direction. This material was nonuniformly doped, with net hole concentrations ranging from 5×10^{14} cm^{-3} to 10^{16} cm^{-3}. Several pieces of unoriented material were also used, most of which were n-type with $(N_D - N_A) \cong 6 \times 10^{14}$ cm^{-3}.

3.1.2 MIS Geometry and Fabrication

The basic MIS structural configuration used for this work is shown in Figure 3.1. The structure consists of a (Hg,Cd)Te substrate upon which a dielectric insulator (typically 4000 Å thick) is deposited. The gate electrodes are 0.015 inch circular gold dots which are evaporated to a thickness of about 100 Å. Smaller indium dots, 0.005 inch in diameter, provide a contact pad onto which a gold wire is thermal compression bonded.

Prior to the fabrication of MIS structures, a slab of (Hg,Cd)Te was cut from an ingot with a wire saw. The slab was then etched in 5:1 methanol/bromine solution to remove the majority of wire saw damage. Next the slab was mounted on a lapping fixture and lapped with successively finer abrasives. The slab was then removed from the fixture, rinsed, cleaned and then etched in a 5:1 methanol/bromine solution for ten seconds. The etching solution was continuously circulated to insure a smooth and uniformly etched surface. The etch was followed by a series of rinses.

If no further surface preparation was required, an insulating coating was then deposited. The insulator which was used for most experiments was Thorium Tetrafluoride (ThF_4). This insulator was chosen primarily for its low pinhole density which resulted in a high yield of operative MIS structures. In addition, it has a high dielectric constant ($\epsilon_i \cong 12\ \epsilon_o$) which allows for a reasonably thick coating (~4000 Å in this case). The

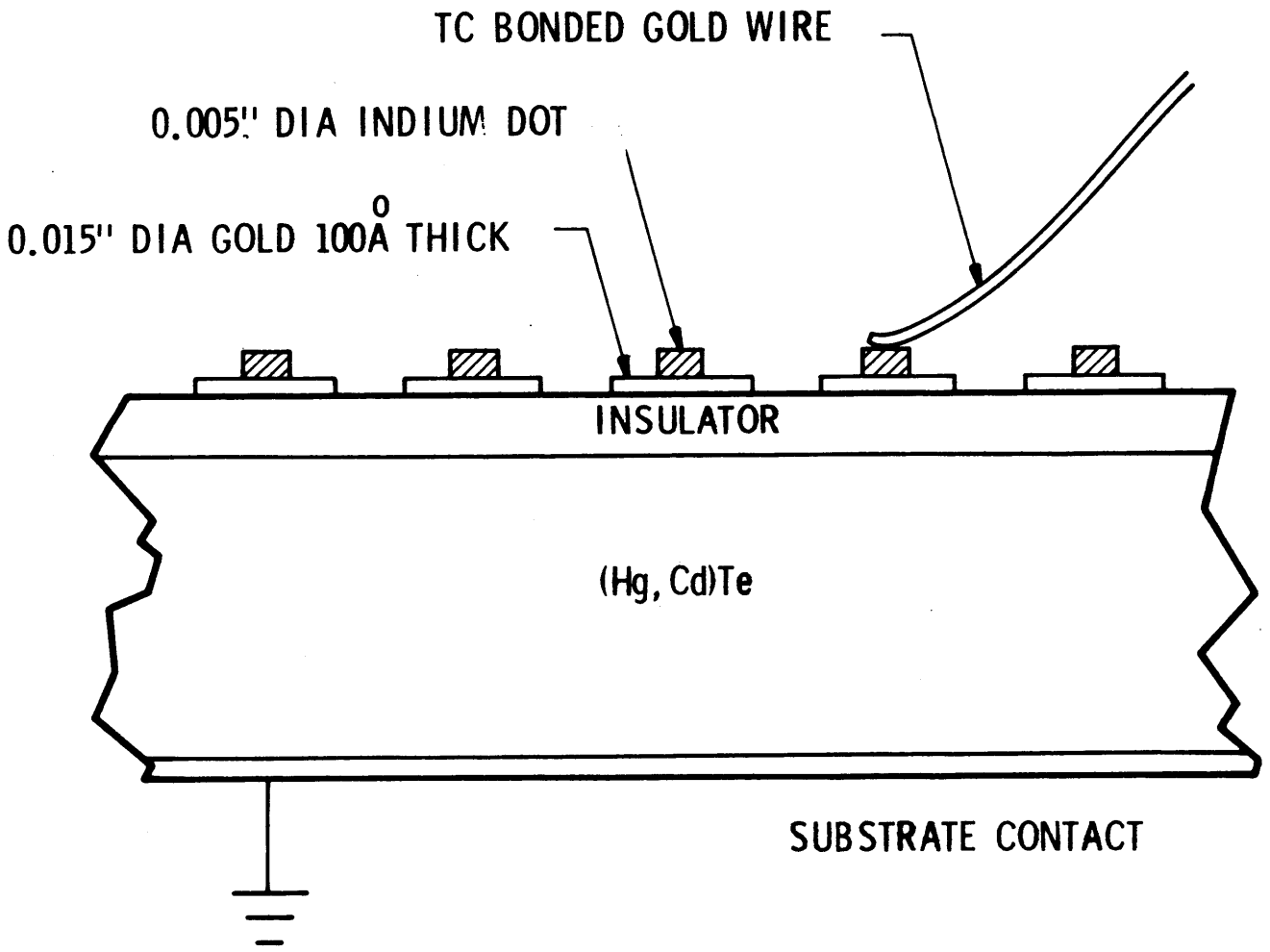

Figure 3.1. MIS STRUCTURE CONFIGURATION

ThF_4(Hg,Cd)Te interface also exhibited lower surface state densities than that of most of the other dielectrics studied. ThF_4 was deposited by evaporation of ThF_4 powder in a vacuum.

The next step was evaporation of the gold field plate. Circular dots, 0.015 inch in diameter, were evaporated to a thickness of approximately 100 Å through a metal mask. Measurements done with a calibrated microscope stage indicated that the actual diameter was 0.0145 inch, which corresponds to an area of 1.07×10^{-3} cm^2. The thin layer of gold was used because it is semitransparent to infrared radiation with wavelengths between 3 and 5 micrometers. It was then possible to measure the bandgap with a spectral response setup described later in this section. Next, indium dots of 0.005 inch diameter were evaporated onto the gold to a thickness of approximately 1.5 micrometer. These relatively soft indium pads could have gold wires bonded to them with little pressure, so that no damage would result to the insulator.

The substrate contact consisted of a conductive silver paste into which the slab was pressed. The slab was now ready to be mounted into a dewar.

3.2 MEASUREMENT TECHNIQUES

3.2.1 Test Dewars

Because of the small bandgap in this material, it is necessary to cool the material to achieve semiconducting properties. This was accomplished by mounting the MIS sample into a vacuum dewar which could subsequently be cooled with a liquid cryogen.

The slab was mounted on top of a pedestal, with the gold wire leads being soldered to pins on the perimeter of the pedestal. A thermistor was also attached to monitor the temperature during testing. A metal "cold" shield was then attached to the pedestal so that the slab was completely shielded from any external background radiation. This was done to meet the requirement that the MIS sample be in external thermal equilibrium.

The dewar lead configuration resulted in a stray capacitance of about 4 pF in parallel with the MIS structure. To facilitate calibration during testing, open pins were left between each pin to which an MIS structure was connected. The stray capacitance could then be measured on the pins adjacent to that of the structure under test, and the average of the strays subtracted from the subsequent measurement. The error introduced into the capacitance measurements by these strays is estimated to be about ± 0.5 pF, which is 3% to 5% of the total capacitance of the structure.

It was very important that no leakage between pins was present, especially when making conductance measurements. For this reason, the dewars were completely cleaned in methanol before testing. In addition, dry nitrogen was circulated around the dewar during testing to prevent the condensation of water vapor.

3.2.2 Capacitance/Conductance Measurements

A test setup was needed which could easily measure the conductance and capacitance of the MIS structure at a variety of frequencies. The PAR Model 124A Lock-In Amplifier fulfilled these requirements and was thus used for most of the testing. A diagram of the basic setup is shown in Figure 3.2.

The signal voltage V_s from the reference output of the lock-in amplifier is applied through the blocking capacitor, C_B, to the MIS structure, which is here modeled as a conductance G in parallel with a capacitance C. The current through the device is sensed at the virtual ground input of the PAR Model 181 current sensitive preamplifier, and is converted to a voltage which is applied to the input of the lock-in amplifier. This signal is compared to the reference signal, so that the real and imaginary components can be determined.

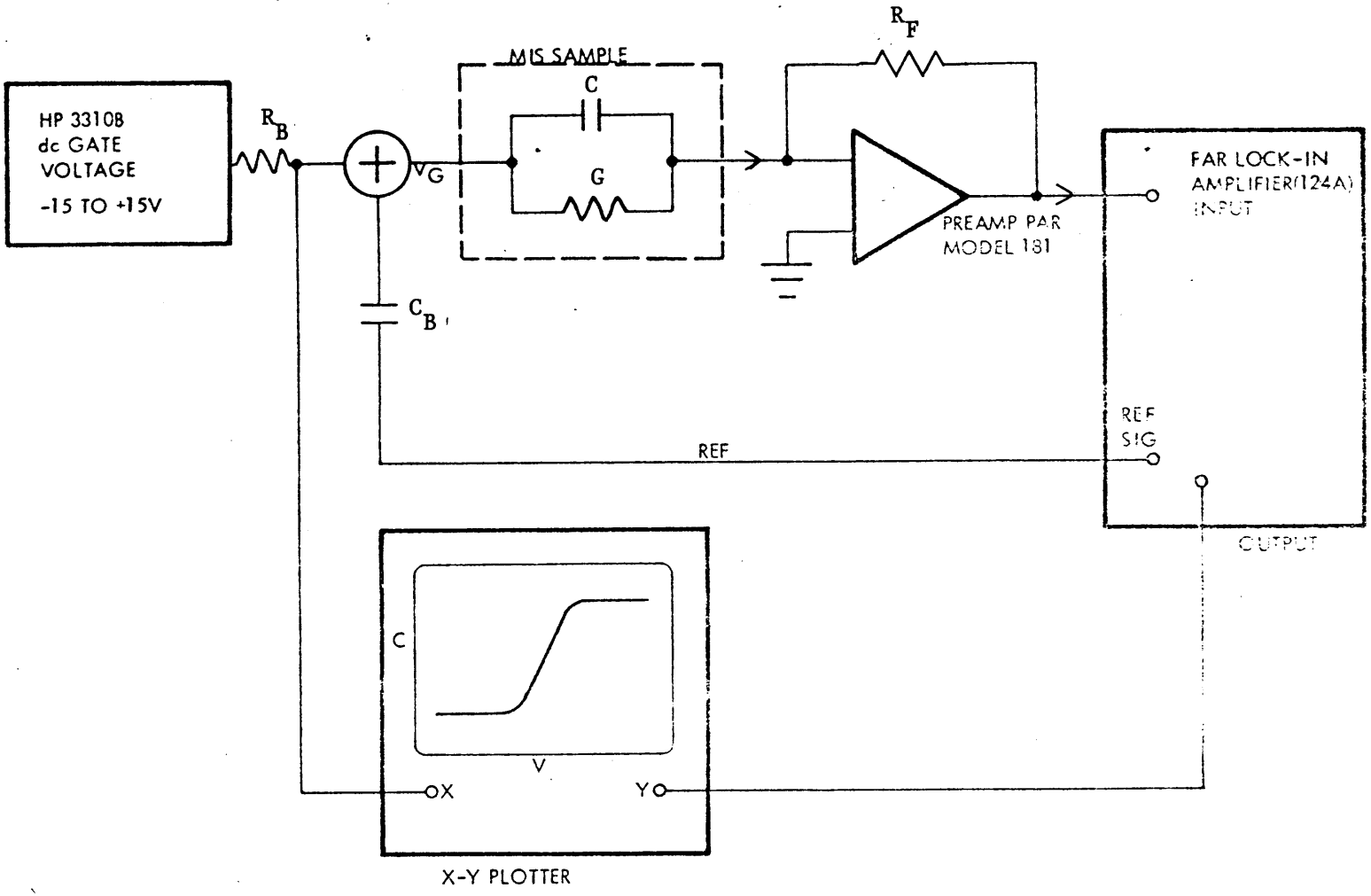

Figure 3.2. MIS CAPACITANCE/CONDUCTANCE-VOLTAGE TEST SYSTEM

The current through the MIS sample is related to the reference signal V_s by:

$$i_s = V_s (G + j\omega C) \tag{3.1}$$

The capacitance component is thus proportional to the frequency, which in the case of the 124A Lock-In can be varied from 10 Hz to 210 kHz. The system is calibrated with a high resistance, 20 pF polystyrene capacitor. First the phase is adjusted for a zero conductive component, and then the amplitude of the reference signal adjusted to give an approximately full scale output. A phase control allows the selection of the imaginary component, which is proportional to the capacitance, or the real component, which is proportional to the conductance divided by the frequency, G/ω.

A voltage is applied to the gate of the MIS structure through a resistor, R_B, with an HP3310B signal generator. The output of the signal generator is either a slowly varying ramp voltage or a square wave, depending on what test is being done. For capacitance-voltage measurements the ramp voltage is also applied to the input of the X-Y plotter. The output of the lock-in amplifier is applied to the Y input of the plotter.

The low frequency time constant ($\tau \approx R_B C_B$) of the circuit associated with the output of the signal generator can be adjusted by selecting the appropriate values for R_B and C_B. The values used most frequently are R_B = 10 kΩ and C_B = 0.01 μF for a time constant of 0.1 ms and R_B = 100 kΩ

and C_B = 0.1 μF for a time constant of 10 ms. The shorter time constant is useful for capacitance-time measurements in which a square wave is applied to the gate. This time constant is much shorter than the duration of the transients under study. The longer time constant is useful for capacitance-voltage measurements, especially for low frequency measurements.

When a capacitance-time measurement is being made, the X-Y plotter is switched to the X-axis time base mode. If the duration of the transient is shorter than the slew-rate of the X-Y plotter, an oscilloscope can be used instead. In the case of a large signal C-t measurement, the signal generator needs only to be switched to a square wave output. For small signal measurements, a battery is added in series with the signal generator to supply the necessary dc offset.

3.2.3 Spectral Response Measurements

The (Hg,Cd)Te bandgap was determined from spectral response measurements on the MIS structures. From the spectral response characteristic, a cutoff wavelength was found. The cutoff wavelength λ_c was used to calculate the width of the intrinsic bandgap Eg by means of the relationship below:

$$Eg = h\, c_o/\lambda_c \qquad (3.2)$$

where:

$h \equiv$ Planck's constant

$c_o \equiv$ Speed of light in a vacuum

The spectral measurement technique took advantage of the fact that the capacitance is a function of the optical generation rate in and near the depletion region of an MIS structure. The depletion width becomes smaller as the number of generated carriers increases, thus the capacitance will increase. In this measurement, the standard Perkin-Elmer spectral station was used as the source of radiation of different wavelengths. The radiation was chopped at a rate of 13 cycles/second. The modulated capacitance amplitude of the MIS structure was then measured with a wave analyzer and a plot of the relative amplitude of the capacitance modulation versus the wavelength was constructed. This produced a spectral response characteristic such as that shown in Figure 3.3. The test setup is shown in Figure 3.4.

The bandgap was used in the calculations of the intrinsic carrier concentration n_i. This parameter was necessary for the interpretation of the MIS data.

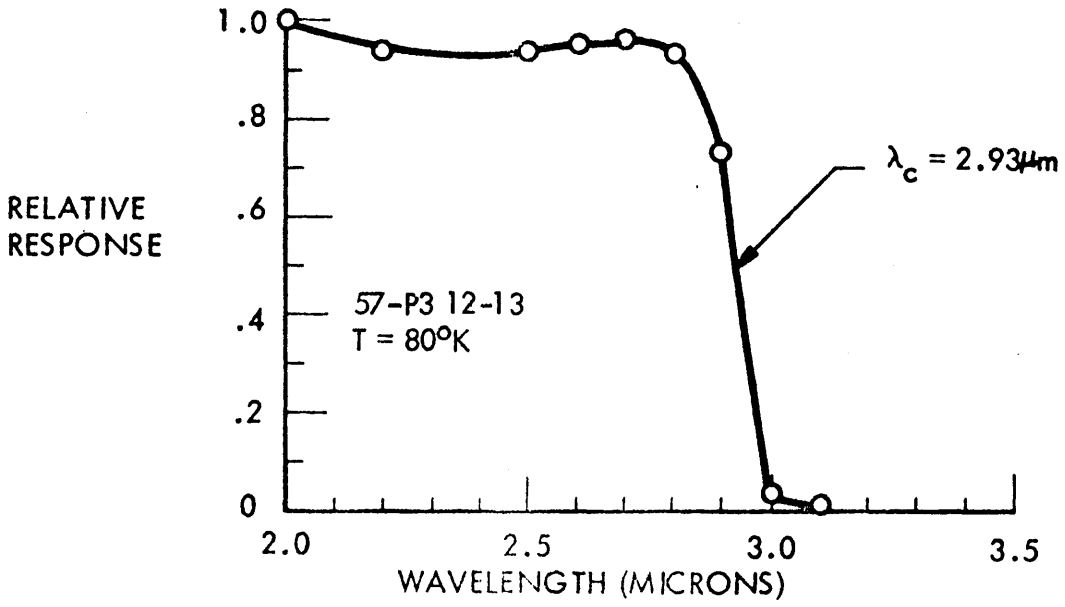

Figure 3.3. SPECTRAL RESPONSE OF AN MIS STRUCTURE (USED TO OBTAIN λ_c)

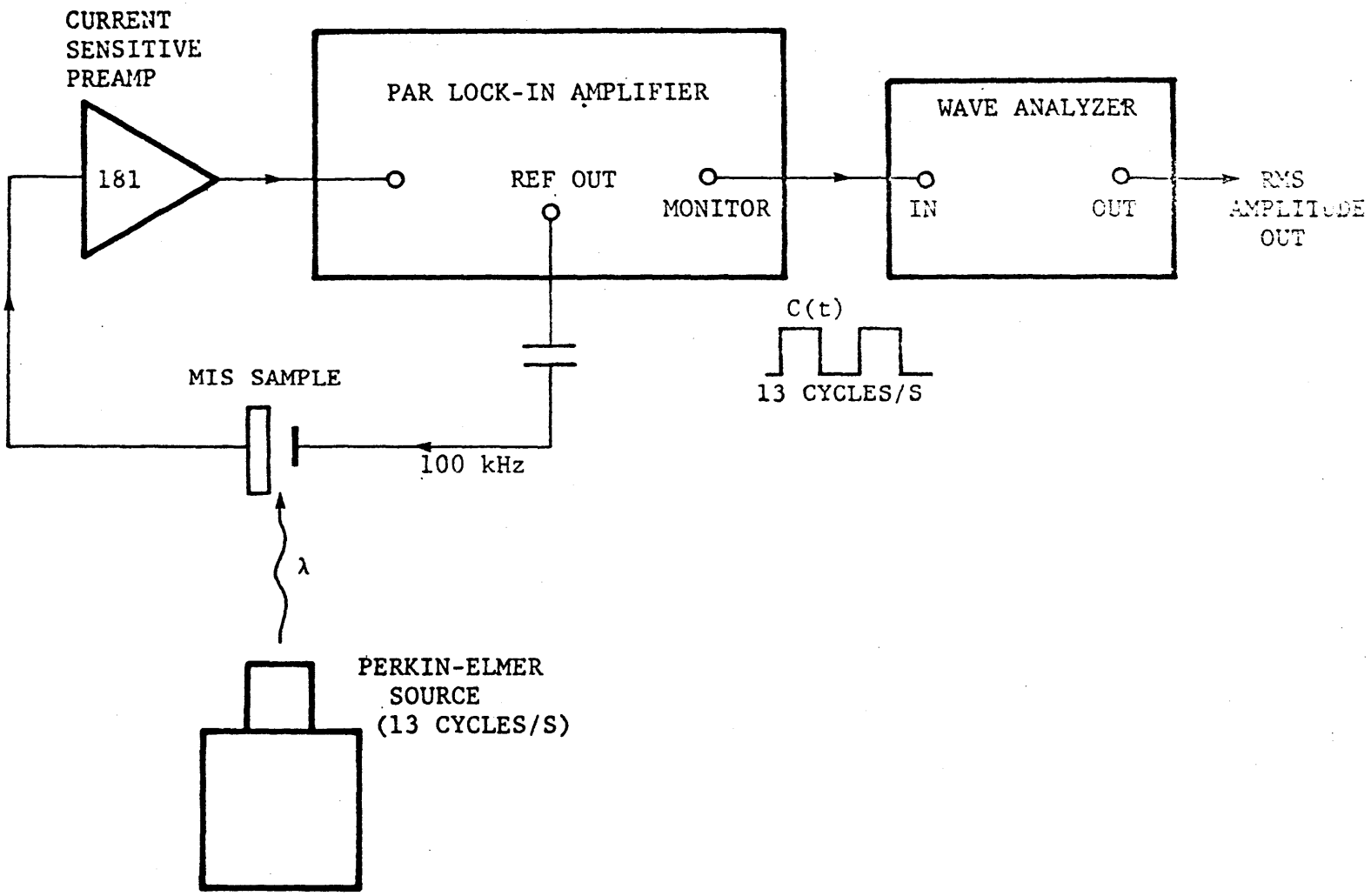

Figure 3.4. MIS SPECTRAL MEASUREMENT SETUP

SECTION 4

EXPERIMENTAL RESULTS

4.1 INSULATORS

One of the first tasks of this project was to select an insulator which resulted in consistantly high yields of operative MIS structures. An insulator was sought which would exhibit the following characteristics; (1) low pinhole density, which would insure that no leakage paths were present in the insulator; (2) high dielectric constant, which would yield a large value of insulator capacitance without requiring prohibitively thin coatings; (3) durability and good adhesion to the (Hg,Cd)Te surface, so that any subsequent processing or testing would not damage the insulator; (4) low density of interface states, resulting in minimal distortion and hysteresis in the capacitance-voltage characteristics; (5) high dielectric strength, ensuring low leakage currents and large breakdown voltages; (6) compatibility with existing deposition techniques, primarily evaporation; and (7) consistent and repeatable results. The properties of the various insulators tried are described in this section.

4.1.1 Zinc Sulfide (ZnS)

Zinc sulfide had been successfully used for (Hg,Cd)Te MIS structures[5] in the past. It had been shown to adhere well to the (Hg,Cd)Te surface and was readily deposited with an evaporator. It was therefore the first insulator to be used.

In the first experiment 3000Å of ZnS was evaporated onto a p-type slab of $x = 0.4$ $Hg_{1-x}Cd_xTe$ after the surface preparation described in Section 3. The structures were probed after evaporation of the gate electrodes. The probes showed that in nearly all structures the gate electrode was shorted to the (Hg,Cd)Te substrate indicating that either the gold or indium diffused through the ZnS to the substrate. The current-voltage characteristics were non-ohmic, implying that either an n-p junction or a Schottky-barrier was formed.

The experiment was repeated, this time with 4000Å of ZnS, and again most structures were shorted. A few capacitance-voltage curves were obtainable, however, which indicated that the material was indeed p-type, with $|N_A - N_D| = 3.5 \times 10^{16}/cm^3$. The characteristics exhibited a large amount of hysteresis and skewing.

Further experiments with ZnS were done using n-type $x = 0.4$ (Hg,Cd)Te, this time with a somewhat thicker coating. The thickness of the layer was determined by optical interference techniques to be 4500Å.

Three different slabs were processed. One slab again exhibited shorted MIS structures, another showed about 50% yield, and the third had a 90% yield. The insulator capacitance was found to be 1.58×10^{-8} F/cm^2 at 80K and 210kHz, yielding a dielectric constant for ZnS of about 8.0, which compares reasonably well with the handbook value of 8.3.

The slab with the larger yield of structures was tested further at Freon 14 temperatures (T = 147K). This slab was oriented in the (111) direction with the structures being fabricated on the B face as determined by the identifying etch described in Appendix A-1. The C-V characteristics at this temperature indicated that the inversion layer was not in equilibrium when the voltage was swept at a rate of 2 V/sec. Non-equilibrium behavior is characterized by a capacitance which decreases below the equilibrium value when the structure is biased further into inversion. The curves exhibited a large amount of hysteresis, the magnitude of which depended on the magnitude and rate of the voltage sweep. The size of the hysteresis "window" was about 5 volts with voltage swing of 25 volts and a rate of 2 V/sec corresponding to a net stored charge ($C_i \Delta V$) over one cycle of 6.3×10^{11}/cm^2. The size of the window decreased with increasing sweep rate and decreasing voltage swing.

The hysteresis made unambiguous determination of the surface potential at zero gate voltage difficult. However, since both the rising and falling portions of the curve fall on the same side of the

origin, one can infer a depleted surface at zero applied voltage. The non-equilibrium behavior also implied that the surface was not inverted around the gate electrode.

In addition to the hysteresis, the capacitance-voltage curves were also quite skewed. It was necessary to increase the sweep rate in order for the capacitance to approach the maximum insulator capacitance in accumulation. These results are indicative of a large density of both fast and slow surface states. An example of a C-V curve obtained at 147K is shown in Figure 4-1.

ZnS showed low and inconsistent yields as well as a rather large density of surface states. It was therefore decided that other insulators should be tried.

4.1.2 Thorium Fluoride (ThF_4)

Thorium Fluoride was an attractive candidate because of the ease in which it could be evaporated and the durability of the films which resulted. Some of the properties of this film are discussed in a paper by Heitmann and Ritter.[26] The ThF_4 is evaporated in a vacuum by heating ThF_4 powder to a temperature of greater than 900°C. The resulting film is amorphous and chemically very stable. As a result the films are difficult to remove chemically. The static dielectric constant was determined to be roughly 13 at room temperature and 1000 Hz.

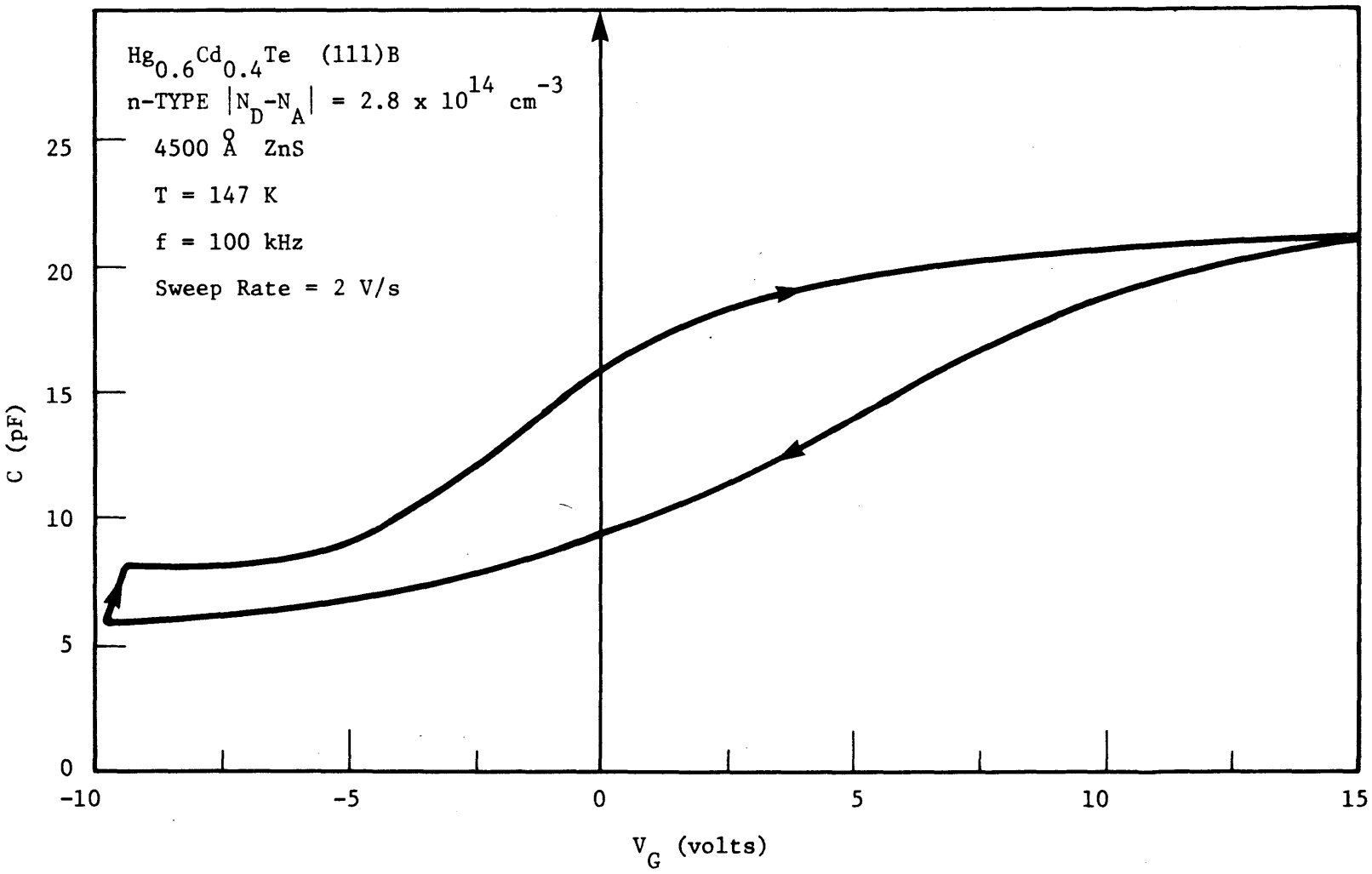

Figure 4.1. C-V CHARACTERISTIC OF AN MIS STRUCTURE USING 4500Å OF ZNS AS THE INSULATOR.

In the first experiment, roughly 4000Å of ThF_4 was evaporated onto the A face of an n-type slab of x = 0.4 (Hg,Cd)Te oriented in the (111) direction. The standard procedure was used in this case except that the gate electrode consisted of 15 mil dots of indium. About 50% of the resulting structures were operative. The insulator capacitance was found to be about 2.1×10^{-8} F/cm^2, implying that the thickness of the coating was greater than 4000Å. The C-V curves exhibited less skewing and hysteresis than ZnS. The hysteresis window at 145K with a voltage swing of 15 volts and a sweep rate of 1.5 V/sec was 1-2 volts. The surface potential at zero gate voltage and the equilibrium behavior of the inversion layer indicated that the free surface was probably weakly inverted.

Further experiments were conducted with ThF_4 coatings of about 4000Å thickness and the gold-indium gate electrode structure. The insulator capacitance was determined to be 2.5×10^{-8} F/cm^2 for a measured thickness of 4280Å, resulting in a dielectric constant at 80K and 210kHz of 12. The yield of operative devices was consistently high, usually greater than 80%. The leakage current through the ThF_4 coating was measured at room temperature, and was found to be typically 1 nA at 5 volts, corresponding to resistance of $5 \times 10^9 \Omega$ and a resistivity of $1.3 \times 10^{11} \Omega$-cm. The leakage current was unmeasurable on a nanoamp scale at 80K, so that the resistivity was in excess of $1 \times 10^{12} \Omega$-cm. The films also exhibited large breakdown voltages, normally in excess of 40 volts, which corresponds to an electric field of 1×10^6 V/cm.

The C-V characteristics of structures fabricated on the (111)B face of n-type x = 0.4 material exhibited less skewing than those of the (111)A face. The hysteresis window was somewhat larger, about 3V at 147K with a 20 volt swing and a sweep rate of 2V/sec. The surface was depleted at zero gate voltage, as determined by the capacitance at zero volts and the nonequilibrium behavior of the inversion layer. A capacitance voltage curve for the (111)B face is shown in Figure 4-2(a). The differences in the surface properties of the (111)A and (111)B faces, as well as other properties of the ThF_4 / (Hg,Cd)Te interface will be discussed in later sections.

Structures using ThF_4 were also fabricated on p-type x = 0.4 (Hg,Cd)Te. The C-V characteristics were similar to those of n-type material. The hysteresis was comparable, but the curves did tend to show less skewing for p-type material. The surface was again depleted with zero gate voltage. This result was somewhat surprising, since it was expected that a depleted n-type surface would imply that the p-type surface would be slightly accumulated. This could be explained in part by a difference in the semiconductor work function between n and p-type material (ϕ_{ms}(p-type) < ϕ_{ms} (n-type)). In addition, the occupation of surface states, which in part determines the surface potential, is different for p-type than it is n-type, because of the difference in Fermi energy. These results indicate that fixed charges in the ThF_4 do not significantly affect the surface potential. A C-V curve obtained from a p-type region is shown in Figure 4-2(b).

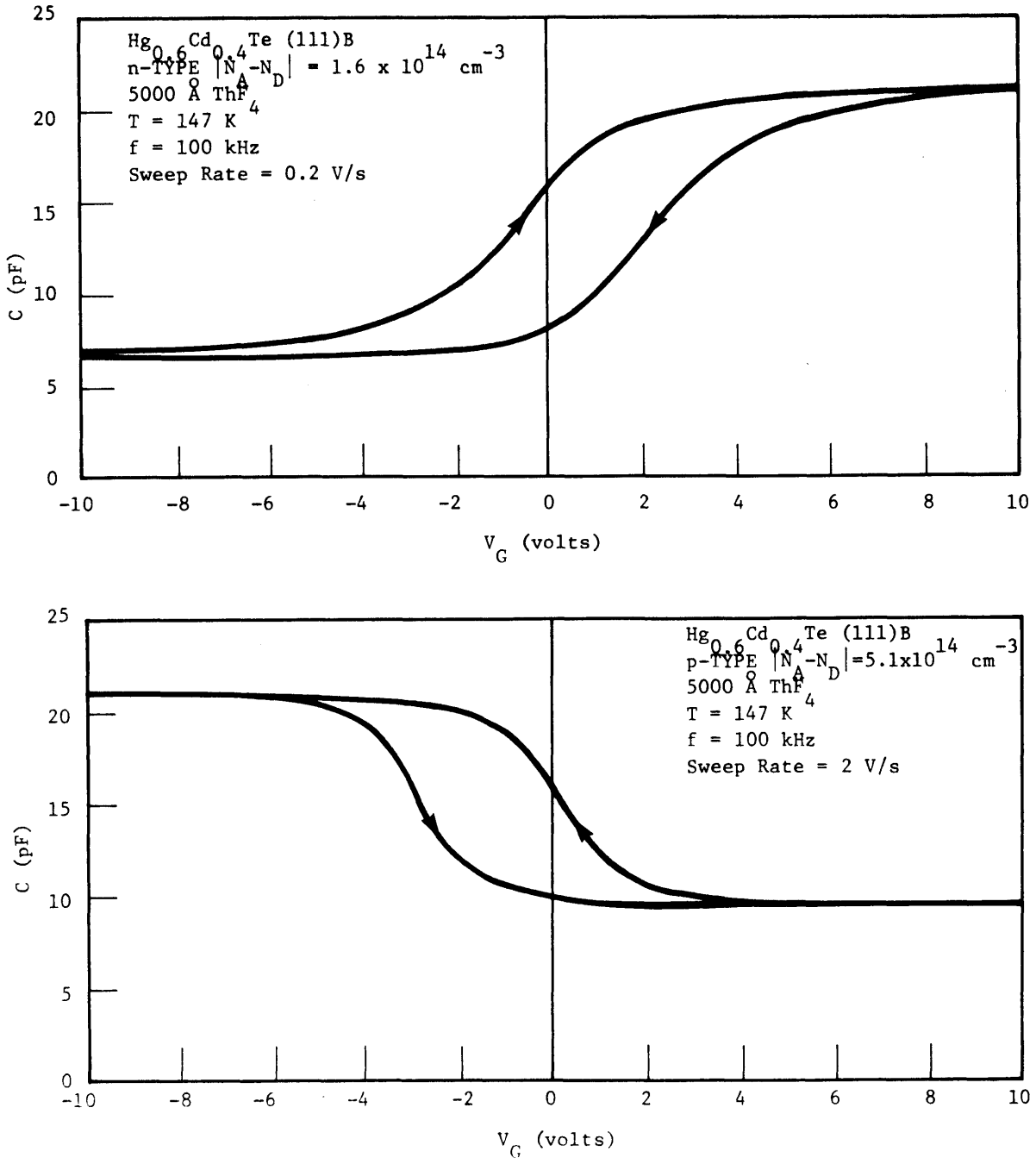

Figure 4.2. C-V CHARACTERISTICS FOR N AND P-TYPE (Hg,Cd)Te USING 5000Å OF ThF_4 AS THE INSULATOR.

A few experiments were conducted to determine the effect of glow discharge cleaning of the (Hg,Cd)Te surface immediately prior to the deposition of the ThF_4 film. In this method, the sample to be cleaned is maintained at a large positive potential with respect to an electrode present in the vacuum chamber. The resulting beam of electrons ionized the residual gas in the chamber, and the resulting ions then bombard the sample. This ion bombardment tends to remove contaminants from the surface and speeds the release of gases from the surface. In addition, it is thought that a very thin film of metal or metal oxide sputters from the cathode onto the surface. The cleaning action results in better adherence of the film which is then evaporated onto the sample.

Two slabs of x = 0.4 material, one n-type and the other p-type, were glow-discharge cleaned with the following results. The C-V characteristics exhibited an almost constant capacitance for all gate voltages, except for a very small dip at negative voltages. This would seem to indicate an extremely large doping at the surface, and further that a fixed positive charge was present at the surface. There are several possible explanations for this result. One would be that excessive heating occured during the cleaning, which would cause the surface to convert to heavily doped p-type. Another is that the ion bombardment caused a large amount of damage at the surface. It is also possible that a thin metallic film was formed on the surface, resulting in a nearly constant capacitance voltage characteristic. No further experiments with glow discharge cleaning were conducted.

Thorium Fluroide was found to result in consistently high yields and very low leakage currents. In addition, the density of surface states was lower for this system than for ZnS and most of the other insulators tried. As a result, most subsequent experiments used ThF_4 as the insulator.

4.1.3 Lanthanum Fluoride (LaF_3)

Lanthanum Fluoride is an easily evaporated insulator that results in durable coatings. It is also evaporated from a boat by heating a powder form of the crystal. The initial experiment used a 4000Å coating of LaF_3 evaporated onto a p-type slab of x = 0.4 (Hg,Cd)Te. The yield of operative structures was about 50%. The leakage current at room temperature was higher than that of ThF_4, about 5 nA at 5 volts, corresponding to a resistivity of 2.6×10^{10} Ω-cm. The insulator capacitance was 2.1×10^{-8} F/cm^2 at 80K and 100kHz, resulting in a dielectric constant of 9.7.

The C-V characteristics exhibited less hysteresis than normally encountered with ZnS or ThF_4 coatings. The size of the hysteresis window was less than 0.5 volts at T = 80K with a sweep rate of 2 V/sec and swing of 20 volts. The surface appeared to be weakly inverted, with many of the structures exhibiting equilibrium behavior even at 80K. The transition between accumulation and inversion was rather sharp, indicating a reasonably low surface state density. A C-V plot is shown in Figure 4-3.

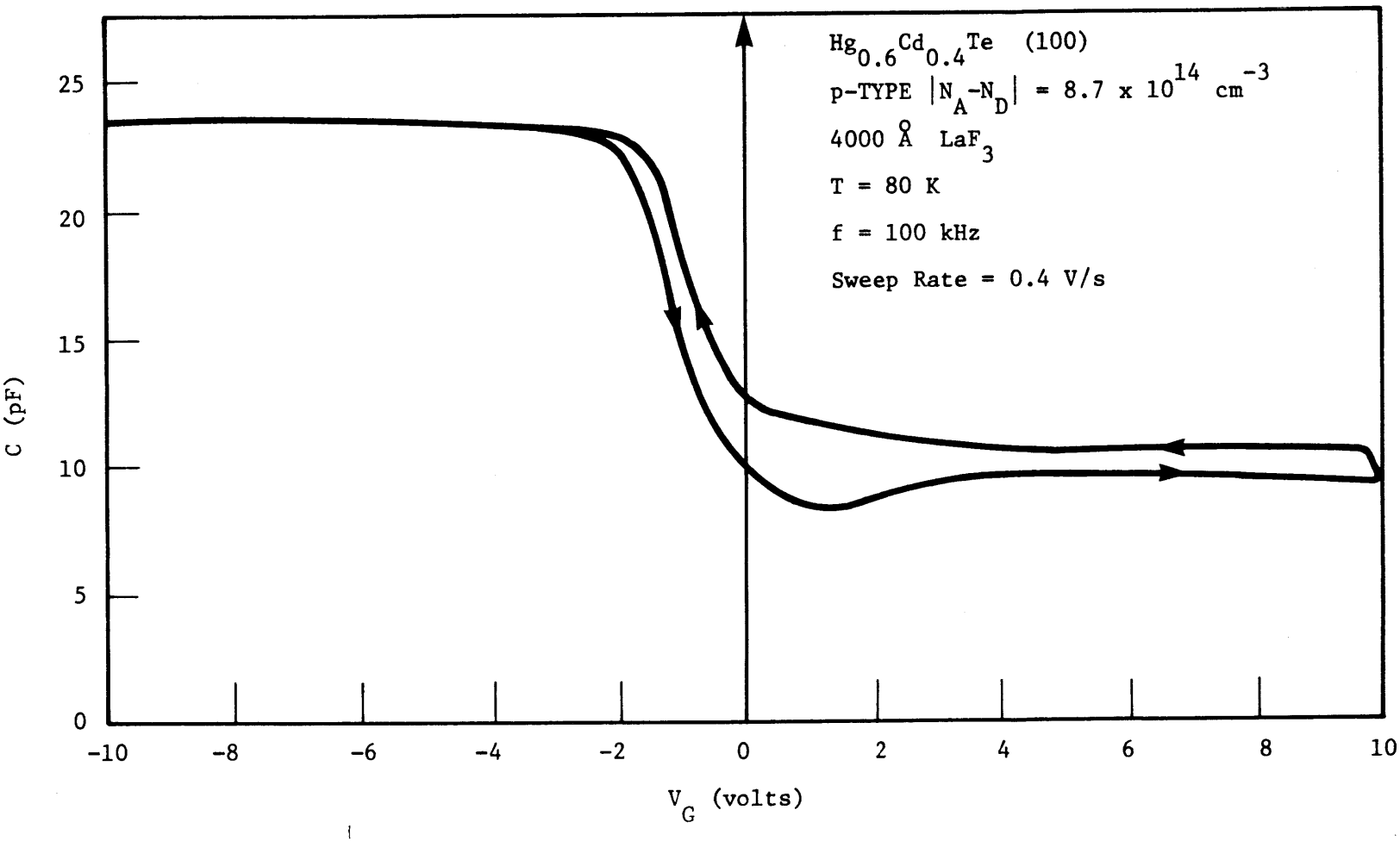

Figure 4.3. C-V CHARACTERISTIC OF P-TYPE (Hg,Cd)Te USING 4000Å LaF_3 AS THE INSULATOR

In a subsequent experiment 4500Å of LaF_3 was evaporated onto an n-type slab of x = 0.4 (Hg,Cd)Te. The C-V data indicated that the surface of the slab was now p-type, with $|N_A - N_D| \cong 5 \times 10^{16}/cm^3$. This result was thought to be due to excessive heating of the (Hg,Cd)Te surface which increases the density of Hg vacancies. Hg vacancies are known to be acceptors in (Hg,Cd)Te.[30,33] In addition, the amount of skewing of the C-V curves was considerably more than in the first experiment. No further experiments were conducted with this insulator.

4.1.4 Silicon Monoxide (SiO_x)

This material was again evaporated thermally using a powder of silicon monoxide. The resulting coating contains a mixture of SiO and SiO_2. The subscript x refers to the average concentration of oxygen in the coating, and can vary between 1 and 2.

The initial attempt was a 4000Å coating on p-type x = 0.4 (Hg,Cd)Te. The yield of non-shorted structures was good in this case, about 80%. The insulator capacitance was quite low, however, due to the small dielectric constant of this material. The capacitance, measured at 147K and 100kHz, was 8.9×10^{-9} F/cm^2 which corresponds to a dielectric constant of 4.0.

The C-V data showed a relatively small amount of hysteresis. With a sweep rate of 2 V/sec and a swing of $\pm$10V, the size of the hysteresis window varied from about 1.0V at 147K to less than 0.25V at 194K. The surface was depleted with zero gate voltage. The transition from accumulation to inversion occured over a range of about 4 volts. An example of a C-V plot obtained at 147K is shown in Figure 4-4.

In order to achieve a larger insulator capacitance, a 2000Å coating of SiO_x was evaporated onto an n-type slab of x = 0.4 (Hg,Cd)Te. The results of this experiment were considerably different from the first. The insulator capacitance was indeed higher, about 2×10^{-8} F/cm^2. The hysteresis was much worse, about 3-4 volts at 147K. In addition, the C-V curves were considerably more skewed. In many cases the surface was inverted with zero gate voltage. The inconsistency of results in this case could be due to a variation in the relative concentrations of SiO and SiO_2 in the film.

4.1.5 Silicon Dioxide (SiO_2)

It was not possible to evaporate a pure film of SiO_2. It was therefore decided to sputter the SiO_2 onto the (Hg,Cd)Te. The sputtering was performed with an RF sputtering system in the microelectronics laboratory at MIT. Approximately 1500Å of SiO_2 was sputtered onto a slab of n-type x = 0.4 (Hg,Cd)Te.

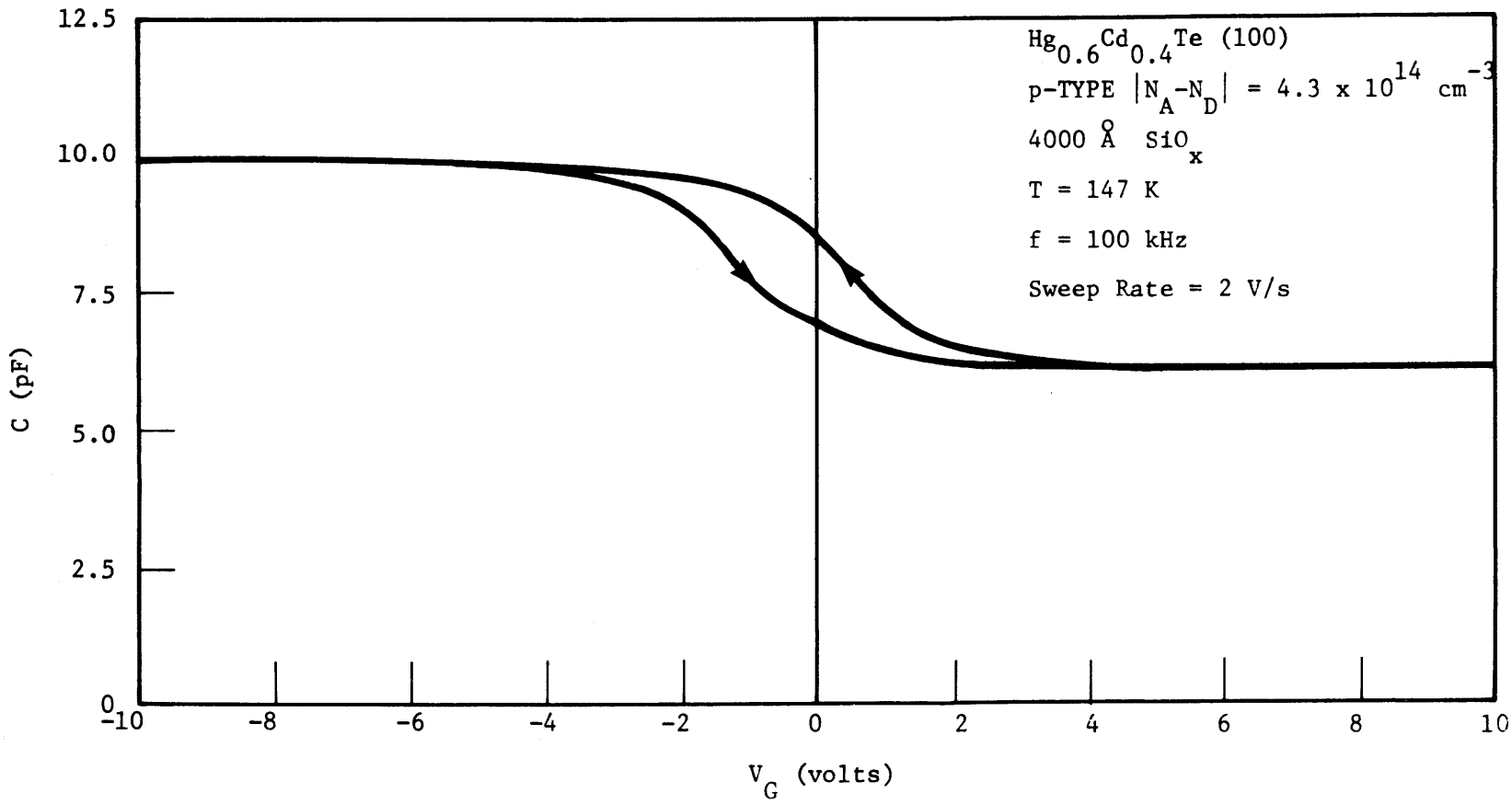

Figure 4.4. C-V CHARACTERISTIC OF P-TYPE (Hg,Cd)Te USING 4000Å OF SiO_x AS THE INSULATOR

Leakage current measurements indicated that in most of the structures the gate was shorted to the substrate. C-V measurements on those elements which were not shorted showed that the surface of the slab had become very heavily p-type. This was again thought to be due to excessive heating during deposition. The temperature of the slab during the sputtering was estimated to be 200°C. As a result no definite conclusions could be made about the properties of the SiO_2 film. Future experiments with sputtered SiO_2 films will require a specially cooled system to prevent the excessive heating.

4.1.6 Cadmium Telluride (CdTe)

Cadmium Telluride is a semiconductor with a bandgap of 1.6 eV. At the cryogenic temperatures of interest, it was therefore expected that CdTe would behave as an insulator. The CdTe could be deposited in two ways, electron-beam evaporation and hot boat evaporation.

The initial experiment was electron-beam evaporation of 1000Å of CdTe onto a slab of n-type (Hg,Cd)Te. A 3000Å overcoating of ThF_4 was then deposited onto the CdTe. The primary purpose of the ThF_4 coating was to insure the presence of an insulating film in case the CdTe was not a good insulator. In subsequent C-V measurements, the capacitance exhibited no change even with a voltage swing of $\pm$ 50 volts. The magnitude of the capacitance agreed with the value calculated for this double insulator coating, indicating that the CdTe was behaving

as an insulator. The reason for the constant capacitance is not understood, but could be due to surface heating or damage from the electron-beam process.

The experiment was repeated using the same slab except that this time the CdTe was evaporated from a hot boat. The C-V data obtained from these structures showed a definite change in capacitance, agreeing with what was expected for this material which was doped n-type at $8.0 \times 10^{14}/cm^3$. The data did, however, exhibit an anomalously wide hysteresis window. The capacitance would change from C_i to C_f almost immediately after the voltage sweep changed direction, especially when the sweep changed from negative going to positive going. This effect was relatively independent of the magnitude or rate of the voltage sweep. Figure 4-5 shows a C-V plot illustrating this effect.

4.1.7 Anodization

Anodization is a process whereby an oxide is electrolytically grown on the substrate. The oxide is formed by electrolysis in a 0.1-M solution of KOH in ethylene glycol and a small amount of deionized water. Films grown by this technique were typically about 1000Å thick.

The first experiment with anodization involved growing an oxide layer of 920 Å on $Hg_{0.7}Cd_{0.3}Te$. Fifteen mil gold dots 200 Å thick were evaporated onto the film. The resulting structures were then cooled to

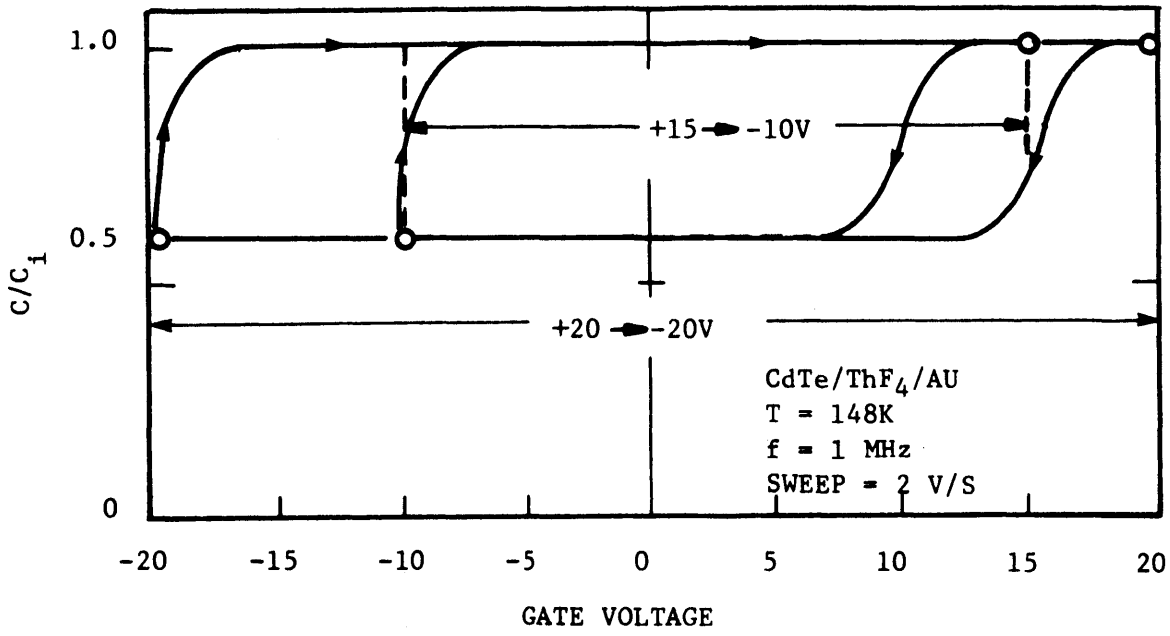

Figure 4.5. C-V CHARACTERISTICS OF $Hg_{0.6}Cd_{0.4}Te$/CdTe INTERFACE FOR TWO DIFFERENT VOLTAGE SWEEP RANGES

80K and probed. The insulator capacitance was determined to be 170 to 180 picofarads, which results in a calculated dielectric constant of 16.1. Attempts were made to bond wire to the MIS structures, but it was found that the bonding process caused the gate electrodes to be shorted to the substrate. Further experiments with anodic films involved evaporating an overcoating of 4000 Å of ThF_4, so that bonds could be made to the metal dots without breaking through the insulator.

C-V characteristics obtained on n-type, x = 0.3 and x = 0.4 $Hg_{1-x}Cd_xTe$ indicated that the surface with zero applied gate voltage was strongly accumulated. Flatband voltages ranged from -2 to -8 volts. Measurements on p-type $Hg_{0.7}Cd_{0.3}Te$ showed that the surface was inverted, with flatband voltages of -4 to -6 volts.

The C-V characteristics of structures fabricated on the B face of n-type x = 0.4 (Hg,Cd)Te oriented in the (111) direction were the most extensively studied. When the structures were tested at 80K, the C-V characteristics exhibited a very small amount of hysteresis. The size of the hysteresis window was typically about 0.25 volt with a sweep rate of 2 volts/s and a swing of 20 volts. In some cases the sense of the hysteresis was positive at this sweep rate, indicating that injection of carriers from the gate into the insulator was the dominant process (See Section 2.2). As the sweep rate was slowed

down, however, the sense of the hysteresis changed to negative. Results similar to this had been observed in the silicon/silicon nitride system by Kendall.[11]

When the structures were tested at higher temperatures (i.e., 147K and 194K) the sense of the hysteresis was negative for all sweep rates. The size of the hysteresis window was considerably larger at these temperatures than at 80K. At 194K, for example, the hysteresis window was typically about 5 volts for a sweep rate of 2 volts/s. In addition, the curve was shifted to a more negative voltage. These results indicate that hole injection from the semiconductor into the insulator becomes the dominant process at higher temperatures. Figure 4.6 shows the C-V characteristics of n-type $Hg_{0.6}Cd_{0.4}Te$ at 80K and 194K.

The transition from accumulation to inversion was generally quite sharp, indicating a very low density of fast surface states. Figure 4.7 is a comparison between an experimentally measured C-V curve, obtained at 80K, and the ideal high frequency curve. The experimental curve has been graphically shifted towards more positive voltages so that a comparison could more easily be made. In addition, only the falling portion of the curve has been presented. It can be seen that the measured curve is very nearly ideal. From this data a plot of effective surface state density versus energy was constructed using the

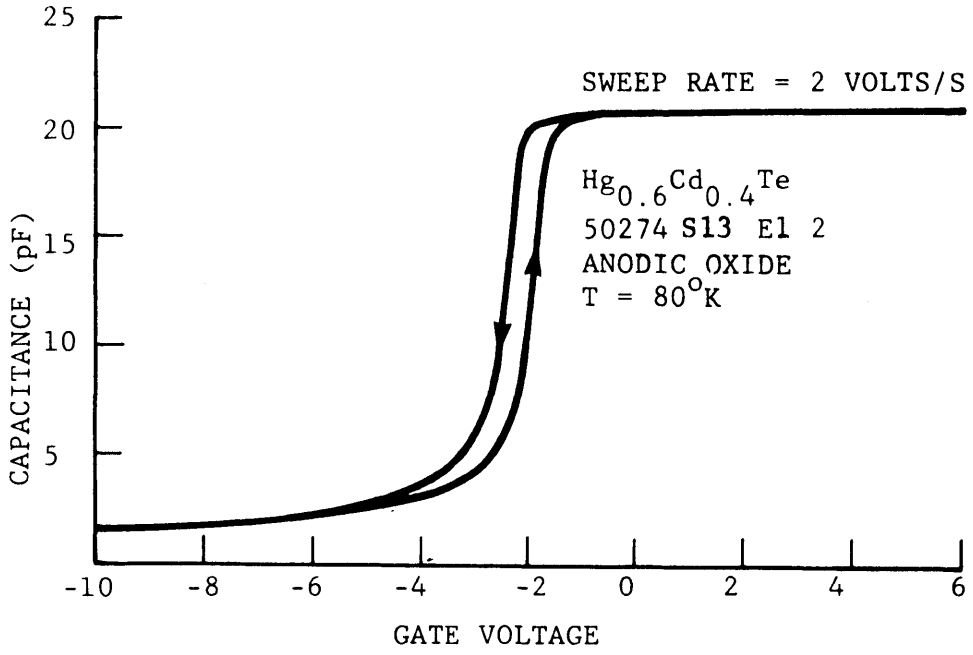

(a) SAMPLE AT 80°K INDICATING POSITIVE HYSTERESIS

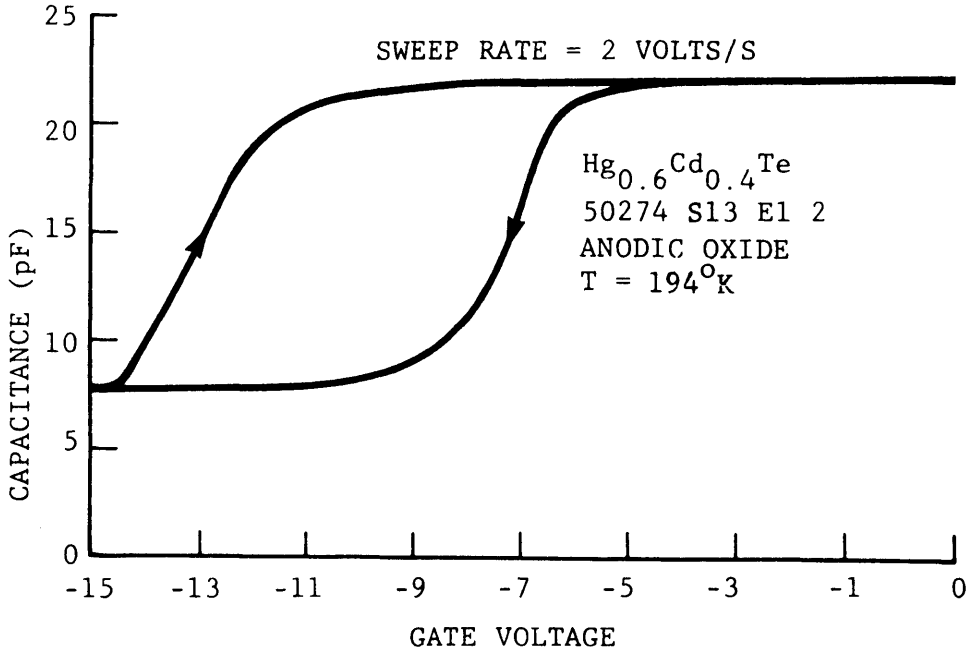

(b) SAMPLE AT 194°K INDICATING NEGATIVE HYSTERESIS

Figure 4.6. CAPACITANCE-VOLTAGE CHARACTERISTICS OF AN ANODIZED MIS STRUCTURE

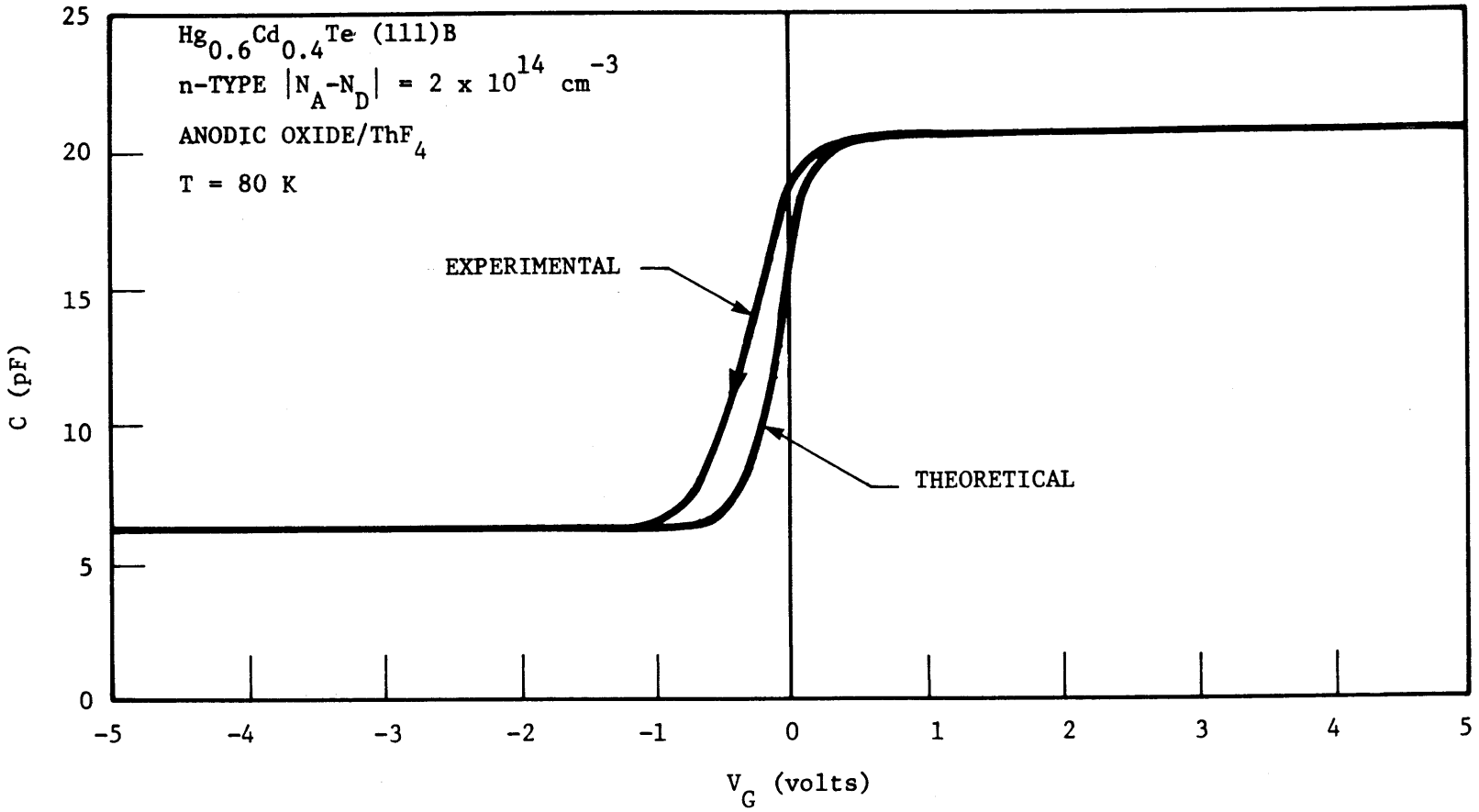

Figure 4.7. COMPARISON OF IDEAL AND MEASURED C-V CURVES FOR ANODIZED SURFACE

differentiation technique described in Section 2.2.3. This plot is shown in Figure 4.8. The surface state density is about 1.5×10^{10} $cm^{-2}ev^{-1}$ near the intrinsic Fermi energy.

Although the fast surface state densities were generally very low for the ThF_4/anodic oxide/(Hg,Cd)Te system, the C-V characteristics were strongly influenced by trapped charges and slow surface states in the anodic film, especially at 147K and 194K. In addition to the large amount of hysteresis observed at these temperatures, the C-V characteristics also exhibited a rather unstable flatband voltage. It was very difficult to repeat results from day to day. In many cases a large number of ramp voltage cycles were required before a steady state could be achieved (i.e., before the C-V relationship would repeat itself for additional ramp cycles). These results indicate a large density of slow surface states and/or charge migration in the anodic oxide.

4.2 MAJORITY CARRIER DOPING

An important parameter which can be determined from MIS capacitance-voltage measurements is the net concentration and type of majority carrier, $N_A - N_D$. This quantity can be easily determined from the maximum and minimum capacitance of the high frequency C-V curve, as explained in Section 2.1. In addition, the type of carrier which predominates can be unambiguously determined by the slope of the C-V

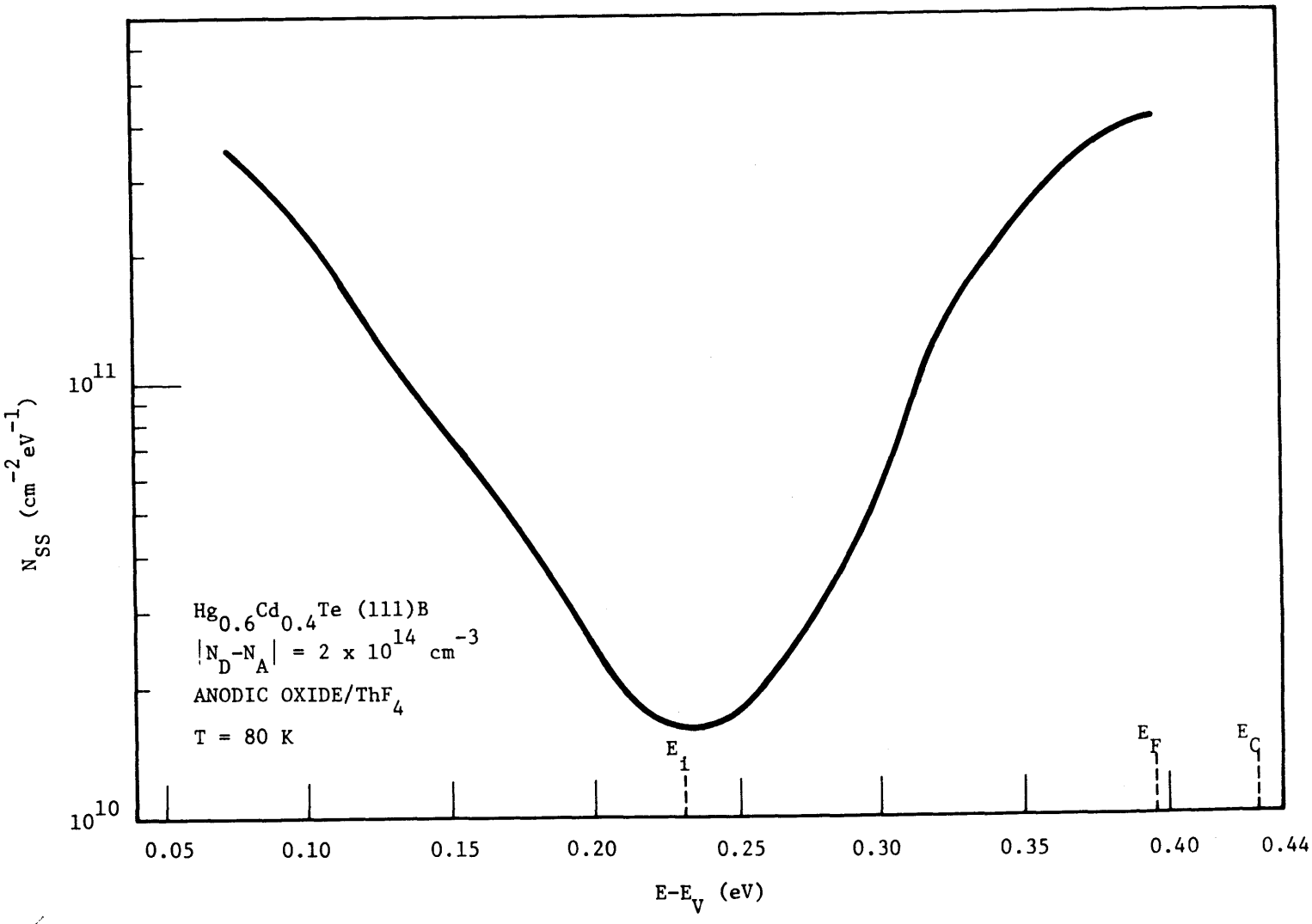

Figure 4.8. SURFACE STATE DENSITY VS ENERGY AS CALCULATED BY THE DIFFERENTIATION TECHNIQUE FOR THE ANODIC OXIDE/ThF_4 INSULATOR SYSTEM.

data in the transition from maximum to minimum capacitance (i.e., if dC/dV is positive, the material is n-type, and if dC/dV is negative, it is p-type).

The procedure in determining the net doping is to first determine the bandgap of the material with a spectral measurement. This determines the intrinsic carrier concentration and the dielectric constant of the semiconductor. Capacitance-voltage measurements are then made to determine the type and the insulator capacitance C_i and the minimum capacitance C_f. The net majority carrier concentration is then calculated using equation 2.23.

The C-V data of x = 0.3 and x = 0.4 material was often non-equilibrium when measured at 80K. It was then necessary to perform the measurements at a higher temperature, such as 147K or 194K, to facilitate determination of the maximum and minimum values of capacitance. High frequency curves were normally obtainable at 100kHz, but in some cases, such as when the surface was inverted, it was necessary to make the measurements at 1MHz to obtain a high frequency curve.

Net doping levels were determined in this manner for all the material used in experiments. In some cases Hall measurements had been made on slabs adjacent to the ones on which MIS structures were

fabricated. Thus, an independent measurement of doping was available to which MIS results could be compared. The agreement of the two methods was found to be quite good.

Capacitance-voltage measurements on 20 MIS structures fabricated on an n-type slab of x = 0.31 (Hg,Cd)Te indicated an average donor concentration of $5.4 \times 10^{14}/cm^3$. This value is 16% lower than the Hall value of $6.2 \times 10^{14}/cm^3$. Measurements on a p-type slab of x = 0.4 (Hg,Cd)Te resulted in $|N_A - N_D| = 3.0\text{-}5.0 \times 10^{16}/cm^3$, which agrees reasonably well with the Hall value of $3.0 \times 10^{16}/cm^3$.

It had been discovered previously[27] that the Hall data was difficult to interpret for lightly doped samples, especially p-type samples. The MIS technique was especially useful in these cases. In one case, for example, Hall data on a portion of a slab seemed to indicate that the material was lightly doped p-type. MIS data from an adjacent slab showed that the slab was predominantly n-type, with a small lightly doped p-region. The MIS technique also enabled one to make a detailed plot of doping variations in a slab. An example of such a plot is shown in Figure 4-9.

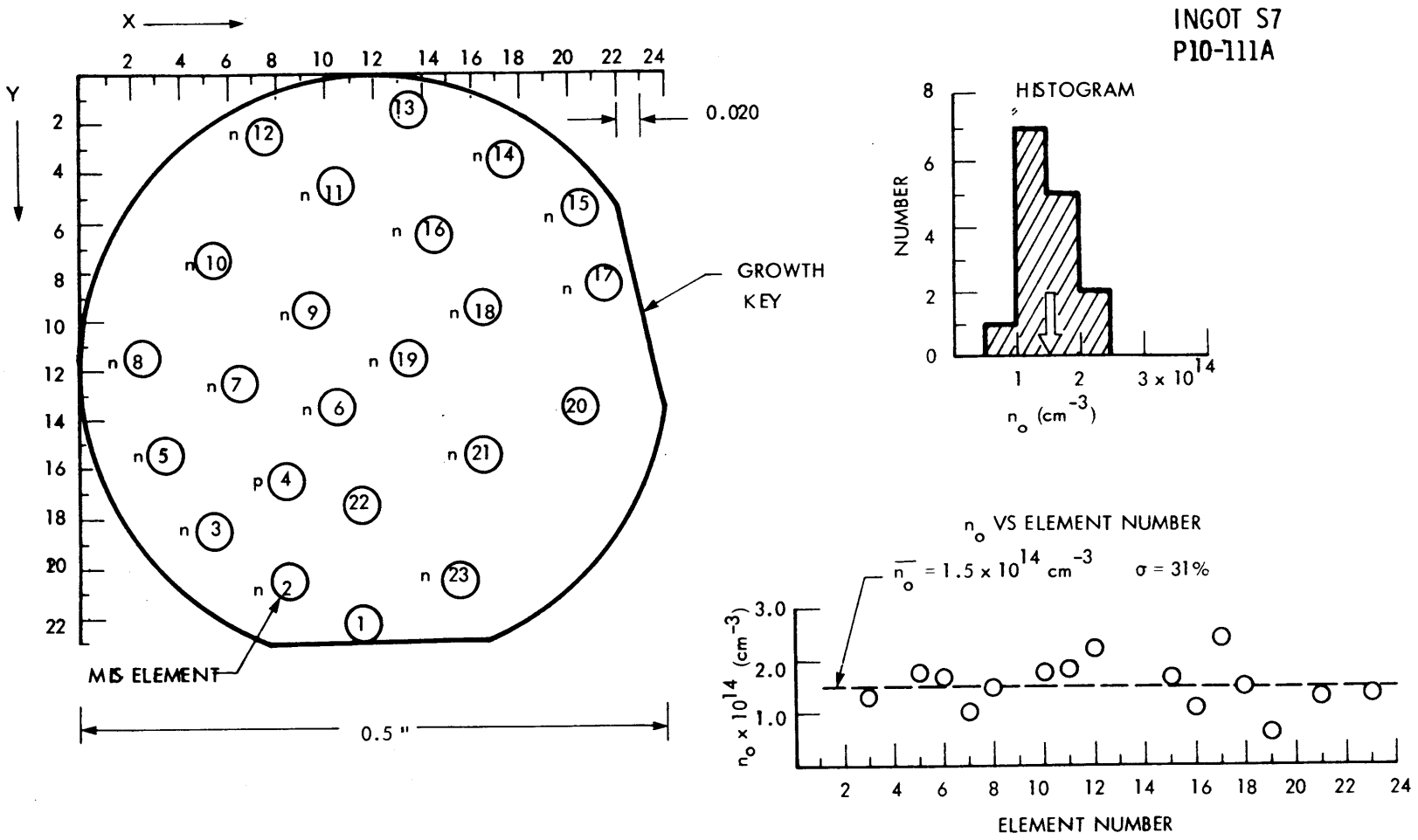

Figure 4.9. DOPING MEASUREMENTS FROM MIS C-V DATA ON A $Hg_{0.6}Cd_{0.4}Te$ SLAB

4.3 SURFACE STATE DENSITIES

Surface state densities for the ThF_4/(Hg,Cd)Te interface were calculated using both the conductance and differentiation techniques. The densities for the (111)A and (111)B faces of $Hg_{0.6}Cd_{0.4}Te$ were compared. In addition, measurements on unoriented material and materials with x-values other than x=0.4 were performed. In some cases comparisons were made between the conductance and differentiation techniques.

4.3.1 Comparison of (111)A and (111)B Surfaces

As mentioned in Section 4.1.2, a marked difference was noted between the C-V characteristics of $ThF_4/Hg_{0.6}Cd_{0.4}Te$ MIS structures fabricated on the (111)A and (111)B surfaces. Specifically, the C-V curves of the (111)A surface exhibited considerably more skewing than those of the (111)B surface. MIS measurements were performed to quantitatively determine the difference in surface state densities between the two surfaces.

The first method to be applied was the conductance technique. The MIS structures were biased into weak inversion, so that the circuit model of Figure 2.13b could be applied. As stated previously, the method involves measuring the conductance and capacitance of the MIS structure as a function of frequency at a specific gate voltage. The equivalent conductance divided by frequency of the parallel branch of the circuit (G_p/ω) is then calculated as a function of frequency using

equation 2.31. The peak in G_p/ω determines the surface state capacitance C_s and the surface state density N_{ss} through equations 2.28 and 2.32.

The C-V relationships of the (111)A and (111)B surfaces for various frequencies are shown in Figure 4-10. The measurements were made at a temperature of 147K. It can be seen quite clearly that the C-V curve for the (111)A surface is affected by surface state capacitance far more than that of the (111)B surface. The equivalent conductance of the parallel branch, G_p/ω, was calculated from the capacitance and conductance data and plotted as a function of frequency. The resulting plots are shown in Figure 4-11. The surface state capacitance for the (111)A surface was 540 pF, which corresponds to a surface state density N_{ss} of $3.2\text{x}10^{12}$ $cm^{-2}eV^{-1}$, and the capacitance for the (111)B surface was 33.5 pF, corresponding to a surface state density of $2.0\text{x}10^{11}$ $cm^{-2}eV^{-1}$.

The surface potential at which these densities are valid was determined by comparing the measured high frequency capacitance with the ideal curve. The capacitance of the structure at high enough frequencies is free of capacitance due to surface states, so that the surface potential can be determined accurately. Once the surface potential is known, the position of the states in the bandgap $E-E_v$ can be determined through the relation:

$$E - E_v = E_F + \psi_s \qquad (4\text{-}1)$$

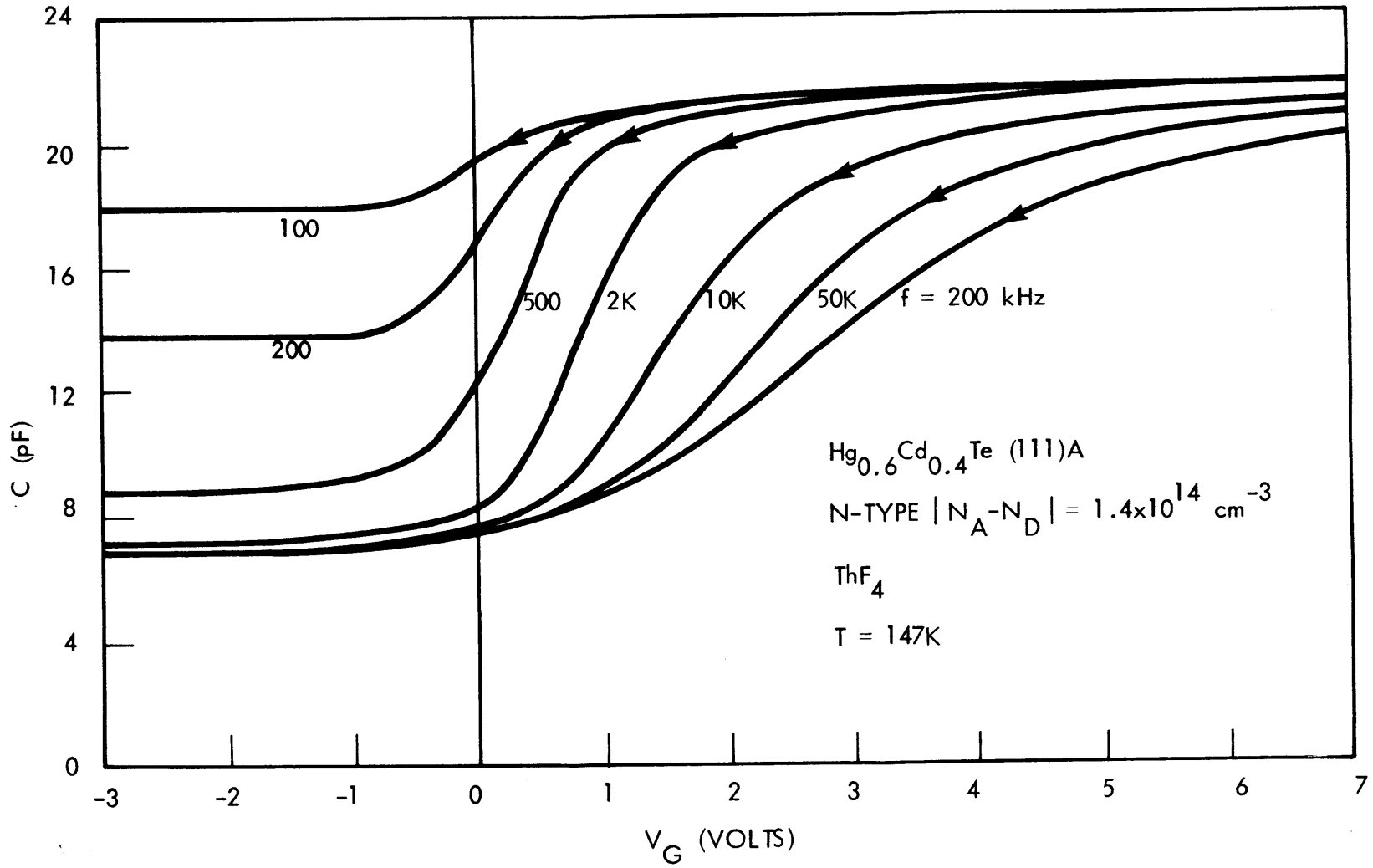

Figure 4.10(a). C-V CURVES OF THE $ThF_4/Hg_{0.6}Cd_{0.4}Te$, (111)A INTERFACE AT VARIOUS FREQUENCIES (N-TYPE)

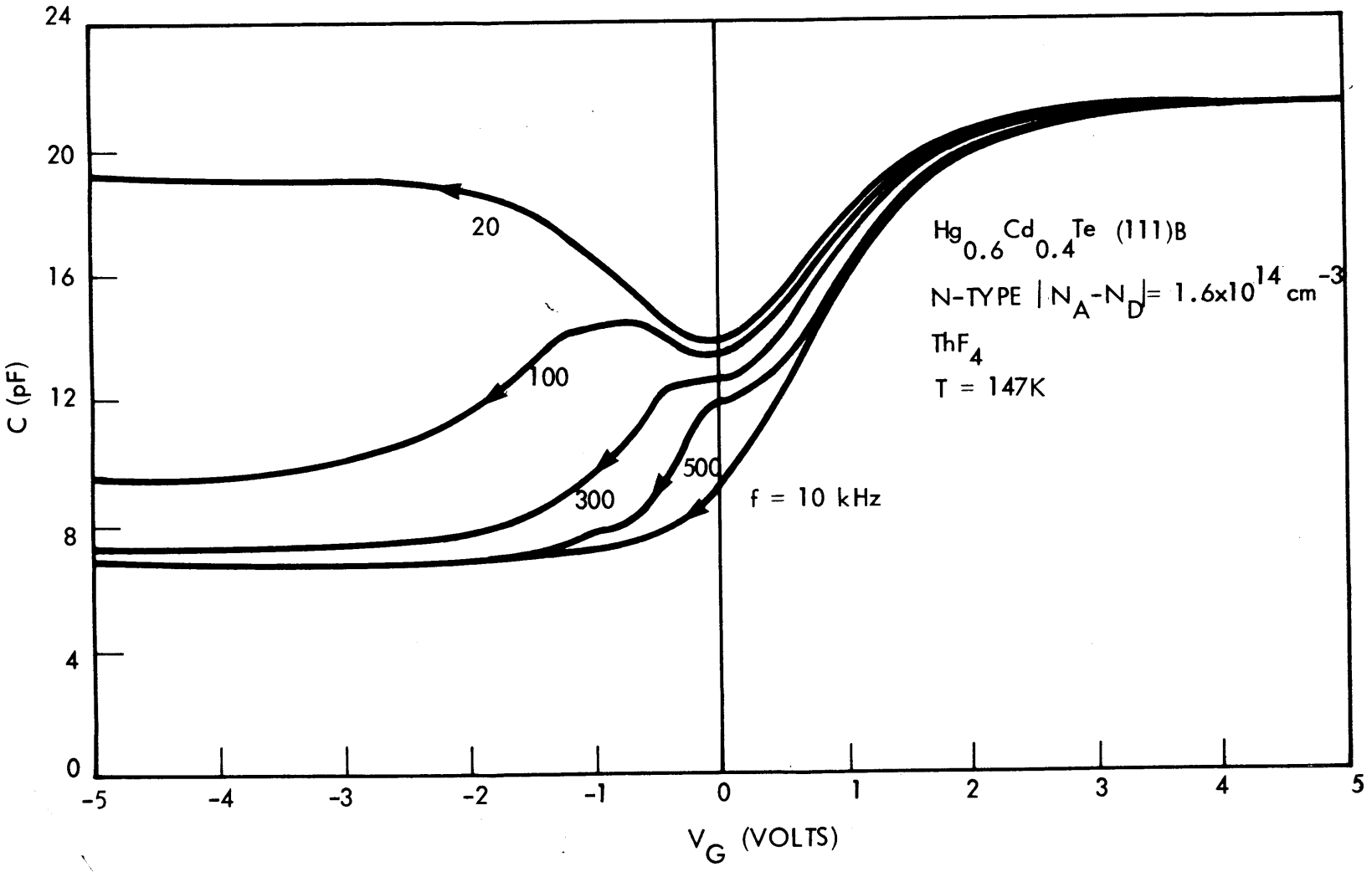

Figure 4.10(b). C-V CURVES OF THE $ThF_4/Hg_{0.6}Cd_{0.4}Te$, (111)B INTERFACE AT VARIOUS FREQUENCIES (N-TYPE)

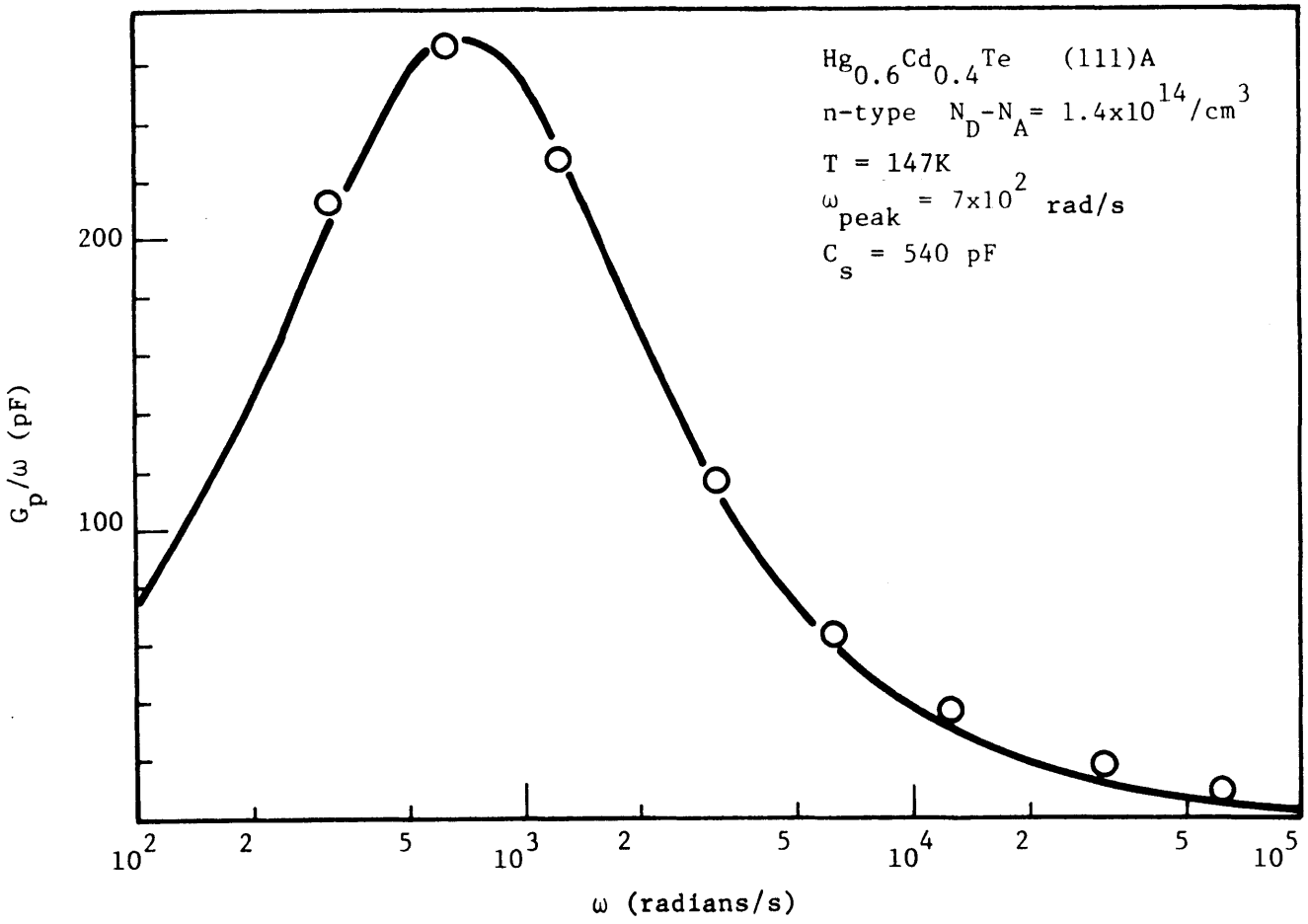

Figure 4.11(a). G_p/ω VERSUS ω ON THE (111)A $Hg_{0.6}Cd_{0.4}Te$ SURFACE

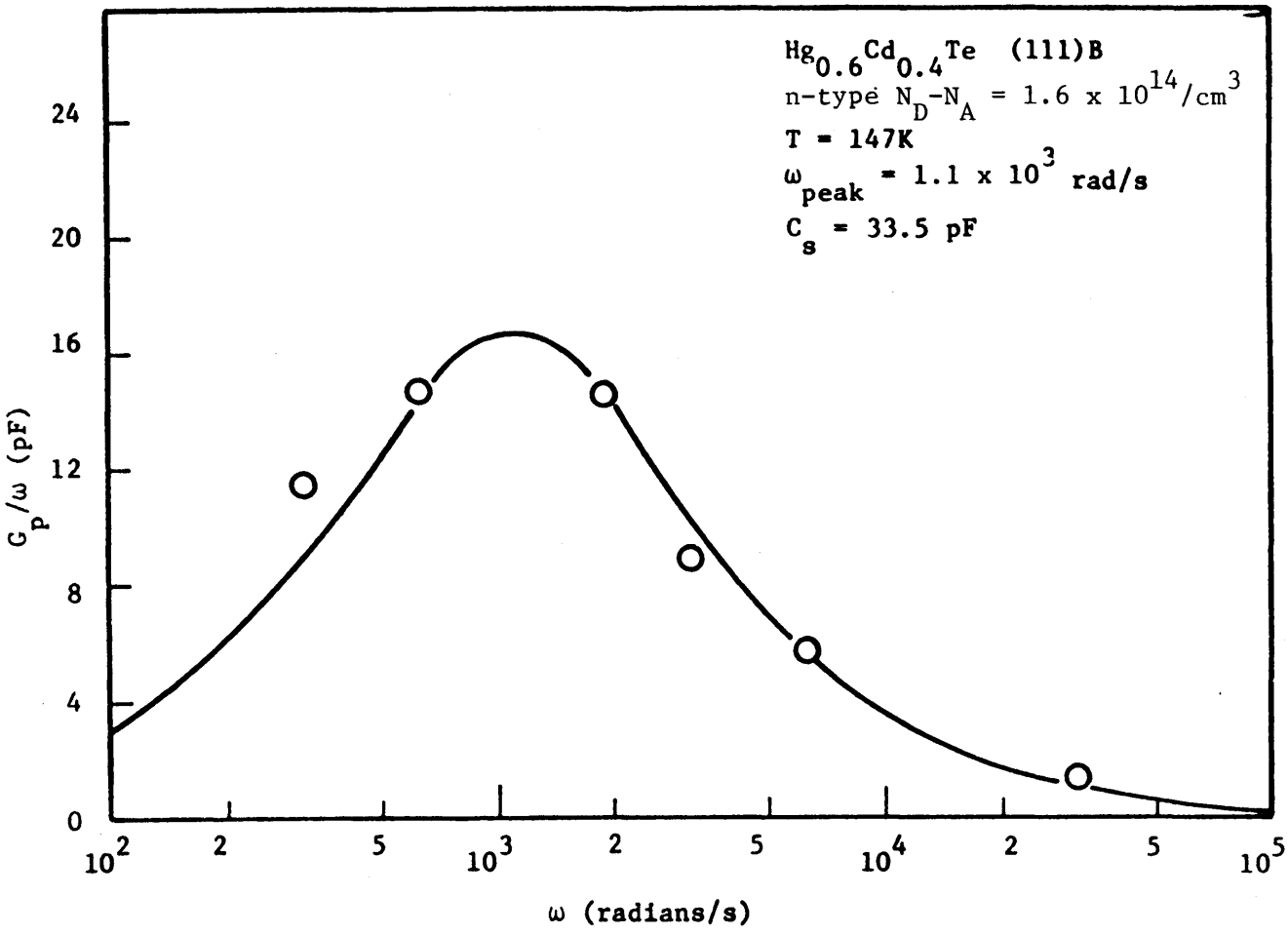

Figure 4.11(b). G_p/ω VERSUS ω ON THE (111)B $Hg_{0.6}Cd_{0.4}Te$ SURFACE

For weak inversion $\psi_B < |\psi_s| < 2\psi_B$. For n-type material ψ_s is negative, so that measurements in weak inversion will yield surface state densities for energies between E_i and $E_i - q\psi_B$. Similarly for p-type material the range of energies will be E_i to $E_i + q\psi_B$. The energy of the surface states was determined in this manner. For the (111)A surface the energy was 0.24 eV and for the (111)B surface the energy was 0.19 eV.

Further conductance measurements were carried out on both n and p type samples on both surfaces. It was discovered that the p-type samples tended to exhibit a somewhat lower surface state density than the n-type samples of the same surface. The difference between the densities on the A and B surfaces was about a factor of ten in both cases.

The differentiation technique was also used for the same samples to which the conductance technique had been applied. This was done partly to provide a comparison between the methods. The differentiation method also yields information over a larger portion of the bandgap.

Data which was derived from an n-type sample on the B surface will be considered to illustrate the procedure used for the differentiation technique. The capacitance was first measured at a high enough frequency so that it was free of capacitance due to surface states. The ideal high frequency curve was then calculated using the measured values of insulator capacitance and substrate doping. In order to facilitate comparison of the ideal and experimental curves, the experimental curve was artificially shifted along the voltage axis. A plot of the experimental and ideal curves

is shown in Figure 4-12. The surface potential at a given capacitance was determined from the theoretical plot of capacitance versus surface potential which is shown in Figure 4-13. The total charge in surface states at a specific surface potential was calculated by determining the difference in voltage between the ideal and experimental curves. A plot of total charge versus surface potential is shown in Figure 4-14. It should be emphasized that neither the true magnitude nor the sign of the total charge can be determined in this way since the effects of metal-semiconductor work function differences and fixed charges in the insulator are not known. This plot does, however, determine the changes in surface state charge with changes in surface potential. Graphical differentiation of this plot yields the surface state density versus surface potential through equation 2-34. The surface potential is then related to the position in the bandgap through equation 4-1 to yield a plot of N_{ss} versus $E-E_v$. Figure 4-15 is plot of N_{ss} versus $E-E_v$ for this example.

This procedure was carried out for n and p-type samples on the A and B surfaces. Figures 4-16 through 4-19 show the resulting plots of N_{ss} versus $E-E_v$ for these cases. Also shown are values determined by the conductance technique. It can be seen that the two methods predict roughly the same densities for the A surface, but disagree considerably for the densities of the B surface. The conductance method results in slightly higher densities for the A surface, but much lower densities for the B surface. It is thought that this discrepancy is due to the fact that the differentiation technique will determine changes in charge in both fast and slow states, while the conductance method is sensitive only to fast

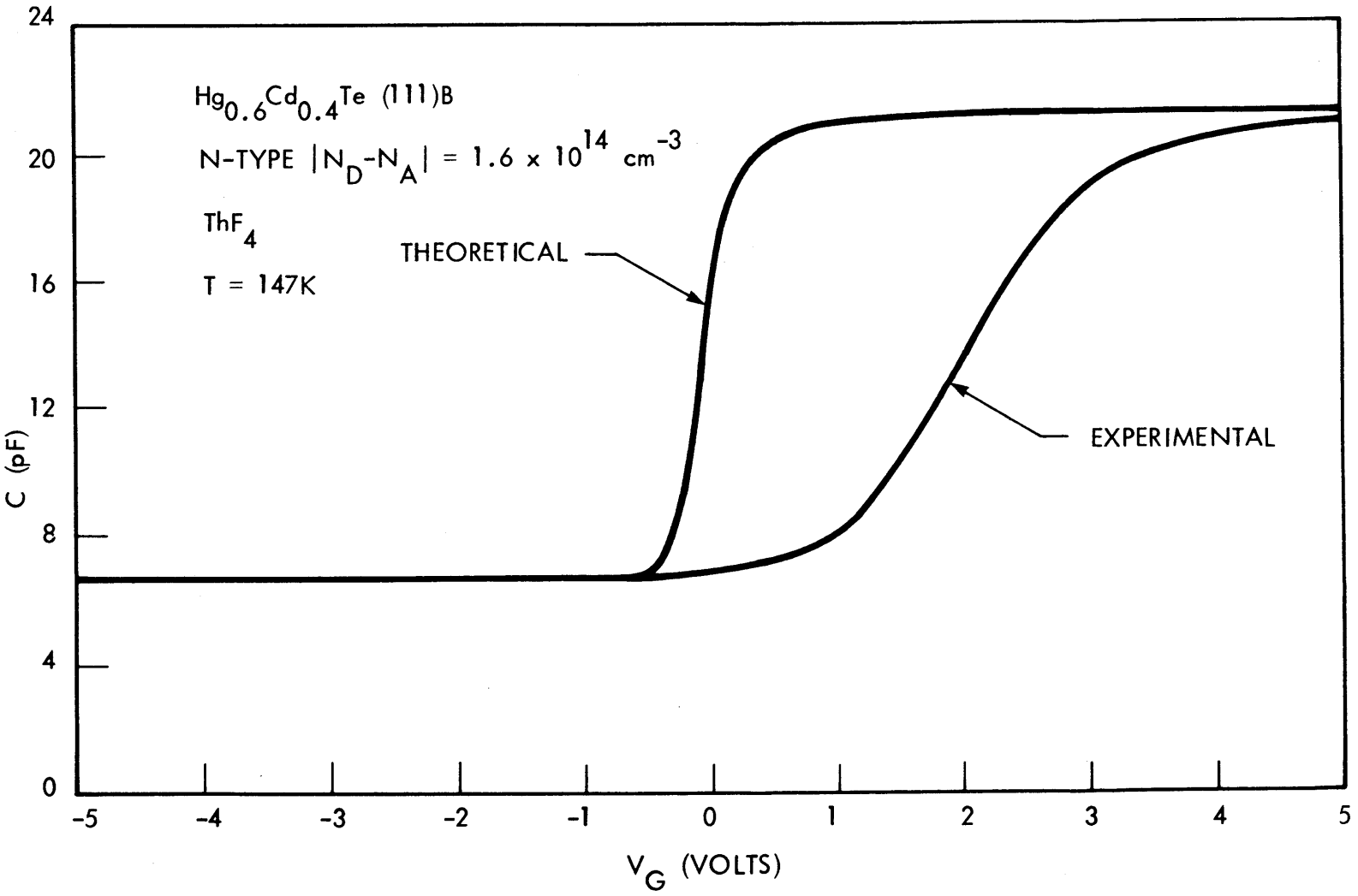

Figure 4.12. COMPARISON OF THE IDEAL AND EXPERIMENTAL C-V CURVES FOR THE $ThF_4/Hg_{0.6}Cd_{0.4}Te$, (111)B INTERFACE

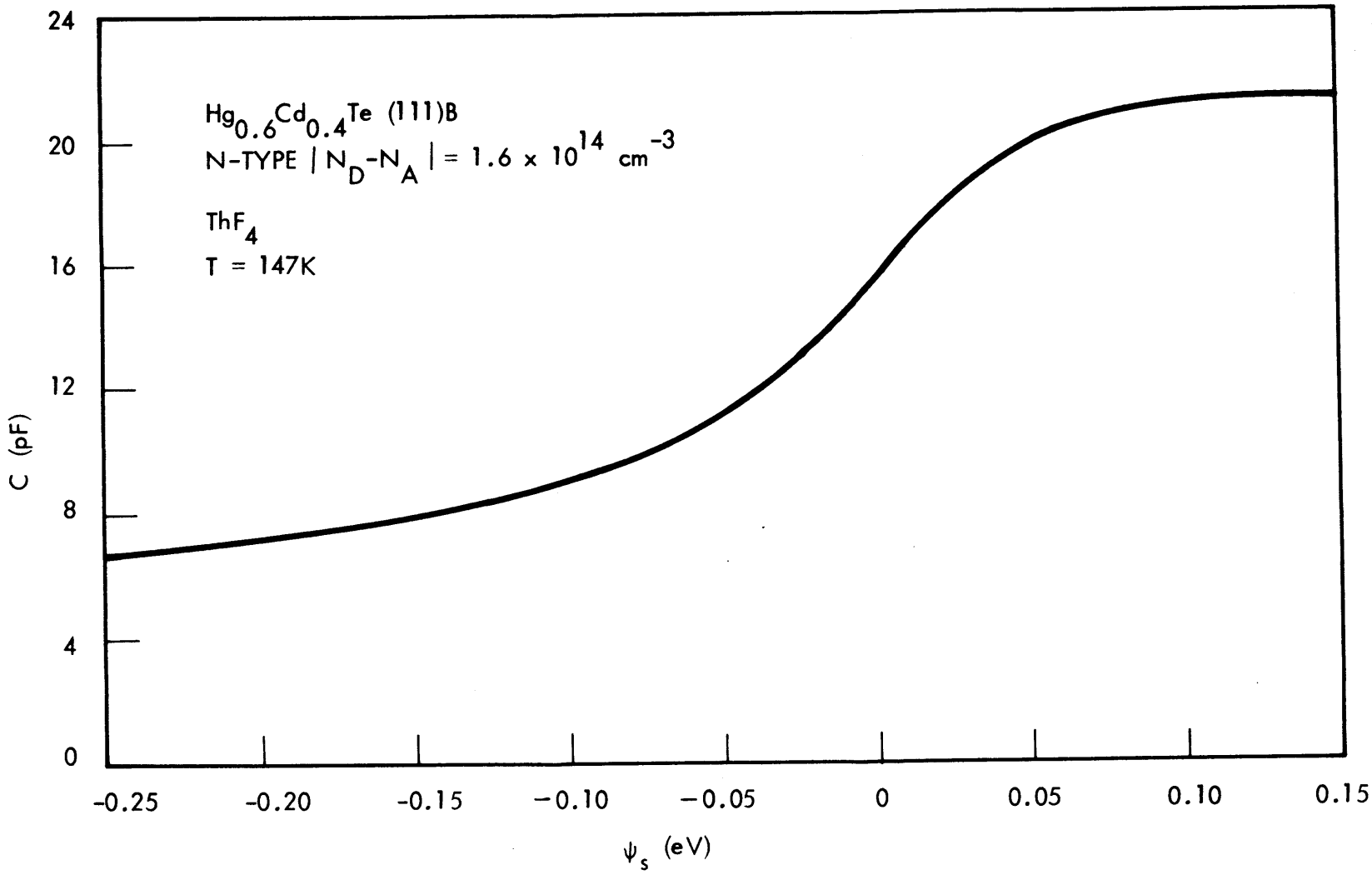

Figure 4.13. PLOT OF CAPACITANCE VERSUS SURFACE POTENTIAL FOR EXAMPLE SHOWN IN FIGURE 4.12.

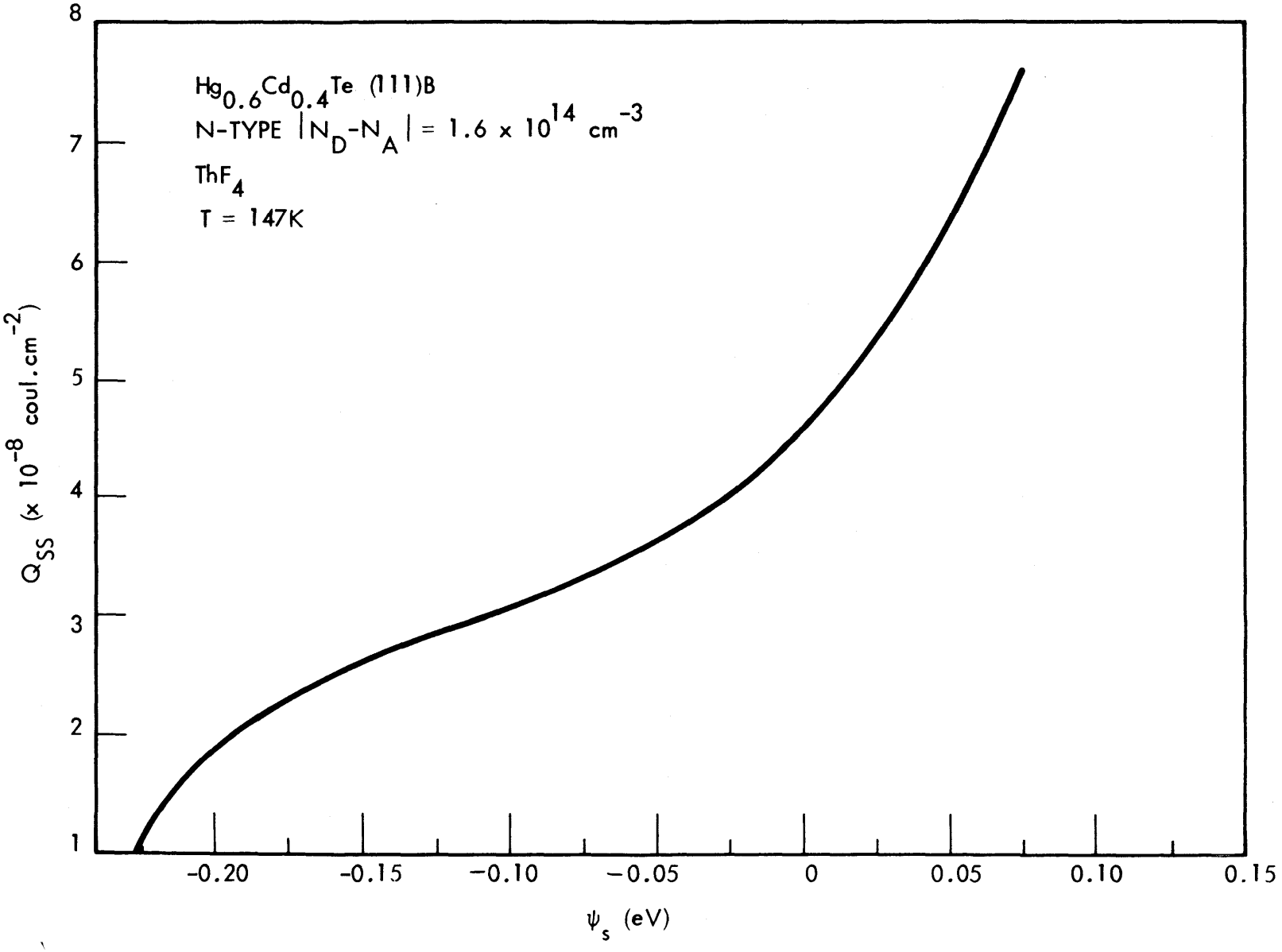

Figure 4.14. SURFACE CHARGE VERSUS SURFACE POTENTIAL FOR EXAMPLE SHOWN IN FIGURE 4.12

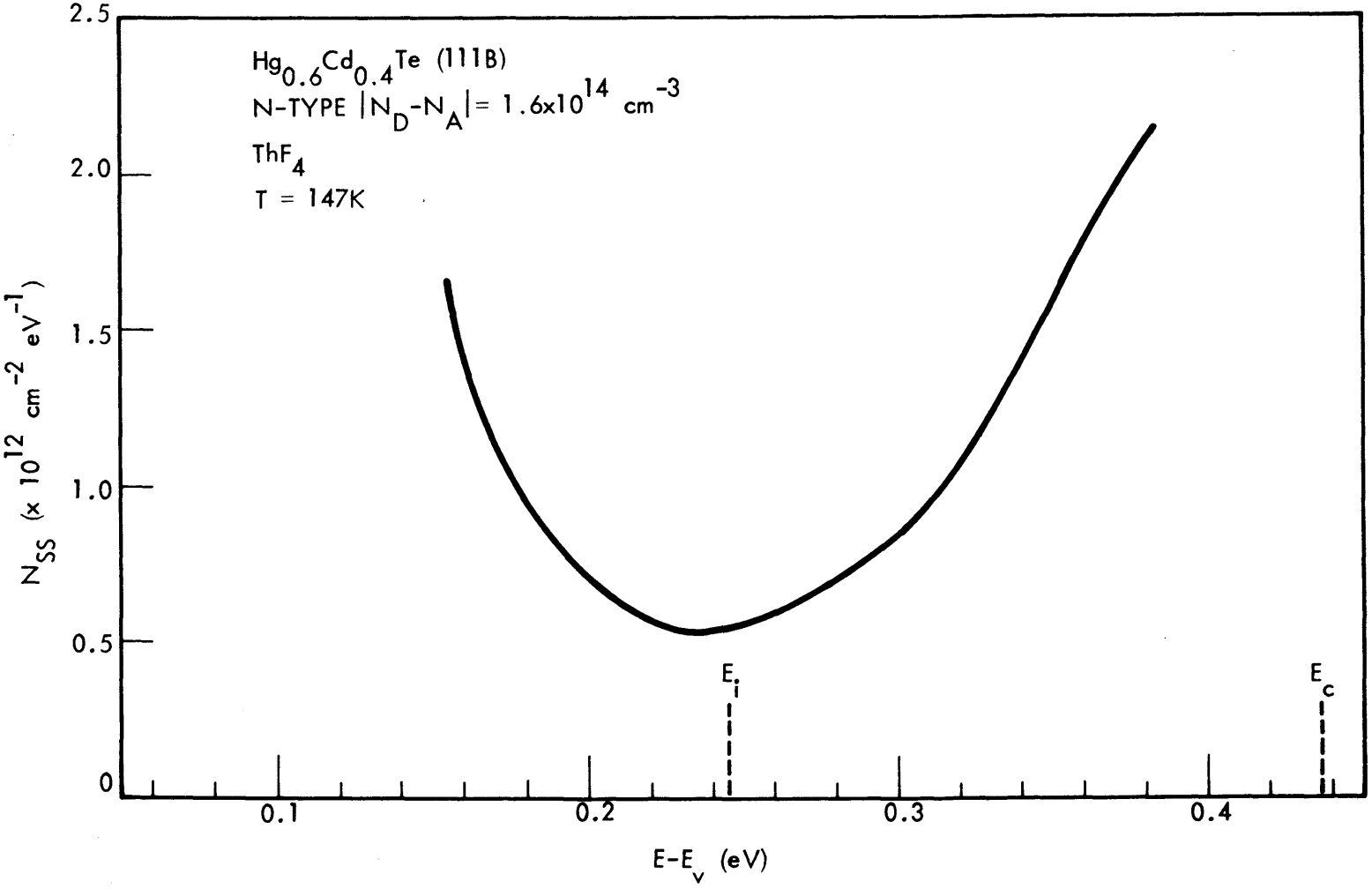

Figure 4.15. SURFACE STATE DENSITY VERSUS ENERGY FOR EXAMPLE SHOWN IN FIGURE 4.12

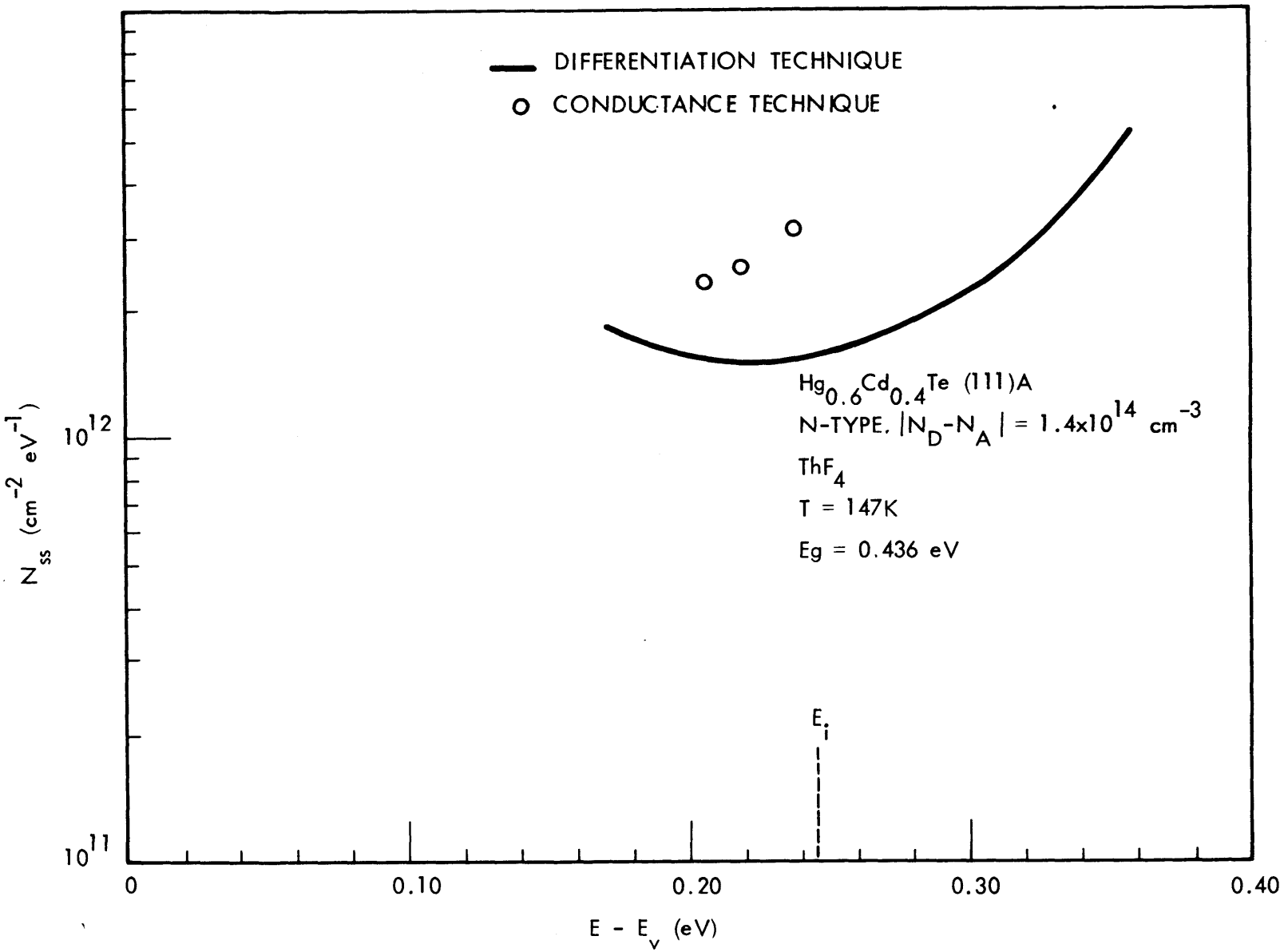

Figure 4.16. SURFACE STATE DENSITY VERSUS ENERGY FOR THE $ThF_4/Hg_{0.6}Cd_{0.4}Te$, (111)A INTERFACE (N-TYPE)

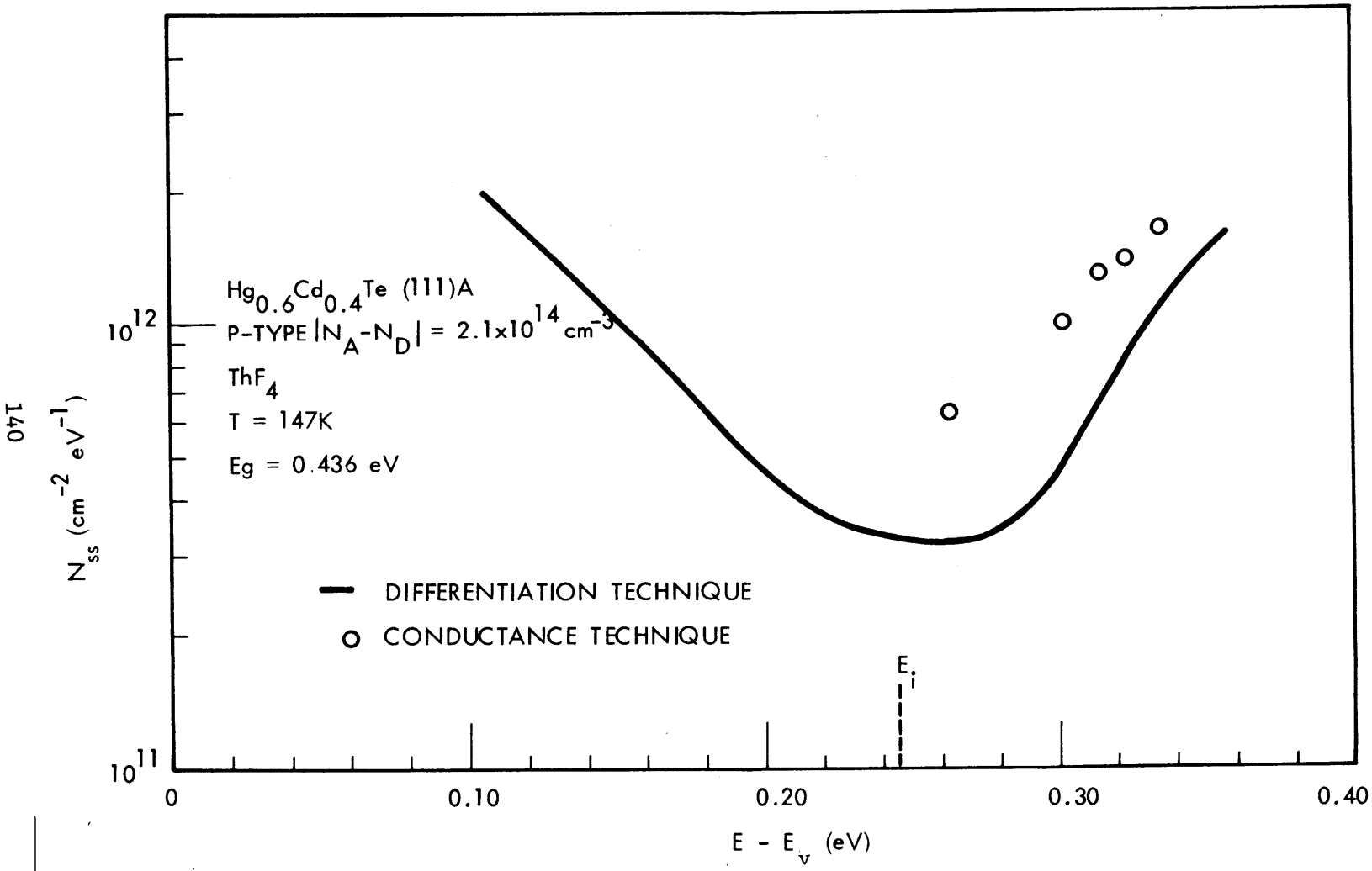

Figure 4.17. SURFACE STATE DENSITY VERSUS ENERGY FOR $ThF_4/Hg_{0.6}Cd_{0.4}Te$, (111)A INTERFACE (P-TYPE)

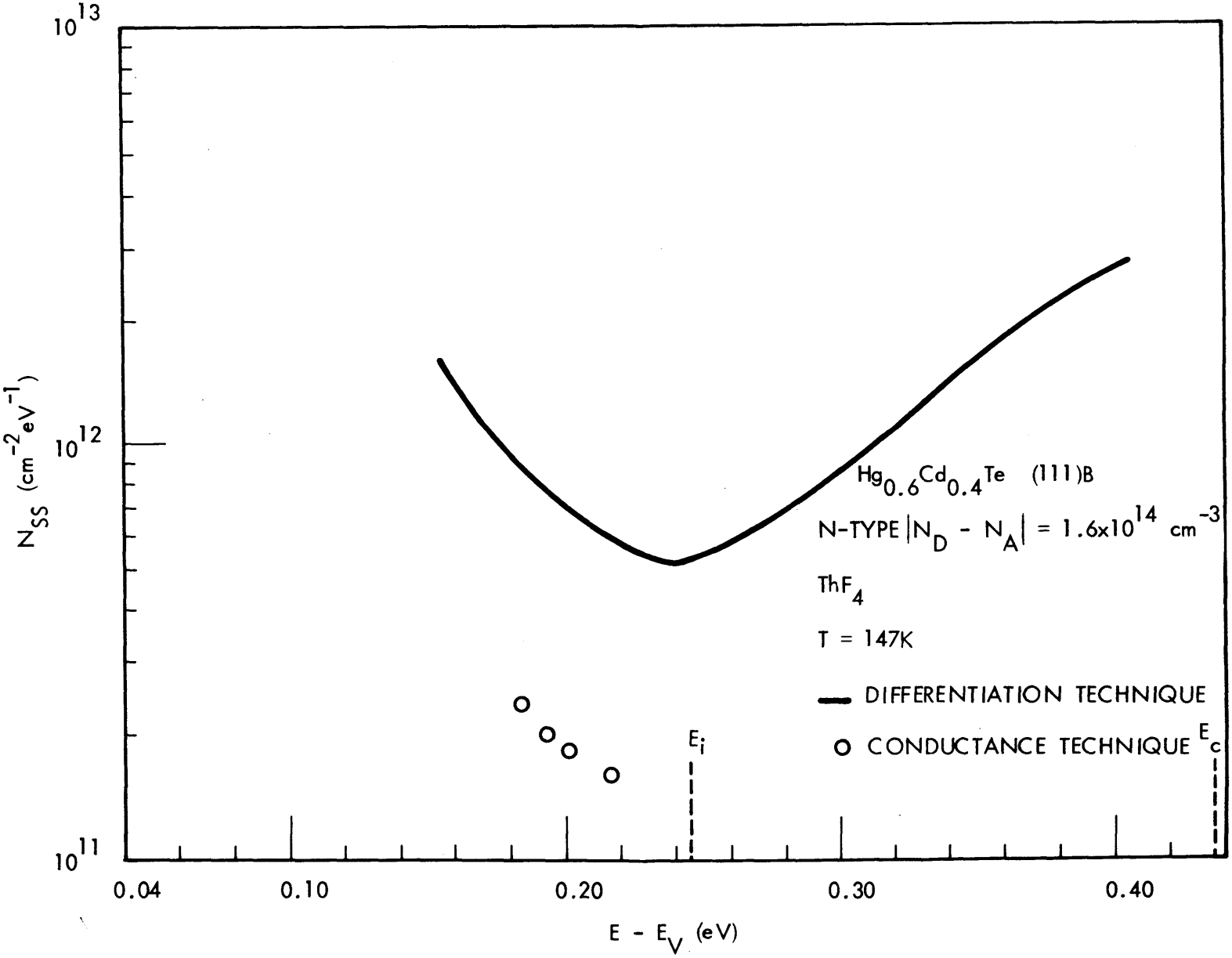

Figure 4.18. SURFACE STATE DENSITY VERSUS ENERGY FOR THE $ThF_4/Hg_{0.6}Cd_{0.4}Te$, (111)B INTERFACE (N-TYPE)

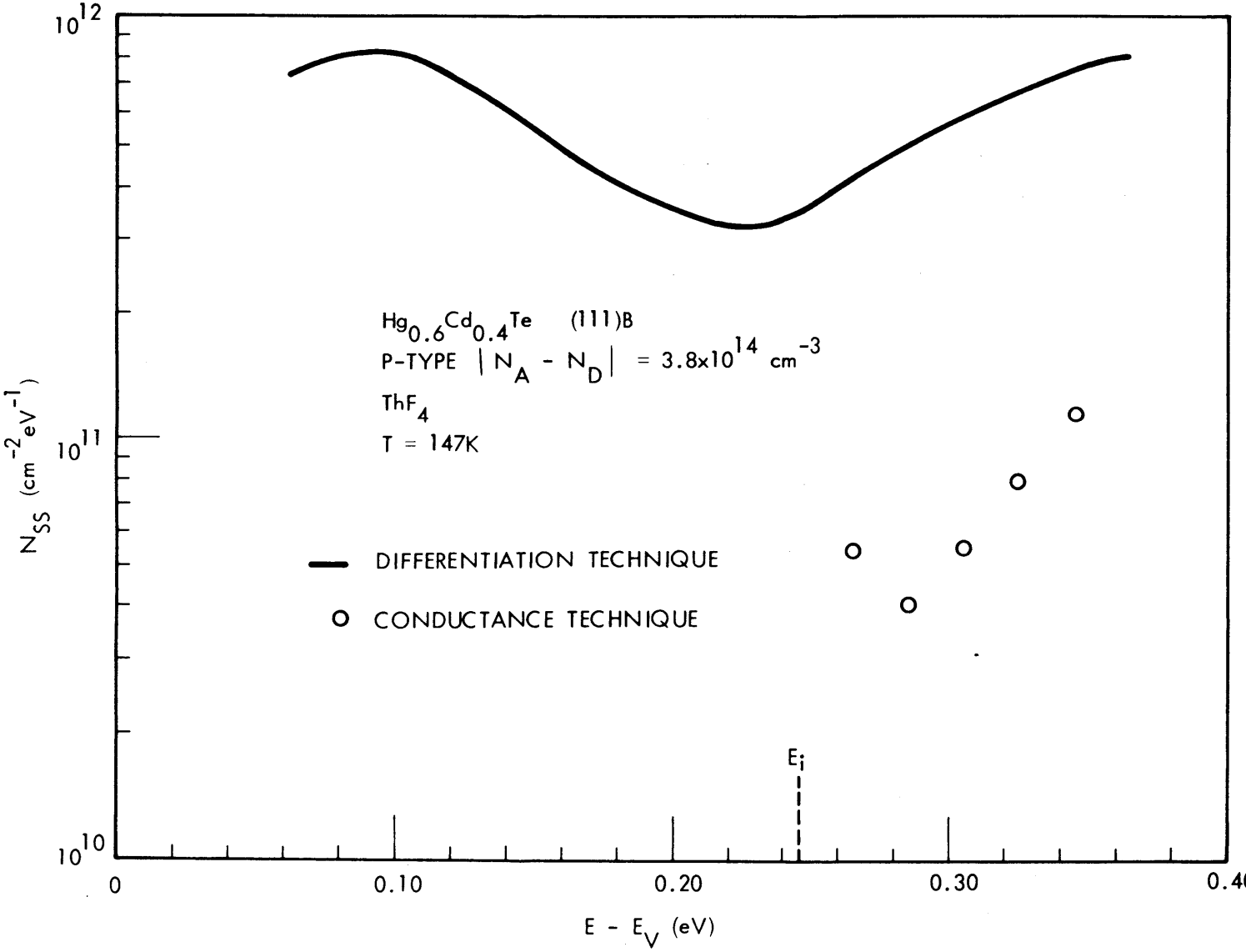

FIGURE 4.19. SURFACE STATE DENSITY VERSUS ENERGY FOR THE $ThF_4/Hg_{0.6}Cd_{0.4}Te$, (111)B INTERFACE (P-TYPE)

surface states. Thus, for large fast surface state densities the effect of the slow states will be relatively small and the methods will be in rough agreement. On the other hand, for much lower fast state densities, such as is the case for the B surface, the effects of the slow states will be relatively larger and thus the differentiation method will predict much higher densities.

It was also observed that the (111)A surface was more depleted than the (111)B surface for zero gate voltage. This shift of the C-V curve in the positive voltage direction implies a larger magnitude of negative charge in the surface states for the (111)A surface. Since the density of surface states was shown to be larger on the (A) surface, the surface states can be assumed to be acceptor like in nature, that is they are negatively charged when occupied by electrons.

4.3.2 Unoriented Material and Other X-Values

Surface state densities were also measured for unoriented materials with x-values between 0.3 and 0.4. These slabs were etched in 1:5 bromine/methanol and coated with an insulating layer of ThF_4. The Au/In gate electrode structure was used.

One slab used was unoriented (Hg,Cd)Te with an x-value of 0.37. Capacitance-voltage curves for this material exhibited less skewing and hysteresis than was normally the case for x=0.4 material oriented in the (111) direction. A C-V curve which was obtained at 194K is shown in

Figure 4-20. The net donor concentration was found to be 4.9×10^{14} cm^{-3}. The surface state densities for this sample as determined by both the conductance and differentiation techniques are shown in Figure 4-21. Although the results of each method are qualitatively similar, the conductance technique again predicts a lower density of surface states. The fast surface state density of 5.5×10^{10} $cm^{-2}eV^{-1}$ near the intrinsic Fermi energy, obtained with the conductance technique, is lower than what was normally observed in the ThF_4/(Hg,Cd)Te system.

MIS structures were fabricated on unoriented n-type x=0.31 (Hg,Cd)Te. The net donor concentration for one sample was found to be 8.5×10^{14} cm^{-3}. A C-V curve obtained at 147K is shown in Figure 4-22. The hysteresis window in this case is only about 0.5 volts wide. The surface appears to be slightly accumulated. It can be seen that the rising portion of the curve has a more gradual slope than the falling portion of the curve. This effect is thought to be due to unequal capture and emission rates of slow surface states. The differentiation method was applied to the falling portion of the curve. The resulting plot of N_{ss} versus $E-E_v$ is shown in Figure 4-23. The effective surface state density was lowest near the intrinsic Fermi energy, about 4.3×10^{11} $cm^{-2}eV^{-1}$.

4.3.3 Time Constant of Surface States

As stated in Section 2.2.3, the time constant of the surface states τ_s is the reciprocal of the frequency at which G_p/ω is maximum. The time constants were calculated for samples on the (111)A and (111)B

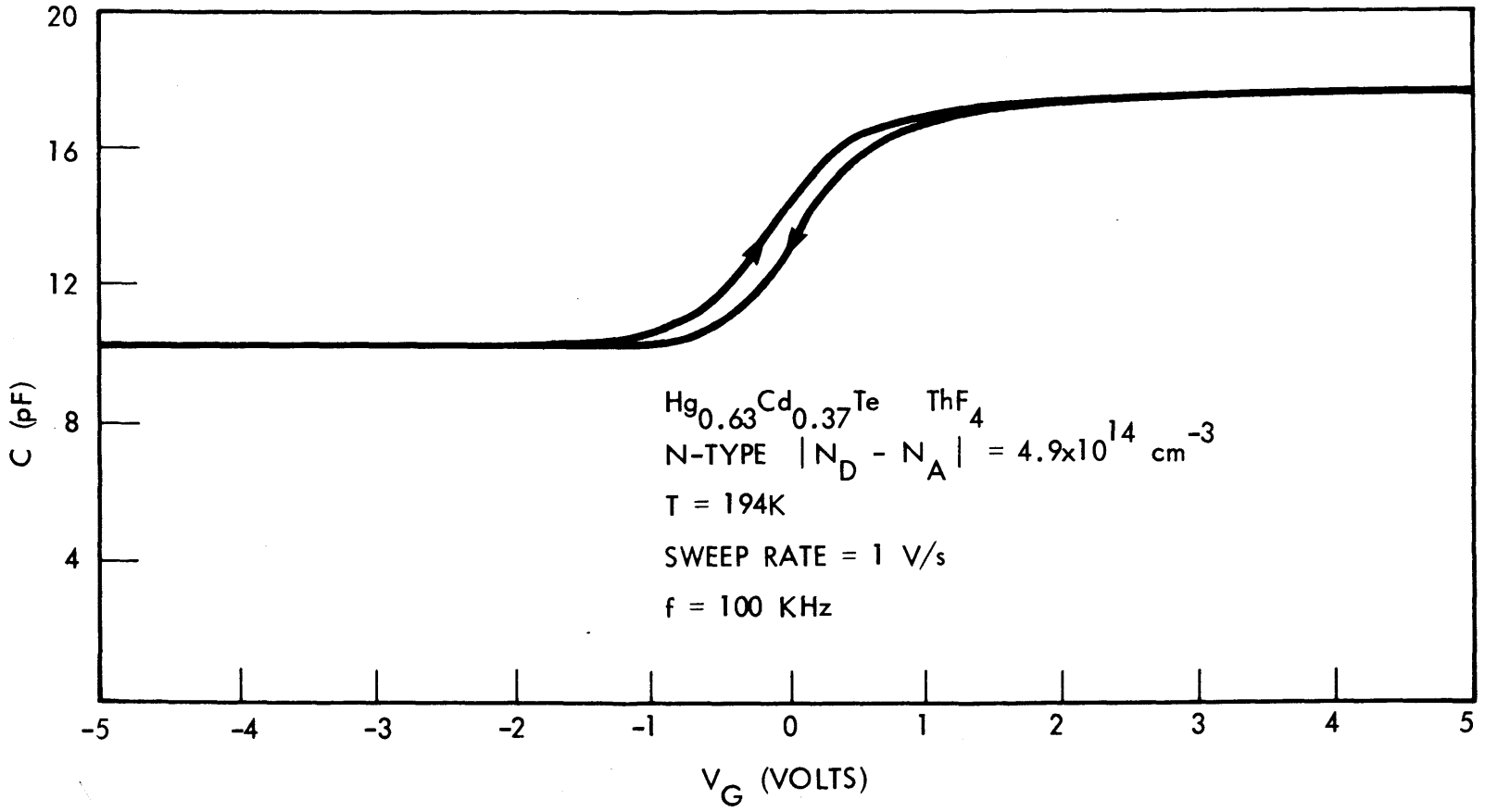

Figure 4.20. C-V PLOT OF A $ThF_4/Hg_{0.63}Cd_{0.37}Te$ MIS STRUCTURE (UNORIENTED MATERIAL)

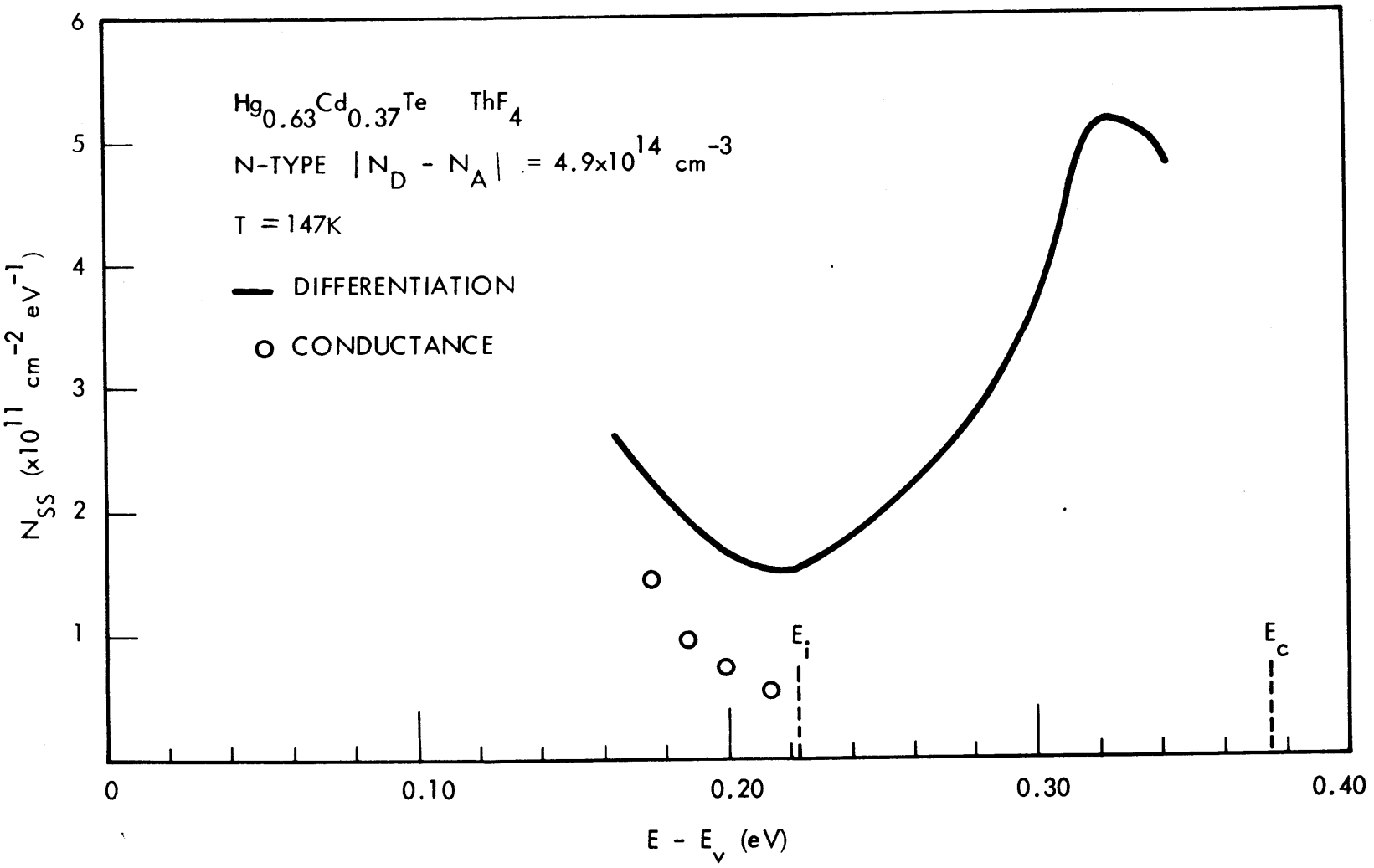

Figure 4.21. SURFACE STATE DENSITY VERSUS ENERGY FOR THE EXAMPLE SHOWN IN FIGURE 4.20

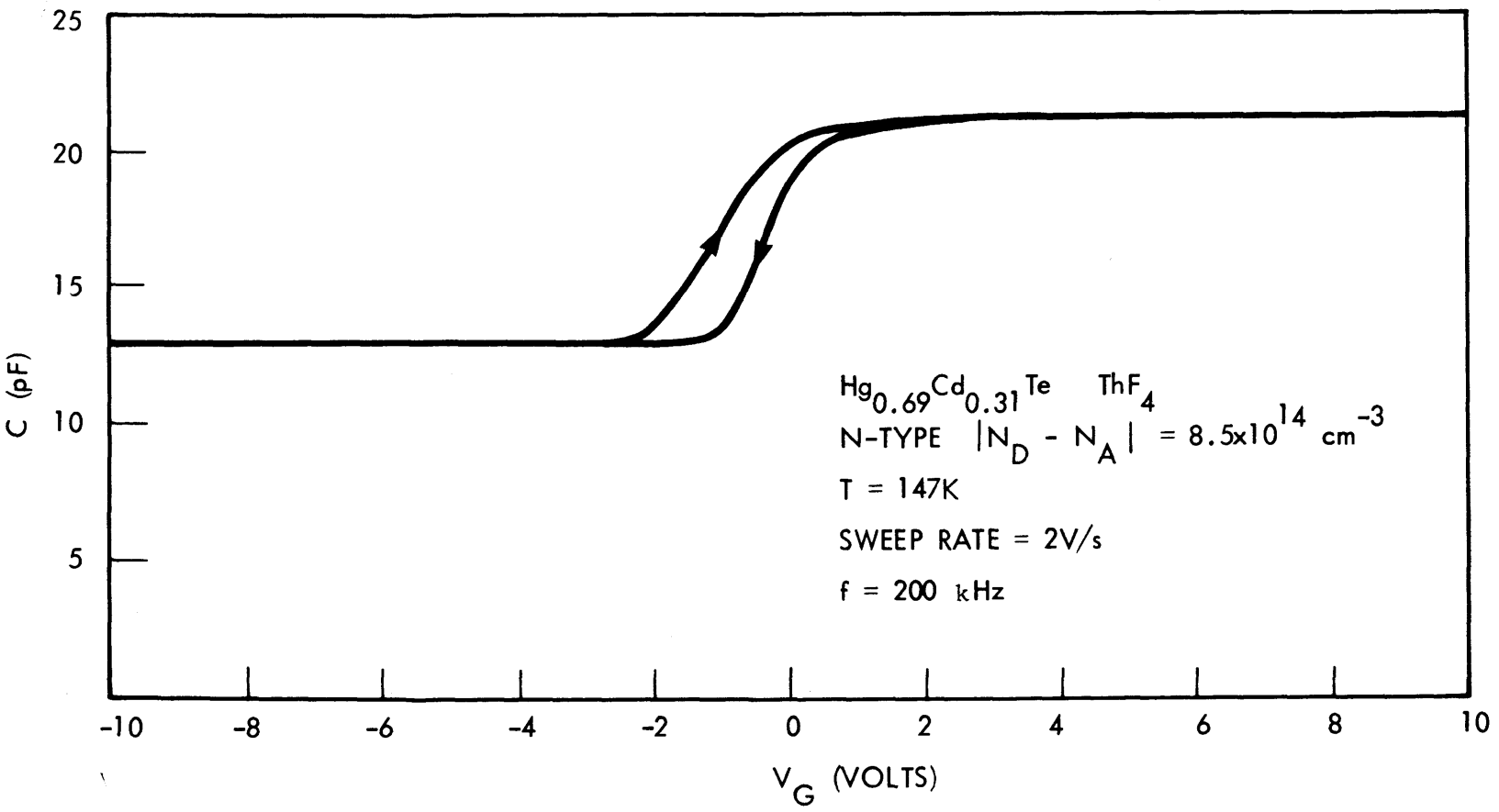

Figure 4.22. C-V PLOT OF A $ThF_4/Hg_{0.69}Cd_{0.31}Te$ MIS STRUCTURE (UNORIENTED MATERIAL)

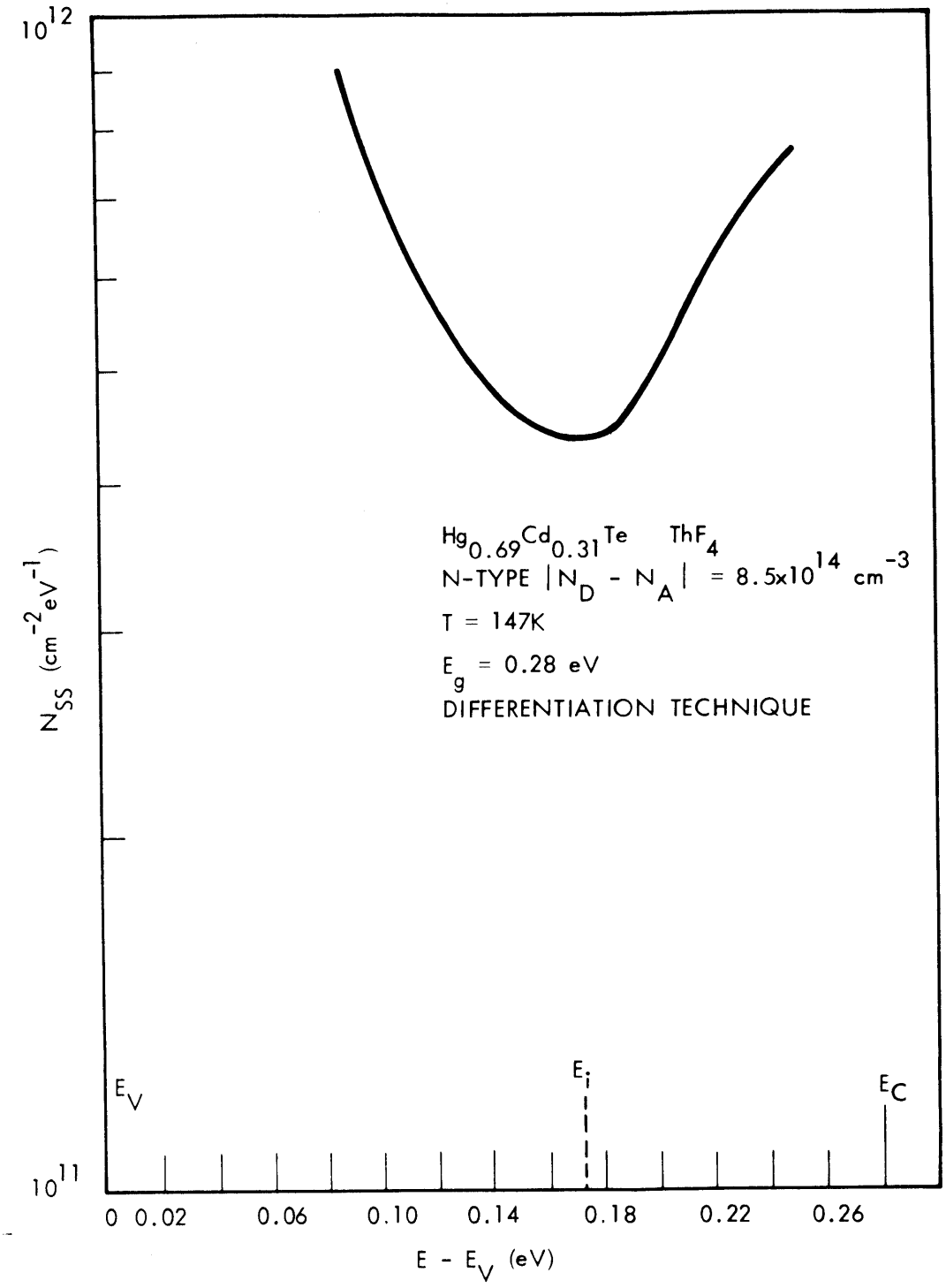

Figure 4.23. SURFACE STATE DENSITY VERSUS ENERGY FOR THE EXAMPLE SHOWN IN FIGURE 4.22

surfaces. The time constants were then plotted as a function of $u_B - u_S$. The resulting plot is shown in Figure 4-24 for two n-type samples and one p-type sample. According to the theory outlined in Section 2.2.3 this plot should yield a straight line with a slope of one for n-type and a slope of minus one for p-type. It can be seen, however, that the slopes are considerably less than one. The slope for the n-type samples is about 0.2 and the slope for the p-type sample is 0.35. The reason for this deviation from the theory is not well understood. It is possible that the assumption that the capture probability of the surface states is constant with energy, as was assumed in Section 2.2.3, is not valid. If that were the case one would have to assume that the capture probability increases exponentially as the energy varies from midgap towards the band edges.

The curves were extrapolated to $u_B - u_S = 0$ in order to obtain an estimate for the capture probabilites for holes and electrons through equations 2-34. This resulted in capture probabilities of 3.1×10^{-8} cm^3/s for electrons on the A surface, 9.3×10^{-8} cm^3/s for electrons on the B surface, and 2.7×10^{-7} cm^3/s for holes on the A surface. For electron-hole recombination at the surface it is expected that the rate of recombination would be limited by the slowest rate which in this case would be the capture of electrons by the surface states. In the following it will be assumed that the effective capture probability is about 5×10^{-8} cm^3/s. The surface recombination velocity is related to the capture probability and surface state density by equation 2-35. For the (111)B surface the density of states near the intrinsic Fermi energy is on the order of 10^{11} cm^{-2} eV^{-1}. At a temperature of 147K the surface recombination velocity

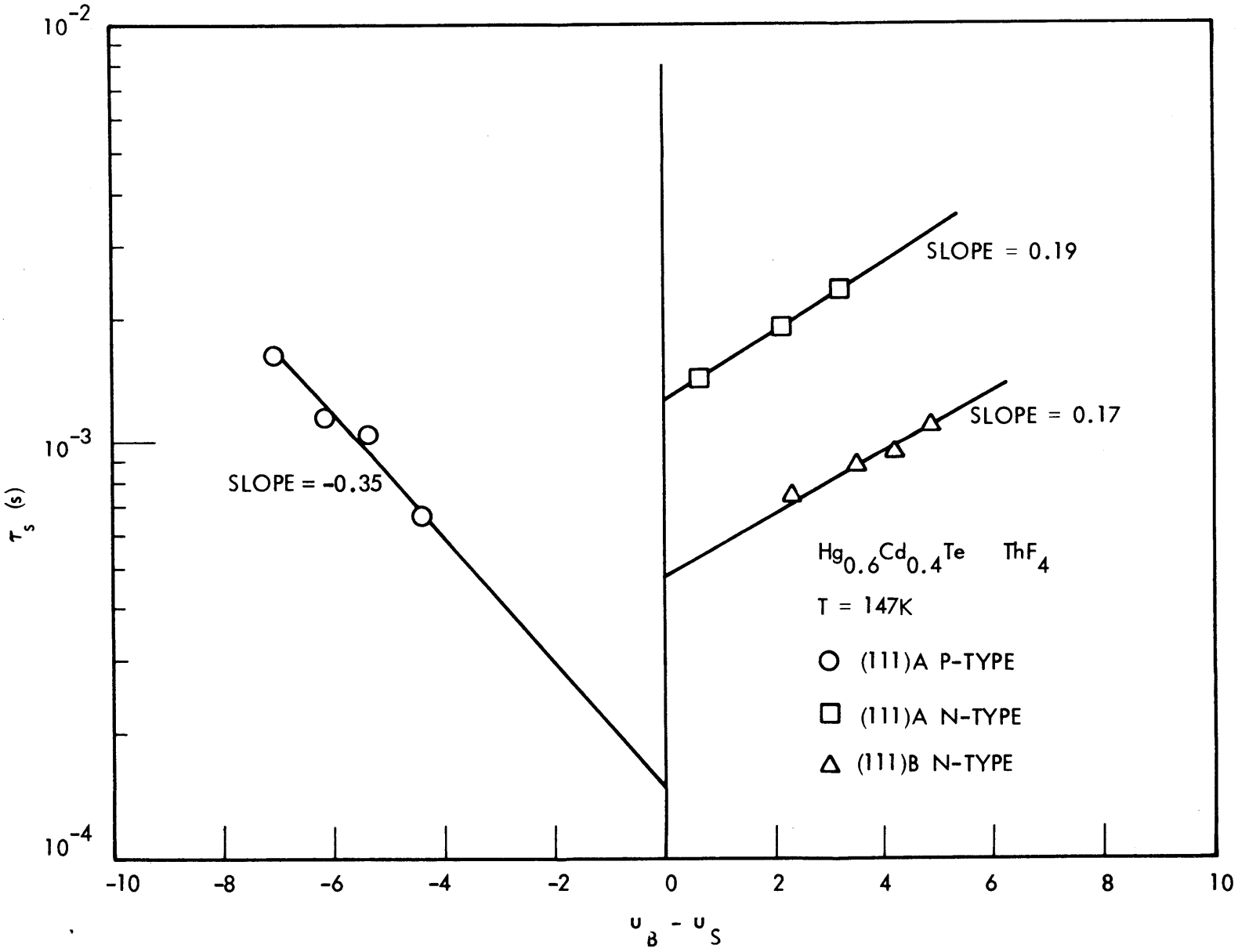

Figure 4.24. TIME CONSTANT OF SURFACE STATES VERSUS $u_B - u_S$ FOR (111)A AND (111)B SURFACES

will then be approximately 100 cm/s. This value is of the same order of magnitude as values which were experimentally determined using the large signal transient technique. This technique will be described in the following section.

Thus it has been shown that the fast surface state densities of the $ThF_4/Hg_{0.6}Cd_{0.4}Te$ interface are on the order of 10^{11} $cm^{-2}eV^{-1}$ for the (111) B surface and 10^{12} $cm^{-2}eV^{-1}$ for the (111) A surface. Unoriented material generally exhibited densities of about 10^{11} $cm^{-2}eV^{-1}$, although densities as low as 5×10^{10} $cm^{-2}eV^{-1}$ were observed. The anodic oxide/(Hg, Cd) Te interface (Section 4.1.7) had the lowest observed densities, about 2×10^{10} $cm^{-2}eV^{-1}$ on the (111) B surface.

4.4 MINORITY CARRIER GENERATION-RECOMBINATION

The MIS technique was used to examine thermal generation and recombination mechanisms in (Hg,Cd)Te. Both small signal (equilibrium) and large signal (non-equilibrium) measurements were carried out. In some cases the results of both types of measurement were compared. The temperature dependence of the thermal rates was determined to identify the range of temperatures which the processes of generation-recombination in the depletion region and diffusion from bulk were dominant.

In most cases (Hg,Cd)Te with an x-value near 0.4 was used. The majority of experiments for this x-value were carried out on the (111)B surface. This material was n-type with $|N_D - N_a| = 2 \times 10^{14}$ cm^{-3}. The thermal processes of p-type material oriented in the (100) direction with $|N_A - N_D| = 1.0 \times 10^{15}$ cm^{-3} were also examined. ThF_4 was the insulator used in most cases, although anodic films were also used.

4.4.1 Small Signal Measurements

There are two ways to carry out the small signal measurement. One is to measure the frequency response of the inversion layer capacitance or conductance. The other is to bias the structure into inversion and observe the transient response of the capacitance or the charge after application of a small voltage step. Both methods were used to determine the small signal time constant.

The inversion capacitance and conductance are a function of the measuring frequency. The capacitance voltage characteristics of a p-type sample from the (111)B face of $Hg_{0.6}Cd_{0.4}Te$ measured at 147K are shown in Figure 4-25 as a function of frequency. It can be seen that the capacitance in strong inversion approaches the insulator capacitance C_i as the frequency approaches zero. The conductance divided by frequency of this same sample as a function of frequency is shown in Figure 4-26. The experimental dependence follows the theory quite well. The small signal time constant τ_{ss} for this sample was found to be 2.8×10^{-4}s. Assuming that diffusion from the bulk was negligible at this temperature the effective lifetime of the depletion region, τ_{g-r}, as defined by equation 2-62, was calculated. The resulting lifetime was 31 nanoseconds.

The transient response methods were also used to determine the small signal time constant. Both the capacitance transient and the charge transient were examined, although in most cases the capacitance transient method was used. The capacitance transient could be easily obtained using essentially the same circuitry as was used to measure the capacitance-voltage characteristics. The main problem with this method was that the voltage levels were very small, on the order of 10 mV, so that the resulting capacitance transient was quite noisy. It was possible to reduce the noise by filtering the output of the 124A lock-in amplifier; this, however, limited the range of time constants which could be measured. The minimum time constant which could be measured with this method was about 20 msec. The charge transient method was less noisy since a great deal of the noise was eliminated by the integrating amplifier. Unfortunately the input offset

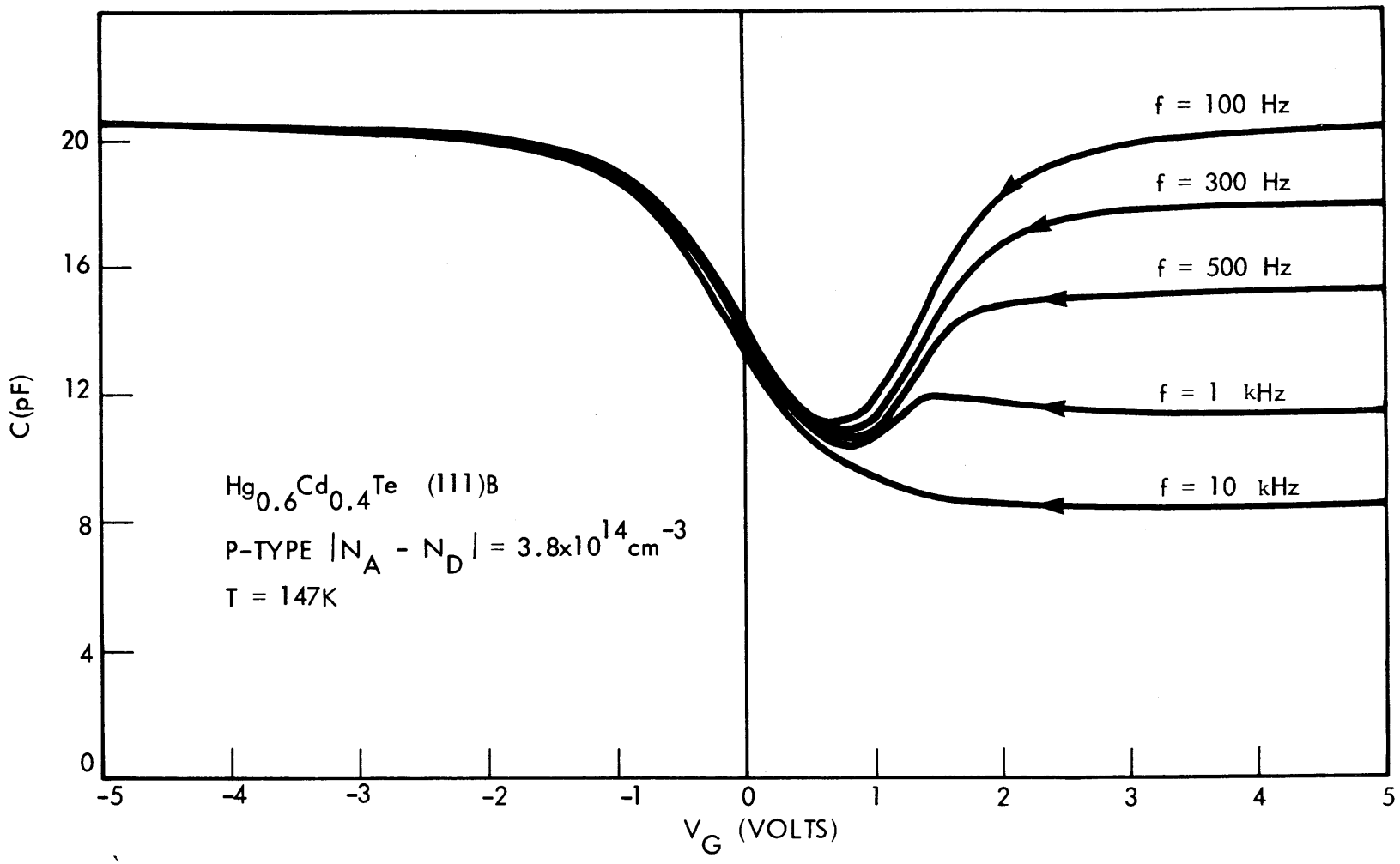

Figure 4.25. C-V CURVES AT VARIOUS FREQUENCIES FOR THE $ThF_4/Hg_{0.6}Cd_{0.4}Te$, (111)B INTERFACE (P-TYPE)

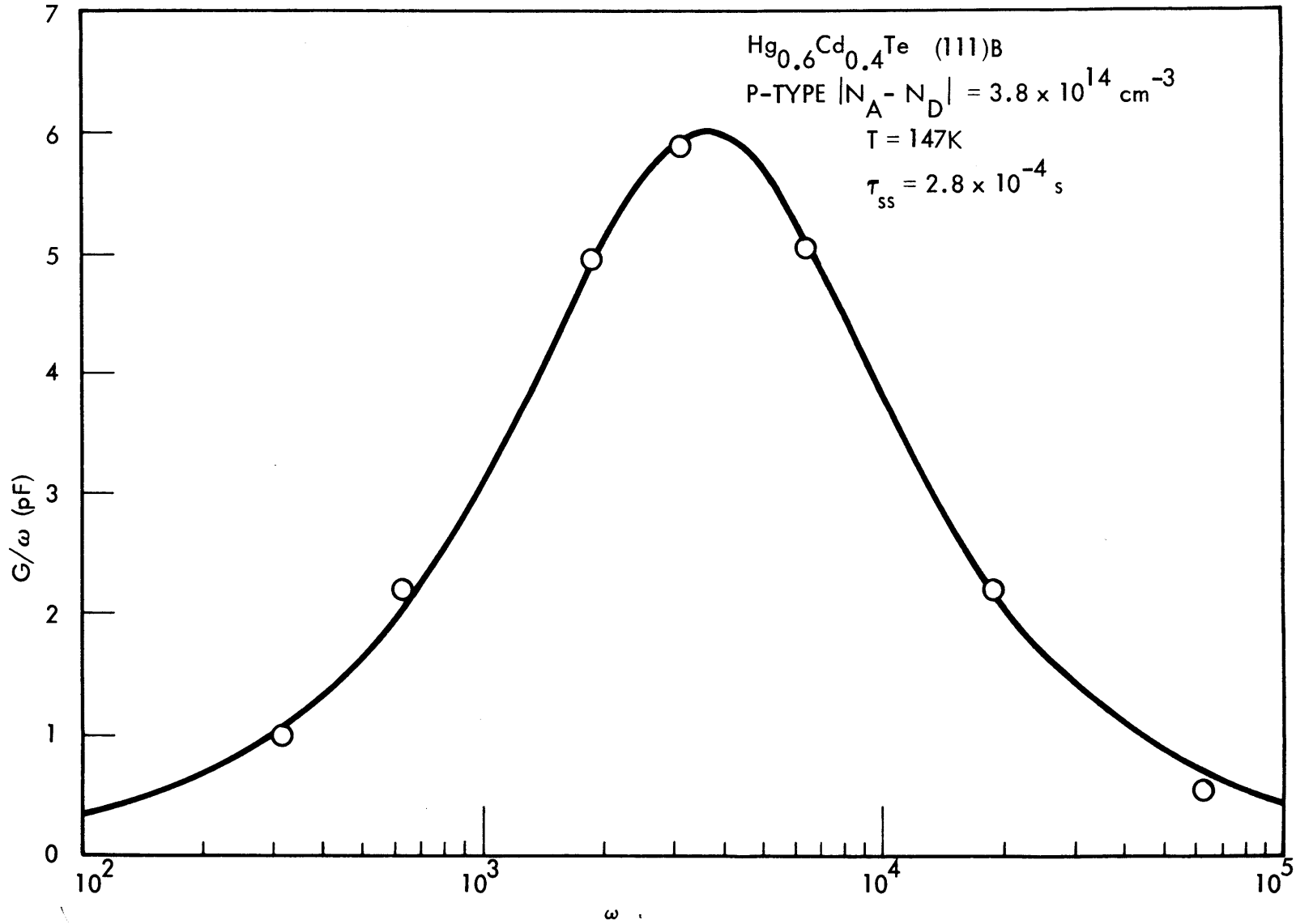

Figure 4.26. G/ω VERSUS ω FOR THE EXAMPLE SHOWN IN FIGURE 4.25

current and any other stray currents were also integrated, resulting in a great deal of instability in the DC output voltage of the amplifier. A more sophisticated integrator would be necessary for this method to be useful. In a few cases both methods were used on the same sample. The time constants which resulted were in agreement to within about 20%.

Figure 4-27 is an example of a capacitance transient which was obtained from an n-type sample of $Hg_{0.6}Cd_{0.4}Te$ at a temperature of 125K. A small amount of asymmetry in the upper and lower capacitance transients can be noted. The upper transient, which corresponds to the recombination of minority carriers, exhibits a smaller time constant than the lower transient, which corresponds to the generation of minority carriers. In this case the time constants for the upper and lower transients were 2.2 s and 3.0 s respectively. This asymmetry increased as the amplitude of the voltage step increased. The asymmetry is probably due to the violation of the requirement that the amplitude of the voltage step be much less than kT/q. In this case a step on the order of kT/q (11 mV) was used.

The frequency response measurement and the transient response measurement were compared in several cases. The frequency response measurement generally yielded a somewhat smaller time constant than did the transient measurement. The time constant determined from the frequency response was typically about 2/3 as long as that determined from the transient. It is expected that the frequency response of the conductance would yield more accurate results since smaller voltage levels could be used. In general the transient method was used for time constants longer

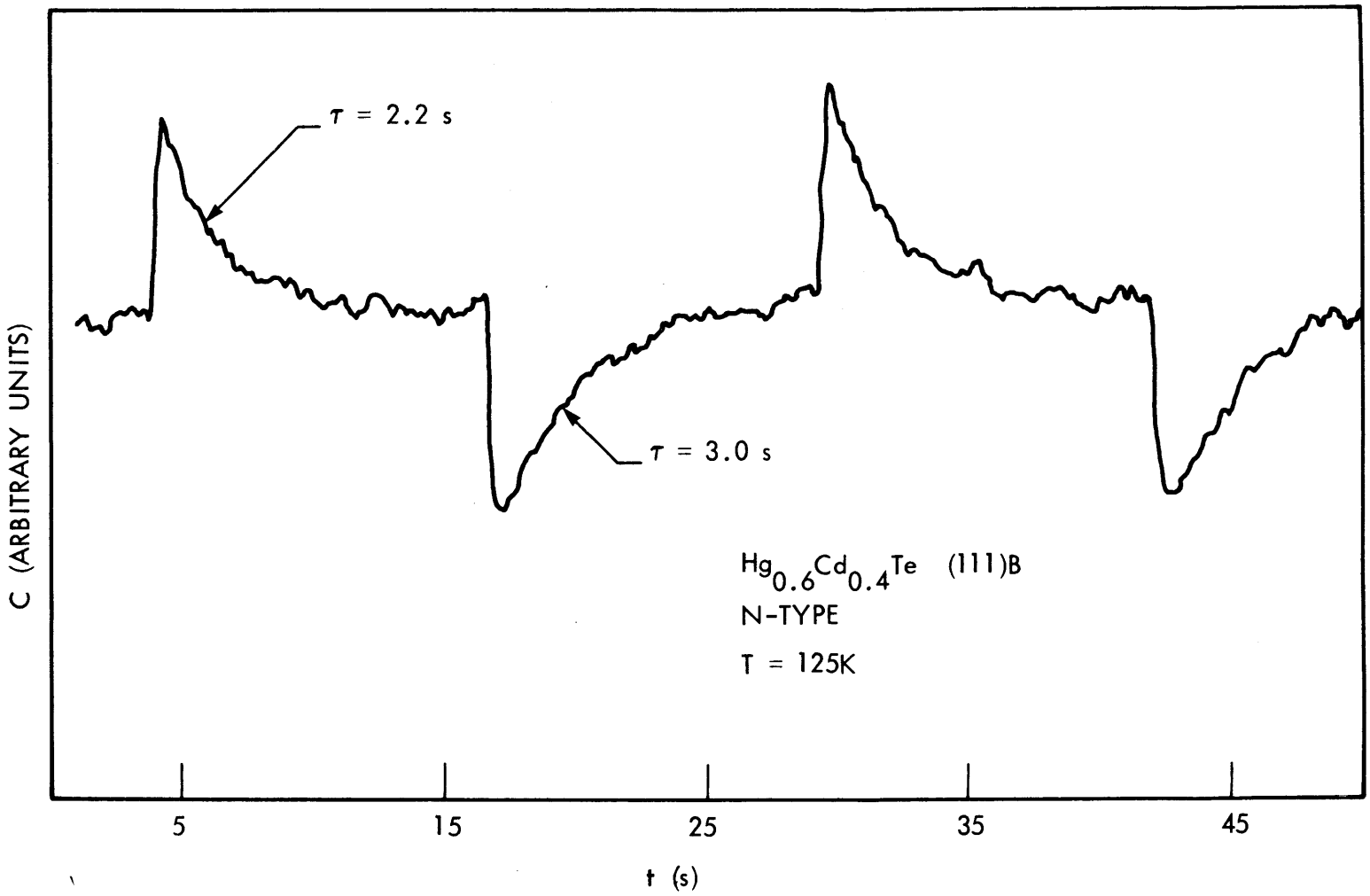

Figure 4.27. SMALL SIGNAL CAPACITANCE TRANSIENT FOR $Hg_{0.6}Cd_{0.4}Te$ AT 125K

than about 20 msec. The frequency response method was difficult to use for this range of time constants because of the difficulty in making very low frequency capacitance and conductance measurements, but was very useful for time constants which were shorter than 20 msec. A quite large range of time constants could thus be measured with a combination of the two techniques.

The majority of small signal measurements were done at a temperature of 147K. At this temperature the predominant thermal mechanism was generation-recombination in the depletion region as was indicated by variable temperature measurements to be described in a later section. A large number of measurements were carried out on MIS structures fabricated on the (111)B surface of n-type slabs of $Hg_{0.6}Cd_{0.4}Te$. The net donor concentrations of this material was typically 2×10^{14} cm^{-3}. The effective depletion region lifetime for this material as calculated with equation 2.62 was typically on the order of 10 to 30 μsec. Measurements were also done on p-type slabs of $Hg_{0.6}Cd_{0.4}Te$ oriented in the (100) direction. The doping level of this material was about 1×10^{15} cm^{-3}. Typical depletion region lifetimes for this material were ~1 μsec.

Measurements at higher temperatures, primarily 194K, revealed that diffusion from the bulk could no longer be neglected. The small signal time constant measured at 194K was considerably smaller than would be expected if generation-recombination in the depletion region was the only important mechanism. The diffusion resistance defined by equation 2.65 was calculated for T = 194K under the following assumptions: the bulk and

depletion region lifetimes were equal, i.e. $\tau_{g-r} = \tau_B$; for n-type material the hole mobility $\mu_h \simeq 200$ cm^2 volt^{-1} s^{-1}, and for p-type the electron mobility $\mu_e \approx 4.5 \times 10^3$ cm^2 volt^{-1}s^{-1}. The calculations showed that for both the n and p-type material the calculated diffusion resistance was comparable to the measured resistance. Thus, neither the diffusion nor the depletion region resistance could be neglected, so that accurate determination of the bulk and depletion region lifetimes was nearly impossible at this temperature.

4.4.2 Large Signal Measurements

Large signal measurements were carried out on both n and p-type $Hg_{0.6}Cd_{0.4}Te$. For the majority of measurements the amplitude of the gate voltage step was 20 to 30 volts. The range of voltage was normally ±10 volts or ±15 volts. This range of gate voltage would bias the MIS structure from heavy accumulation to deep depletion. A temperature of 147K was most commonly used. At this temperature the duration of the capacitance transient was typically on the order of 10 seconds, so that the transient could be easily recorded on graph paper using the time base mode of an X-Y plotter. For shorter transients a memory oscilloscope was used.

MIS structures were fabricated on the (111)B surface of n-type $Hg_{0.6}Cd_{0.4}Te$ with a net doping level of about 2×10^{14} cm^{-3}. ThF_4 was the insulator used in this case. Structures which exhibited non-equilibrium capacitance-voltage characteristics at T = 147K were selected for the large signal pulse measurements. The structures were pulsed from +10 volts to

-10 volts and the resulting capacitance transients were recorded with an X-Y plotter. A typical transient is shown in Figure 4-28.

The transient was then analyzed and a plot of $-d/dt\ (1/C^2)$ versus $C_f/C-1$ was constructed, where all capacitances were normalized to the insulator capacitance C_i. This plot, which has been named a "Zerbst" plot, is shown in Figure 4-29. It can be seen that the plot is linear only for low values of $C_f/C-1$, which corresponds to the latter portion of the transient. This Zerbst plot is indicative of an increased generation rate of minority carriers towards the beginning of the transient. Similar results had been noted by Schroder for Si/SiO_2 MIS structures (see Section 2.3.1). He attributed this result to a larger generation of carriers by surface states at the beginning of the transient. His analysis was applied to this transient. From the initial value of $d/dt\ (1/C^2)$ a surface generation velocity S_o of 40.9 cm/s was determined. Using this value of generation velocity and the slope of the linear portion of the curve a minority carrier generation lifetime (τ_g) of 110 microseconds was calculated (equations 2.83, 2.85).

Generation lifetimes determined with this technique varied from 30 μs to 200 μs for this particular slab. The surface generation velocity of the (111)B surface of the (Hg,Cd)Te/ThF_4 system was found to vary from 10 - 100 cm/s. This compares reasonably well with the value of 100 cm/s calculated in Section 4.3 based on the results of variable frequency surface state conductance measurements.

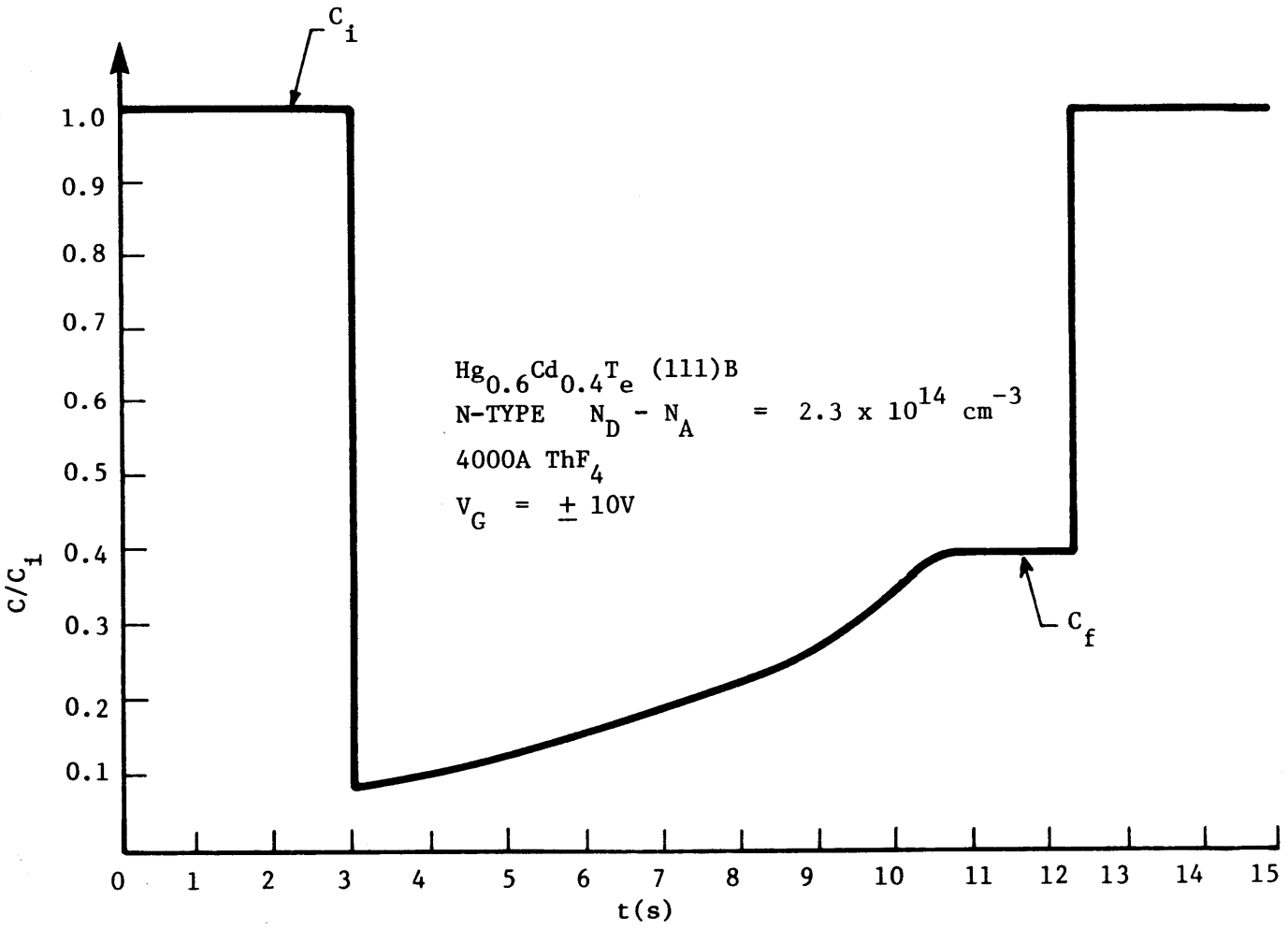

Figure 4.28. TRANSIENT RESPONSE TO DEPLETING VOLTAGE STEP

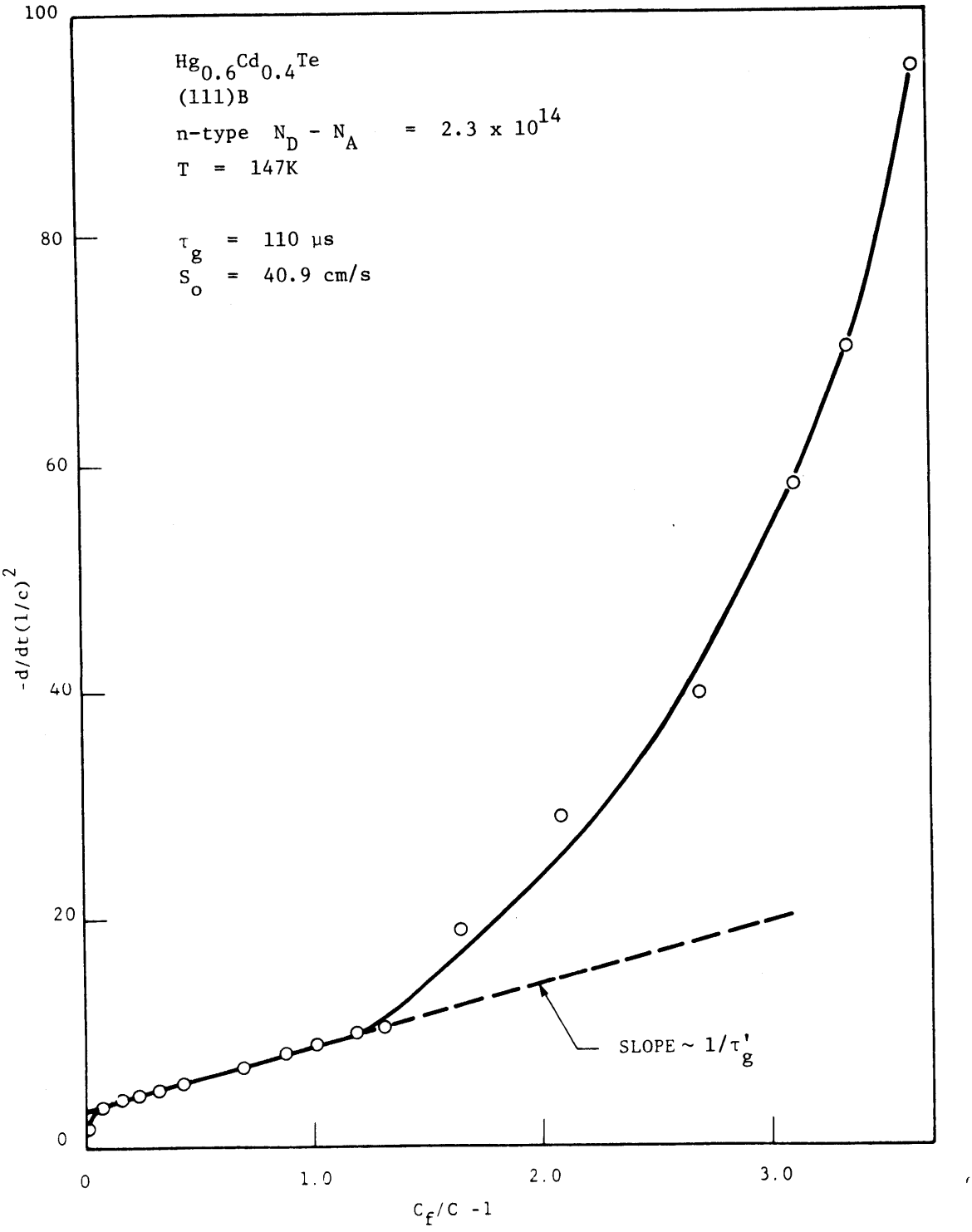

Figure 4.29. ZERBST PLOT FOR TRANSIENT SHOWN IN FIGURE 4.28

Large signal measurements were done on p-type $Hg_{0.6}Cd_{0.4}Te$ oriented in the (100) direction with $|N_A - N_D| \approx 1 \times 10^{15}$ cm^{-3}. ThF_4 was again the insulator used. Surface generation velocities ranges from 5-50 cm/s. The generation lifetime was found to vary from 2-10 microseconds.

The (Hg,Cd)Te/anodic oxide/ThF_4 system was also examined with the large signal technique. Structures were fabricated on the (111)B surface of n-type $Hg_{0.6}Cd_{0.4}Te$. Measurements were done at a temperature of 147K. Since the free surface was accumulated the structures were pulsed from 0 volts to -15 volts. One of the resulting capacitance transients is shown in Figure 4.30. The net doping for this sample was determined to be 9.7×10^{13} cm^{-3}. The Zerbst plot which was constructed from this transient is shown in Figure 4.31. It can be noted that the linear portion extends over most of the plot. This indicates that generation by recombination centers in the depletion region was the dominant process during most of the transient. The surface generation velocity calculated from the initial value of $d/dt\ (1/C^2)$ was only about 2 cm/s, which was considerably lower than what was normally observed in the (Hg,Cd)Te/ThF_4 system. The generation lifetime in this case was found to be 206 μs.

The total duration of the capacitance transient is a function of the initial capacitance and thus the initial potential which appears across the depletion region (see equation 2.93). Specifically the duration of the transient increases as the magnitude of the initial surface potential increases. This implies that the duration of the transient should get longer as the magnitude of the gate voltage step gets larger. This was found to be

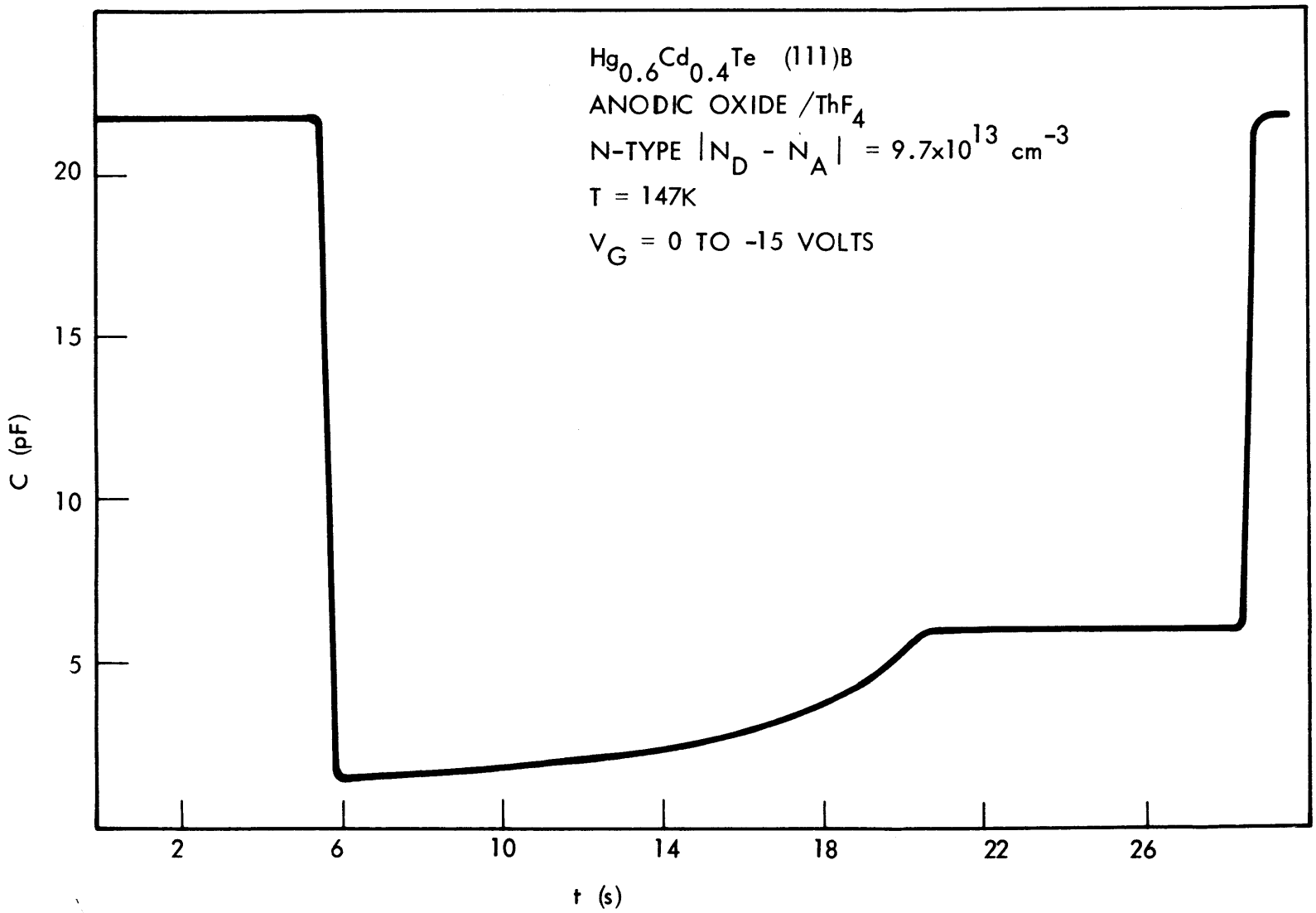

Figure 4.30. TRANSIENT RESPONSE FOR ANODIZED $Hg_{0.6}Cd_{0.4}Te$

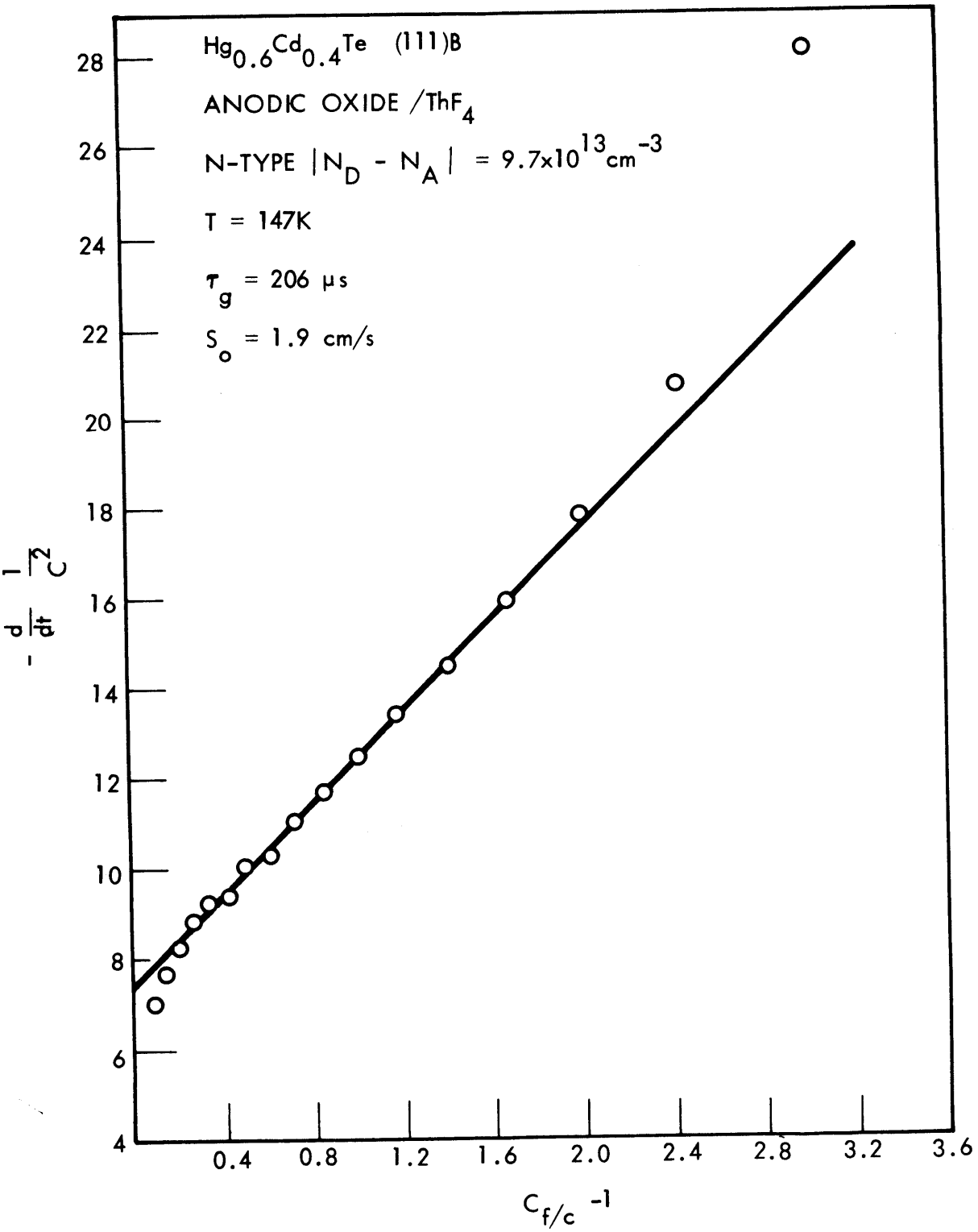

Figure 4.31. ZERBST PLOT FOR TRANSIENT SHOWN IN FIGURE 4.30

the case in most of the samples tested for a certain range of voltage steps. Pictured in Figure 4.32 are capacitance transients for various voltage step sizes obtained from a p-type sample of x = 0.4 (Hg,Cd)Te. The duration of the transient does indeed increase with increasing step sizes. It was noticed, however, that the duration of the transient would no longer increase after a certain voltage step size was reached. In some cases the duration would actually decrease when the step size was increased further. In addition, the initial capacitance would no longer decrease with increasing step sizes. These results indicate that the breakdown voltage of the substrate had been reached.[7] The surface potential at which breakdown occurred could be calculated from the minimum capacitance which was achieved through equation 2.26. The potential at which breakdown occurred was found to vary considerably from slab to slab and even from sample to sample on the same slab. N-type x = 0.4 material with a doping level of about 2×10^{14} cm^{-3} had breakdown voltages of about 10 volts. More heavily doped materials generally had smaller breakdown voltages. For the sample shown in Figure 4-32 (p-type, $|N_A - N_D| = 3.2 \times 10^{15}$ cm^{-3}) the breakdown voltage was 3 volts.

4.4.3 Comparison of Large and Small Signal Measurements

In many cases both large and small signal measurements were performed on the same MIS sample. The large signal generation lifetime, τ_g, and the small signal lifetime, τ_{g-r}, were calculated from the experimental data. A large discrepancy was noted between the values of the two lifetimes.

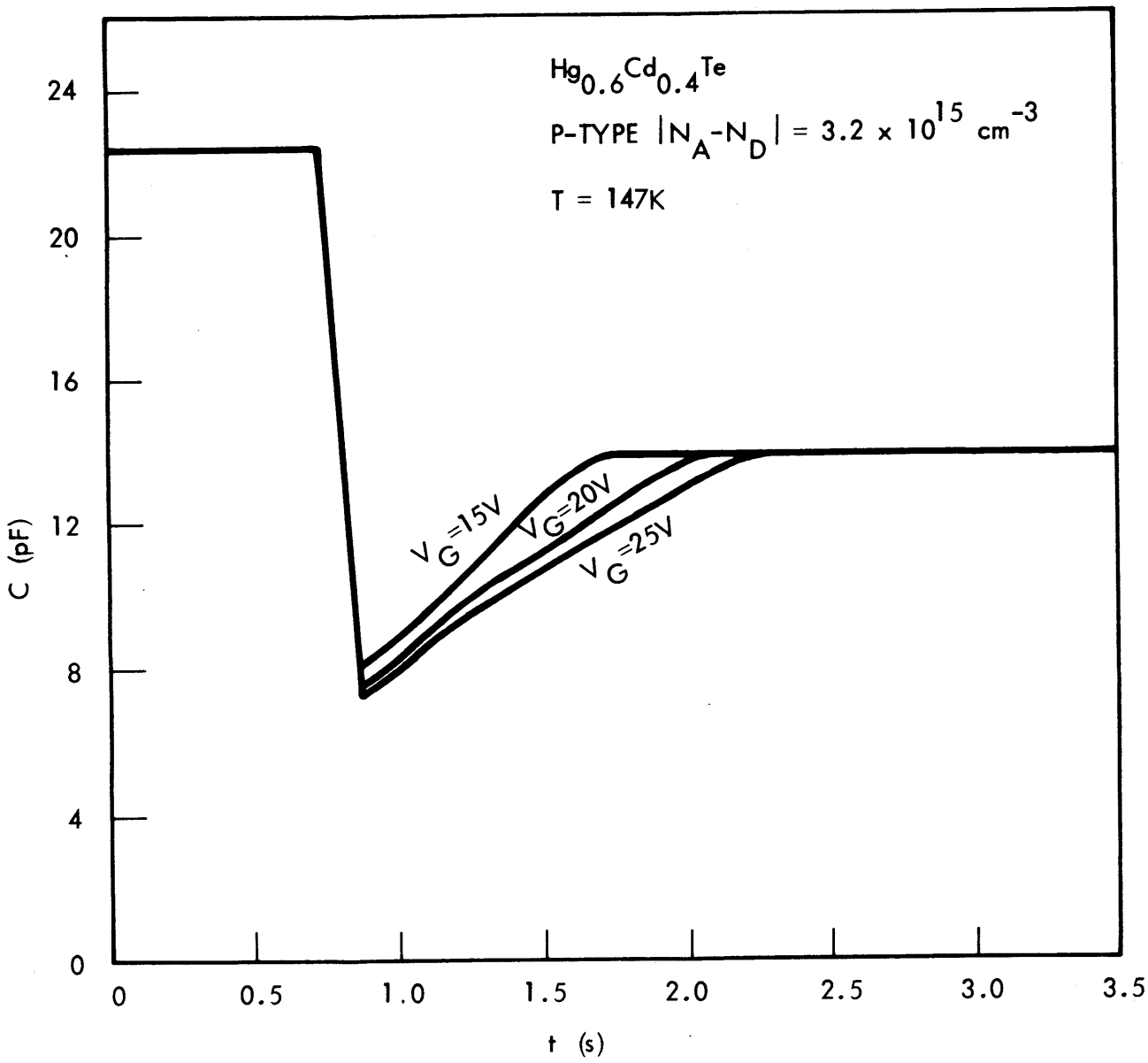

Figure 4.32. TRANSIENT RESPONSE FOR INCREASING VOLTAGE STEP SIZES

The discrepancy was particularly evident when measurements were performed on n-type x = 0.4 $Hg_{1-x}Cd_xTe$ with a net donor concentration of 2×10^{14} cm^{-3}. Structures were fabricated on the (111)B surface of this material. Lifetime measurements on this material have already been described to some extent in the previous two subsections. Many of the structures exhibited large signal generation lifetimes on the order of 100 μsec. Small signal measurements made on the same structures yielded small signal lifetimes which were considerably smaller, about 10 μsec. Thus the small signal measurements resulted in lifetimes which were about a factor of ten smaller than the large signal generation lifetimes.

The agreement between the measurements wasn't as bad for materials with shorter lifetimes. For example. p-type $Hg_{0.6}Cd_{0.4}Te$ with $|N_A - N_D| \approx 1 \times 10^{15} cm^{-3}$ exhibited large signal lifetimes of 2 - 10 μsec. The small signal lifetime was a factor of 2 to 5 times small than this. Similar results were seen on n-type material with comparable lifetimes.

There are several explanations which could in part explain the large discrepancy. One possibility is that the small signal measurement is affected by surface generation-recombination, primarily at the perimeter of the space charge region. Another possibility is that the trapping levels responsible for the generation-recombination reside at an energy different from the intrinsic Fermi energy, or that the capture cross-sections of the traps for holes and electrons are considerably different. It is also quite possible that more than one type of trap is present in the forbidden gap. The effects of multiple trapping levels will not be considered in detail here, due to the complexity of the analysis.

It had been assumed in the derivation of the small signal time constant (Section 2.3.1) that generation-recombination by surface states was negligible due to the screening effect of the inversion layer. There is, however, a portion of the depletion region which extends laterally beyond the edge of the gate electrode in which the surface potential will not be sufficient to invert the surface. It is this region which will contribute most of the surface generation, as will be shown in the following.

Figure 4.33 illustrates the depletion region of an MIS structure for the case of strong inversion. It will be assumed that the depletion region extends laterally to a distance equal to the width of the depletion region, W_m. The actual lateral distance will be somewhat smaller. It will be further assumed that the surface recombination can be characterized by a single level trap located at the intrinsic Fermi energy with equal capture cross-sections for holes and electrons. With this assumption it has been shown[9] that the surface recombination rate U_s is given by:

$$U_s = 2S_o \frac{p_s n_s - n_i^2}{n_s + p_s + 2n_i} \tag{4.2}$$

where $S_o = 1/2\sigma V_{th} N_{st}$ is the surface recombination velocity, σ is the capture cross-section, $V_{th} \equiv \sqrt{3kT/m}$ is the thermal velocity, N_{st} is the density of traps, and n_s and p_s are the concentrations of electrons and holes at the surface, respectively. Under the quasi-equilibrium assumption the product $p_s n_s$ will be given by

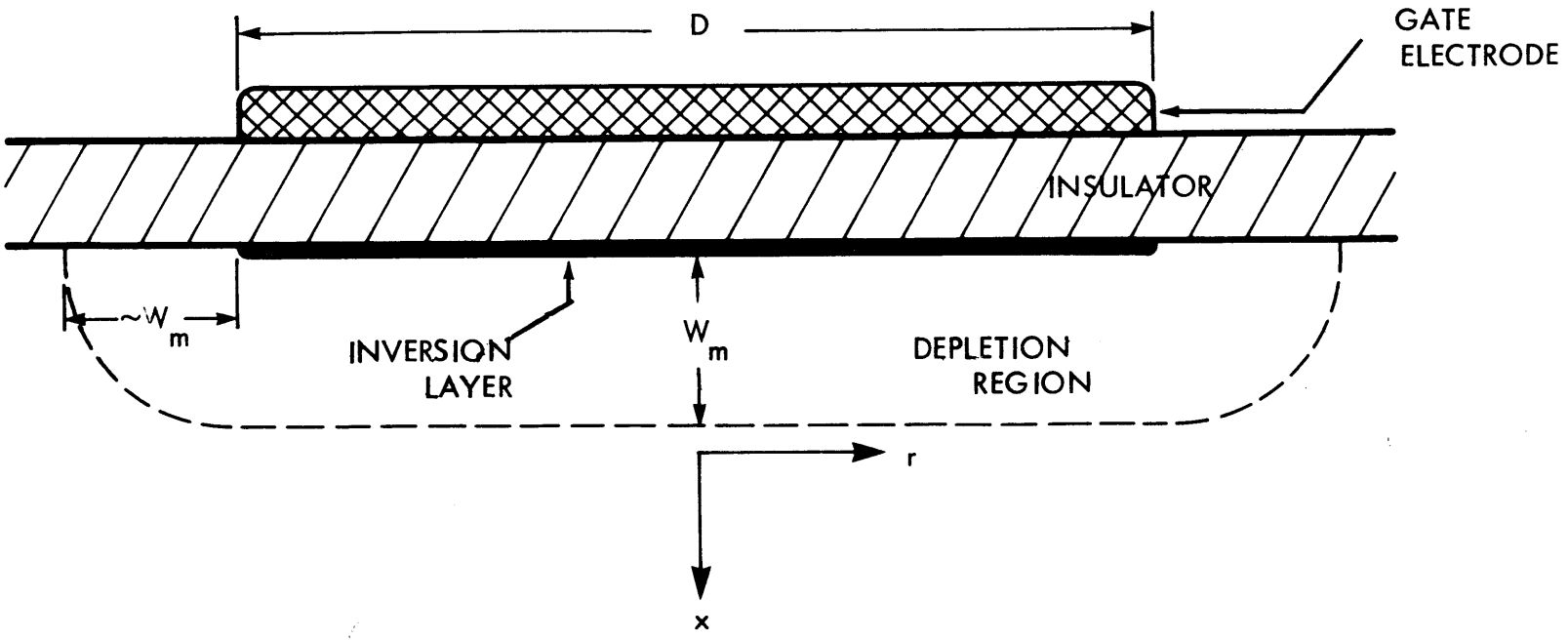

Figure 4.33. SKETCH OF MIS STRUCTURE BIASED INTO STRONG INVERSION, SHOWING LATERAL EXTENSION OF DEPLETION REGION

$$p_s n_s = n_i \, e^{qV_D/kT} \tag{4.3}$$

where V_o is the applied voltage across the depletion region. Substitution into equation 4.2 results in

$$U_s = 2S_o n_i^2 \; \frac{e^{qV_D/kT} - 1}{n_s + p_s + 2n_i} \tag{4.4}$$

for $V_D \ll kT/q$ equation 4.4 becomes

$$U_s = \frac{2S_o n_i^2 qV_D}{kT} \qquad \frac{1}{n_s + p_s + 2n_i} \tag{4.5}$$

The current density flowing to the surface will then be given by

$$J_s = qU_s = \frac{2S_o n_i^2 q \; V_D}{kT} \qquad \frac{1}{n_s + p_s + 2n_i} \tag{4.6}$$

For the portion of the surface under the gate electrode $n_s + p_s \approx |N_A - N_D| = N_B$. In this case the effective resistance R_{SG} due to surface recombination which appears in parallel with the depletion capacitance will be given by

$$R_{SG} = \frac{1}{A_G} \left(\frac{\partial J_{SG}}{\partial V_D} \right)^{-1} = \frac{kT \; N_B}{2S_o q^2 n_i^2 A_G} \tag{4.7}$$

where $A_G = \frac{\pi}{4} D^2$ is the area of the gate. It is difficult to calculate exactly the recombination current due to surface states in the lateral portion of the depletion region since that would require knowing the exact surface concentration of holes and electrons and therefore the exact potential variation. In the following it will be assumed that the surface potential varies linearily from $2\Psi_B$ at the edge of the gate region to zero at a distance W_m from the edge, so that for r >D/2

$$\Psi_s(r) = 2\,\Psi_B \left(1 - \frac{r - D/2}{W_m}\right) \tag{4.8}$$

Substitution of the relations

$$\begin{aligned} n_s &= n_i \exp\left[\left(E_F - E_i\right)/kT\right] \\ P_s &= n_i \exp\left[\left(E_i - E_F\right)/kT\right] \end{aligned} \tag{4.9}$$

and $$\left(E_F - E_i\right)|q = \Psi_s - \Psi_B \tag{4.10}$$

into equation 4.6 yields

$$J_{SP}(r) = \frac{S_o n_i\, q\, V_D}{kT} \quad \frac{1}{\cosh \frac{q\Psi_B}{kT}\left[\left(1 - 2\left(\frac{r - D/2}{W_m}\right)\right)\right] + 1} \tag{4.11}$$

The total current I_{SP} will then be given by:

$$I_{SP} = \int_0^{2\pi} \int_{D/2}^{D/2 + W_m} J_{SP}(r)\, r\, d\theta\, dr \tag{4.12}$$

$$I_{SP} \cong \frac{S_o n_i q\, V_D}{kT}\, \pi D \int_{D/2}^{D/2 + W_m} \frac{dr}{\cosh\left[\frac{q\Psi_B}{kT}\left(1-2\left(\frac{r-D/2}{W_m}\right)\right)\right] + 1}$$

This integral can be solved exactly to yield

$$I_{SP} = \frac{\pi D\, W_m\, S_o n_i q\, V_D}{\Psi_B} \tag{4.13}$$

so that the resistance R_{SP} will be given by

$$R_{SP} = V_D / I_{SP} = \frac{\Psi_B}{\pi D\, W_m\, S_o n_i q} \tag{4.14}$$

The ratio of the resistances R_{SG} and R_{SP} is then

$$R_{SG}/R_{SP} = \frac{2N_B W_m}{n_i D \ln\,(N_B/n_i)} \tag{4.15}$$

where $\Psi_B = kT/q \ ln(N_B/n_i)$ has been used. For most of the MIS structures which were tested, $N_B \approx 2 \times 10^{14}$ cm^{-3}, $D \approx 3.7 \times 10^2$ μm, $n_i \approx 2 \times 10^{10}$ cm^{-3} and $W_m \approx 1.5$ μm so that $R_{SG}/R_{SP} \approx 8.8$. Thus in this case $R_{SG} >> R_{SP}$ and surface generation recombination under the gate can be neglected. The equivalent circuit of the MIS structure in strong inversion including the effects of surface states is shown in Figure 4.34, where

$$R_{g-r} = \frac{2\Psi_B \tau_{g-r}}{q \ n_i W_m A_G} \tag{4.16}$$

The effective resistance R_{eff} is the parallel combination of R_{g-r} and R_{SP}, so that

$$R_{eff}^{-1} = \left(\frac{2\Psi_B \tau_{g-r}}{q n_i W_m A_G}\right)^{-1} + \left(\frac{\psi_B}{\pi D \ W_m S_o n_i q}\right)^{-1} \tag{4.17}$$

or

$$R_{eff} = \frac{2\Psi_B \tau'_{g-r}}{q n_i W_m A_G} \tag{4.18}$$

where

$$\frac{1}{\tau'_{g-r}} = \frac{1}{\tau_{g-r}} + \frac{8S_o}{D} \tag{4.19}$$

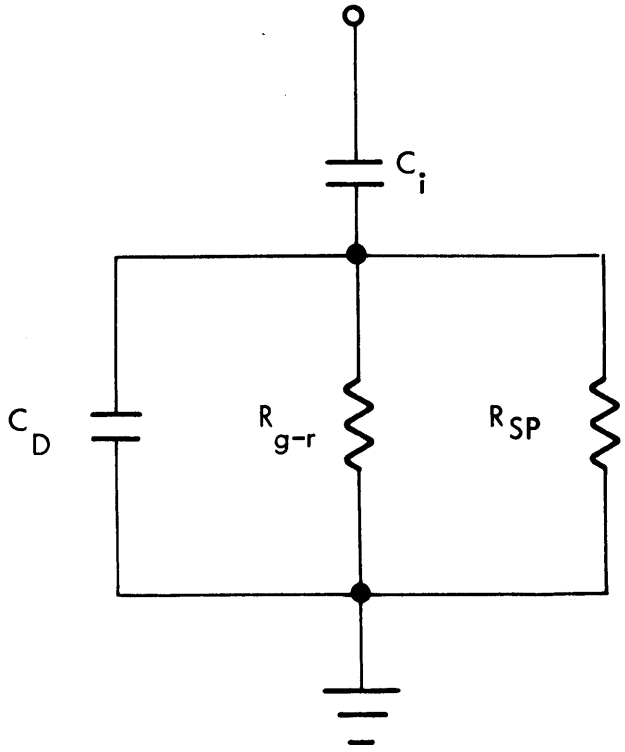

Figure 4.34. CIRCUIT MODEL VALID IN STRONG INVERSION INCLUDING EFFECTS OF SURFACE RECOMBINATION

An equation similar to 4.19 was encountered in the analysis of the large signal capacitance transient technique (see Section 2.32, equation 2.85). Comparison of equations 2.85 and 4.19 reveals that surface generation recombination affects both measurements equivalently. It is possible, however, that the quantity S_o could differ considerably in the measurements since one is an equilibrium measurement while the other is done under strongly non-equilibrium conditions. It is unlikely though that surface effects could account for the factor of ten difference between the large and small signal lifetimes. The large discrepancy persisted even when the surface generation component was very low. For example, anodic films were found to have low surface state densities. Large signal transient measurements on structures using anodic films, such as that shown in Figure 4.31, resulted in a surface generation velocity of only 2 cm/sec, however, the large signal lifetime τ_g was about 200 μsec, while the small signal lifetime was only 20.3 μsec.

The effects of recombination centers whose energy is different from the intrinsic Fermi energy and whose capture cross-sections for holes and electrons are different will be considered next. It was stated that according to the theory of single level recombination centers the generation lifetime τ_g and the small signal lifetime τ_{g-r} are not in general equal. The ratio of τ_g to τ_{g-r} is defined by equation 2.91. The functions b and g (b, τ_{po}, τ_{no}) are both functions of the capture cross-sections for holes (σ_p) and electrons (σ_n) and the energy level of the trap (E_t) as can be seen by examining equations 2.46, 2.47, 2.56, and 2.61. For $\sigma_p = \sigma_n$ (or, equivalently, $\tau_{po} = \tau_{no}$) the ratio τ_g/τ_{g-r} will

increase as the magnitude of E_t-E_i increases from zero. The ratio was calculated for both n and p-type $Hg_{0.6}Cd_{0.4}Te$ with $|N_D-N_A| = 2 \times 10^{14} cm^{-3}$ and T=147K as a function of $(E_t-E_i)/kT$ with τ_{po}/τ_{no} as a parameter. The resulting plots for p-type and n-type are shown in Figures 4.35 and 4.36, respectively. It can be seen that for cases such that τ_{po}/τ_{no} or $E_t \neq E_i$ the ratio τ_g/τ_{g-r} can be considerably greater than one. The ratio appears to approach a limiting value of about nine. For high ratios the trap is an ineffective recombination center. The ratios of $\tau_g/\sqrt{\tau_{po}\tau_{no}}$ and $\tau_{g-r}/\sqrt{\tau_{po}\tau_{no}}$ for n-type $Hg_{0.6}Cd_{0.4}Te$ are plotted in Figures 4.37 and 4.38 respectively as a function of $(E_t-E_i)/kT$ with τ_{po}/τ_{no} as a parameter. As expected the trap is most effective (the ratio is smallest) for $(E_t-E_i)/kT + \ln(\sqrt{\tau_{po}/\tau_{no}}) = 0$. The ratio increases very rapidly when the magnitude of this quantity increases from zero.

Thus it has shown that traps with $E_t \neq E_i$ or $\tau_{po} \neq \tau_{no}$ can cause the generation lifetime τ_g to be considerably larger than the small signal lifetime τ_{g-r}. Ratios near ten are, however, unlikely since in that case the traps would be very ineffective generation-recombination centers. It is expected that multiple trap levels could also lead to a large difference between τ_g and τ_{g-r}. Not enough is known, however, about recombination centers in (Hg,Cd)Te to warrant analysis of more complicated situations than single level traps.

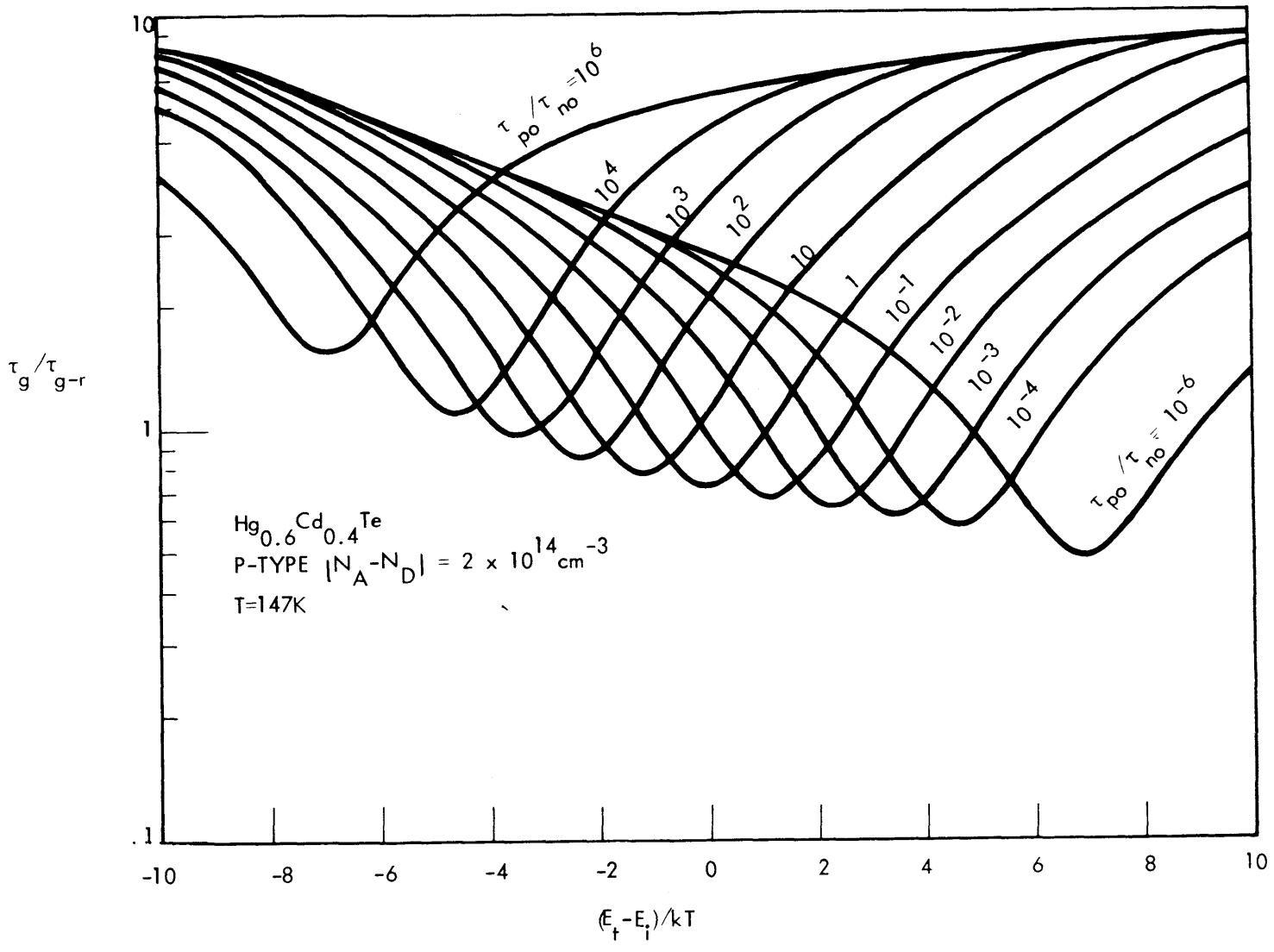

Figure 4-35. τ_g/τ_{g-r} VERSUS $(E_t-E_i)/kT$ WITH τ_{po}/τ_{no} AS A PARAMETER FOR P-TYPE (Hg,Cd)Te

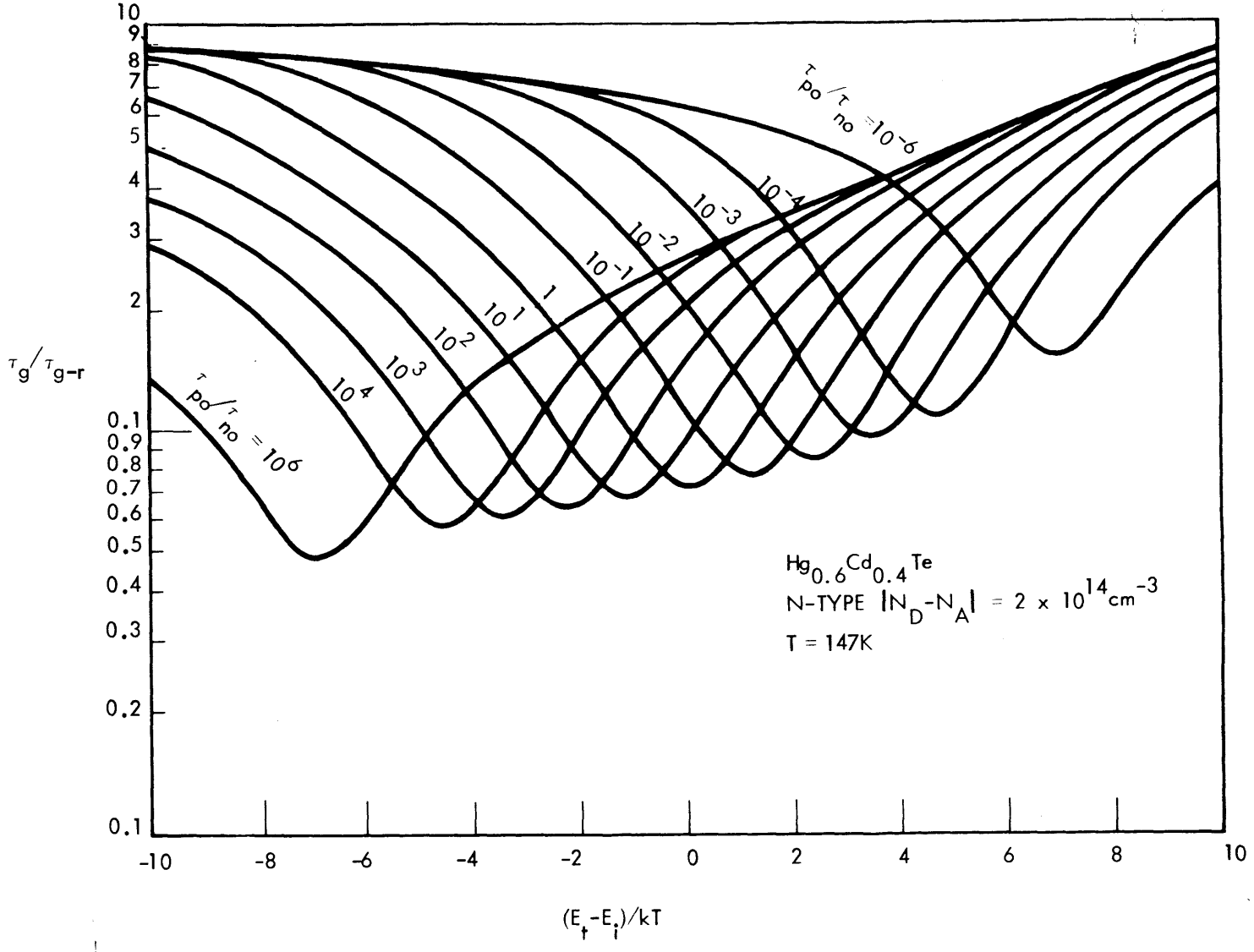

Figure 4-36. τ_g/τ_{g-r} VERSUS $(E_t-E_i)/kT$ WITH τ_{po}/τ_{no} AS A PARAMETER FOR N-TYPE (Hg,Cd)Te

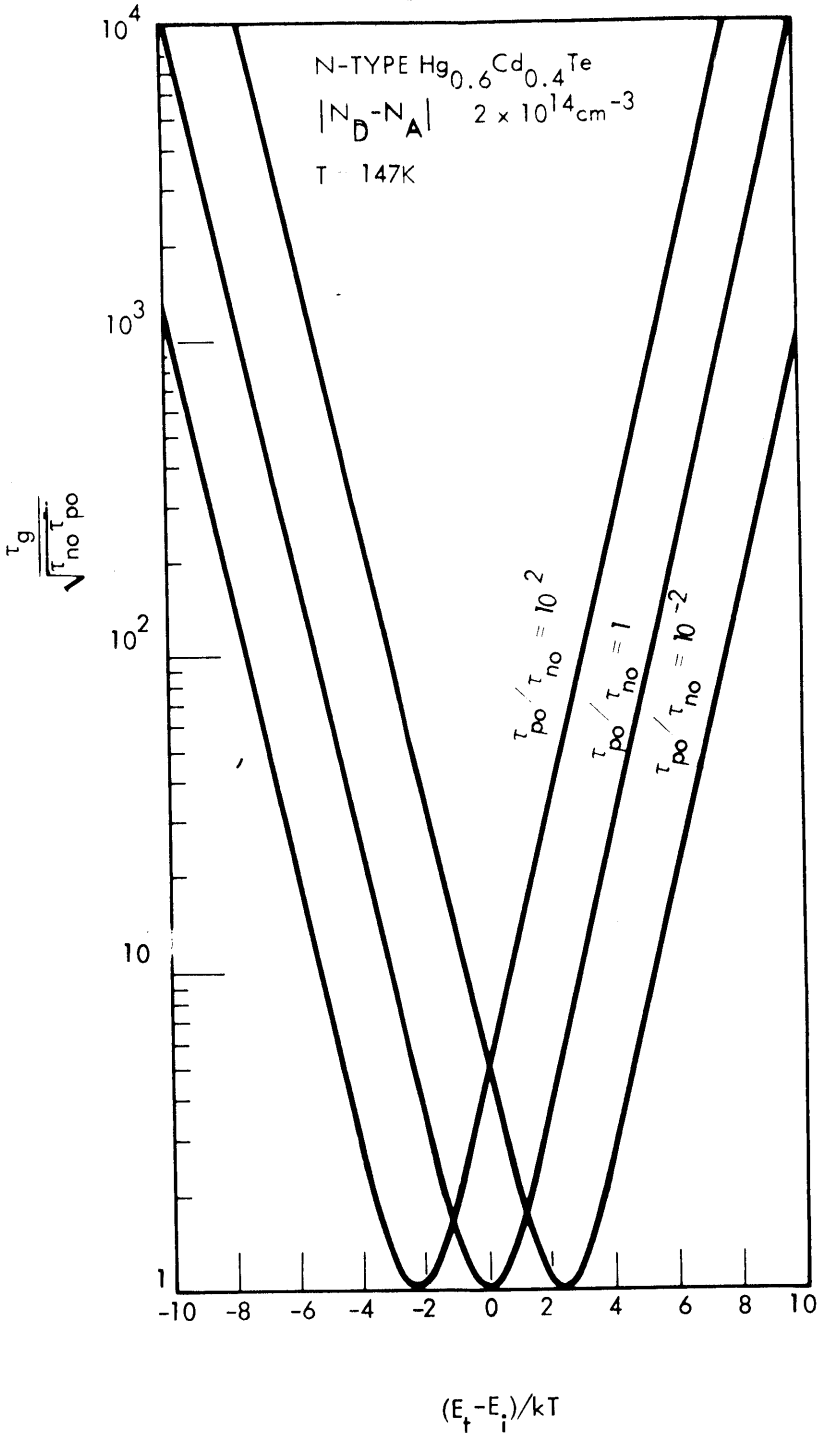

Figure 4-37. $\tau_g/\sqrt{\tau_{po}\tau_{no}}$ VERSUS $(E_t-E_i)/kT$ FOR N-TYPE (Hg,Cd)Te

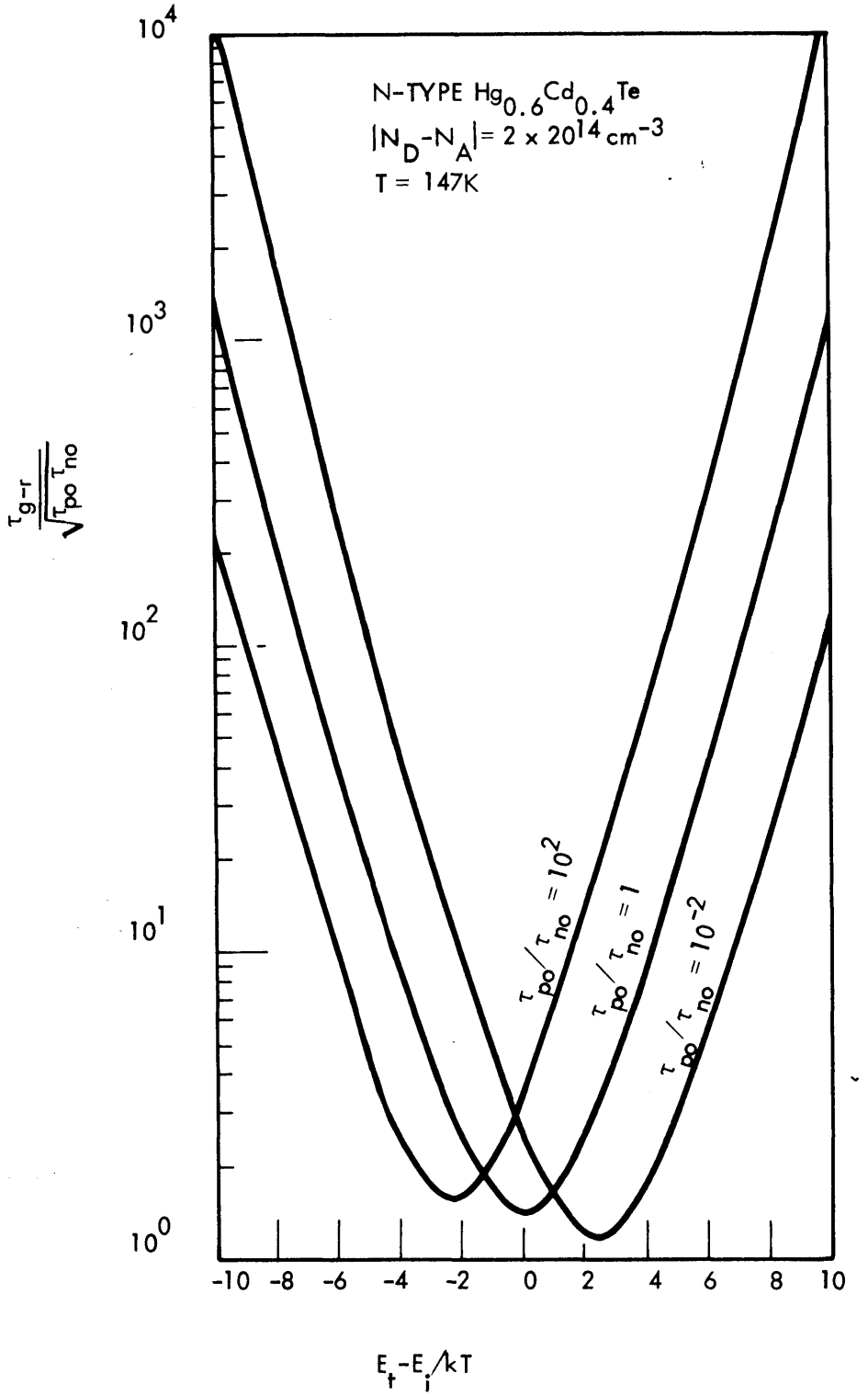

Figure 4-38. $\tau_{g-r}/\sqrt{\tau_{po}\tau_{no}}$ VERSUS $(E_t-E_i)/kT$ FOR N-TYPE (Hg,Cd)Te

4.4.4 Temperature Dependence

The temperature dependence of the large and small signal parameters for x=0.4 (Hg,Cd)Te was determined. These measurements were done in order to gain information about the mechanisms responsible for the generation and recombination of minority carriers in (Hg,Cd)Te. The material used for this experiment was n-type $Hg_{0.6}Cd_{0.4}Te$ with $|N_D-N_A| \approx 2 \times 10^{14} cm^{-3}$. The MIS structures were fabricated on the (111)B surface of this material. The surfaces were etched in 1:5 bromine/methanol and ThF_4 was used as the insulator. Three samples were chosen for this study. The slab of material was mounted onto a copper pedestal in a stainless steel dewar. The temperature of the pedestal, which was cooled with liquid nitrogen, was varied by changing the voltage which was applied to a heater attached to the pedestal. The temperature was monitored with a calibrated silicon temperature sensor that was also attached to the pedestal. The range of temperatures used in this experiment was 110K to 215K.

4.4.4.1 Small Signal Measurements

The small signal time constant τ_{ss} was measured as a function of temperature. For low temperatures (i.e., less than 140K-150K) the time constant was long so that the small signal capacitance transient method was used. At higher temperatures the variable frequency conductance method was used.

As stated in previous sections the small signal time constant τ_{ss} is a function of generation-recombination in the depletion region, generation-recombination by surface states, and diffusion from the bulk. The effects of these processes can be modeled by a resistance which appears in parallel with the depletion capacitance C_D. The resistance is the parallel combination of the resistance due to generation-recombination in the depletion region, R_{g-r}, the resistance due to diffusion from the bulk, R_D, and the resistance due to generation-recombination by surface states, R_{SP}. The total resistance, which is the experimentally measured quantity, will be defined here as R_o. R_o is related to the time constant by equation 2.38, i.e.,

$$R_o = \tau_{ss}/(C_i + C_D) \tag{4.20}$$

Equations 2.59 and 4.14 show that the resistances R_{g-r} and R_{SP} are inversely proportional to the intrinsic carrier concentration, n_i. The quantity n_i varies rapidly with temperature, approximately as $\exp(-E_g/2kT)$.

It is therefore expected that the temperature dependence of the quantities R_{g-r} and R_{SP} would be dominated by the temperature dependence of n_i, assuming that the other parameters vary much more slowly. The resistance R_D, defined by equation 2.65, is inversely proportional to n_i^2. R_D should thus vary with temperature approximately as exp (E_g/kT). It is expected that generation-recombination (g-r) processes will dominate at low temperatures, so that $R_D >> R_{g-r}$ and $R_D >> R_{SP}$. The temperature dependence of the quantity R_o should then be approximately the same as n_i^{-1}, or exp $(E_g/2kT)$. At high temperatures diffusion processes will eventually dominate, so that the temperature dependence of R_o will be the same as n_i^{-2}, or exp (E_g/kT).

The resistance R_o was calculated from the experimentally determined values of τ_{ss}, C_i, and C_f using the relation

$$R_o = \tau_{ss} \frac{C_i - C_f}{C_i^2} \tag{4.21}$$

which can easily be derived from equation 4.20 using the relation $C_D = C_i C_f / C_i - C_f$. A plot of R_o versus 1/T for three samples is shown in Figure 4.39. Also indicated on this graph are the temperature dependences of $1/n_i$ and $1/n_i^2$. It can be seen that the temperature dependence of sample one for temperatures less than 155K is essentially the same as $1/n_i$.

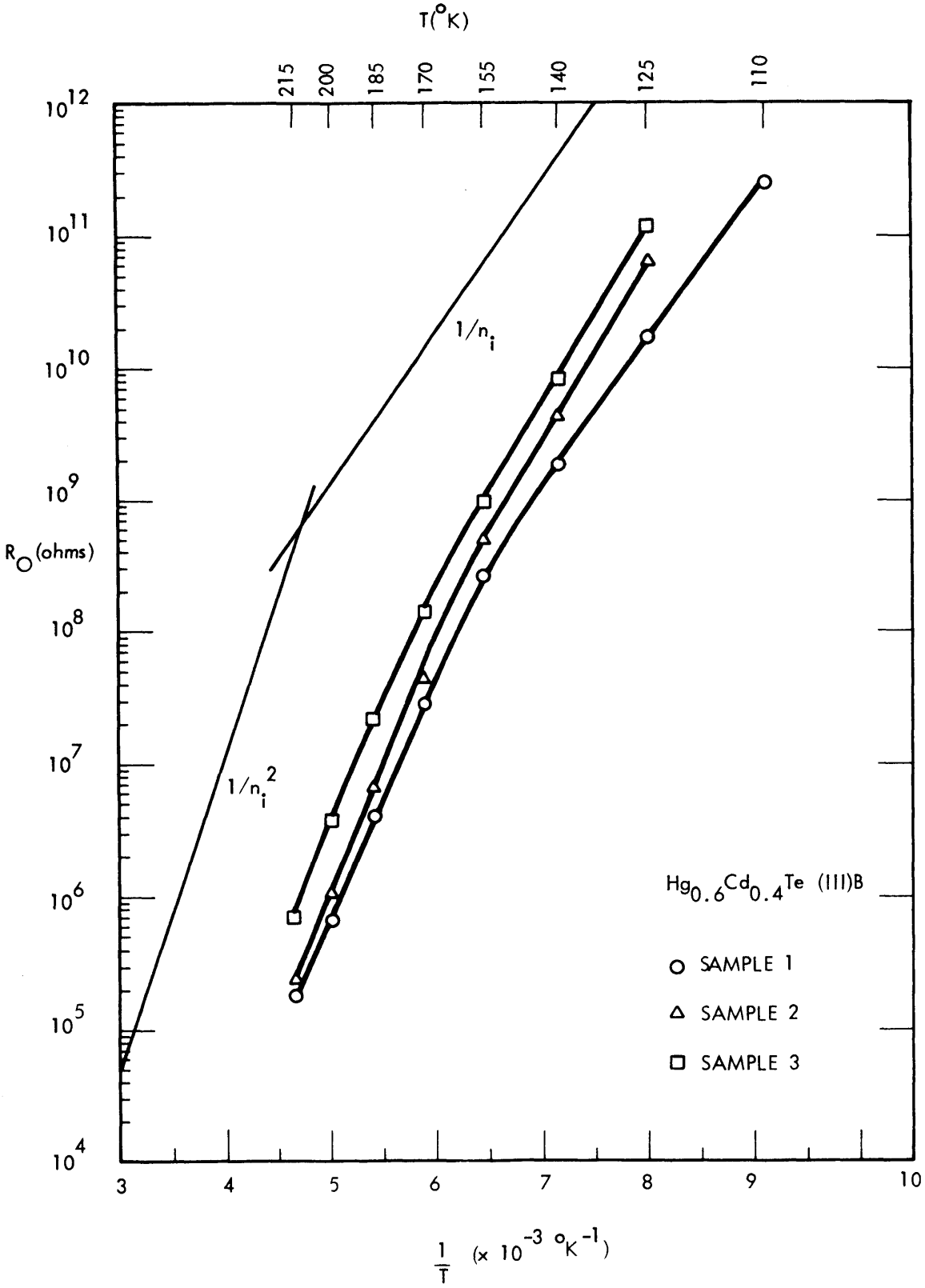

Figure 4.39. MEASURED R_o VERSUS 1/T FOR $Hg_{0.6}Cd_{0.4}Te$

Samples two and three, however, show a considerably steeper slope than $1/n_i$ in that temperature range. At temperatures above 155K the temperature dependence approaches that of $1/n_i^2$ for all three samples.

The effective small signal lifetime τ_{g-r} was calculated from the low temperature data using equation 4.16 with the assumptions that diffusion from the bulk and generation by surface states were negligible. For sample one the calculated lifetime was approximately constant for temperatures up to 155K at 1.8 microseconds. Samples two and three, however, showed lifetimes which decreased with increasing temperature, as would be expected since the dependence of R_o was faster than $1/n_i$. Shown in Figure 4.40 on a semi-log graph are the calculated values of τ_{g-r} versus 1/T for samples two and three for temperatures of 125K, 140K, and 155K. It can be seen that the dependence is linear in this temperature range. It was thought that this sort of dependence might be caused by a recombination center whose energy was different from the intrinsic Fermi energy. In order to examine this possibility it was necessary to determine the temperature dependence of the quantity $g(b, \tau_{po}, \tau_{no})$ defined by equation 2.61. It was assumed that the values of τ_{po} and τ_{no} were independent of temperature. The expression defining $g(b, \tau_{po}, \tau_{no})$ was solved numerically with a computer and the inverse of $g(b, \tau_{po}, \tau_{no})$ then plotted on semilog graph paper as a function of 1/T. The calculated temperature dependence with $(E_t - E_i)/k = 4.8 \times 10^2$ °K for various values of τ_{po}/τ_{no} is shown in Figure 4.41. For the temperature range of interest (125K to 155K) the calculated dependence is approximately linear. The slope $\Delta \ell n(1/g)/\Delta(1/T)$ is somewhat less than $(E_t - E_i)/k$ and decreases as the quantity τ_{po}/τ_{no}

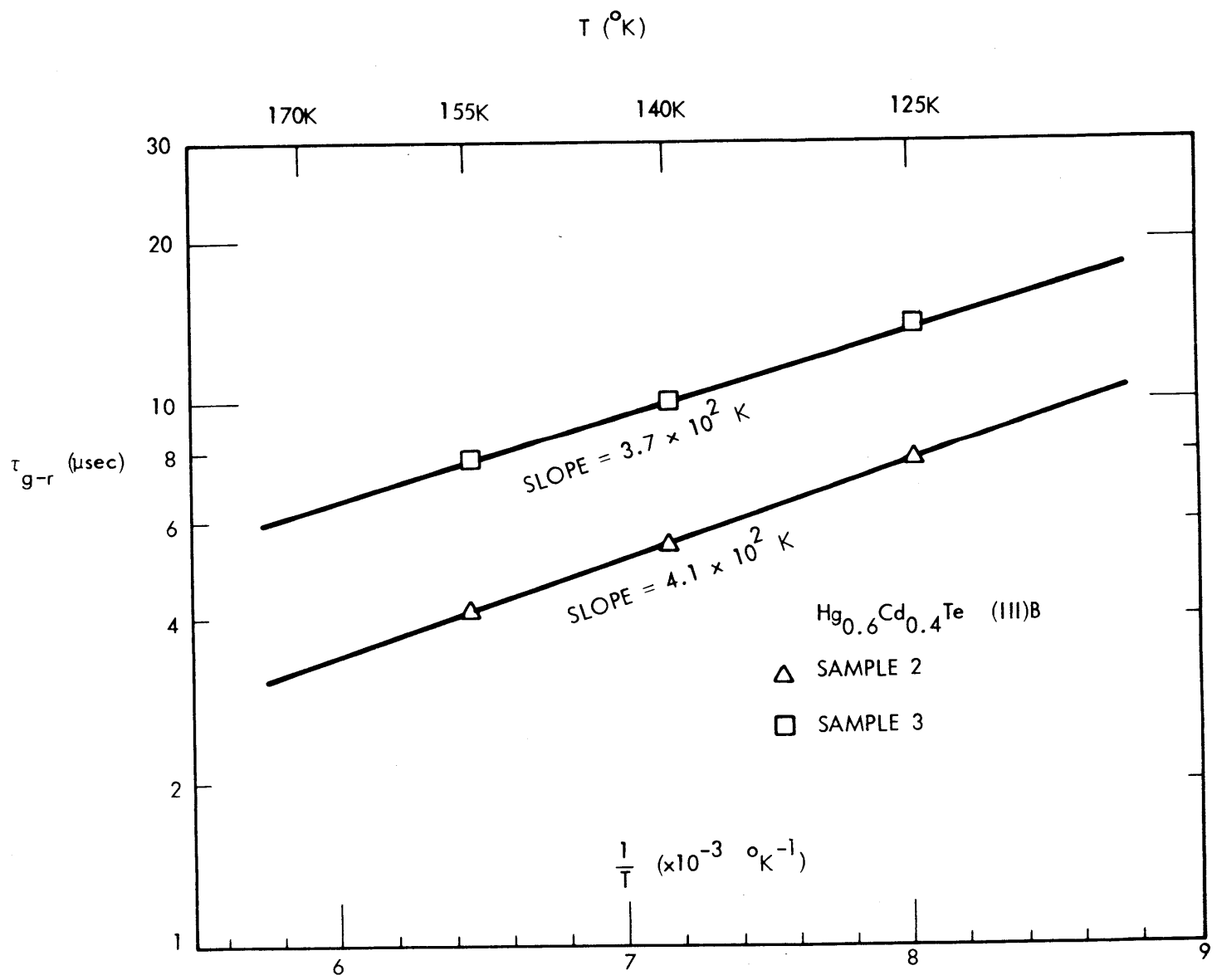

Figure 4.40. τ_{g-r} VERSUS 1/T FOR SAMPLES TWO AND THREE

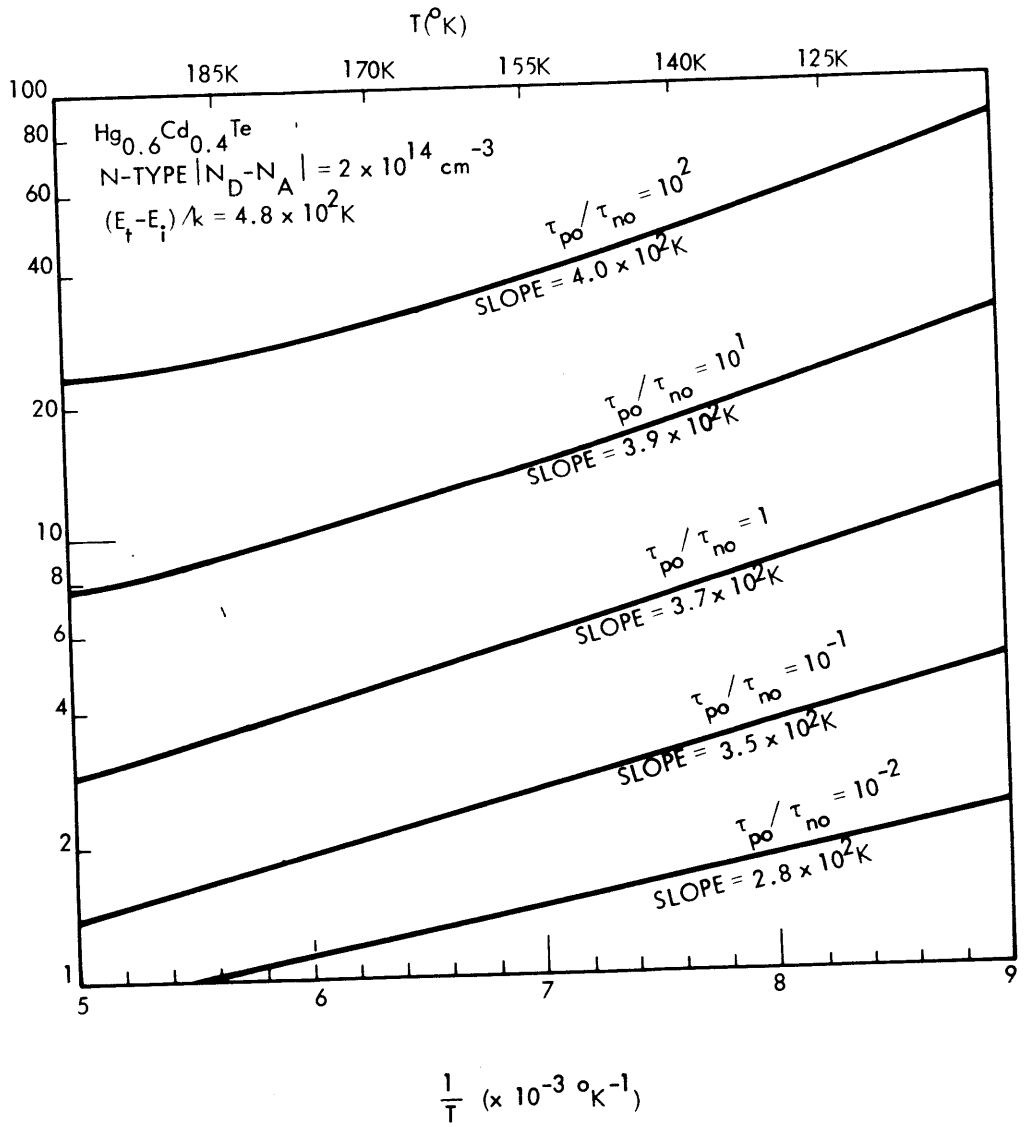

Figure 4.41. CALCULATED TEMPERATURE DEPENDENCE OF $\tau_{g-r}/\sqrt{\tau_{po}\tau_{no}}$ FOR $(E_t - E_i)/k = 4.8 \times 10^2 K$

decreases. It is possible then to explain the experimental result by assuming that $(E_t - E_i)/k \neq 0$. It is not possible, however, to determine the magnitude or sign of $(E_t - E_i)/k$ from the data since the quantity τ_{po}/τ_{no} is not known.

For temperatures greater than 155K diffusion from the bulk becomes important as indicated by the steeper slope of the temperature dependence of R_o. In this case it is necessary to use a combination of equations 2.59 and 2.65 to determine the effective bulk lifetime τ_B. The bulk mobility μ_h for holes was estimated from Hall mobility data on p-type $Hg_{0.6}Cd_{0.4}Te$. The value used here was 200 cm^2/volt sec and it was assumed to be independent of temperature. The depletion lifetime τ_{g-r} was assumed to have the same temperature dependence at high temperatures as it did at lower temperatures. For sample one τ_{g-r} was assumed to be constant at 1.8 μsec. The calculated bulk lifetime was found to increase with increasing temperature from 0.2 μsec at 170K to 1.7 μsec at 215K. A similar result was seen for sample two which the bulk lifetime increased from 1.4 μsec at 170K to 9.5 μsec at 215K. The bulk lifetime for sample three on the other hand, was found to decrease from 98 μsec at 185K to 65 μsec at 215K.

The temperature dependence of the bulk lifetime depends on the mechanism responsible for generation-recombination in the bulk. The theoretical Auger lifetime τ_A was calculated for n-type x = 0.4 (Hg, Cd)Te with $|N_D - N_A| = 2 \times 10^{14} cm^{-3}$ using equation 2.72 and calculations of τ_{Ai} carried out by Kinch et al.[19] The Auger lifetime was found to be on the order of milliseconds and could thus be neglected. The theoretical

radiative lifetime τ_R was determined for this material according to equation 2.70 and calculations of G_r also carried out by Kinch. The radiative lifetime was found to increase from 57 μsec to 80.1 μsec for sample one, from 87 μsec to 122 μsec for sample two, and from 76.3 μsec to 108 μsec for sample three as the temperature increased from 170K to 215K. The measured values are much less than the radiative lifetime for samples one and two, but the measured value for sample three is on the same order as the calculated radiative lifetime. It is possible then that the radiative mechanism could be important for sample three. It is likely that generation-recombination via recombination centers in the bulk is the limiting mechanism for samples one and two. The temperature dependence of the Shockley-Read (S-R) lifetime, as defined by equation 2.66, depends on the location of the trap level with respect to the intrinsic Fermi level and the magnitudes of τ_{po} and τ_{no}, as can be seen by examining equations 2.49 and 2.66. If $(E_t - E_i)/kT \neq 0$, the S-R lifetime will increase with temperature from τ_{po} for n-type and τ_{no} for p-type. For a more detailed treatment of the temperature dependence, see the original paper (Ref. 16) or Blakemore (Ref. 18).

Analysis of the experimental dependence of τ_B will not be presented here, primarily because of the large possible error involved in the calculation of τ_B. Examination of equation 2.65 shows that the diffusion resistance R_D depends on the square root of the lifetime, τ_B, and on n_i^2. A calculation of τ_B will depend on R_D^2 and n_i^4, so that any error in R_D or n_i will result in very large errors in the calculated lifetime. A considerable error is possible for R_D since in calculating R_D it is necessary

to subtract the depletion resistance R_{g-r} from the measured resistance R_D, except at the highest temperatures. The exact value of R_{g-r} is not known for temperatures above 155K. The accuracy of the expression defining the temperature dependence of n_i (equation 2.24) has not been sufficiently verified experimentally to allow confidence in any calculation which depends on n_i^4. These possible errors are not expected to be a great problem in the calculation of τ_{g-r}, since τ_{g-r} depends directly on R_{g-r} and n_i.

4.4.4.2 Large Signal Measurements

The large signal capacitance transient was recorded as a function of temperature for the three samples. The total duration of the transient, or storage time, T_s, was determined at each temperature. For low temperatures Zerbst plots were constructed from the data to determine the generation lifetime τ_g and the surface generation velocity S_o.

The generation lifetime τ_g was determined from the slope of the linear portion of the Zerbst plot and the initial surface generation velocity S_o. Element one had a lifetime of 8.1 μsec and a surface velocity of 39 cm/sec at 140K. This was a factor of 4.5 greater than the small signal lifetime (1.8 μsec). Elements 2 and 3 had lifetimes of 49.3 μsec and 170 μsec and surface generation velocities of 10.4 and 20 cm/sec, respectively, at 140K. These generation lifetimes were factors of 9.1 and 17 greater than the small signal lifetimes for elements 2 and 3, respectively.

The temperature dependence of τ_g could not easily be determined with the Zerbst plot analysis. Since the duration of the transient became shorter with increasing temperature, it was necessary to record the transient on film from a memory oscilloscope. The error involved with determining the slope dC/dt from the picture was considerable. In addition, determination of the quantity $d/dt(C_i/C)^2 = -2dC/dt\ C_i^2/C^3$ involved the quantity C^3, so that any error in C, such as might result from errors in the determination of the stray capacitance, would result a large error in the magnitude of $d/dt\ (C_i/C)^2$. It was therefore decided that Zerbst analysis at all temperatures would be too time consuming and not accurate enough to be worthwhile.

A quantity that could be easily and accurately determined was the duration of the transient, or storage time T_s. Shown in Figure 4.42 are the temperature dependencies of T_s for samples 1, 2, and 3. As was the case for the small signal measurement, the dependence of sample 1 follows that of $1/n_i$ reasonably closely for temperatures from 110K to 140K. The dependence of samples 2 and 3 again is faster than $1/n_i$ over most of the temperature range. Since the depletion region width is large for most of the transient it is expected that generation in the depletion region would be the dominant process over most of the temperature range, so that the temperature dependence should follow that of $1/n_i$ for most temperatures. Equation 2.94 approximately defines the storage time in terms of τ_g, τ_B, and S. It is assumed that the effective τ_g and S are constant over the duration of the transient, an assumption which is probably not entirely accurate. The low temperature value of τ_g, as determined from analysis of

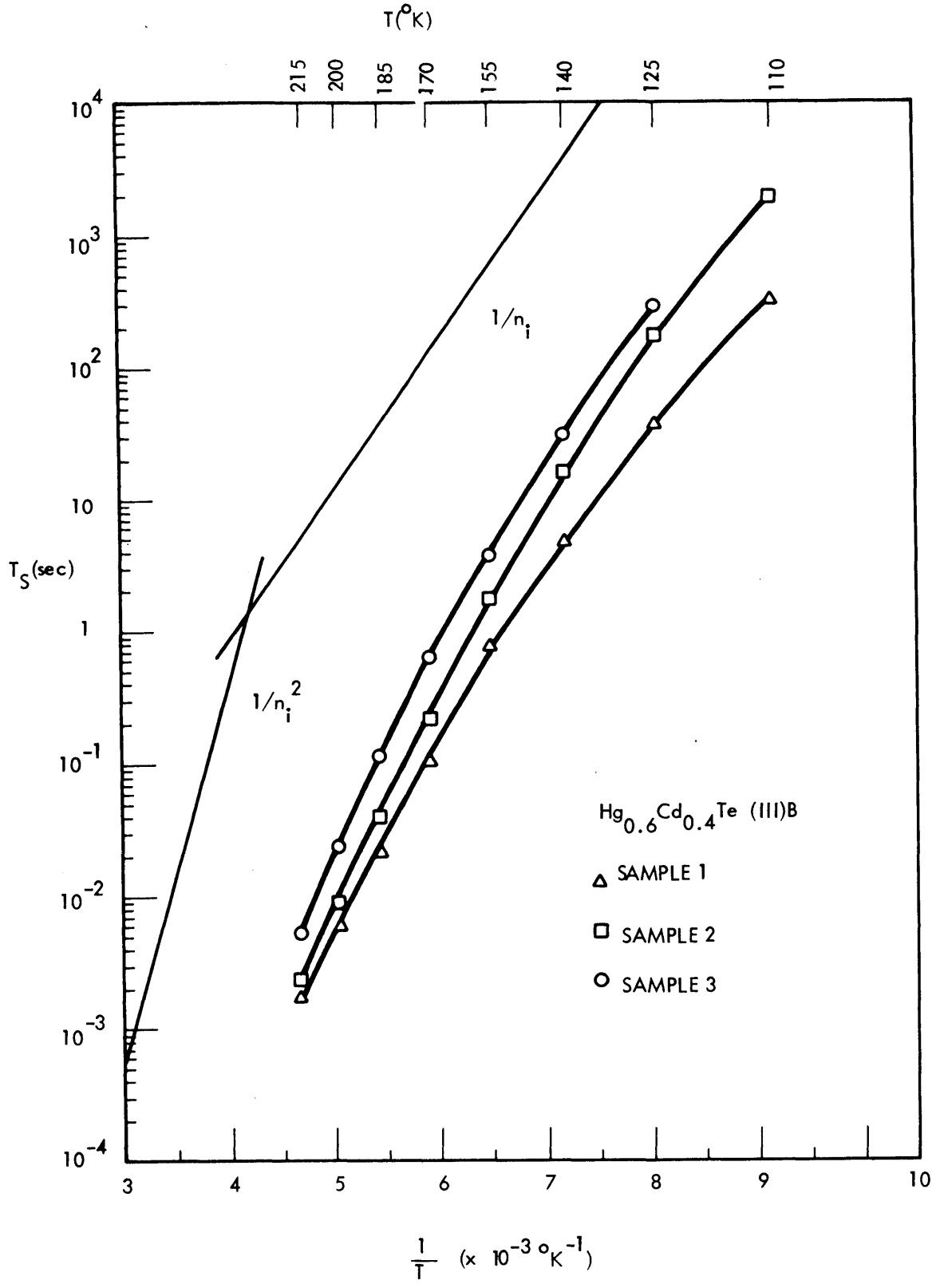

Figure 4.42. STORAGE TIME VERSUS 1/T FOR 3 SAMPLES

the Zerbst plot, was substituted into Equation 2.94. The effective surface generation velocity S was then varied until agreement with the experimentally determined value of T_s was achieved. The effective S which resulted in agreement with the data was found to be 1-2 cm/sec for all three samples. The temperature dependence of T_s for higher temperatures was then determined from Equation 2.94 with the following assumptions: the generation lifetime τ_g was constant with temperature; the effective surface generation velocity S was constant with temperature; and the bulk lifetime was equal to the high temperature bulk lifetime as determined with small signal measurements. The resulting calculations for sample 3, which had τ_g = 170 μsec, S = 1.8 μsec, and τ_B = 75 μsec, and for sample 2, which had τ_g = 49.3 μsec, S = 1.4 μsec and τ_B = 9.5 μsec, are plotted in Figures 4.43 and 4.44, respectively. It can be seen that the measured storage times are considerably lower than the calculated storage times in the temperature range 140K to 200K. This result could be explained by assuming that τ_g is a function of temperature. The parameter τ_g was varied at each temperature above 140K until the calculated storage time agreed with the measured value. The resulting plots of τ_g versus 1/T for samples 2 and 3 are shown in Figure 4.45. It can be seen that the temperature dependence of $\ln(\tau_g)$ is approximately linear with 1/T. The slopes are 7 x 10^2K and 7.3 x 10^2K for samples 2 and 3, respectively.

This can be explained in the following way. According to equation 2.88 the generation lifetime is equal to

$$\tau_g = \sqrt{\tau_{po}\tau_{no}} \cosh\left[\left(E_t - E_i\right)/kT + \ln\sqrt{\tau_{po}/\tau_{no}}\right] \qquad (4.22)$$

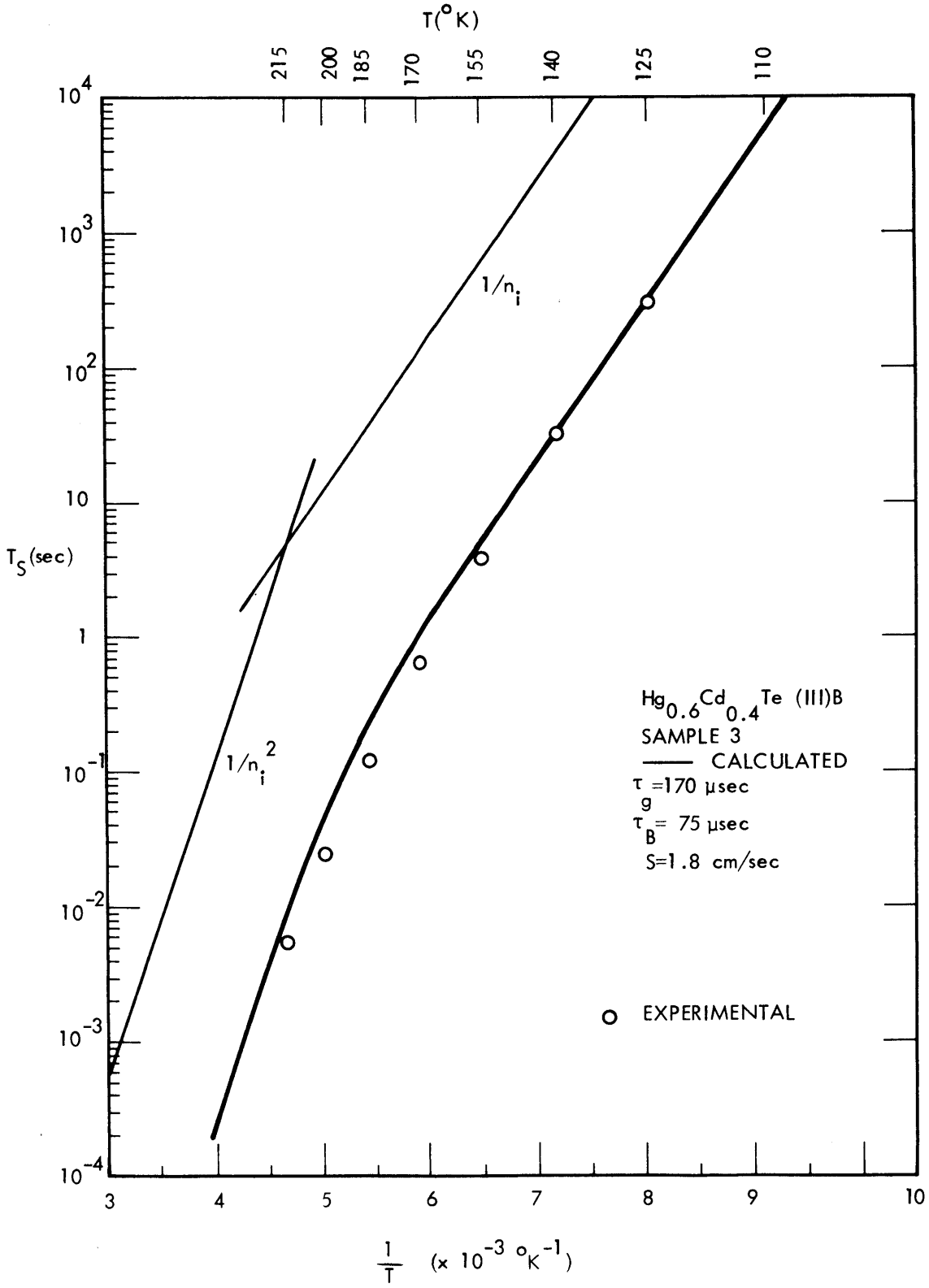

Figure 4.43. CALCULATED AND EXPERIMENTAL T_s VERSUS 1/T FOR SAMPLE 2

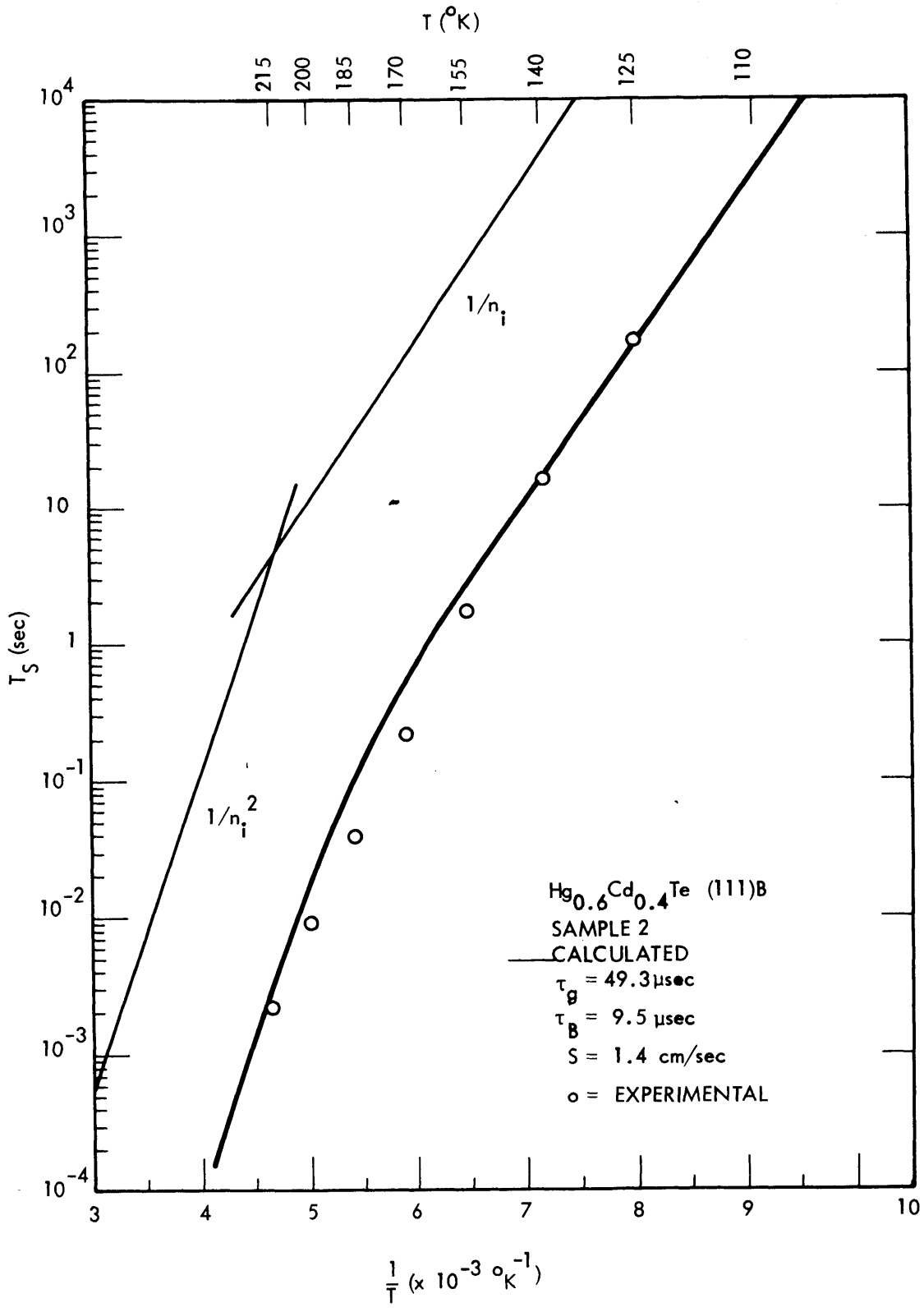

Figure 4.44. CALCULATED AND EXPERIMENTAL T_s VERSUS 1/T FOR SAMPLE 2.

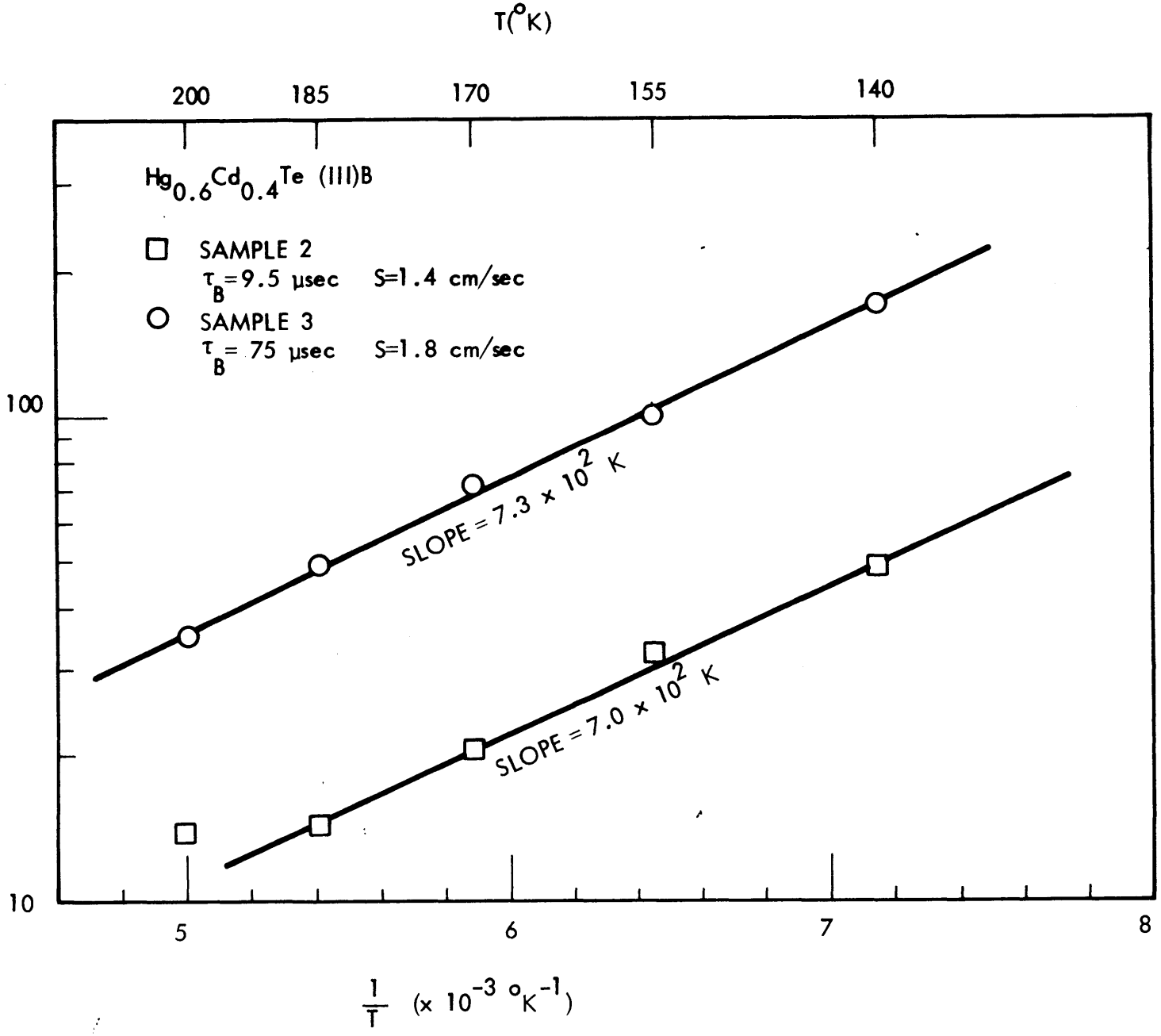

FIGURE 4.45. τ_g VERSUS 1/T FOR SAMPLES 2 AND 3

For large values of the magnitude of the argument of the cosh function equation 4.22 reduces to

$$\tau_g = \tau_{po} \exp\left[\left(E_t - E_i\right)/kT\right] \tag{4.23}$$

for positive arguments, and

$$\tau_g = \tau_{no} \exp\left[\left(E_i - E_t\right)\right]/kT \tag{4.24}$$

for negative arguments. Thus for trap levels different from the intrinsic Fermi energy the generation lifetime τ_g will decrease with increasing temperature, and the slope of $\ln(\tau_g)$ versus $1/T$ will be equal to $\left|\left(E_t - E_i\right)/k\right|$. The experimental data implies that $\left|\left(E_t - E_i\right)/k\right| \approx 7 \times 10^2 K$, or $\left|E_t - E_i\right| = 0.06$ eV.

In conclusion, the experimental lifetime data indicates that the Shockley-Read recombination mechanism is responsible for the observed lifetimes in most cases. It was, however, necessary in some cases to assume that the energy of the trap level was different from the intrinsic Fermi level in order to fit the model to the experimental data. It is possible as well that more than one trap was present, although this possibility was not examined.

4.5 DIFFUSION OF IMPURITIES

Since the MIS capacitance-voltage characteristics are a function of the net doping at the surface of a semiconductor, it was felt that the MIS technique could be used to study the diffusion of impurities into (Hg,Cd)Te. In addition to the doping of the (Hg,Cd)Te, the effect of the impurity on such parameters as the minority carrier lifetime, surface state density, and surface potential could be studied. By angle lapping the surface of the (Hg,Cd)Te after a diffusion the depth of the diffusion could also be determined. The procedure for determining the depth of diffusion was as follows. First the diffusion of the impurity was carried out at a specific temperature. Then the slab was angle lapped using a fine abrasive, and subsequently etched in 10:1 methanol/bromine to remove most of the surface damage resulting from the lap. Approximately one micrometer of material was removed with this etch. The angle of the lap was determined with either a microscope which had a calibrated focusing knob, or a Dektak depth recorder. An insulating coating of ThF_4 was then deposited, and MIS structures were fabricated. Figure 4-46 illustrates the relationship between the angle of the lap and the change in depth between each MIS structure. The diffusion of four impurities, gallium, indium, gold, and aluminum, were studied.

4.5.1 Gallium

Gallium is a column III metal with a low melting point of 30°C. It was thought that gallium would be a donor in (Hg,Cd)Te.

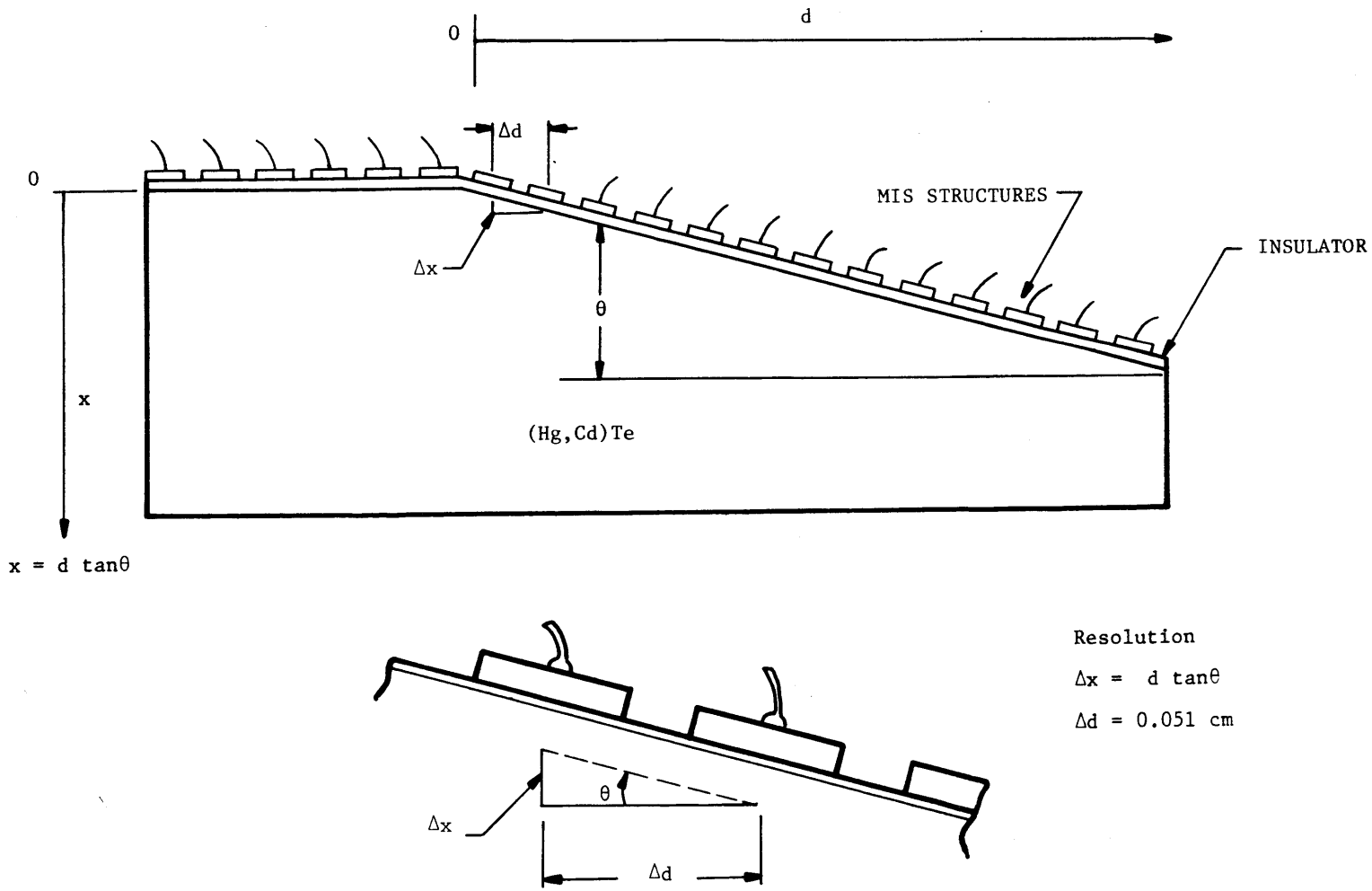

Figure 4.46. ILLUSTRATION OF THE PROCEDURE FOR DETERMINING DOPING DEPTH PROFILES. MIS STRUCTURES ARE FABRICATED ON A SURFACE WHICH HAS BEEN LAPPED AT A SMALL ANGLE.

N-type slabs of $Hg_{0.6}Cd_{0.4}Te$ with a net donor concentration of $2 \times 10^{14}/cm^3$ were chosen for this experiment. After the slabs were etched in 1:5 bromine/methanol, about 5000Å of gallium was vacuum evaporated onto the surface of two pieces. One piece was baked at 71°C for one hour in a dry nitrogen atmosphere and the other piece was allowed to sit a room temperature for one hour before attempts were made to remove the excess gallium in concentrated HCl. It was discovered that in both cases the gallium formed an alloy with the (Hg,Cd)Te that could not be removed in HCl. Other etchants were also tried, but also failed to remove the alloy. It was decided that the surface condition was not good enough to warrant the fabrication of MIS structures.

The piece which had undergone the 71°C bake was lapped to a depth of about 10 micrometers and then polished with 1:5 bromine/methanol. MIS structures were then fabricated. The data indicated a net donor concentration of about $1 \times 10^{15} cm^{-3}$. Since the original concentration was $2 \times 10^{14}/cm^3$ this implied that the gallium had affected the donor concentration to at least a depth of 15 micrometers.

Attempts were made to diffuse gallium from a gallium-doped silica film produced by Emulsitone Corp. The film is applied to the slab in liquid form and then the slab is spun on a photoresist spinner, which spreads the liquid evenly on the slab. A subsequent heat treatment hardens the film and causes the gallium to diffuse from the film into the slab. After applying the silica film to the surface of n-type material in this manner, the slabs were baked at 95°C and 120°C for three hours in a dry nitrogen atmosphere.

The film was then removed in HF, ThF_4 was evaporated onto the surface and MIS structures were then fabricated. The C-V data showed no significant change in the net donor concentration of the substrate for either the 95°C or 120°C bake. Higher temperatures are probably needed to cause the gallium to diffuse from the film significantly. Since higher temperatures would lead to decomposition of the (Hg,Cd)Te, no further attempts were made to diffuse gallium in this manner.

4.5.2 Indium

N-type $Hg_{0.6}Cd_{0.4}Te$ with a doping level of 2-3 x $10^{14} cm^{-3}$ and oriented in the (111) direction was chosen for these experiments. All diffusions were carried out on the B face. A coating of indium was evaporated onto a freshly etched surface and annealed at various temperatures in a dry nitrogen atmosphere. The indium coating was then removed in concentrated HCl after which MIS structures were fabricated.

In the first experiment the slab with the indium coating was allowed to sit for one hour at room temperature before the indium was removed in HCl. C-V data indicated no increase in net donor concentration over a depth of about one micrometer. There was however, a quite significant effect on the surface properties. The amount of hysteresis was considerably reduced compared to what had been normally observed for the ThF_4/(Hg,Cd)Te interface. In addition, the transition from accumulation to inversion occurred over a smaller range of gate voltage than normal, indicating a lower effective density of fast surface states. An example of a

C-V plot obtained at 80K is shown in Figure 4-47. The surface appeared to be depleted with zero gate voltage. The time constant of the inversion layer was much smaller than was expected for this material. Instead of being nonequilibrium at 80K, the C-V curves exhibited a behavior which was intermediate between high and low frequency behavior. This indicated an increased generation rate of minority carriers at or near the surface. One possible cause for this phenomenum is surface damage caused by the evaporation of the indium. It is also possible that the indium introduces energy levels near the intrinsic Fermi energy which would result in a reduced minority carrier lifetime in the bulk.

The second experiment was 71°C anneal for one hour. C-V measurements indicated that, within the first 0.8 micrometers from the surface, the average net donor concentration increased from 2-3 x $10^{14}cm^{-3}$ to 1.0 x $10^{15}cm^{-3}$. It was not possible to directly obtain the diffusion profile in this case. It was possible, however, to estimate the depth of diffusion by assuming a value of 1.5 x $10^{15}cm^{-3}$ for the concentration of electrically active indium at the surface. This value was estimated from the results of a later 95°C bake. In this manner the diffusion constant for indium at 71°C was estimated to be 9 x $10^{-17}m^2/sec$.

The hysteresis in the C-V curves was larger in this case. In some cases the surface was inverted with zero gate voltage. The time constant of the inversion layer was even smaller than was the case after the room temperature anneal.

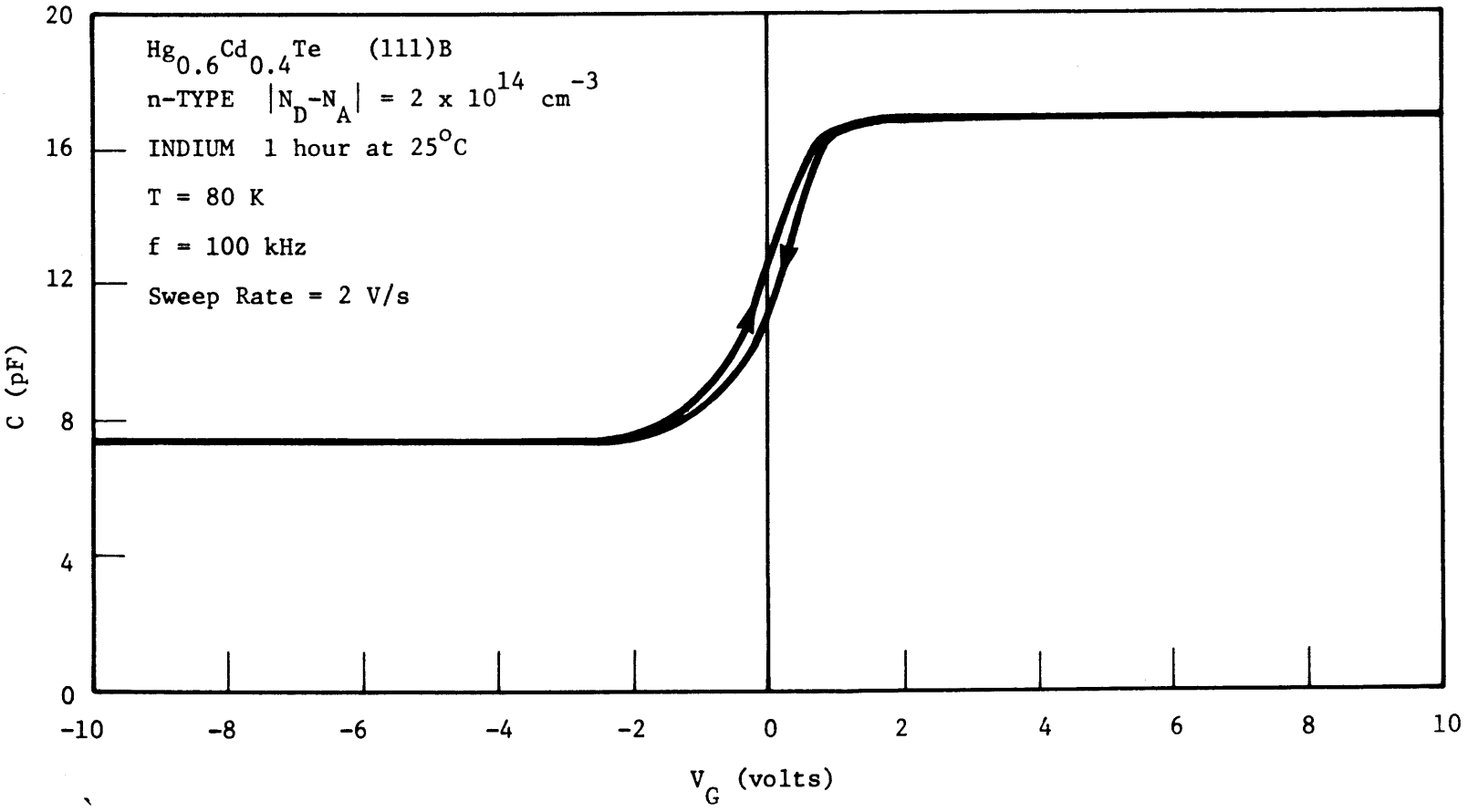

Figure 4.47. MIS C-V CURVE AFTER ONE HOUR, ROOM TEMPERATURE INDIUM DIFFUSION

The slab was lapped and coated with a fresh indium film. After a $95^{o}C$ anneal for one hour, the indium was removed and the slab was angle lapped at an angle of 0.3 degree. This lap resulted in a difference in depth of 2.5 micrometers between adjacent MIS elements. After the lap, about one micrometer of material was etched away to remove the lapping damage, and MIS structures were fabricated. Net donor concentration was then measured as a function of depth into the slab. The net bulk donor concentration of 2-3 x $10^{-14}cm^{2}$ was then subtracted from the measured values to yield a plot of the electrically active indium concentration versus depth into the slab.

Since some material was etched away, it was difficult to determine the surface concentration of indium, but it was estimated to be about 1.5 x $10^{15}cm^{3}$. The concentration of electrically active indium was down to half its surface value (7.5 x $10^{14}cm^{3}$) at a depth of about three micrometers. By fitting the profile to an error function distribution, which would be expected in this type of diffusion, a value for diffusion constant at $95^{o}C$ was estimated. This value is 3.4 x $10^{-15}m^{2}/s$. A plot of the electrically active indium concentration versus depth is shown in Figure 4-48. The calculated distributions for T = $71^{o}C$ and T = $95^{o}C$ are shown in Figure 4-49.

Diffusion processes are expected to follow an exponential relationship with temperature and activation energy, that is:

$$D = D_{o}e^{-E_{a}/kT}$$

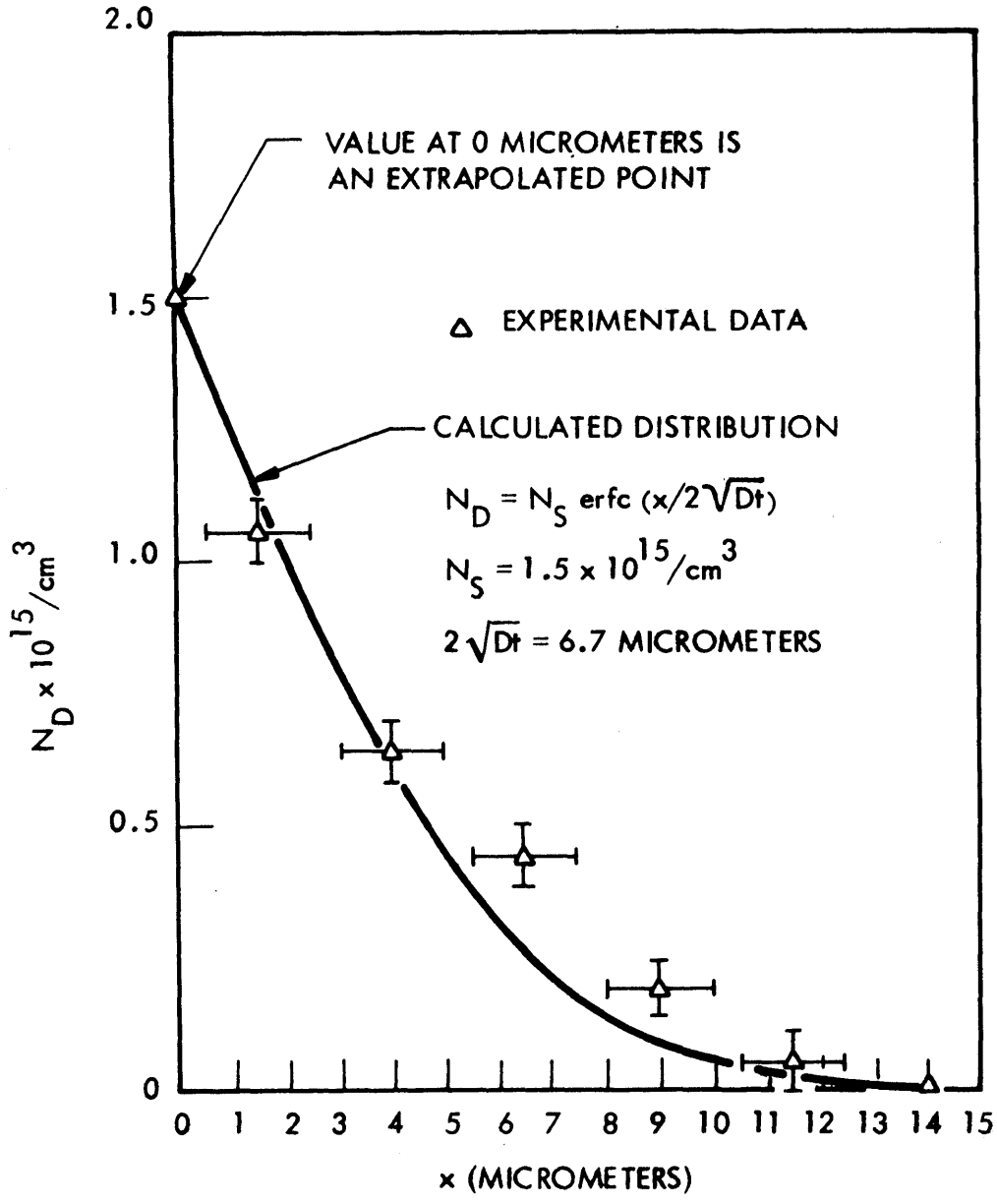

Figure 4.48. NET INDIUM DONOR LEVEL VERSUS DEPTH AT T = 95°C AND t = 1 HOUR

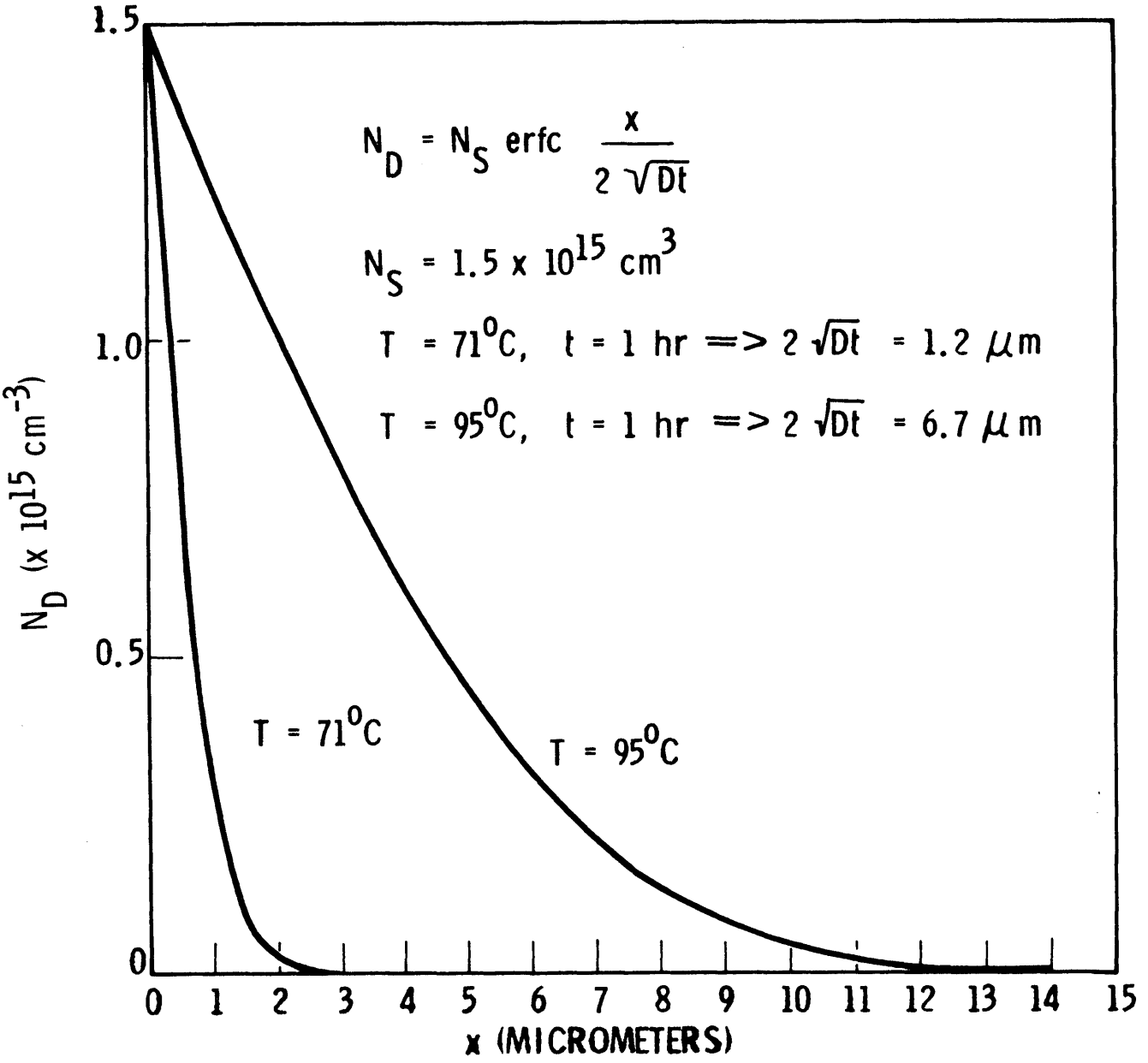

Figure 4.49. NET INDIUM DONOR LEVEL VERSUS DEPTH FOR T = 71°C AND T = 95°C. (CALCULATED DISTRIBUTIONS)

From the diffusion constants calculated at 71°C and 95°C, values for D_o and E_a were calculated. They are:

$$D_o = 8.7 \times 10^{7} m^2/s \text{ and } E_a = 1.6 \text{ eV}$$

It should be emphasized that, due to the very small angle lap, a large error in D_o is possible. Because of an uncertainty in the angle of the lap and estimated value for the surface concentration, the value calculated for D at 95°C could be in error by as much as a factor of four or greater. However, the calculated value of activation energy seems quite reasonable, since it is well-known that activation energies for silicon and germanium are about 3-4 times the bandgap. It this case, the calculated activation energy (1.6 eV) is four times the bandgap (0.4 eV).

4.5.3 Aluminum

Aluminum was deposited onto n-type $Hg_{0.6}Cd_{0.4}Te$ with a net doping of $2 \times 10^{14} cm^3$. First, the slab was etched in 1:5 bromine/methanol and then 5000Å of aluminum was evaporated onto the surface. The slab was then baked in a dry nitrogen atmosphere for one hour. The aluminum was removed in concentrated HCl and MIS structures were fabricated.

The first bake was done at 71°C. Capacitance-voltage measurements indicated that the net doping level was not significantly changed over a depth of about one micrometer from the surface. Subsequent bakes at 95°C and 120°C also resulted in no increase in donor level. Previous

experiments on the diffusion of aluminum in (Hg,Cd)Te showed evidence for the formation of an aluminum oxide barrier which prevented the diffusion of aluminum at low temperatures.[28] Thus, it is likely that a prohibitively high bake temperature is needed to diffuse aluminum.

On the other hand, the effect of the aluminum bake on the surface properties was pronounced. Capacitance-voltage characteristics exhibited almost negligible hysteresis, especially after 71°C bake. In some cases, the characteristics were almost ideal, indicating a very low effective surface state density.

A C-V plot obtained at 147K with a voltage sweep of $\pm$15 volts is shown in Figure 4.50. A portion of this data was plotted on a $\pm$2 volt scale and compared with the ideal high frequency curve, as shown in Figure 4.51. By using the differentiation technique described in Section 2.2 it was possible to construct a plot of effective surface state density versus energy for a portion of the bandgap. This plot is shown in Figure 4.52. The density of states was lowest near the intrinsic Fermi level, about $2 \times 10^{11} cm^{-2} eV^{-1}$. Since the differentiation technique tends to overestimate the density of fast surface states, this value is an upper bound on the density of fast states.

The C-V data showed that the surface was depleted with zero gate voltage. As was the case with the indium diffusion, the time constant of the inversion layer was considerably reduced compared to typical values. In this case the time constant was roughly a factor of one hundred lower than would be the case for no aluminum bake.

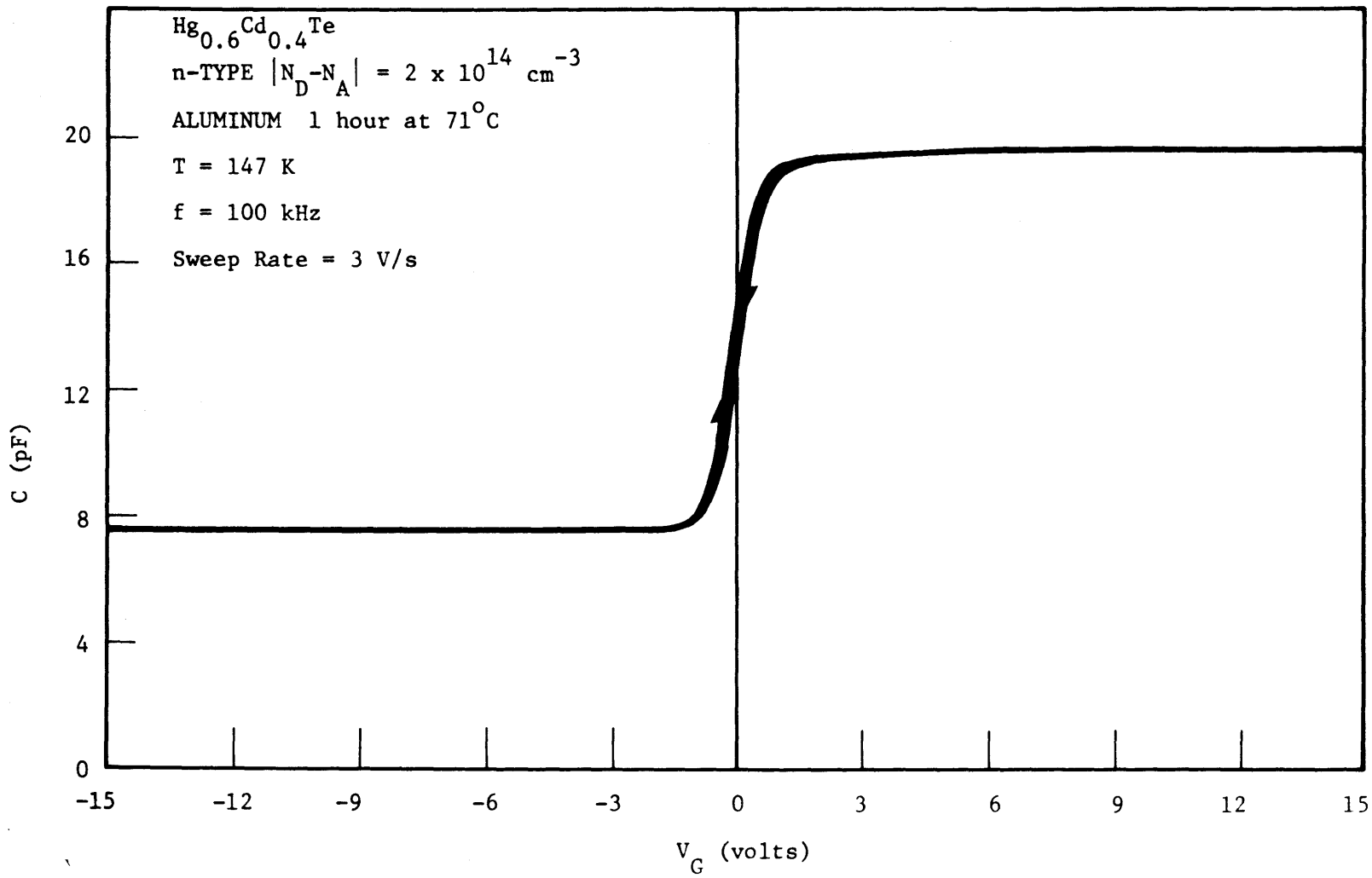

Figure 4.50. MIS C-V CHARACTERISTIC OBTAINED AFTER A 71°C, ON HOUR ALUMINUM DIFFUSION

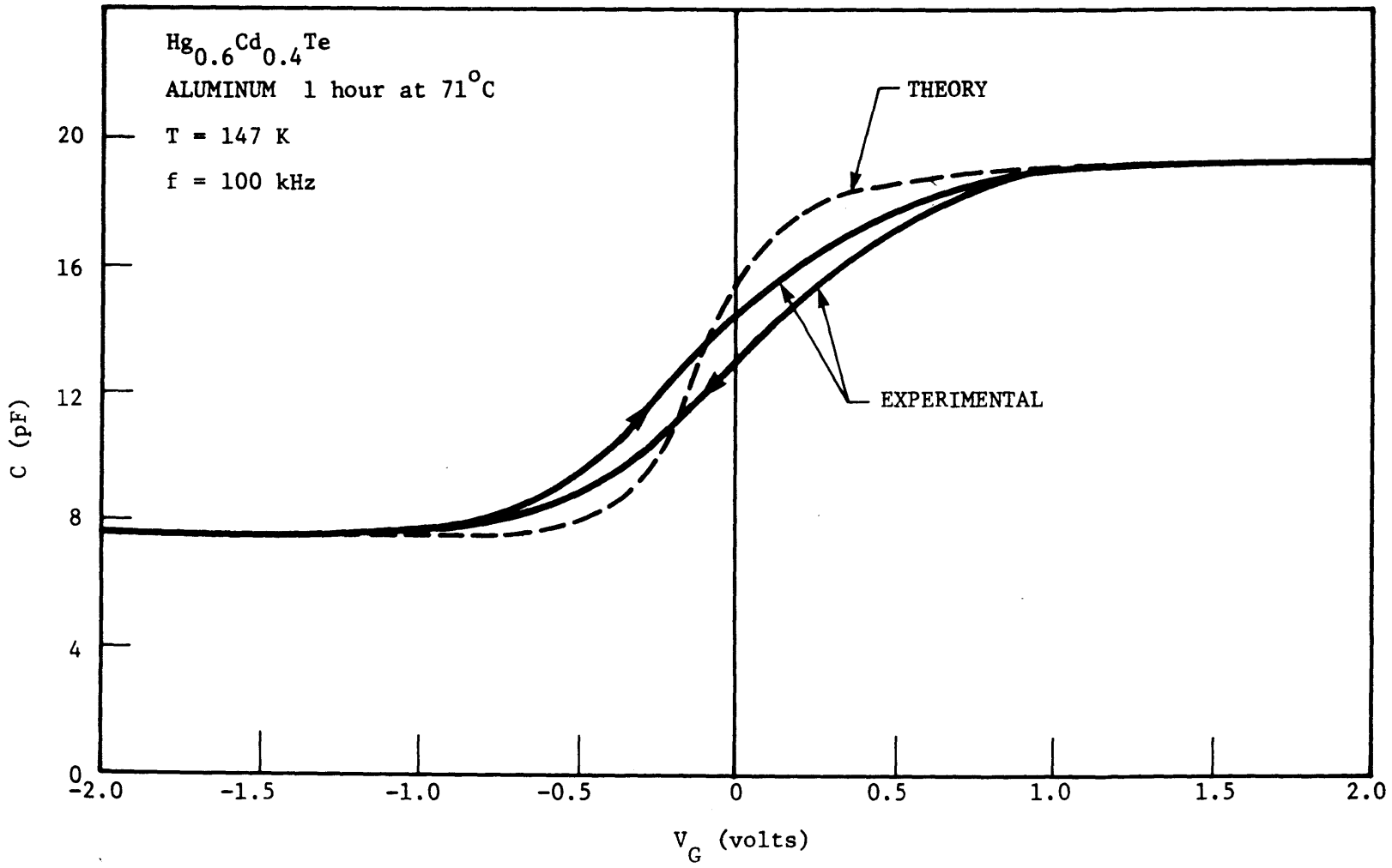

Figure 4.51. COMPARISON OF THE C-V PLOT OF FIGURE 4.50 WITH IDEAL CURVE

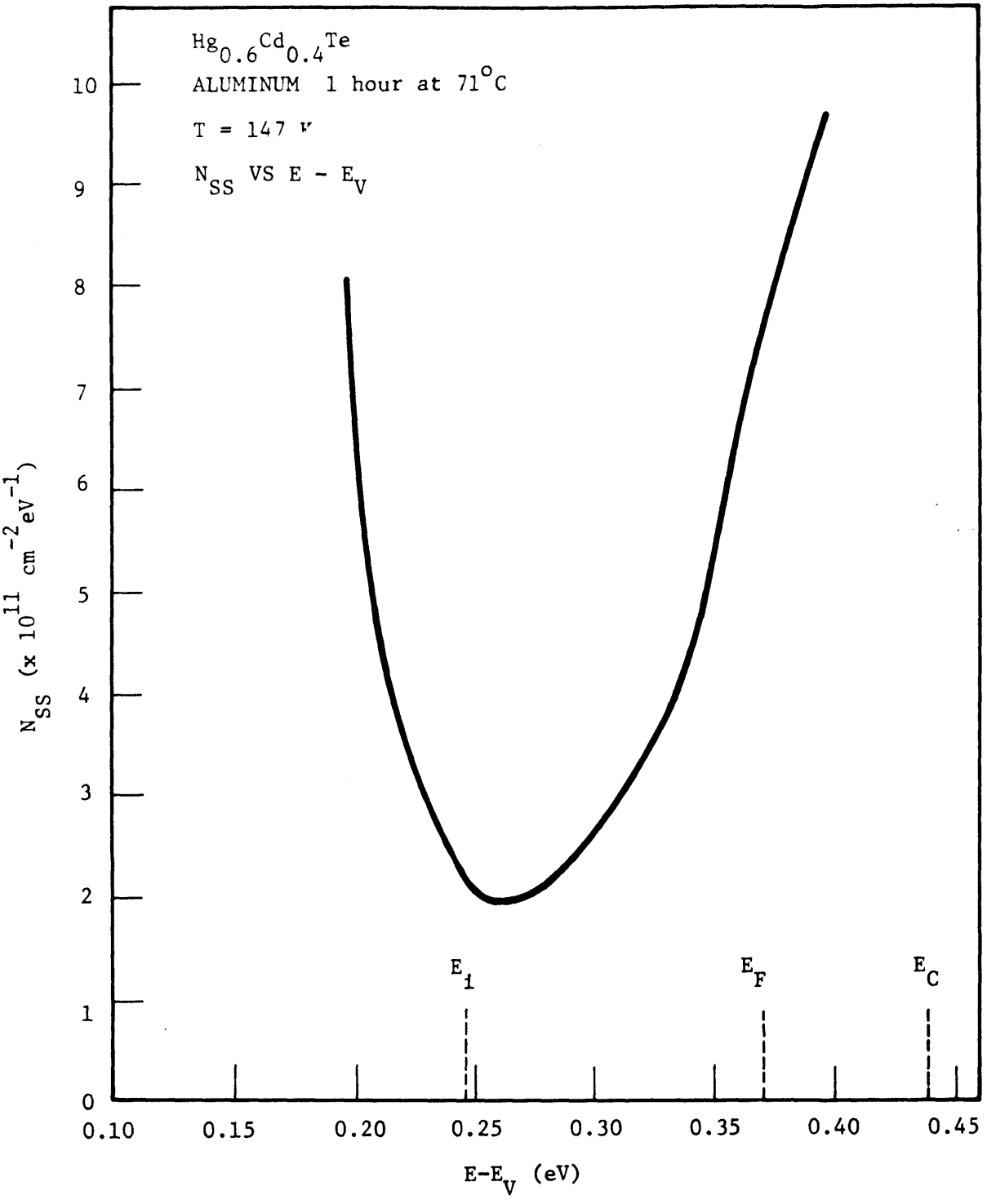

Figure 4.52. SURFACE STATE DENSITY VERSUS ENERGY AS CALCULATED WITH THE DIFFERENTIATION TECHNIQUE FOR THE 71°C ALUMINUM ANNEAL

The cause of the lower effective density of states and reduced hysteresis is not well understood. Control experiments were undertaken in which a slab with no aluminum was baked in dry nitrogen. The C-V data showed a large density of surface states in this case, thus indicating that the aluminum was somehow responsible for the reduced density of states. The results could be due in part to the presence of a very thin n+ region near the surface of the (Hg,Cd)Te.

4.5.4 Gold

It was expected the gold would be acceptor in (Hg,Cd)Te. An unoriented p-type slab of $Hg_{0.6}Cd_{0.4}Te$ was selected for the gold diffusions. The bulk doping level was $2 \times 10^{14}/cm^3$ as determined previously with MIS C-V data.

In the initial experiment, gold was deposited on the surface using an electrodeless gold precipitation process in which gold is plated directly from a $AuCl_3$ solution. The slab was then baked at 120^oC for one hour in a dry nitrogen atmosphere. Attempts were made to remove the excess gold with a KCN etch. Although most of the gold film was removed, a thin film was still visible. MIS structures were fabricated on this surface. The C-V data showed no change in capacitance over a wide range of voltages. This indicated that a gold film was indeed present, and that no information about the effect of the gold on the net doping was possible.

The experiment was repeated except that this time a different method of depositing the gold was used. A thin film of gold was plated onto the surface at room temperature using the "Engelhard E-56 Acid Gold" plating solution. After rinsing in deionized H_2O, the slab was baked at $120^{\circ}C$ in a dry nitrogen atmosphere for one hour. The gold film was subsequently removed by plating a thicker layer onto the already existing film. The gold layer, including the original film, was then peeled off. MIS structures fabricated on this surface indicated the presence of a very highly doped p-type surface with an average doping level of 2.2×10^{17} cm^{-3}. For this doping level, the maximum depletion depth is only in the neighborhood of 600Å in the MIS structures. It was, therefore, to this depth that the average doping was determined.

The slab was then stripped of the MIS structures without removing any of the semiconductor surface. (This was done by forcing the ThF_4 to peel off by subjecting it to a series of rinses in acetone and HCl.) All but a small portion of the slab was then etched for one second in a 20% solution of bromine/methanol. By measuring the height of the step between the etched and unetched regions, it was determined that approximately 2.5 micrometers of material was removed. The MIS data on this surface showed that the doping level had returned to its original value. This indicated that a very shallow and a quite abrupt diffusion of gold had taken place with this process.

This data is in apparent contradiction with previous data on the diffusion of gold in (Hg,Cd)Te, which had indicated that gold diffuses much more rapidly.[29] These results, however, had been obtained using the $AuCl_3$ plating solution. It is quite possible that the two methods of plating gold mentioned here could result in very different diffusion characteristics.

4.6 STOICHIOMETRIC MERCURY ANNEAL

It has been reported previously[30] that mercury (Hg) vacancies in (Hg,Cd)Te behave as acceptors. The concentration of Hg vacancies, and thus the concentration of acceptors, can be changed by annealing the (Hg,Cd)Te under appropriate conditions of temperature and Hg pressure. Specifically, the concentration of Hg vacancies decreases as the anneal temperature is lowered as long as the Hg pressure is maintained at the maximum pressure possible for the given anneal temperature. Figure 4-53, which was reproduced from an article by Schmit and Stelzer[30], illustrates the dependence of net carrier concentration on the anneal temperature for the cases of Hg-saturation and Te-saturation for $Hg_{0.6}Cd_{0.4}Te$. It can be seen that some of the samples converted to n-type for temperatures below 350°C. In these cases the acceptor concentration was reduced below the concentration of donors present in the material.

Two experiments were carried out using the MIS technique to determine the effects of the anneal on bulk properties. In the first experiment the slab of (Hg,Cd)Te was maintained at a constant temperature of 300°C, but the Hg pressure was varied. The slab and excess Hg were sealed in a quartz capsule. The capsule was placed in a furnace in which the temperature profile could be varied. The slab, which was located at one end of the capsule, was maintained at a temperature of 300°C. The temperature of the Hg, which was located at the other end of the capsule, was varied between 150°C and 300°C depending on the location of the capsule in the furnace. In this manner the Hg vapor pressure could be varied.

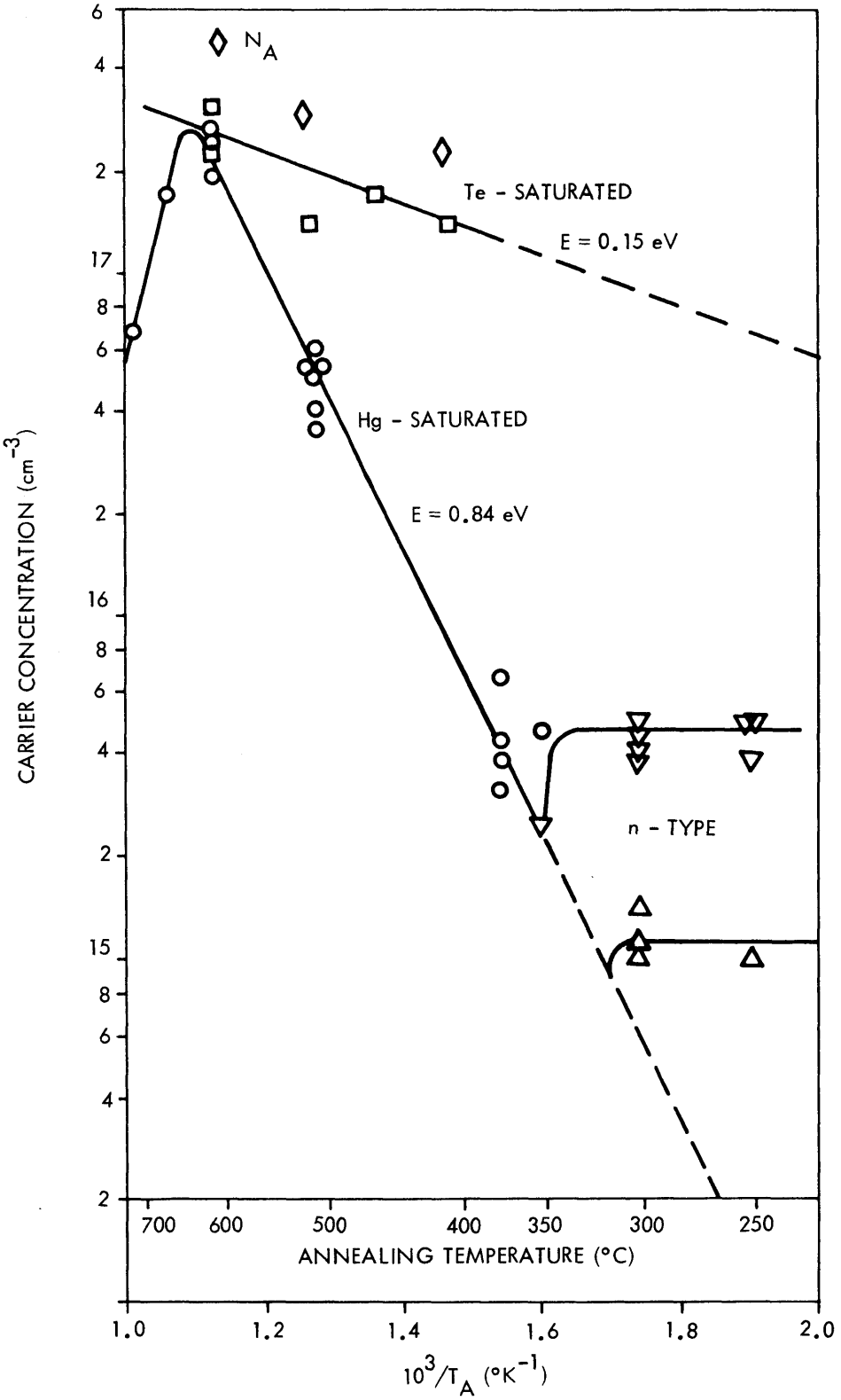

Figure 4.53. DEPENDENCE OF NET CARRIER CONCENTRATION VERSUS ANNEAL TEMPERATURE FOR THE Hg ANNEAL

Two slabs of x = 0.4 (Hg,Cd)Te were used for this experiment. MIS measurements on these slabs indicated a net acceptor level of 2-3 x 10^{16} cm^{-3}. One slab was carried through a series of anneals in which the Hg temperature was varied from 150°C to 300°C. The other slab was subjected to an isothermal anneal only, in which the Hg and the slab were maintained at 300°C. In all cases the slabs were annealed for about 5 days, so that the concentration of acceptors would be affected to a depth of approximately 30 micrometers.

The results of C-V measurements after the first anneal, in which the Hg temperature was 155°C, showed an increase in acceptor concentration to 1.7 x 10^{17} cm^{-3}. In addition the effective minority carrier lifetime, τ_{g-r}, as determined in heavy inversion with the conduction technique, was found to be extremely small, about 1 x 10^{-16} s. The effective lifetime before the anneal was on the order of one nanosecond. It is improbable that an effective lifetime this small could be due to Shockley-Read recombination in the depletion region. It is thought that this extremely short effective lifetime was due in part to tunneling through the potential barrier of the depletion region.

The results of subsequent anneals with Hg temperatures of 200°C, 250°C and 300°C were somewhat erratic. The 200°C Hg anneal resulted in a reduction of net acceptor concentration to 6.8 x 10^{15} cm^{-3}. The anneal with a Hg temperature of 250°C resulted in a small reduction of acceptor concentration to 3.8 x 10^{15} cm^{-3}. Finally with a Hg temperature of 300°C the acceptor concentration actually increased to 1 x 10^{16} cm^{-3}. This was

a surprising result since it was expected that the isothermal anneal would convert the material to n-type. The slab which had undergone only the 300°C isothermal anneal did, however, show some conversion to n-type and a lower acceptor concentration. There were both n and p-type regions with doping levels on the order of 10^{14} cm^{-3}, indicating very close compensation of donors and acceptors.

Because of the erratic results of this experiment, it was impossible to make any conclusions about the dependence of acceptor concentration on Hg vapor pressure. It had been expected that the anneals would lower the acceptor concentration following an $N_A \propto P_{Hg}^{-1/3}$, where P_{Hg} is the mercury vapor pressure. This is based on the assumption the native metal vacancies are doubly ionized acceptors. Unfortunately, the validity of this assumption could not be determined in this case.

The next experiment was a 14-day, 300°C isothermal Hg anneal. A slab of (Hg,Cd)Te with $x \approx 0.39$ was used. Hall data on an adjacent slab indicated that the material was originally p-type with carrier concentrations on the order of 1×10^{16} cm^{-3}. After the anneal, thermal probe measurements revealed that the surface of the slab had converted to n-type. MIS structures were fabricated on slab and, using C-V diagnostics, the average carrier concentration was found to be 5.4×10^{14} cm^{-3}.

The MIS structures were removed and slab was given a 0.9° angle lap, as verified by a Dektak depth recorder. MIS structures were then refabricated onto the slab. The C-V data indicated that the slab was n-type with

a uniform carrier concentration of 5.9×10^{14} cm^{-3} to a depth of 3.6 mils. At a depth of about 4 mils the slab became p-type with N_A increasing from 2×10^{14} cm^{-3} to 2.5×10^{15} cm^{-3} at a depth of 4.9 mils. A plot of the net carrier concentration versus depth is shown in Figure 4.54.

The process of the self-diffusion of Hg in (Hg,Cd)Te has been studied in the past.[33] The approach in the previous work was to measure the junction depth as a function of the anneal temperature and time of diffusion for x-values ranging from x = 0.2 to x = 0.4. It was found that the junction depth varied linearly with the square root of the time of diffusion for a given x-value at a given temperature. This implied that the diffusion process was of a conventional nature, i.e., infinite source or finite source diffusion, with a characteristic length of $2\sqrt{Dt}$, where D is an effective diffusion coefficient. Such parameters as the effective surface concentration of Hg could not, however, be determined. Therefore a precise value of D could not be calculated. A junction depth of about 3.6 mils was measured for the case of a 2 week, 300°C Hg diffusion into $Hg_{0.6}$ $Cd_{0.4}$ Te with $(N_A-N_D) = 6\text{-}7 \times 10^{16}$ cm^{-3}. This agrees well with the value of 4 mils determined in the experiment carried out here, which was done under the same conditions except that the initial concentration of acceptors was slightly lower ($\sim 1 \times 10^{16}$ cm^{-3}).

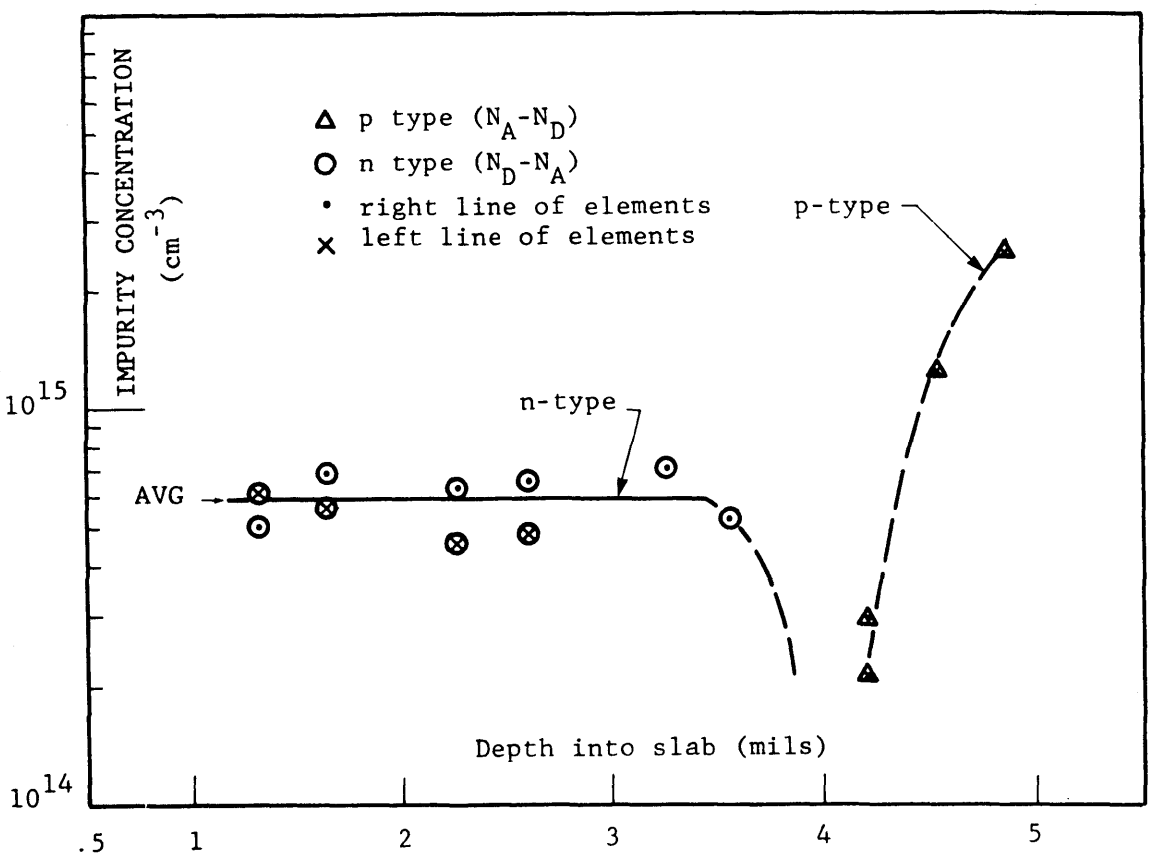

Figure 4.54. NET IMPURITY CONCENTRATION VERSUS DEPTH: Hg ANNEAL

4.7 SURFACE PREPARATION EXPERIMENTS

4.7.1 Chemical Etches

The effects of various chemical solutions on the surface properties of (Hg,Cd)Te were studied using the MIS technique. In all cases the surfaces were etched in 1:5 bromine/methanol before the chemical etch under study was applied to the surface. Fabrication of MIS structures then proceeded in the normal manner with ThF_4 used as the insulator.

4.7.1.1 Hydrochloric Acid (HCl)

HCl reacts very weakly with (Hg,Cd)Te. Since it had been used to remove the metal films during the diffusion experiments, it was decided to determine if the HCl etch alone had a significant effect on the surface properties.

Two pieces of an n-type slab of $Hg_{0.6}Cd_{0.4}Te$ were used for this experiment. One piece was given a final etch in 1:5 bromine/methanol and the other piece was given a final etch in HCl. No discernible difference was found in the C-V data of the two etches. Both resulted in a depleted surface condition. This indicates that HCl does not significantly alter the surface condition obtained after the bromine/methanol etch.

4.7.1.2 Hydrogen Peroxide (H_2O_2)

The H_2O_2 treatment consisted of a 10-minute bath in 30% H_2O_2 solution at 40°C followed by a 10-minute rinse in isopropyl alcohol. Unoriented n-type slabs of $Hg_{0.6}Cd_{0.4}Te$ with net donor concentrations of 2×10^{14} cm^{-3} were used for this experiment. The slabs were cut from the same ingot that the (111) oriented slabs were cut from, but at a slightly different angle. The orientation was therefore expected to be near the (111) direction. Capacitance-voltage data obtained from nearby slabs which were etched in bromine/methanol only was indeed quite similar to that obtained from (111) oriented slabs. The H_2O_2 etch was done on the face which corresponded approximately to the A face of the oriented section.

The C-V results following the H_2O_2 etch were considerably different than those normally obtained after a bromine/methanol etch. The amount of hysteresis was unusually large. At 147 K, for example, the hysteresis window was typically 10 volts wide with a voltage swing of ±25 volts and a sweep rate of 2 V/s. The surfaces were generally accumulated, although the large amount of hysteresis made accurate determination of the surface potential impossible. A typical C-V plot measured at 147 K is shown in Figure 4.55. The C-V curve was considerably less skewed in the transition from accumulation to inversion than was the case for bromine/methanol etched surfaces, especially for the negative-going voltage sweep. This indicates a lower fast surface state density in the upper portion of the bandgap for the H_2O_2 etched surface.

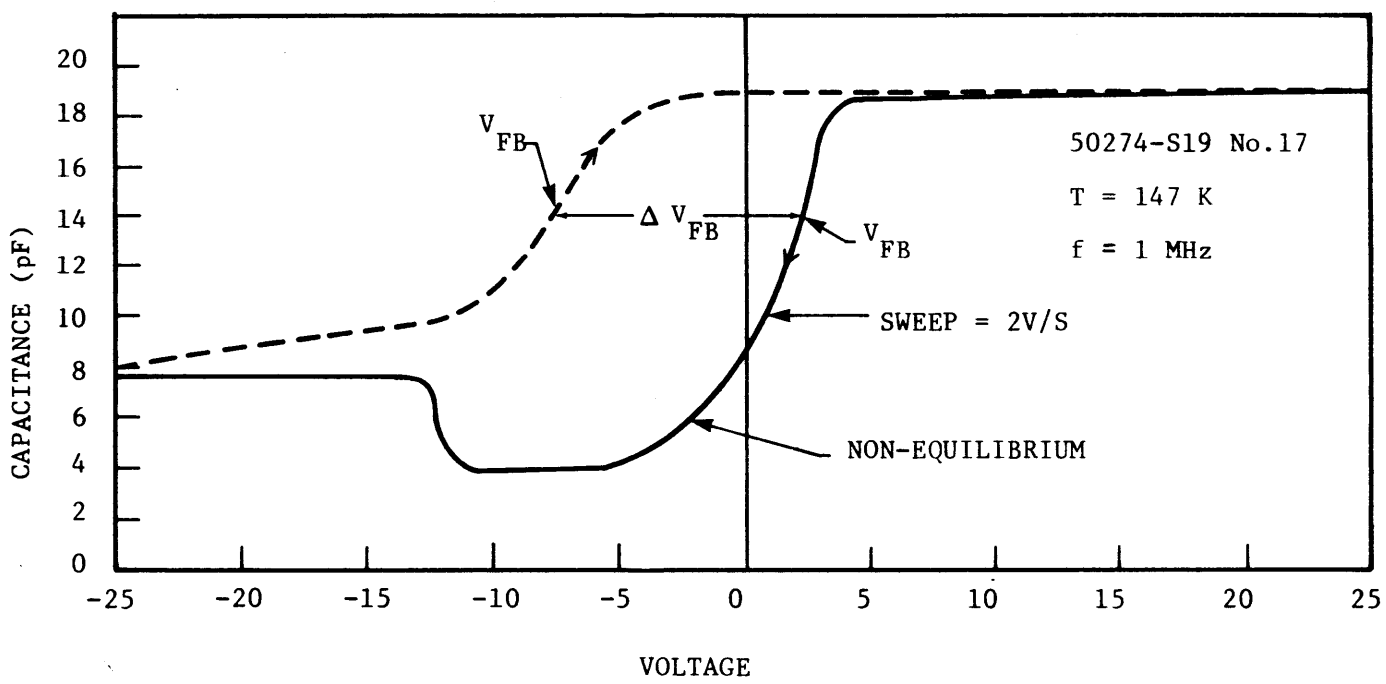

Figure 4.55. MIS C-V DATA ON AN H_2O_2 TREATED SURFACE. THE HYSTERESIS WINDOW AS MEASURED BETWEEN THE TWO FLATBAND VOLTAGES, IS 10 V. NON-EQUILIBRIUM BEHAVIOR IS EVIDENT WITH THE 2 V/S SWEEP RATE.

It is quite possible that the reaction of (Hg,Cd)Te with H_2O_2 led to the formation of a thin layer of native oxide on the surface. The results of this etch were in some ways similar to those obtained from anodic oxide films, which will be presented in a later section.

4.7.1.3 Sulfuric Acid (H_2SO_4)

The H_2SO_4 treatment involves a 10-minute ultrasonic etch in concentrated H_2SO_4 at room temperature followed by rinses in deionized water and ethanol. N-type slabs from the same region of the ingot as those which were etched in H_2O_2 were used. The surface which roughly corresponded to the (111)B face was treated with H_2SO_4.

The C-V characteristic of this surface exhibited a low density of both fast and slow surface states, as can be seen in Figure 4.56. The hysteresis window was typically 1 volt at T = 147K with a voltage swing of -10 to +15 volts and a sweep range of 2 V/s. The gradual slope which can be seen on the negative-going sweep portion of the curve is probably due to slow surface states, since it occurs only in one sweep direction. The transition from maximum to minimum occurs over a narrow range of voltage, indicating a low density of fast surface states.

The zero bias capacitance was close to the minimum capacitance, implying that the surface was weakly inverted. A second indication of weak inversion was the fact that the inversion region under the gate was in equilibrium with the gate voltage. This is not normally the case with a sweep

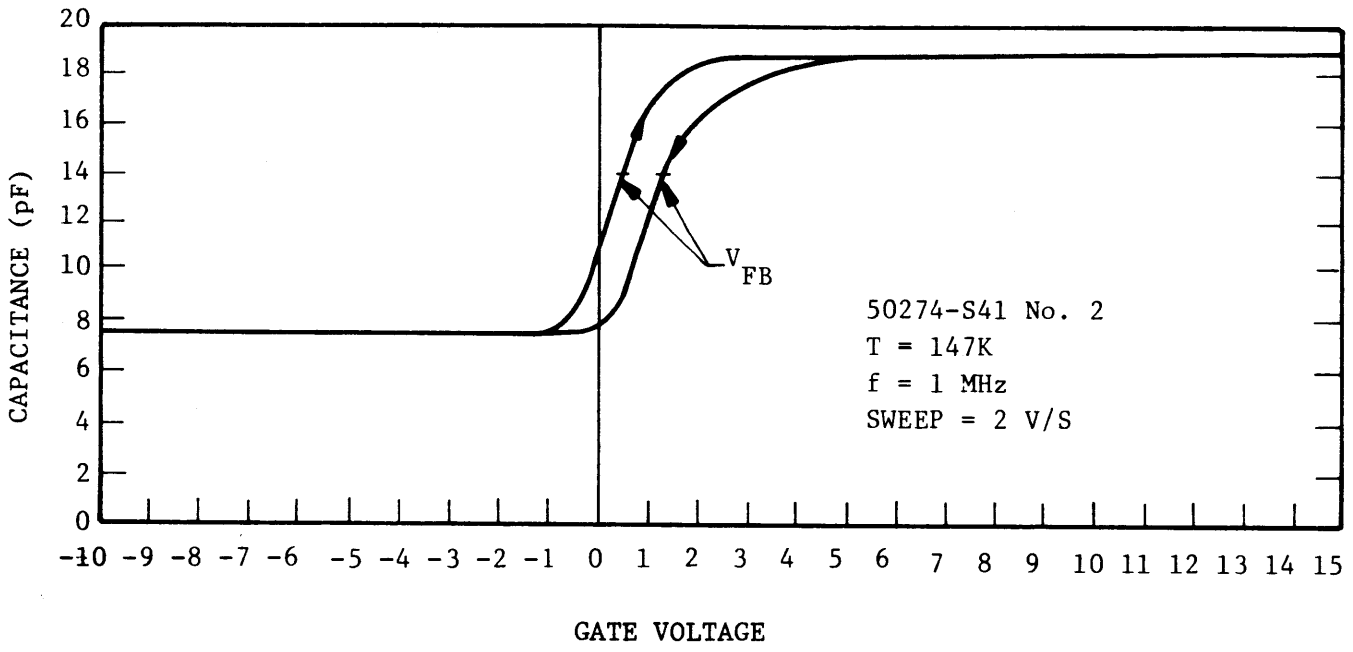

Figure 4.56. MIS C-V DATA ON A H_2SO_4 TREATED SURFACE. THE FLATBAND VOLTAGES ARE +0.3 AND +1.3 INDICATING A DEPLETED SURFACE CONDITION AND A HYSTERESIS WINDOW WIDTH OF 1 V. THE INITIAL GRADUAL SLOPE AT THE CAPACITANCE IN THE NEGATIVE SWEEP DIRECTION WAS SEEN IN NEARLY ALL OF THE SAMPLES.

rate of 2 V/s if the surface is depleted or accumulated. Figure 4.55 is an example of nonequilibrium behavior for the case of an accumulated surface.

The effects of chemical etches on the surface properties were not studied in detail. An extensive, controlled study was not possible due to time limitations.

4.7.2 Mechanical Polish

This experiment was conducted to compare mechanically polished surfaces with surfaces given a final etch in 1:5 bromine/methanol. An n-type slab of $Hg_{0.6}Cd_{0.4}Te$ which was approximately oriented in the (111) direction was used. The A surface of the slab was polished with a fine abrasive. Half of the surface was given a ten second etch in 1:5 bromine/methanol solution. MIS structures were then fabricated on both the etched and polished surfaces.

All but one of the eight MIS samples on the polished half showed low frequency C-V characteristics at a temperature of 147 K and a frequency of 200 kHz. The C-V curves also exhibited more skewing than was normally the case, indicating a large density of fast surface states. In some cases the surface was strongly inverted. The etched half on the other hand resulted in C-V data which was typical for bromine/methanol etched surfaces. The C-V data from samples on the polished and etched surfaces are compared in Figure 4.57.

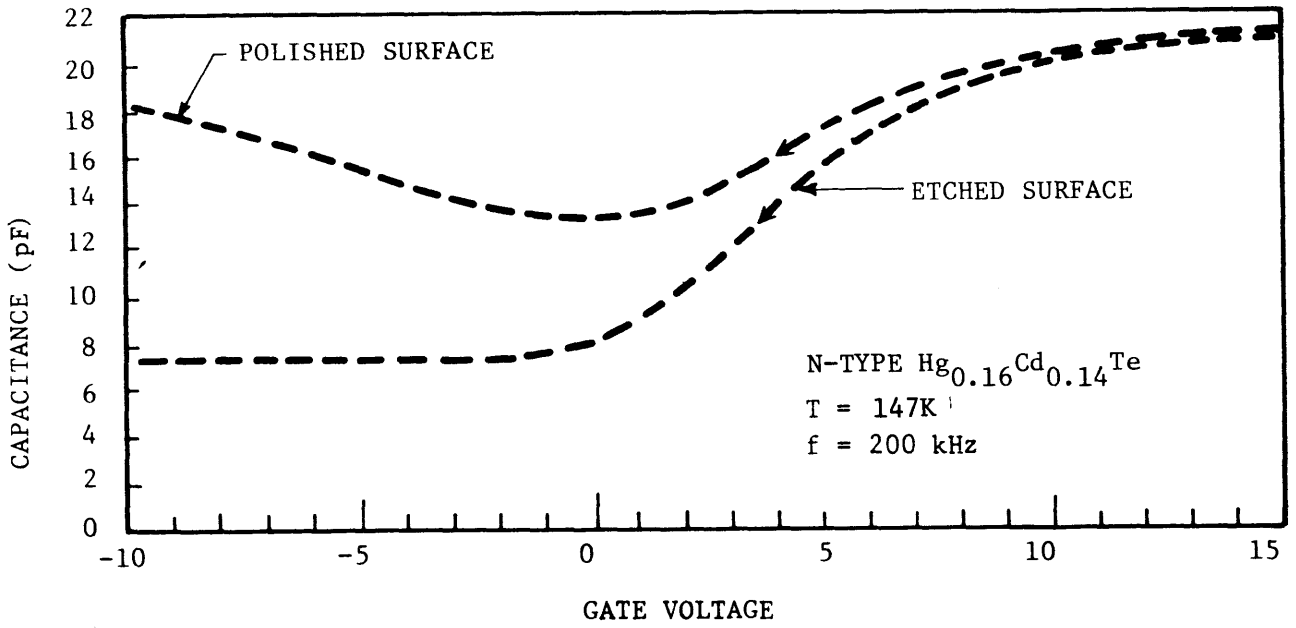

Figure 4.57. MIS C-V DATA COMPARING POLISHED AND ETCHED SURFACES

The low frequency behavior of the MIS structures on the polished half can be attributed to the considerable surface damage which results from the mechanical polish. This damage can lead to a drastically increased minority carrier generation rate near the surface. In addition the charge trapped in surface states can cause the surface to be inverted, as was the case for most of the samples tested.

4.7.3 Heat Treatments

It was thought that the heating of the (Hg,Cd)Te could affect the surface properties. Two experiments were conducted: one in which the slab was baked prior to the deposition of the ThF_4, and the other in which the slab was baked after the deposition of the ThF_4.

The first experiment has already been mentioned in conjunction with the aluminum diffusion experiment (Section 4.3.3.). A slab of n-type $Hg_{0.6}Cd_{0.4}Te$ was baked in dry nitrogen at 71°C for one hour. The C-V data obtained from MIS structures which were subsequently fabricated exhibited a large amount of hysteresis as well as a considerable fast surface state density. Most of the structures also showed some low frequency behavior. It can be concluded that the prebake of the slab worsened the condition of the surface.

In the second experiment a slab was baked after the deposition of the ThF_4. A p-type slab of $Hg_{0.6}Cd_{0.4}Te$ was cut into two pieces. Both pieces received a 10-second etch in 1:5 bromine/methanol after which a

4000 Å coating of ThF_4 was deposited. One pice was baked in dry nitrogen at 72°C for 12 hours. Gate electrodes were then deposited onto both slabs.

The C-V data indicated that in both cases the surfaces were near flatband. The C-V characteristics of both pieces were very similar, except at large positive voltages. The structures from the unbaked piece exhibited nonequilibrium characteristics at large positive voltages. The structures from the baked piece on the other hand generally exhibited equilibrium characteristics. In addition, the capacitance was found to increase above the equilibrium value for gate voltages greater than 5 volts. It is thought that this effect was due to a larger density of surface states in the upper portion of the bandgap for the baked piece. It would thus seem that the effect of the bake was to increase the density of surface states in the upper portion of the bandgap while leaving the surface states in the rest of the bandgap unaffected.

SECTION 5

DISCUSSION

5.1 BULK PROPERTIES

5.1.1 Bandgap

The bandgap is one of the most important parameters which can be determined with the MIS technique. Nearly all the measurements which can be done on MIS structures depend in some way on the bandgap or, equivalently, the x-value of the material under study. It is, therefore, important that the bandgap be determined reasonably accurately before other measurements are undertaken.

It was shown that the cutoff wavelength could be determined by measuring the photosignal of the MIS structure as a function of the wavelength of the incident radiation. The cutoff wavelength was defined as the wavelength at which the relative spectral response was 50% of the peak response near the cutoff wavelength. It was necessary to use a thin enough layer of gold (~100A) for the gate electrode so that the transmission through the gold was sufficiently high at wavelengths near the cutoff to allow accurate determination of the cutoff wavelength. The maximum error in cutoff wavelengths was estimated to be $\pm$ 0.1 μm.

The most important parameter affected by the bandgap is the intrinsic carrier concentration, n_i. The intrinsic carrier concentration was determined from an expression derived by Schmit[8] (equation 2.24) and is reproduced here:

$$n_i = (8.445 - 2.875x - 0.00342T)\ 10^{14}\ Eg^{3/4}\ T^{3/2}\ \exp(-Eg/2kT) \tag{5.1}$$

The non-parabolicity of the bands of (Hg,Cd)Te was taken into account in this derivation by using the k·p method (Kane model).[34] The original expression was multiplied by a factor of 1.5 to conform with experimental data. While the absolute accuracy of this expression is not well known, the temperature dependence should be sufficiently accurate for the purposes of this work.

The error in n_i resulting from uncertainty in the bandgap was calculated for x=0.4 (Hg,Cd)Te ($\lambda_c \approx 3\mu m$) assuming that the error in λ_c was $\pm$ 0.1 μm ($\Delta Eg \approx \pm$ .014eV). The error was largest at low temperatures. For the case of T=147K (the most commonly used temperature) and λ_c = 3.0 μm $\pm$ 0.1 μm, n_i changed about a factor of 1.7 either way from the nominal λ_c = 3 μm value.

5.1.2 Majority Carrier Concentration

An important bulk parameter which can be determined with the MIS technique is the net doping, $|N_A-N_D|$. It was necessary to know the doping in the determination of other parameters, such as the minority carrier lifetime, the surface potential, and the surface state density. Knowledge of the doping was also clearly necessary in the study of the diffusion of impurities in (Hg,Cd)Te.

The estimates of net doping concentrations $N_B = |N_D-N_A|$ from MIS C-V data repeatably shows very good agreement with Hall data. There are, however, several sources of error in this determination both in the analysis and the measurement.

In the analysis there are three approximations. The first approximation is that used in the calculation of the depletion region capacitance in strong inversion. The second approximation is the empirical expression for the intrinsic carrier concentration of $Hg_{1-x}Cd_xTe$. The third approximation is that used in the estimation of the static dielectric constant which is a linear extrapolation with x-value between measured values for CdTe and $Hg_{0.8}Cd_{0.2}Te$. These errors are constant from measurement to measurement.

The calculation of N_B (described in Section 2.1) used the simple Grove model[9] which assumes that the space charge region is entirely depleted

of carriers. The equation which relates the high frequency capacitance to N_B is the following:

$$C_D = \sqrt{\frac{q\,\varepsilon_s N_B}{4kT\,\ln\left(N_B/n_i\right)}} \tag{5.2}$$

More exact calculations of the high frequency depletion capacitance were carried out by Brews.[12] It was found that the Grove approximation results in a depletion capacitance which is about 4% higher than the more exactly calculated value. Thus, for a given value of N_B the measured capacitance will be lower than predicted by the Grove model. Calculations of N_B from the insulator and minimum capacitance of the MIS structure using the Grove formula will then result in an underestimate of the net doping by about 8%.

Another source of error is inaccuracies in the determination of n_i. The doping is, however, relatively insensitive to errors in n_i, as can be seen by examining the following equation (equation 2.23):

$$N_B = \frac{4kT\,\ln\,(N_B/n_i)}{\varepsilon_s q^2\,(1/C_f - 1/C_i)^2} \tag{5.3}$$

The doping calculation contains only a logarithmic dependence on n_i. A factor of two error in n_i at 147K with x = 0.4 would correspond to an error of only 10%.

Equation 5.3 also shows that the doping is inversely proportional to the dielectric constant ϵ_s. As stated previously, the static dielectric constant is determined for a given x-value via a linear extrapolation between the measured values of $Hg_{0.8}Cd_{0.2}Te$ and CdTe. The error in this extrapolation is not known, but it is expected to be small since many of the parameters of (Hg,Cd)Te have been found to vary in an approximately linear fashion with x-value. For example, the optical dielectric constant was measured as a function of the x-value by Baars and Sorgen[35], and it was found that ε_∞ departed from a linear variation by less than 10% over the entire compositional range from CdTe to HgTe.

The greatest source of error arises from errors in the measurement of the true capacitance. It can be seen from equation 5.3 that the calculation of N_B depends on the square of the measured capacitances. The primary source of error in the capacitance measurement was the stray capacitance of the dewar, which was about 4 pF. Even though the stray capacitance was measured on adjacent open pins and nulled out, it was estimated that an error of about $\pm$ 0.5 pF was possible. This uncertainty resulted in a calculated error in N_B of + 15% to $\pm$ 20%.

5.1.3 Lifetime Measurements

Lifetime measurement techniques and experimental results were described in detail in Sections 2.3 and 4.4, respectively. It was found that at most temperatures, Shockley-Read generation-recombination in the depletion region was the dominant mechanism. Most of the experimental

results could be explained by the Shockley-Read model for single level traps, but some anamolous results were noted, especially the large discrepancy between the large and small signal methods.

One of the advantages of the MIS techniques for measuring the generation-recombination parameters is that the duration of the measured quantity is approximately a factor of N_B/n_i longer than the actual lifetime which one is trying to determine.

This fact, however, is a disadvantage when one considers the error involved in the calculation of a lifetime. Since the measurement is not a direct measure of the lifetime, the accuracy of the results depends directly on the accuracy to which the parameters used in the calculations are known. Equations 2.62 and 2.83 show the lifetimes τ_g and τ_{g-r} are related to the observed time constant by a factor of roughly n_i/N_B. The errors in N_B were shown to be about 20%, so that this error is not too important. On the other hand, n_i could easily be in error by a factor of two, so that errors in n_i are probably the main cause of inaccuracies in the calculated lifetime.

Uncertainties in the capacitance measurement can also cause error in the final result. This is expected to be more of a problem for the large signal measurement than the small signal measurement. In the small signal transient methods, the small signal time constant τ_{ss} is a directly measured quantity and is independent of the accuracy to which the capacitance can be determined. Equation 2.42 relates the time constant τ_{ss} to

the capacitances C_i and C_f and the conductance G. It can be seen that τ_{ss} depends only on the difference between C_i and C_f, and thus, the calculation is not affected by uncertainties in the stray capacitance. The large signal method on the other hand depends strongly on the magnitudes of the capacitance. As was stated in section 4.4, the quantity $d/dt(C_i/C)^2$, which is calculated in the Zerbst plot analysis, depends on C^3, so that uncertainties in the magnitude of C can cause considerable error. In addition, the capacitance transient must be graphically differentiated, a procedure which can also add considerably to the error.

As is the case for many lifetime measurement techniques, both the large and small signal measurements are affected by generation-recombination by surface states. The analysis of Schroder provided a method for separating the bulk and surface generation components in the case of the large signal method. The accuracy of his method depends largely on the accuracy to which the surface generation velocity, S_o, can be determined. As was pointed out in Section 2.3, the determination of S_o can be greatly complicated by interband impact ionization effects which might occur at the beginning of the transient when large electric fields are present. As a result only an order of magnitude estimate of S_o is possible. For cases when the surface generation component is comparable to the bulk component, very large errors in the values of both S_o and τ_g are possible. The analysis presented in Section 4.4 showed that the small signal measurement is affected by surface generation-recombination in approximately the same way as the large signal measurement. In the small signal measurement, however, there is no way of ascertaining the relative magnitudes of the

surface and bulk components, without knowing accurately the surface recombination velocity. Examination of equations 2.85 and 4.19 show that the surface component is relatively less important for smaller lifetimes. The equations also show that the effect of the surface component can be minimized by increasing the diameter (D) of the gate electrode.

The temperature dependence study showed that both the small signal time constant and the large signal storage time decreased more rapidly then did $1/n_i$ in the temperature range where generation-recombination in the depletion region was expected to dominate. This result might be explained in part by an error in the determination of the bandgap. If the bandgap was actually larger than was measured, the dependence of $1/n_i$ would be steeper than expected, as implied by equation 5.1. The bandgap would have to be larger than the experimental value by about 0.1 eV in order to explain the experimental dependence. This value is far larger than the error in E_g of about 0.01 eV estimated in Section 5.1.1, so that it is unlikely that the experimental results could be explained by error. The best explanation for the data is that the energy of the recombination centers is different from the intrinsic Fermi energy, which results in a lifetime that decreases with increasing temperature. The magnitude of the difference, E_t-E_i, would have to be about 0.06 eV to explain the experimental dependence of τ_g and τ_{g-r}.

One experimental result that has not been adequately explained is the factor of ten difference between the large signal lifetime, τ_g, and the small signal lifetime, τ_{g-r}. It was shown in section 4.4 that part of the

discrepancy could be explained in terms of the S-R model by assuming that $E_t - E_i \neq 0$ and/or $\tau_{po} \neq \tau_{no}$. There is other evidence that implies that $E_t - E_i \neq 0$. The relative magnitudes of τ_{po} and τ_{no} could not be determined in these experiments. It is unlikely, however, that a factor of ten discrepancy could be explained in this manner, since in that case the trap levels would be extremely inefficient recombination centers. It is possible that part of the discrepancy could be due to surface effects. The discrepancy did not, however, seem to depend on the magnitude of the surface generation velocity. Future experiments should nevertheless be designed to minimize the surface generation component.

Finally, it should be emphasized that the lifetimes τ_g and τ_{g-r} are effective depletion lifetimes and are thus most useful for characterizing the behavior of depletion regions. It is possible to determine the neutral bulk lifetime, τ_B, with MIS measurements if the measurements are done at a high enough temperature such that diffusion of minority carriers from the neutral bulk is the dominant mechanism. There is a very large error possible, however, in the calculation of τ_B from the experimental data since the calculations depend on the quantity n_i^4. A factor of two error in n_i, for example, would result in a factor of 16 error in the bulk lifetime.

5.2 SURFACE PROPERTIES

5.2.1 Surface Potential

It is important to know the surface potential at zero gate voltage for a given insulator-semiconductor interface. The surface potential can, in principle, be determined from the capacitance of the MIS structure when V_G=0 (see Section 2.2.3). For most of the MIS structures on (Hg,Cd)Te, however, a considerable amount of hysteresis in the capacitance-voltage characteristics was noted. This hysteresis created an ambiguity in the capacitance of the structure at zero gate voltage. It was thus not possible to quantitatively determine the surface potential in most cases. Several experiments were undertaken to reduce the amount of hysteresis. Most of them were attempts either to reduce the occupation of the slow surface states or to wait for a long enough time in order that a stationary condition was attained. The occupation of the slow surface states could be affected by varying the gate voltage sweep rate. It was found that increasing the sweep rate generally resulted in a reduced amount of hysteresis. One is normally interested, however, in the equilibrium surface potential as a function of gate voltage. The hysteresis could also be reduced by sweeping the gate voltage over a smaller range of voltages. It was found that the average capacitance at zero volts (i.e., the average of the capacitance of rising and falling portions of the C-V curve) did not change very much when the magnitude of the voltage sweep was reduced.

In some cases the voltage sweep was stopped at zero volts until the capacitance stopped changing very much. It was found that the "final" capacitance achieved was different depending on whether the voltage had been sweeping in the positive or negative direction, indicating that a true equilibrium had not been reached. In both cases, however, the capacitance decayed to a value intermediate between the capacitances of the rising and falling portion of the C-V curve. Average capacitances, or these intermediate values of capacitance were used in calculations of estimated surface potentials for the zero gate voltage condition.

Thus, it was generally possible to only qualitatively determine the surface potential, that is whether the surface was accumulated, depleted, or inverted. For cases when it was difficult to tell whether the surface was depleted or inverted, it was often possible to infer the true surface potential by observing the behavior of the capacitance when the structure was biased into strong inversion. It had been found that at certain temperatures for certain materials, the structures exhibited non-equilibrium behavior when biased towards inversion. If structures fabricated on the same material were found to exhibit equilibrium or low frequency behavior, it could be inferred that an inversion layer was present at the surface beyond the gate, and thus, that the surface was weakly or strongly inverted. This effect was observed, for example, when structures were fabricated on the (111)A and (111)B surfaces. The structures on the B face exhibited non-equilibrium behavior, indicating a depleted surface, while the structures on the A face showed equilibrium

behavior, indicating an inverted surface. Some prior knowledge of the material's properties is necessary, of course, for this method to be useful.

In addition to the hysteresis, there is the problem that the metal-semiconductor work function difference (ϕ_{ms}) is not known for the gold-indium/ThF_4/(Hg,Cd)Te system. This makes it difficult to know how the surface potential would be affected if no metal gate was present. This problem was considered to be a second-order effect when compared to the hysteresis problem.

Most of the insulators used resulted in surfaces which were either near flatband or depleted for both n-type and p-type material. The surface potential was, however, affected by the orientation of the (Hg,Cd)Te. Anodization was found to strongly accumulate n-type surfaces and strongly invert p-type surfaces. The surface potential was also affected by the type of chemical etch used prior to the deposition of the insulator.

5.2.2 Surface State Densities

Surface state densities were measured for several insulator - (Hg,Cd)Te systems and for a few different orientations. The densities were generally in the 10^{11} - 10^{12} states per eV per cm^2 range. Both the conductance and the differentiation techniques were used.

The conductance technique was a useful method for measuring the fast surface densities of the (Hg,Cd)Te surface. Since the method determines the frequency response of the surface states, it is sensitive only to those surface states whose time constants are in within the range of frequencies being used. The method is therefore not affected by the "slow" states, whose time constants are considerably longer. For many applications it is most important to know the fast state density, since it is this density that determines the surface recombination velocity.

The method is expected to be reasonably accurate, since the measured conductance arises solely from the steady state loss due to the capture and emission of carriers by interface states, and is thus a more direct measure of these properties[13]. It is not necessary to match the experimental curve with the theoretical curve to obtain the results. The primary error is probably due to errors in the MIS capacitance, which must be known in order to convert the measured conductance to the equivalent conductance in parallel with the depletion capacitance (see equation 2.31). Some care must be taken, however, to measure the conductance at a potential at which the conductance associated with loss due carrier transitions to bulk recombination centers in the depletion region is negligible. Thus, this measurement cannot be done at surface potentials which are close to the potential required to strongly invert the surface.

The analysis presented in this work was valid for surface potentials corresponding to weak inversion. For measurements done in depletion and accumulation a statistical model must be used[13], which is somewhat more

difficult to apply. For most of the structures studied in this work the conductance divided by frequency (G/ω) was very small for this range of potentials, so that a more accurate measurement setup than the lock-in amplifier would have been required. Thus, the range of energies which could be examined with the conductance technique was rather small in this work.

The differentiation technique had the advantage that a wider range of energies could be examined. There are many disadvantages of this technique which limits its usefulness, however, One of the major disadvantages is that the method cannot distinguish between the effects due to fast and slow states. Since the measurement of a C-V curve took place in a time on the order of 20 seconds, the C-V curve was affected by surface states with time constants as large as 20 seconds. Another disadvantage is that the experimental curve had to be compared with the theoretical curve. This requires exact knowledge of the bulk doping and the insulator capacitance. Finally, the method involves graphical differentiation, which can result in considerable error. If one is concerned with the densities of both the fast and slow surface states, however, this method is still useful in the comparison of different insulator/(Hg,Cd)Te systems.

In comparing the effective surface state densities obtained with the two methods, it was found that the methods were in agreement only for high densities of fast surface states ($10^{12}cm^{-2}eV^{-1}$). If the density of fast surface states was low ($10^{11}cm^{-2}eV^{-1}$), the differentiation method almost always predicted a larger density of surface states than did the

conductance method. It is felt that this result is due to the fact that for low densities of fast states, the effect of slow states on the differentiation measurement is relatively more important than for high densities of fast states.

In both measurements it was necessary to determine the surface potential at which the measurement was being made in order to relate a particular surface state density to the position of the states in the energy gap. This was done by computing the surface potential from the measured high frequency capacitance. Since the capacitance and the doping was not known with absolute accuracy, some error in the surface potential was possible. It is felt, however, that knowing the exact energy dependence of the surface state density is not as important as knowing the magnitude of the surface state density.

Most surface state density measurements were done on n-type $Hg_{0.6}Cd_{0.4}Te$ oriented in the (111) direction. The orientations (110) and (100) were not studied due to a lack of similar material oriented in those directions. Some measurements were done on unoriented x=0.3 and x=0.4 (Hg,Cd)Te. Both the ThF_4/(Hg,Cd)Te and the ThF_4/Anodic Oxide/(Hg,Cd)Te systems were studied.

The (111)A and (111)B surfaces were found to exhibit very different surface characteristics. The density of fast surface states near the intrinsic Fermi energy was typically on the order of $10^{11}cm^{-2}eV^{-1}$ for the B surface and $10^{12}cm^{-2}eV^{-1}$ for the A surface, when ThF_4 was used as the

insulator. The B surface was depleted and the A surface was weakly inverted. The surface state densities for anodic films on the B surface were the lowest observed, about 2 x $10^{10}cm^{-2}eV^{-1}$ near midgap. It is interesting to note that the densities for anodic films were obtained using the differentiation method, so that the measured densities were due to both fast and slow states. The C-V curves used in the analysis were, however, obtained at a temperature of 80K. The time constants of the slow states were expected to be very long at this temperature, and in fact, the C-V curves exhibited very few of the effects, such as hysteresis, normally associated with slow surface states. Conductance measurements could not be done on these films due to instabilities in the surface potential. The properties of unoriented material were somewhat different than observed for the (111) orientation. The C-V curves exhibited a smaller amount of hysteresis, and in some cases the n-type surfaces were slightly accumulated. Fast surface state densities as low as 5 x $10^{10}cm^{-2}eV^{-1}$ were observed on unoriented x=0.4 material with a ThF_4 insulator. Clearly, a more complete study of the orientation dependence of the surface properties is necessary to fully characterize (Hg,Cd)Te surfaces.

5.3 OTHER EXPERIMENTS

5.3.1 Insulators

A variety of insulators were examined, most of which were deposited by vacuum evaporation techniques. Of all the insulators tried, ThF_4 met the requirements outlined in section 4.1 the best. Although some of the

insulators exhibited properties superior in some ways to those of ThF_4, there were some bad properties that ruled out their use. Anodic films had lower densities of fast surface states, but also exhibited large densities of slow states and instability in flatband voltage, expecially at high temperatures. The anodic films also contained a large amount of fixed surface charge which caused p-type surfaces to be heavily inverted, so that the films were only useful for characterizing n-type material. The insulators LaF_3 and SiO_x did show some promising characteristics, but the characteristics were not very repeatable. It is expected that sputtered insulators would exhibit better properties than evaporated insulators. Unfortunately, the proper sputtering equipment was not available during this research.

5.3.2 Diffusion Experiments

The diffusion of various impurities and the self-diffusion of Hg were studied with the MIS technique. Indium was found to be a donor in $Hg_{0.6}Cd_{0.4}Te$. The surface concentration of electrically active indium was found to be about $1.5 \times 10^{15} cm^{-3}$ with a diffusion temperature of 95°C. An angle lap experiment determined the diffusion constant of indium at 95°C to be $3.4 \times 10^{-15} m^2/sec$. An activation energy of 1.6 eV was determined by comparing the depths of diffusion at 71°C and 95°C. This activation energy is approximately four times the bandgap, indicating a vacancy assisted diffusion process.

The donor aluminum did not significantly diffuse into the bulk even when annealed at 120°C for three hours. This is thought to be due to the presence of a thin aluminum oxide layer which prevented the diffusion. The effects of the aluminum anneal on the surface were quite pronounced. Almost no hysteresis in the C-V curves was noticeable, and the transition from maximum to minimum capacitance was very sharp. Variable frequency measurements did, however, indicate considerable distortion of the capacitance voltage curve due to surface states at low frequencies for biases close to strong inversion. Time did not permit a detailed examination of the possible causes for this phenomenon.

A study of the diffusion of the donor gallium was hampered by the fact that the gallium seemed to form an alloy with the (Hg,Cd)Te. There was some evidence, however, that the gallium had diffused to a depth of at least 15 μm after a 71°C, one-hour anneal.

The acceptor gold when electroplated onto a p-type (Hg,Cd)Te surface did not diffuse significantly into the bulk after a one-hour anneal at 120°C. The average doping over a depth of 600A was $2 \times 10^{17} cm^{-13}$. However, when 2.5 micrometers of material were removed, no increase in acceptor concentration over the bulk value ($2 \times 10^{14} cm^{-3}$) was observed. This result is considered preliminary and seems vastly different from the results obtained by others[29] with the electrodeless $AuCl_3$ gold deposition process.

The process of the self-diffusion of Hg into $Hg_{0.6}Cd_{0.4}Te$ was also studied. The results on an experiment, in which the Hg vapor pressure was

varied while the temperature of the (Hg,Cd)Te was held constant at 300°C, were erratic, and thus, no definite conclusions could be made. In a subsequent experiment the depth of the diffusion of Hg was measured after a two-week, 300°C isothermal anneal. The junction depth of 4.0 mils was nearly the same as the value of 3.6 mils obtained in a previous study[33] which was carried out under similar conditions.

5.3.3 Surface Preparation Experiments

The effects on the C-V characteristics of several different methods of preparing the surface prior to the fabrication of MIS structures were examined. These treatments were not considered in detail, however, and therefore the results are considered to be only tentative.

A few chemical etches were surveyed. The chemical etch was applied after an etch in 1:5 bromine/methanol. An etch in concentrated HCl was found to not significantly alter the MIS properties. Both H_2SO_4 and H_2O_2 were found to affect the MIS characteristics significantly. The H_2O_2 treatment, which consisted of a 10 minute bath in 30% H_2O_2 at 40°C followed by a 10 minute rinse in isopropyl alcohol, seemed to reduce the fast surface state density, but resulted in considerably more hysteresis than normal. The n-type surfaces were slightly accumulated. The H_2SO_4 treatment, which was a 10 minute ultrasonic etch in concentrated H_2SO_4 at room temperature, resulted in a somewhat reduced density of both fast and slow surface states. The n-type surfaces were weakly inverted. These etches

SECTION 6

SUMMARY AND CONCLUSIONS

The goal of this thesis was to develop and characterize the properties of MIS structures on $Hg_{0.6}Cd_{0.4}Te$. After having developed a workable MIS structure, the MIS techniques were used to characterize the bulk and surface properties of (Hg,Cd)Te and study surface treatments and the diffusion of impurities.

A variety of vacuum evaporated insulators were studied. ThF_4 was found to be a durable insulator which resulted in consistantly high yields of operative MIS structures with reasonably low surface state densities. The Au-In/ThF_4 (Hg,Cd)Te structure consistently resulted in depleted surfaces on both n and p-type (Hg,Cd)Te.

The surface properties of various insulator/(Hg,Cd)Te systems were determined. The (111)A surface was found to have significantly different properties than the (111)B surface. With an insulating coating of ThF_4, the A surface was weakly inverted and had fast surface state densities on the order of $10^{12}cm^{-2}eV^{-1}$, while the B surface was depleted and had fast surface state densities on the order of $10^{11}cm^{-2}eV^{-1}$. Surface state densities as low as $5 \times 10^{10}cm^{-2}eV^{-1}$ were measured on unoriented material.

Anodic oxide films were found to have the lowest density of fast surface states, with densities on the (111)B surface of about 2 x $10^{10} cm^{-2} eV^{-1}$. The anodic films storngly accumulated n-type surfaces and were found to result in unstable flatband voltages, especially at high temperatures.

The MIS structure was successfully used to determine bulk parameters. In particular, the majority carrier type and concentration were determined. Furthermore, the optical sensitivity of the structures permitted the determination of the bandgap.

Methods for determining the rate of the generation and recombination of minority carriers were analyzed and further developed. Both the large and small signal methods were applied to x=0.4 (Hg,Cd)Te MIS structures. A large discrepancy between the methods was noted, which could be partly explained in terms of the Shockley-Read single level trap model by assuming that the trap level was different than the intrinsic Fermi level. It was found that the surface effects both measurements in approximately the same way. Variable temperature measurements indicated the Shockley-Read mechanism was the most important, but it was again necessary to assume that the trap level was different than the intrinsic Fermi level to obtain a good fit to the data. An activation energy, $E_t - E_i$, of about 0.06 eV was determined from large signal measurements. Typical values of the large signal lifetime at 147K were 10-100 μsec for lightly doped n-type material and 1-10 μsec for lightly doped p-type material. The small signal lifetimes at 147K were about 10 μsec for n-type and 1 μsec for p-type material. Surface generation velocities determined with the large signal

method were typically about 10-100 cm/sec for ThF_4 coated (111)B surfaces and 1-10 cm/sec for anodized (111)B surfaces.

The MIS technique was applied to several engineering problems. Because of the ability to measure net doping, the MIS technique was useful in studying the diffusion of impurities into (Hg,Cd)Te such as indium, gold, gallium, and aluminum and the self-diffusion of mercury. The technique could also determine the effects of the impurities on the minority carrier lifetime and the surface condition. A brief survey of the effects of various surface treatments on the MIS properties was conducted. These studies were not carried out in great detail, and serve more to illustrate the potential usefulness of the MIS technique in studying surface treatments.

Several areas of future study are indicated by the results of this thesis. Other methods of depositing insulators, such as sputtering, should be examined. A great deal more work could be done in studying different ways of preparing the surface prior to fabrication of MIS structures. The effects of the aluminum anneal on the surface properties of (Hg,Cd)Te were interesting, and require more study to determine the mechanism responsible for the improved characteristics. The surface properties of other orientations besides the (111) orientation should be examined. In addition, (Hg,Cd)Te with other x-values than x=0.4 should be studied since the MIS properties could be significantly different. The MIS technique provided a great deal of information about generation-recombination mechanisms in (Hg,Cd)Te. Other techniques such as optical absorption and bulk lifetime measurement, used in conjunction with the MIS techniques, could more definitely identify the recombination centers in (Hg,Cd)Te.

In conclusion, an MIS technology for (Hg,Cd)Te was developed which:

(1) Enabled the accurate measurement of bulk doping levels.

(2) Permitted bandgap determination.

(3) Determined the dominant generation/recombination mechanisms in the material and their characteristics.

(4) Quantitatively determined surface state densities.

(5) Demonstrated the usefulness of MIS diagnostics in the study of insulators and surface treatments.

(6) Was used to study impurity diffusion processes in (Hg,Cd)Te.

It is felt, however, that further development of the MIS technology in (Hg,Cd)Te is warranted, particularly in the areas of insulator selection and surface processing.

APPENDIX

A.1 IDENTIFICATION OF (111)A AND (111)B FACES

Mercury-cadmium-telluride consists of Group II atoms (mercury and cadmium) and Group VI atoms (tellurium) in a zinc-blende crystal structure. The (111) surface of this structure will terminate either with Group II atoms or Group VI atoms. The surface which terminates on the Group II atoms is called the (111)A surface and the other surface is called the (111)B surface. These surfaces will generally exhibit different physical properties and it is, therefore, important to distinguish between them.

An etch has been developed which distinguishes these two faces[31]. This etch consists of one part HCl, two parts HNO_3, and three parts H_2O. The procedure is to polish and etch the slab to produce a smooth surface on both sides. The slab is then immersed in the HCl: HNO_3 solution for fifteen seconds. After rinsing in H_2O, the slab surfaces are compared. One side will stain with either a white or brown appearance while the other side will remain clear. The side which remains clear exhibits triangular etch pits which in some cases define grain boundaries, while the stained side shows a flat, uniform "grainy" appearance.

There is strong evidence that the (111)A surface is the surface which shows the triangular etch pits, and that the (111)B surface is the surface which stains. This conclusion is based upon the results of studies[32] done on HgTe and CdTe at MIT Lincoln Laboratory. The (111)A and (111)B surfaces of HgTe and CdTe were etched in a similar solution, i.e., one part (by volume) concentrated HCl and one part concentrated HNO_3. In both cases the Group II surfaces exhibited triangular etch pits which sometimes defined grain boundaries while the Group VI (tellurium) surface exhibited a film which consisted of a random distribution of very flat triangular figures for CdTe and exhibited a grainy, unstructured appearance for HgTe. Thus in our work the surface that stained has been defined as the B surface and the surface which exhibited etch pits has been defined as the A surface.

A.2 AUGER AND RADIATIVE GENERATION-RECOMBINATION IN DEPLETION REGIONS

The effects of generation-recombination in the depletion region of an MIS structure via the Auger and radiative mechanisms will be considered in this section for both the large and small signal measurement. It will be shown that these mechanisms are negligible in the depletion regions of $Hg_{0.6}Cd_{0.4}Te$ MIS structures.

A.2.1. Radiative Mechanism

The net rate of recombination U is defined as

$$U = r\text{-}g \ \text{sec}^{-1}\text{cm}^{-3} \qquad \text{(A.1)}$$

where r is the recombination rate in $sec^{-1}cm^{-3}$ and g is the generation rate in $sec^{-1}cm^{-3}$. It has been shown[18] that for the radiative mechanism the net recombination rate is given by

$$U_r = G_r \left(\frac{np - n_i^2}{n_i^2} \right) \tag{A.2}$$

where G_r is defined by equation 2.69 and n and p are the densities of electrons and holes, respectively. In general the concentrations of electrons and holes will be functions of position. This equation will be used to derive expressions relating to the large and small signal measurements.

Large Signal Measurements

As is normally the case when treating strongly reverse biased depletion regions the carrier densities will be assumed to very small in the depletion region, so that $n \ll n_i$, $p \ll n_i$ and thus $np \ll n_i^2$, which reduces equation A.2 to

$$U_r = -G_r \tag{A.3}$$

This is equivalent to assuming that the recombination of carriers in the depletion region is negligible. The net generation rate of electron-hole pairs per unit area in the depletion region by analogy to equation 2.74 will then be given by

$$g = G_r (W-W_f) \tag{A.4}$$

Eqn. 2.71 defines the intrinsic radiative lifetime τ_{Ri} for an intrinsic semiconductor as

$$\tau_{Ri} = \frac{n_i}{2G_r} \tag{A.5}$$

so that

$$G_r = \frac{n_i}{2\tau_{Ri}} \tag{A.6}$$

and equation A.4 can be rewritten as

$$g = \frac{n_i}{2\tau_{Ri}} \quad (W-W_f) \tag{A.7}$$

Comparison of equation A.7 with 2.74 reveals that the effective lifetime for radiative generation in a reverse biased depletion region is equal to the intrinsic radiative lifetime τ_{Ri}. The ratio of the extrinsic radiative lifetime τ_R, as defined by equation 2.70, and the intrinsic lifetime is given by

$$\tau_{Ri}/\tau_R = \frac{N_B}{2n_i} \tag{A.8}$$

For temperatures at which generation in the depletion region is the dominant process $N_B >> n_i$ so that the intrinsic lifetime is much greater than the extrinsic lifetime. For most of the material used in this work (x = 0.4 (Hg,Cd)Te), $|N_D - N_A| \approx 2 \times 10^{14}$ cm^{-3}. At 147K $n_i \approx 2 \times 10^{10}$ cm^{-3} so that $\tau_{Ri}/\tau_R \approx 5 \times 10^3$. The calculated extrinsic radiative lifetimes were on the order of 50 μsec, so that $\tau_{Ri} \approx 250$ msec. The measured generation lifetimes were on the order of 100 μsec, so that the radiative mechanism is clearly not important in the depletion regions of $Hg_{0.6}Cd_{0.4}Te$ for the large signal measurement.

Small Signal Measurements

In this case the carrier densities will be a function of position in the depletion region. The carrier densities will be defined in terms of the potential ψ and the quasi-Fermi potentials ϕ_p and ϕ_n for holes and electrons respectively as

$$n = n_i \exp\left[q/kT\ (\psi - \phi_n)\right]$$
$$p = n_i \exp\left[q/kT\ (\phi_p - \psi)\right] \qquad \text{(A.9)}$$

The product np will be given by

$$np = n_i^2 \exp\left[q/kT\ (\phi_p - \phi_n)\right] \qquad \text{(A.10)}$$

which for small applied voltages, $V_D = \phi_p - \phi_n << kT/q$, reduces to

$$np \approx n_i^2 \left(qV_D/kT + 1 \right) \tag{A.11}$$

Substitution of equation A.11 into A.2 results in

$$U_r \approx -G_r \; qV_D/kT \tag{A.12}$$

The current J_r resulting from U_r will then be given by

$$|J_r| = q \int_o^{W_m} |U_r| dx = \frac{q^2 W_m G_r V_D}{kT} \tag{A.13}$$

and the resistance R_r will thus be

$$R_r^{-1} = \frac{\partial J_r}{\partial V_D} = \frac{q^2 W_m G_r}{kT} \tag{A.14}$$

Substitution of $\psi_B = \frac{kT}{q} \ln \left(\frac{N_B}{n_i} \right)$ and $\tau_{Ri} = \frac{n_i}{2G_r}$ into A.14 results in

$$R_r^{-1} = \frac{q \; n_i \; W_m}{2\psi_B \tau_{Ri}} \ln \left(\frac{N_B}{n_i} \right) \tag{A.15}$$

which is of the same form as equation 2.59, i.e.,

$$R_r^{-1} = \frac{q \; n_i W_m}{2\psi_B \tau_{reff}} \tag{A.16}$$

where $\tau_{reff} = \tau_{Ri}/\ln\left(\frac{N_B}{n_i}\right)$ (A.17)

For T = 147K, $N_B \approx 2 \times 10^{14} cm^{-3}$ and $n_i \approx 2 \times 10^{10} cm^{-3}$, $\ln\left(\frac{N_B}{n_i}\right) \approx 10$ so that $\tau_{reff} \approx \tau_{Ri}/10 = 25$ msec. This effective radiative lifetime is 3 orders of magnitude larger than observed small signal lifetimes, which were on the order of 10 μsec.

A.2.2. Auger Mechanism

It has been shown[18] that the net recombination rate for the Auger mechanism is given by,

$$U_A = \frac{(np - n_i^2)(n + \beta p)}{2n_i^2 \tau_{Ai}} \quad (A.18)$$

where $\beta = \frac{\mu^{1/2}(1 + 2\mu)}{2 + \mu} \exp\left[-\left(\frac{1-\mu}{1+\mu}\right)\frac{Eg}{kT}\right]$ (A.19)

μ is the effective mass ratio m_e^*/m_h^*, Eg is the bandgap, and τ_{Ai} is the intrinsic Auger lifetime. Equation A.18 will be used to derive expressions for the large and small signal measurements.

Large Signal Measurement

As was the case for the radiative mechanism, $np \ll n_i^2$ in the depletion region. Equation A.18 then reduces to

$$U_A \approx - \frac{n + \beta p}{2\tau_{Ai}} \tag{A.20}$$

The net generation rate per unit area in the depletion region will thus be given by

$$g = \frac{n + \beta p}{2\tau_{Ai}} \quad (W-W_f)$$

$$= \frac{n + \beta p}{n_i} \times \frac{n_i}{2\tau_{Ai}} \quad (W-W_f) \tag{A.21}$$

$$= \frac{n_i}{2\tau_{Aeff}} \quad (W-W_f)$$

where $$\tau_{Aeff} = \frac{n_i}{n + \beta p} \tau_{Ai} \tag{A.22}$$

Since $n \ll n_i$ and $p \ll n_i$ in the depletion region, the effective Auger lifetime will be much less than the intrinsic Auger lifetime. As was mentioned in section 4.4, the extrinsic Auger lifetime, defined by equation 2.72, for n-type $Hg_{0.6}Cd_{0.4}Te$ at 147K with $N_D - N_A = 2 \times 10^{14} cm^{-3}$ was on the order of milliseconds. The intrinsic Auger lifetime is a factor of $\left(N_B/n_i\right)^2$ larger than the extrinsic lifetime. Thus the effective Auger lifetime for this measurement will be far larger than the effective radiative lifetime.

Small Signal Measurement

In this case one must consider the variation of the carrier densities n and p with position. Substitution of eqns. A.9 and A.10 into A.19 results

$$U_A = \frac{n_i}{2\tau_{Ai}} \left[\exp\left[\left(\phi_p-\phi_n\right) q/kT\right] - 1\right] \left[\exp\left[\frac{q}{kT}\left(\psi-\phi_n\right)\right] + \beta\exp\left[q/kT(\phi_p-\psi)\right]\right] \tag{A.23}$$

which with the small signal assumption ($\phi_p-\phi_n=V_D \ll kT$) reduces to

$$U_A = \frac{n_i q\, V_D}{\tau_{Ai} kT}\, \beta^{\frac{1}{2}} \cosh\left[\frac{q}{kT}\left(\psi - \frac{\phi_n+\phi_p}{2} - \frac{kT}{q} \ln \beta^{\frac{1}{2}}\right)\right] \tag{A.24}$$

It will be assumed that the potential varies linearily across the depletion region, so that equation 2.54 can be substituted for the quantity $\psi - \frac{\phi_n+\phi_p}{2}$. In that case the total current J_A can be written as

$$J_A = q \int_0^{W_m} U_A dx = \frac{n_i q^2 V_D}{\tau_{Ai} kT}\, \beta^{\frac{1}{2}} \int_0^{W_m} \cosh\left[\frac{q\psi_B}{kT}\left(1 - 2x/W_m\right) - \ln\beta^{\frac{1}{2}}\right] dx \tag{A.25}$$

The integral can be solved exactly to yield the following expression for J_A:

$$J_A = \frac{q\, n_i W_m V_D}{2\psi_B \tau_{Ai}} (\beta+1) \sinh\left(\frac{q\psi_B}{kT}\right) \tag{A.26}$$

The resistance R_A will then be defined by

$$R_A^{-1} = \frac{\partial J_A}{\partial V_D} = \frac{q\, n_i W_m}{2\psi_B \tau_{Ai}} (\beta+1) \sinh\left(\frac{q\psi_B}{kT}\right)$$

$$= \frac{q\, n_i W_m}{2\psi_B \tau_{Aeff}} \qquad (A.27)$$

where $$\tau_{Aeff} = \tau_{Ai} \left[(\beta + 1) \sinh \left(\frac{q\psi_B}{KT}\right)\right]^{-1} \qquad (A.28)$$

For n-type semiconductors with $\mu < 1$, $\beta << 1$ and also $\left| q\psi_B/kT \right| >> 1$ so that equation A.28 can be simplified to

$$\tau_{Aeff} = \tau_{Ai} \frac{n_i}{N_B} \qquad (A.29)$$

Since the extrinsic Auger lifetime τ_A is defined as

$$\tau_A = \left(\frac{n_i}{N_B}\right)^2 \tau_{Ai} \qquad (A.30)$$

equation A.29 can be rewritten as

$$\tau_{Aeff} = \frac{N_B}{n_i} \tau_A \qquad (A.31)$$

For n-type $Hg_{0.6}Cd_{0.4}Te$ at 147K with $N_B = 2 \times 10^{14}$ cm^{-3} and $n_i \simeq 2 \times 10^{10}$ cm^{-3}, $\tau_{Aeff} = 10^4 \tau_A$. Thus the effective Auger lifetime for the small signal measurement is four orders of magnitude larger than the extrinsic Auger lifetime which was on the order of a millisecond for this material. Again the effective lifetime Auger lifetime is much larger than the effective radiative lifetime, and both are much larger than experimentally measured values.

A.3 Small Signal Capacitance Transient

In this section it will be shown that small signal capacitance transient is characterized by an exponential decay with time constant $\tau_{ss} = R_o (C_i + C_D)$ where R_o is the equivalent resistance in parallel with the depletion capacitance, C_D.

For the case of strong inversion the total voltage across the MIS structure is given by

$$V_G = V_i + \psi_s(inv)$$

$$= \frac{Q_n + qN_B W_m}{C_i} + \frac{qN_B W_m^2}{2\varepsilon_s} \qquad (A.32)$$

Upon application of a small voltage step, ΔV_G, equation A.32 becomes

$$V_G + \Delta V_G = \frac{(Q_n + \Delta Q_n) + qN_B(W_m + \Delta W)}{C_i} + \frac{qN_B(W_m + \Delta W)^2}{2\varepsilon_s} \tag{A.33}$$

$$= \frac{Q_n + qN_B W_m}{C_i} + \frac{\Delta Q_n + qN_B\ \Delta W}{C_i} + \frac{qN_B\left[W_m^2 + 2W_m\Delta W + (\Delta W)^2\right]}{2\varepsilon_s} \tag{A.34}$$

$$= V_i + \Delta V_i + \psi_s(\text{inv}) + \Delta\psi_s \tag{A.35}$$

where $$\Delta\psi_s = \frac{qN_B\ W_m\ \Delta W}{\varepsilon_s} \tag{A.36}$$

if $\Delta W << W_m$, and

$$\Delta V_i = \frac{\Delta Q_n + qN_B\ \Delta W}{C_i} \tag{A.37}$$

Equation A.37 can be solved for ΔW and the resulting expression substituted into equation A.36 to result in the following expression for $\Delta\psi_s$:

$$\Delta\psi_s = \frac{C_i}{C_D}\ \Delta V_i - \frac{\Delta Q_n}{C_D} \tag{A.38}$$

where the relation $C_D = \varepsilon_s/W_m$ has been used. Since $\Delta V_i = \Delta V_G - \Delta\psi_s$, equation A.38 can be rewritten as

$$\Delta\psi_s = \left(\frac{C_i}{C_i + C_D}\right)\Delta V_G - \left(\frac{1}{C_i + C_D}\right)\Delta Q_n \tag{A.39}$$

Differentiation of equation A.39 with respect to time results in

$$\frac{d\ (\Delta\psi_s)}{dt} = -\frac{1}{C_i + C_D}\ \frac{d\ (\Delta Q_n)}{dt} \tag{A.40}$$

For small signals the current which flows to the surface, J_s, will be linearily related to $\Delta\psi_s$ by the resistance R_o. Thus

$$\frac{d\ (\Delta Q_n)}{dt} = J_s = \Delta\psi_s/R_o \tag{A.41}$$

which results in the following differential equation for $\Delta\psi_s$:

$$\frac{d\ (\Delta\psi_s)}{dt} + \frac{1}{R_o(C_i + C_D)}\ \Delta\psi_s = 0 \tag{A.42}$$

The solution of this equation due to a step change in voltage is:

$$\Delta\psi_s = \Delta\psi_s(t = 0)\ e^{-t/\tau_{ss}} \tag{A.43}$$

where $\tau_{ss} = R_o (C_i + C_D)$. The change in depletion capacitance is related to the change in depletion width by

$$\Delta C_D = \frac{\varepsilon_s}{W_m + \Delta W} - \varepsilon_s / W_m$$

$$\simeq \frac{C_D^2}{\varepsilon_s} \Delta W \tag{A.44}$$

for $\Delta W_m << W_m$. The change in depletion width is related to the change in surface potential by equation A.36, so that

$$\Delta C_D = \frac{C_D^3}{qN_B \varepsilon_s} \Delta\psi_s \tag{A.45}$$

Finally, ΔC_D is related to the change in the MIS capacitance ΔC by

$$\Delta C = \frac{C_i (C_D + \Delta C_D)}{C_i + C_D + \Delta C_D} - \frac{C_i C_D}{C_i + C_D}$$

$$\simeq \frac{C_i \Delta C_D}{C_i + C_D} \tag{A.46}$$

for $\Delta C_D << C_D$. Equations A.46, A.45, and A.43 can be combined to yield

$$\Delta C(t) = \frac{C_i C_D^3}{qN_B \varepsilon_s (C_i + C_D)} \Delta\psi_s \ (t = 0) \ e^{-t/\tau_{ss}} \qquad (A.47)$$

Thus it has been shown that the capacitance will decay with a time constant $\tau_{ss} = R_0 (C_i + C_D)$.

References

1. A.F. Tasch, R.A. Chapman and B.H. Breazeale, "Field Effect Measurements in the (Hg,Cd)Te Surface," Jour. App. Phys. 41, 4202 (1970).

2. A.F. Tasch, D.D. Buss, R.T. Bate and B.H. Breazeale, "Landau Levels in the Inversion Layer on p-Type $Hg_{1-x}Cd_xTe$," Proc. Tenth International Conference on the Physics of Semiconductors, Cambridge, MA, Aug. 19-21, 1970, p. 458.

3. M.R. Johnson, M.A. Kinch and B.H. Breazeale, "Short Wavelength (Hg,Cd)Te Detectors (U)," Proc. IRIS Detector Specialty Group Meeting, March 1972, p. 115(S).

4. M.A. Kinch, "(Hg,Cd)Te IR Detector Processing Techniques (U)," Technical Report AFAL-TR-72-118(C), Air Force Contract No. F33615-70-C-1529, May 1972.

5. A.A. Pellegrino, "Surface Related Effects in (Hg,Cd)Te," Masters Thesis, Department of Electrical Engineering, Massachusetts Institute of Technology, May 1974.

6. M. Michael, W.F. Leonard, "MIS Capacitance and Derivative of Capacitance with Application to Non-parabolic Band Semiconductors," Solid State Electronics, Vol. 17, 1974, pp. 71-85.

7. S.M. Sze, Physics of Semiconductor Devices, (Wiley, New York, 1969), Chap. 9.

8. J.L. Schmit, "Intrinsic Carrier Concentration of $Hg_{1-x}Cd_xTe$ as a Function of x and T Using k·p Calculations," J. Applied Physics, Vol. 41, pp. 2876-2879, June 1970.

9. A.S. Grove. Physics and Technology at Semiconductor Devices (Wiley, New York, 1967), Chap. 12.

10. F.P. Heiman, "The Effects of Oxide Traps on the MOS Capacitance," I.E.E.E. Trans. on Electron Devices, Vol. ED-12, April 1965, pp. 167-178.

11. E.J.M. Kendall, "On the Hysteresis and Memory Properties of the Silicon-Silicon Nitride System," Solid State Electronics, Vol. 14, pp. 791-798, September 1971.

12. J.R. Brews, J. Appl. Phys., 45, No. 3, March 1974, p. 1276.

13. E.H. Nicollian and A. Goetzberger, "The Si-SiO_2 Interface-Electrical Properties as Determined by the Metal-Insulator-Silicon Conductance Technique," Bell System Tech. J., No. 6, Vol. 46, p. 1055, July-August, 1967.

14. L.M. Terman, "An Investigation of Surface States at a Silicon/Silicon Dioxide Interface Employing Metal-Oxide-Silicon Diodes," Solid State Electron., 5, 285, (1962).

15. S.R. Hofstein, "Minority Carrier Lifetime Determination from Inversion Layer Transient Response," IEEE Transactions on Electron Devices, Vol. ED-14, November 1967.

16. W. Shockley and W.T. Read, Jr., "Statistics of Recombinations of Holes and Electrons," Phys. Rev., Vol. 87, pp. 835-842, September 1952.

17. C. Sah, R. Noyce, W. Shockley, "Carrier Generation and Recombination in P-N Junctions and P-N Junction Characteristics," Proceedings of the IRE, September 1957.

18. J.S. Blakemore, Semiconductor Statistics, (Pergamon Press, Inc., New York, 1962) Chap. 5, 6, 8.

19. M.A. Kinch, M.J. Brau, and A. Simmons, "Recombination Mechanisms in 8-14-μ HgCdTe," J. Appl. Phys., Vol. 44, No. 4, pp. 1649-1663, April 1973.

20. F. Heiman, "On The Determination of Minority Carrier Lifetime from the Transient Response of an MOS Capacitor," IEEE Transactions on Electron Devices, Vol. ED-14, pp. 781-784, November 1967.

21. M. Zerbst, "Relaxation Effekte on Halbeiter-Isolator-Grenz Flachen," Z. Angew Phys, Vol. 22, pp. 30-33, May 1966.

22. D. Schroder and H. Nathanson, "On the Separation of Bulk and Surface Components of Lifetime Using the Pulsed MOS Capacitor," Solid State Electronics, Vol. 13, pp. 577-582, May 1970.

23. C.T. Sah and H.S. Fu, "Current and Capacitance Transient Responses of MOS Capacitor, Part I," Phys. Stat. Sol., 11, 297 (1972).

24. C.T. Sah and H.S. Fu, "Current and Capacitance Transient Responses of MOS Capacitor, Part II," Phys. Stat. Sol., 14, 59, (1972).

25. A.J. Steckl, R.D. Nelson, B.T. French, R.A. Gudmundsen, and D. Schecter, "Application of Charge-Coupled Devices to Infrared Detection and Imaging," Proc. of the IEEE, Vol. 63, No. 1, January 1975.

26. W. Heitman and E. Ritter, "Production and Properties of Vacuum Evaporated Films of Thorium Fluoride," Applied Optics, Vol. 7, pp. 307-309, February 1968.

27. T.T.S. Wong, "Theoretical and Experimental Study of the Anomalous Hall Properties of (Hg,Cd)Te," Masters Thesis, Department of Electrical Engineering, Massachusetts Institute of Technology, May 1974.

28. J. Schmit and E. Johnson, "Exploratory Development on $Hg_{1-x}Cd_xTe$ Improvement, Phase II," Interim Technical Report, AFML Contract No. F33615-74-C-5041, July 1976.

29. A.L. Andrievskii, A.S. Teodorovich, and A.D. Shneider, Sov. Phys. Semicond., 7, No. 8 (1974), American Institute of Physics, translated, p. 1112.

30. J. Schmit and E. Stelzer, "Effect of Annealing on the Carrier Concentration of $Hg_{0.6}Cd_{0.4}Te$," Honeywell Interoffice Correspondence, July 1976.

31. J. Schmit and M. Hitchell, "Orientation Dependent Etching of (Hg,Cd)Te," Honeywell Interoffice Correspondence Memo, 1974.

32. E.P. Warekois, M.C. Lavine, A.N. Mariano, and H.C. Gatos, "Crystallographic Polarity in the II-VI Compounds," J. Appl. Phys., Vol. 33, No. 2, pp. 690-696, February 1962.

33. H.R. Huff, H. Kraus, and B.H. Breazeale, "Diffusion of Mercury in $Hg_{1-x}Cd_xTe$," Proc. of the IRIS Specialty Group on IR Detectors, July 1974.

34. E.O. Kane, J. Phys. Chem. Solids, 1, 249, (1957).

35. J. Baars and F. Sorgen, S.S. Comm. 10, 875 (1972).

36. K. Zaininger and F. Heiman, "The C-V Technique as an Analytical Tool," Solid State Tech., Vol. 13; Part 1, May 1970, Part 2, June 1970.